Optical Excitations in Biological Systems: Multiscale-Simulation Strategies and Applications to Rhodopsins

VON DER FAKULTÄT FÜR LEBENSWISSENSCHAFTEN
DER TECHNISCHEN UNIVERSITÄT CAROLO–WILHELMINA
ZU BRAUNSCHWEIG
ZUR ERLANGUNG DES GRADES EINES
Doktors der Naturwissenschaften
(DR. RER. NAT.)

GENEHMIGTE

DISSERTATION

VON DIPL. PHYS. MARIUS WANKO
AUS BERLIN-WILMERSDORF

1. Referent: Professor Dr. Marcus Elstner
2. Referent: Professor Dr. Thomas Frauenheim
eingereicht am: 14.01.2009

mündliche Prüfung (Disputation) am: 05.06.2009

Druckjahr: 2009

Publications

Teilergebnisse aus dieser Arbeit wurden mit Genehmigung der Fakultät für Lebenswissenschaften, vertreten durch den Mentor der Arbeit, in folgenden Beiträgen vorab veröffentlicht:

[1] *A global investigation of excited state surfaces within time-dependent density-functional response theory*
Wanko, M.; Garavelli, M.; Bernardi, F.; Niehaus, T. A.; Frauenheim, T.; Elstner, M. *J. Chem. Phys.* **2004**, *120*, 1674–1692.

[2] *Calculating Absorption Shifts for Retinal Proteins: Computational Challenges*
Wanko, M.; Hoffmann, M.; Strodel, P.; Koslowski, A.; Thiel, W.; Neese, F.; Frauenheim, T.; Elstner, M. *J. Phys. Chem. B* **2005**, *109*, 3606–3615.

[3] *Color Tuning in Rhodopsins: The Mechanism for the Spectral Shift between Bacteriorhodopsin and Sensory Rhodopsin II*
Hoffmann, M.; Wanko, M.; Strodel, P.; König, P. H.; Frauenheim, T.; Schulten, K.; Thiel, W.; Tajkhorshid, E.; Elstner, M. *J. Am. Chem. Soc.* **2006**, *128*, 10808–10818.

[4] *Computational Photochemistry of Retinal Proteins*
Wanko, M.; Hoffmann, M.; Frauenheim, T.; Elstner, M. *J. Comput. Aided Mol. Des.* **2006**, *20*, 511–518.

[5] *Effect of Polarization on the Opsin Shift in Rhodopsins. 1. A Combined QM/QM/MM Model for Bacteriorhodopsin and Pharaonis Sensory Rhodopsin II*
Wanko, M.; Hoffmann, M.; Frauenheim, T.; Elstner, M. *J. Phys. Chem. B* **2008**, *112*, 11462–11467.

[6] *Effect of Polarization on the Opsin Shift in Rhodopsins. 2. Empirical Polarization Models for Proteins*
Wanko, M.; Hoffmann, M.; Frähmcke, J.; Frauenheim, T.; Elstner, M. *J. Phys. Chem. B* **2008**, *112*, 11468–11478.

Abstract

In this work, novel computational approaches are developed for the quantitative calculation of optical properties of biologic chromophores embedded in a complex and heterogeneous environment. The spectral shifts (tunability) of the protonated Schiff base of retinal in the gas phase and in different proteins of the rhodopsin family are employed for a case study that demonstrates the various methodological challenges that may occur in theoretical spectroscopy of biosystems. In these proteins, which serve as visual pigments and light-driven ion pumps in halobacteria, the absorption maximum of retinal is shifted over a wide range in the optical spectrum. To understand and predict these shifts, the different kinds of interaction between the chromophore and its environment (protein, membrane, solvent) must be modeled. This is achieved by combining different theoretical approaches that describe the matter at different length- and timescales, in a "multi-scale" approach.

The most important prerequisite for quantitative results is the proper approximation in the quantum mechanical description of the chromophore. Established and novel quantum chemical approaches are tested for their ability to describe the response of structural and optical properties of the chromophore to steric, electrostatic, and non-classical interactions with the protein environment. In particular, deficiencies in the popular time-dependent density functional theory and the role of static and dynamic electron correlation are studied.

The conventional QM/MM scheme, which couples the quantum mechanical (QM) description of the active part of the system with a classical molecular mechanical (MM) description of the remainder of the protein/membrane/solvent system is extended to establish a self-consistent mutual polarization of the QM and MM fragments. For this purpose, an interacting atomic induced dipole model is implemented and assessed for application in polypeptides. This polarization model is fully variational and reproduces the polarizability tensors of amino-acid side chains with high accuracy. It is integrated in a multi-state QM/MM scheme for the calculation of excitation energies, which incorporates the instantaneous polarization response of the protein/solvent environment to the excitation-induced charge redistribution on the chromophore.

The effects of charge transfer and dispersive interactions between the chromophore and its molecular environment are usually neglected in QM/MM studies, because the size of the QM zone is limited by the computational cost. In this work, the influence of these effects on the optical spectrum are quantified for different rhodopsins, and simple tests are suggested to predict their relevance for the system under study.

With the proposed multi-scale scheme, the experimental shifts in the absorption maximum between the isolated chromophore *in vacuo* and in different wild-type and mutated rhodopsins are reproduced with unprecedented accuracy. These results proof theoretical spectroscopy a powerful tool to analyze the relation between structural and spectroscopic features in biologic systems.

Kurzfassung

In dieser Arbeit werden neue computergestützte Ansätze für die quantitative Berechnung der optischen Eigenschaften von biologischen Chromophoren entwickelt, die in eine komplexe, heterogene Umgebung eingebettet sind. Die spektralen Verschiebungen (Stimmbarkeit) der protonierten Schiff'schen Base von Retinal in der Gasphase und in verschieden Proteinen der Rhodopsin Familie dienen als Fallstudie, in der die diversen Herausforderungen der Theoretischen Spektroskopie an Biosystemen demonstriert werden. In diesen Proteinen, die als Sehpigmente oder Licht-getriebene Ionenpumpen in Halobakterien dienen, wird das Absorptionsmaximum des Retinals im optischen Spektrum über einen weiten Wellenlängenbereich verschoben. Um diese Verschiebungen verstehen und vorhersagen zu können, müssen die verschiedenen Arten der Wechselwirkung zwischen dem Chromophor und seiner Umgebung (Protein, Membran, Solvent) modelliert werden. Dazu werden verschiedene theoretische Ansätze, welche die Materie auf unterschiedlicher Längen- und Zeitskala beschreiben, in einem „Multiskalen-Ansatz"kombiniert.

Die wichtigste Voraussetzung für quantitative Ergebnisse besteht in der Wahl geeigneter Näherungen für die quantenmechanische Beschreibung des Chromophors. Es wird untersucht, wie etablierte und neuartige quantenchemische Ansätze die Reaktion des Chromophors (Geometrie und optische Eigenschaften) auf sterische, elektrostatische und nicht-klassische Arten der Wechselwirkung mit der Umgebung beschreiben. Insbesondere werden die Defizite der zeitabhängigen Dichtefunktionaltheorie und die Rolle statischer und dynamischer Elektronenkorrelation analysiert.

Das übliche QM/MM-Schema, welches die quantenmechanische (QM) Beschreibung der aktiven Region des Systems mit einer klassisch-mechanischen Beschreibung der Umgebung verbindet, wird erweitert, um eine selbst-konsistente gegenseitige Polarisation von QM und MM Fragment zu erreichen. Zu diesem Zweck wird ein Modell wechselwirkender atomarer induzierter Dipole implementiert und für die Anwendung an Polypeptiden getestet. Dieses Polarisationsmodell ist variational und reproduziert die Polarisierbarkeitstensoren von Aminosäure-Seitenketten mit großer Genauigkeit. Es wird in ein QM/MM-Schema zur Berechnung vertikaler Anregungsenergien integriert, welches die instantane Polarisations-Antwort des Protein–Solvent-Systems auf die anregungsinduzierte Ladungsumverteilung auf dem Chromophor einbezieht.

Die Effekte von Ladungstransfer und dispersiven Wechselwirkungen zwischen dem Chromophor und seiner molekularen Umgebung werden in herkömmlichen QM/MM-Modellen vernachlässigt, da die Größe der QM-Zone durch den Rechenaufwand beschränkt wird. In dieser Arbeit wird der Einfluss dieser Effekte auf das optische Spektrum in verschiedenen Rhodopsinen quantifiziert. Es werden einfache Tests vorgeschlagen, mit denen sich die Relevanz dieser Effekte für das untersuchte System bestimmen lässt.

Mit dem vorgeschlagenen Multiskalen-Schema werden die experimentellen Verschiebungen im Absorptionspektrum zwischen Retinal *in vacuo* und diversen Rhodopsinen und Mutanten mit bislang unerreichter Genauigkeit vorhergesagt. Diese Ergebnisse belegen, dass die theoretische Spektroskopie ein mächtiges Instrument

darstellt, um die Beziehung zwischen strukturellen und spektroskopischen Eigenschaften biologischer Makromoleküle zu analysieren.

Contents

List of Figures

List of Tables

List of Abbreviations

AA	amino acid
ALDA	adiabatic local density approximation to TDDFT
ANO	average natural orbitals
AO	atomic orbital
BLA	bond length alternation
CASSCF	complete active space self-consistent field
CASPT2	complete active space perturbation theory 2nd order
CC	coupled cluster
CCSD(T)	coupled cluster singles, doubles and perturbative triples correction
CI	configuration interaction

CIS, CISD	configuration interaction singles, singles and doubles
CISD(T)	configuration interaction singles doubles with PT treatment of triples
CT	charge transfer
DFRT	density functional response theory
DFT	density functional theory
DFTB	density functional theory based tight binding
ESP	electrostatic potential
FC	Franck–Condon
FOIS	first-order interacting space
GGA	generalised gradient approximation
HBN	hydrogen-bonded network
HK	Hohenberg–Kohn
HOMO	highest occupied molecular orbital
IC	internal conversion
IRC	intrinsic reaction coordinate
IRD	initial relaxation direction
IVO	improved virtual orbitals
KS	Kohn–Sham
LCAO	linear combination of atomic orbitals
LDA	local density approximation
LMO	localized molecular orbital
LUMO	lowest unoccupied molecular orbital
MCSCF	multi-configurational self-consistent field
MD	molecular dynamics
MM–VB	molecular mechanics–valence bond
MO	molecular orbital
MP2	second-order Møller–Plesset perturbation theory
MR	multi reference (multi configurational)
MRCI	multi-reference configuration interaction
MRDDCI2/3	multi-reference difference dedicated CI with 2/3 degrees of freedom
MRMP	multi-reference Møller–Plesset perturbation theory
MRPT	multi-reference perturbation theory
NEB	nudged elastic band
NO	natural orbital
NPA	natural population analysis
OAO	orthogonalized atomic orbital
OM2	orthogonalization method 2
PBE	Perdew–Burke–Ernzerhof GGA functional
PBE0	1-parameter hybrid of PBE
PES	potential energy surface
PSB11	11-*cis* conformer of the protonated schiff base of retinal
PSB5	5-*cis* model of PSB11 with 5 conjugated double bonds
PSB3	3-*cis* model of PSB11 with 3 conjugated double bonds
PW91	Perdew–Wang 1991 exchange functional
RESP	restrained fit to the electrostatic potential
RR	resonance Raman
RPA	random-phase approximation
SCC	self-consistent charge

SCF	self-consistent field
SCVB	spin-coupled valence bond (method)
SOS	sum over states
SORCI	spectroscopy-oriented configuration interaction
SP	saddle/stationary point
TB	tight binding
TDDFT	time-dependent density functional theory
TDHF	time-dependent Hartree–Fock
TICT	twisted structure with intramolecular charge transfer
TS	transition state
UHF	spin-unrestricted Hartree–Fock
UDFT	spin-unrestricted DFT
VB	valence bond (method)
XC	exchange and correlation

Chapter 1

Introduction

. . . el gran libro, siempre abierto y que hay que esforzarse en leer, es el de la Naturaleza; los otros libros han salido de éste y ahí residen las equivocaciones e interpretaciones de los hombres.
. . . the great book, always open and which we must make efforts to read, is the book of Nature; the other books are based on it and have the mistakes and interpretations of mankind.

— A. Gaudí

1.1 Theoretical Spectroscopy of Biologic Systems

The most fundamental understanding of biologic processes on the level of atoms and molecules is a goal that brings together different research disciplines. Molecular biology focusses on the interplay between proteins and genes, biochemistry studies the chemical processes vital to the functioning of the molecular units (cells, organelles, proteins, DNA, etc.) in living organisms, while molecular genetics deals with the effects of gene expression and mutation on the function of these units. Molecular biophysics, by itself a highly interdisciplinary science, adds physical aspects to the understanding of their function and interactions, such as bioenergetics, thermodynamics, and the interaction of biomolecules with radiation.

All these different fields have emerged in the last century and have been advanced by the development of numerous experimental techniques. New forms of microscopy as well as x-ray crystallography (combining crystallization techniques for biologic molecules and structural imaging by x-ray diffraction) allowed for the first time to determine the three-dimensional molecular structure of large biomolecules like DNA or proteins. Today, x-ray crystallography represents a standard technique and has provided the structures of tens of thousands of biomolecules at angstrom and sub-angstrom resolution.[12,13]

Beside the structure-resolving techniques, a wide range of new spectroscopic techniques has been developed that provide essential information about the structural dynamics and chemical reactions that determine the function of biomolecules. They probe the vibrational, electronic, and nuclear magnetic degrees of freedom of

biomolecules and can detect extremely small changes in structure and interactions and access the ultrafast dynamics of chemical reactions. For example, differential Raman spectroscopy can detect changes in hydrogen-bonded networks in proteins and the transfer of protons between different acceptor sites. The development of the femtosecond (fs) pump probe techniques, based on the generation of ultrashort laser pulses represents a key technology that allows the study of the dynamics of photoinduced chemical reactions and has been appreciated by the nobel price in chemistry.[14]

To achieve the ultimate goal and provide an understanding of biology on the atomic level, i.e., reveal how biomolecules perform their complex tasks, the structural features ("design") must be related to their dynamics. Here, the problem arises that the dynamical information obtained from spectroscopy is often abstract and difficult to interpret in terms of the underlying physical and chemical processes (structural evolution). Therefore, theoretical modeling and theoretical spectroscopy have become a viable tool for interpreting the experimental data and test the validity of conceptional models. By simulating the spectroscopic features based on alternative structural assumptions, an atomistic model of the structural dynamics can be created that unites the complementary experimental information and resolves contradictions and inconsistencies in their interpretation.

Certainly, this most ambitious aim of theoretical models cannot always be achieved to a satisfactory degree. The reliability and predictive power of the theoretical approaches depends on the quality of the structural model as well as on the accuracy of the methods applied to obtain the simulated spectral features. Concerning the first, the major breakthroughs were achieved during the 1970s by the progress in x-ray crystallography, providing 3D structures of macromolecules at near-atomic resolution and the development of molecular mechanics force fields that allowed for the first time to simulate the molecular dynamics of these macromolecules. The second has approached a quantitative level with the application of modern quantum chemistry to larger and larger fragments of the studied systems, promoted by the advances in computer technology, and via the coupling of quantum mechanical (QM) methods and molecular mechanics (MM) force fields in the hybrid QM/MM schemes. These "multiscale" approaches allow to define a part of the system that is involved in a chemical reaction, in structural changes, or couples to an external field and describe its vibronic (infrared spectra) and electronic (electrostatic and optical properties and excited-state electron dynamics) features at the level of quantum mechanics. At the same time, the influence of the biologic environment (protein, solvent, membrane, ions, cofactors, etc.) on these features is considered and can be analyzed.

1.2 Scope of this Work

It is the aim of this work to develop new computational strategies for the quantitative prediction of the spectroscopic features of molecules embedded in a complex biological environment. The focus is on optical excitation spectra, but the results are relevant also for other spectroscopic calculations. Established and novel quantum chemical methods are tested and compared for application to biologic chromophores in their ground and electronically excited states. Their performance, reliability and applicability in the framework of the QM/MM scheme is investigated for geometry optimization, electrostatic properties and the simulation of optical absorption bands,

including the effect of structural fluctuations at room temperature. General errors, insufficiencies and limitations of the applied methods are illustrated to give an impetus to further methodological developments and to support the interpretation and judgment of other theoretical studies. Furthermore, the short-comings of the conventional QM/MM scheme itself are investigated by extending the scheme to incorporate the effects that are usually neglected: Inter-residual charge redistribution in proteins, dispersive interactions and their effect on the optical excitation, and the self-consistent electrostatic representation of proteins and their polarization response to excitation-induced charge transfer on the embedded chromophore.

For these investigations, the protonated Schiff base of retinal, the common chromophore of all rhodopsin proteins, serves as template that covers all the aspects and challenges that may occur in other biologic chromophores. The extremely high sensitivity of its optical excitation energy to the molecular environment is responsible for the fact that rhodopsins are photoactive all over the visual range of the optical spectrum (spectral tuning). This sensitivity arises from its structural flexibility, high polarizability and extended charge-transfer upon excitation into the lowest-lying excited singlet state. Its binding site in the center of the protein is surrounded by charged, polar and highly polarizable aromatic groups whose steric and electrostatic interactions with the chromophore are responsible for the different absorption properties of different rhodopsins. Furthermore, drastic shifts in the absorption maximum occur along the photocycle that is initiated by the absorption of a photon and involves a series of conformational and chemical changes. Hence, the retinal chromophore can be used as a sensitive probe to detect structural changes in its environment along the photocycle. From a different point of view, retinal's high sensitivity to interactions with the environment represents an ideal test case for theoretical models, as it is a great challenge for the multi-scale approach to accurately describe these interactions and for the employed QM methods to quantitatively describe the response of the chromophore to these interactions. Due to the extended intramolecular charge transfer upon excitation and the strong correlation of the π electrons in the conjugated polyene chain of retinal, the calculated optical, electrostatic, and geometrical properties depend severely on the employed QM approach.

The work is organized as follows:

Chapters 2–4 give an introduction to the computational approaches employed in this work with a strong focus on the practical aspects and problems that are relevant for the discussions in the following chapters. The SORCI method and the semiempirical OM2 multireference configuration interaction method are discussed in more detail, as the literature on these approaches is still limited.

Chapter 5 investigates the intrinsic optical properties of the retinal chromophore in the light of different QM methods, their dependence on the geometry and interactions with different environments. Differences in the QM descriptions are analyzed and related to the errors an insufficiencies inherent to these methods. Based on the gained methodological insights, previous theoretical studies on the spectral tuning of bacteriorhodopsin are reviewed.

Chapter 6 describes the implementation and assessment of an atomic polarization model for polypeptides and suggests schemes to calculate vertical excitation energies in the context of QM/MM with a polarizable MM description. Applications to different retinal proteins investigate the practical relevance of the protein polarizability for the calculation of optical properties.

In **chapter 7**, the effects of charge exchange and dispersion interactions between the chromophore an its molecular environment on the vertical excitation energy are considered. The individual extensions of the conventional QM/MM scheme are combined to obtain quantitative predictions for the absorption maximum of six different vertebrate and archaeal rhodopsin models.

Chapter 2

Quantum Mechanical Methods for the Electronic Ground State

2.1 Introduction

In this chapter, some aspects of quantum chemical approaches to the description of molecular systems will be discussed, with a focus on electron correlation. Atomic units are used in the following, i.e., $\hbar$, electronic charge and mass take the value 1. A common nomenclature for molecular orbitals (MO's) will be used. Doubly occupied MO's will be labeled by the indices $i, j, k, \ldots$, unoccupied (virtual) MO's by $a, b, c, \ldots$, and MO's with fractional or arbitrary ("active" orbitals) by $p, q, r, s, \ldots$. Integrals of MO's over the one-particle and two-particle (Coulomb) operators of the many-body Hamiltonian will be written in the chemical notation:

$$h_{ij} = (i|h|i) = \int \psi_i^*(x_1)\hat{h}(1)\psi_j(x_1)\,\mathrm{d}x_1 \tag{2.1}$$

$$g_{ijkl} = (ij|kl) = \int\int \psi_i^*(x_1)\psi_j(x_1)\frac{1}{r_{12}}\psi_k^*(x_2)\psi_l(x_2)\,\mathrm{d}x_1\,\mathrm{d}x_2 \tag{2.2}$$

As a starting point, we consider the time-independent "non-relativistic" Schrödinger equation of N identical fermions in the potential v of classic nuclei (Born–Oppenheimer approximation):

$$\hat{H}\Psi = E\Psi\,, \tag{2.3}$$

$$\hat{H} = \sum_{i=1}^{N}(-\tfrac{1}{2}\nabla_i^2) + \sum_{ij=1}^{N}\frac{1}{r_{ij}} + \sum_{i=1}^{N} v_i\,,$$

$$v_i = -\sum_A \frac{Z_A}{|r_i - R_A|}\,.$$

The exact solution to eq 2.3 is given by an antisymmetric N-particle wave function $\Psi(x_1, ..., x_N)$ of spin and spatial coordinates $x = \{r, \sigma\}$. Any explicit algebraic approach to solve eq 2.3 projects Ψ into a finite subspace of the N-particle Hilbert space $\mathcal{H}^N$. Apart from explicitly-correlated r_{12} methods, these approaches expand Ψ in a finite set of products of single-particle functions $\psi_i(x)$ (orbitals):

$$\Psi(\mathbf{x}) = \sum_{p,q,\ldots s} C_{pq\ldots s}\psi_p(x_1)\psi_q(x_2)\ldots\psi_s(x_N) \tag{2.4}$$

As the Pauli postulate requires an antisymmetric wave function for fermions, Ψ can be re-written as a sum (linear combination) of Slater determinants

$$\Phi = \frac{1}{N!}\det(\psi_{ik})\,, \qquad \psi_{ik} = \psi_i(x_k)\,, \tag{2.5}$$

which are defined by the N orbitals that occur (are "occupied") in each summand.

The one-particle functions ψ themselves are represented on a grid (real-space methods), expanded into plane waves (satisfying periodic boundary conditions at the border of a finite box), or expanded in a basis of localized analytic functions (mostly atom-centered Gaussian- or Slater-type orbitals):

$$\psi_i = \sum_j c_i^j \phi_j \tag{2.6}$$

Different quantum chemical approaches are distinguished by their strategy to determine the wave function and orbital coefficients C and c, respectively, and estimate the eigenvalues of $\hat{H}$ based on approximate guesses of these coefficients. The exact solution of eq 2.3 in a given subspace is equivalent to the task of finding the stationary points of the Rayleigh quotient

$$\overline{E} = \frac{\langle\Psi|H|\Psi\rangle}{\langle\Psi|\Psi\rangle}\,. \tag{2.7}$$

For the ground-state, this is referred to as Rayleigh–Ritz variational principle: $\overline{E}$ obtained from any guess of the wave function represents an upper bound for the exact ground-state energy. Moreover, given a finite subspace of $\mathcal{H}^N$, defined by a set of orbitals ψ_i and Slater determinants Φ_i, the Hylleraas–Undheim–MacDonald theorem[15,16] provides that the n-th eigenvalue of the Hamiltonian matrix $H_{IJ} = \langle\Phi_I|\hat{H}|\Phi_J\rangle$ represents an upper bond to the eigenvalue of $\hat{H}$ in $\mathcal{H}^N$. Methods that predict ground or excited-state energies based on the variational or Hylleraas–Undheim–MacDonald theorem are called "variational" methods. They have the advantage that they provide an explicit guess of the many-body wave function whose quality correlates with the deviation of the energy from the exact solution. The main drawback of these methods is that energies (and energy differences) are systematically overestimated and that the errors are usually larger than those of non-variational approaches at the same computational expense. The most important alternative to the variational approach is many-body perturbation theory.

2.2 Hartree–Fock Theory

In Hartree–Fock (HF) theory, the N-electron ground-state wave function is approximated by a single Slater determinant Φ of N spin-orbitals. In in the case of restricted HF (RHF), the spin-orbitals for up- and down-spin electrons have the same spatial part, whereas in unrestricted HF (UHF) they are allowed to differ. If all RHF orbitals are doubly occupied (closed shell perfect pairing), or all unpaired electrons are of the same spin (high spin case), the RHF wave function is an eigenstate of the spin operators S^2 and S_x. The expectation value of the exact non-relativistic Hamiltonian in

Born-Oppenheimer (BO) approximation, $\hat{H}$, with the RHF wave function yields an upper bound for the ground-state energy:

$$\begin{aligned} E_{\mathrm{RHF}} &= \langle \Phi | \hat{H} | \Phi \rangle \\ &= 2\sum_i (i|h|i) + 2f\sum_p (p|h|p) + \sum_{ij} [2(ii|jj) - (ij|ij)] \\ &\quad + 2f\sum_{ip} [2(ii|pp) - (ip|ip)] + f^2 \sum_{pq} [2a(pp|qq) - b(pq|pq)] \,, \end{aligned} \tag{2.8}$$

where $0 < f < 1$ is the occupation number of the open shell orbitals ($f = 1$ means doubly occupied, i.e., closed shell) and a and b are the so-called Roothaan parameters,[17,18] which depend on the particular configuration. For a single open-shell electron, obviously $a = b = 0$, while for the high spin case $a = 1$ and $b = 2$.

The UHF wave function is in general not an eigenstate of the total spin operator S^2, but can be used to describe the spin polarization in open shell systems (radicals or magnetic materials), or as the simplest possible approximation that fixes the breakdown of RHF for nearly degenerate ground states (e.g., bond dissociation).

The UHF total energy results in

$$\begin{aligned} E_{\mathrm{UHF}} &= \sum_i (i|h|i) + \frac{1}{2}\sum_{i(\alpha)j(\alpha)} [(ii|jj) - (ij|ij)] + \frac{1}{2}\sum_{i(\beta)j(\beta)} [(ii|jj) - (ij|ij)] \\ &\quad + \sum_{i(\alpha)j(\beta)} (ii|jj) \end{aligned} \tag{2.9}$$

The MO's can be represented in a plane-wave basis, or as a linear combination of atomic orbitals (LCAO), in the following labeled with Greek indices

$$\psi_i = \sum_\mu c_i^\mu \phi_\mu \tag{2.10}$$

Since (2.8) is an upper bond for the true ground state energy, the variational principle can be applied to obtain the MO coefficients c_i^μ under the constraint of orthonormal MO's. This leads to a generalized eigenvalue problem, referred to as Roothaan–Hall equations:

$$FC = SCE \tag{2.11}$$

Here, F and E are the tensors of an effective one-particle Hamiltonian (Fock operator) in the LCAO basis and its diagonalized form, respectively. C is the matrix of its eigenvectors, and S is the overlap matrix $S_{\mu\nu} = \langle \mu | \nu \rangle$. Introducing the reduced one-particle density matrix for spin α electrons,

$$P_{\mu\nu}^\alpha = \sum_i c_i^{\mu *} c_i^\nu \,, \tag{2.12}$$

the Fock operator for α electrons in the LCAO basis is

$$F_{\mu\nu}^\alpha = h_{\mu\nu} + \sum_{\sigma\tau} \left\{ \left[P_{\sigma\tau}^\alpha + P_{\sigma\tau}^\beta \right] (\mu\nu|\sigma\tau) - P_{\sigma\tau}^\alpha (\mu\sigma|\nu\tau) \right\} \tag{2.13}$$

In terms of the Fock matrix eigenvalues $\epsilon_i = E_{ii}$, the total energy can be written

$$E_{\mathrm{HF}} = \sum_i \epsilon_i - E_{\mathrm{ee}} = \sum_i \epsilon_i - \frac{1}{2}\sum_{ij}[(ii|jj) - (ij|ji)] \tag{2.14}$$

As the Fock operator depends on the orbital coefficients C via the density matrix P, eq 2.11 and 2.13 are coupled. In the self-consistent field (SCF) approach, they are solved iteratively until convergence in P or the total energy is achieved.

2.3 Correlation in Many-Body Systems

Due to the variational principle, the HF method yields always an upper bound to the exact ground state solution of the Schrödinger equation (2.3). Assuming the HF energy is converged w.r.t. the basis set, its difference to the exact ground-state energy is called correlation energy

$$E_{\mathrm{cor}} = E_{\mathrm{exact}} - E_{\mathrm{RHF}} \tag{2.15}$$

This name implies that electron correlation is completely neglected in the HF method and that the energy difference 2.15 can be understood as the effect of electron correlation. A more specific definition of correlation is provided by the concept of the correlation hole, which shall be introduced here in brevity. Correlation in quantum systems is caused by preparation and interactions. In the Schrödinger system 2.3, electrons interact only with classic nuclei and with other electrons. As the Coulomb interaction is a pair interaction, only pair correlations arise by the electron–electron interaction, which is completely defined in terms of the two-particle density $g(x_1, x_2)$,[1] which is the diagonal of the second-order reduced density matrix

$$\gamma_2(x_1, x_2; x_1', x_2') = N(N-1)\int \Psi^*(x_1, x_2, x_3, \ldots)\Psi(x_1', x_2', x_3, \ldots)\,\mathrm{d}x_3 \ldots \mathrm{d}x_N \tag{2.16}$$

$$g(x_1, x_2) = \gamma_2(x_1, x_2; x_1, x_2)$$

and describes the probability to find any of the N electrons in the state x_1 (position r_1 and spin state σ_1) and simultaneously a second one in x_2. To isolate the effect of correlation in the particle coordinates, we consider the conditional probability of finding a second particle in x_2, assuming a first particle (reference electron) has already been measured in x_1. This conditional probability is given by $g(x_1, x_2)/\rho(x_1)$. In absence of any correlation, we simply obtain $\frac{N-1}{N}\rho(x_2)$. If we subtract $\rho(x_2)$, we obtain the so-called exchange-correlation hole

$$h_{\mathrm{xc}}(x_2|x_1) = g(x_1, x_2)/\rho(x_1) - \rho(x_2) \tag{2.17}$$

The reason why we did not subtract $\frac{N-1}{N}\rho(x_2)$ is that the hole function, in absence of correlation, shall reduce to the unconditional probability of finding one particular electron in x_2, $1/N\rho(x_2)$, so that h_{xc} integrates to -1. If we then calculate the Coulomb

[1] This is simply the pair correlation function, as used in statistical physics, applied to coordinates of quantum mechanical particles.

interaction between this specific electron and its hole, we obtain its Coulomb "self interaction". With the help of this artificial term, the electron–electron interaction energy can be written in the elegant form

$$\begin{aligned} E_{\mathrm{ee}} &= \frac{1}{2}\int \frac{g(x_1,x_2)}{r_{12}}\,\mathrm{d}x_1\,\mathrm{d}x_2 \\ &= \frac{1}{2}\int \frac{\rho(x_1)\rho(x_2)}{r_{12}}\,\mathrm{d}x_1\,\mathrm{d}x_2 + \frac{1}{2}\int \frac{\rho(x_2)h_{\mathrm{xc}}(x_2|x_1)}{r_{12}}\,\mathrm{d}x_1\,\mathrm{d}x_2 \end{aligned} \tag{2.18}$$

The first term in (2.18) represents the classical electrostatic interaction of a charge density with itself (Hartree term). The second term adds all the quantum effects: it subtracts the electron–electron self interaction and accounts for all correlation in the particle coordinates, as described by $g(x_1, x_2)$.

For systems without spin-polarization, two different cases can be distinguished: (a) the second (probe) electron has the same spin as the reference electron. Then the function

$$h_{\mathrm{xc}}(r_2,\alpha|r_1,\alpha) = h_{\mathrm{xc}}(r_2,\beta|r_1,\beta) = h_{\mathrm{xc}}^{\sigma_1=\sigma_2}(r_2|r_1) \tag{2.19}$$

describes the probability to find the probe electron with the same spin as the reference electron at r_2, subtracted by the (unconditional) probability to find an electron at that position with that spin. In case (b), probe and reference electrons have opposite spins:

$$h_{\mathrm{xc}}(r_2,\alpha|r_1,\beta) = h_{\mathrm{xc}}(r_2,\beta|r_1,\alpha) = h_{\mathrm{xc}}^{\sigma_1\neq\sigma_2}(r_2|r_1) \tag{2.20}$$

The sum of eq 2.19 and 2.20 is called the total exchange-correlation hole

$$h_{\mathrm{xc}}^{\mathrm{total}}(r_2|r_1) = h_{\mathrm{xc}}^{\sigma_1=\sigma_2}(r_2|r_1) + h_{\mathrm{xc}}^{\sigma_1\neq\sigma_2}(r_2|r_1) \tag{2.21}$$

and describes the probability to find a second electron in r_2 and arbitrary spin state, subtracted by the spin-integrated probability $\rho(r_2) = \rho(r_2,\alpha) + \rho(r_2,\beta)$ to find any electron at that position.

The concept of the hole function represents a powerful tool to visualize the effects of correlation and discuss its origin and its representation in different quantum chemical methods. For the single determinantal RHF wave function, e.g., $h_{\mathrm{xc}}^{\sigma_2\neq\sigma_1}$ is constant zero, independent of the state x_1 of the reference electron. This means that electrons of different spin are uncorrelated in RHF, i.e., they interact with the *mean field* of the electrons in the opposite spin state. For this reason, HF is sometimes called "mean field theory". However, the same is not true for two particles of equal spin: From the anti-symmetry of the wave function it follows that $g(x_1, x_1)$ equals zero, and therefore

$$\lim_{r_2\to r_1} h_{\mathrm{xc}}^{\sigma_2=\sigma_1}(r_2|r_1) = -\rho(x_1) \tag{2.22}$$

This is the Paul principle: the probability of finding two fermions in the same state is zero. Therefore, $h_{\mathrm{xc}}^{\sigma_2=\sigma_1}$ is also called *Fermi hole*. In RHF, this condition is fulfilled, as the wave function is constructed as a Slater determinant, and hence electrons of equal spin *are* spatially correlated in HF. Moreover, the Fermi hole integrates to -1, like the total hole $h_{\mathrm{xc}}^{\mathrm{total}}(r_2|r_1)$.

In general, the Fermi hole of a RHF wave function will also depend on the position of the reference electron—with one exception: For a two-electron system (H_2, or a

helium atom) in its singlet ground state, the probability of finding the probe electron in the same spin state as the reference electron is trivially zero. Hence, the Fermi hole globally annihilates the probability to find any probe electron of the same spin and is given by $-\rho(x_2) = -\frac{1}{2}\rho(r_2)$.

The Coulomb interaction between the probe electron and its Fermi hole produces the exchange energy term in HF, and is therefore essential for forming chemical bonds. The vanishing $h_{\mathrm{xc}}^{\sigma_2 \neq \sigma_1}$ term, however, is physically uncorrect for interacting particles. The Coulomb repulsion in the Hamiltonian 2.3, e.g., has a singularity at $r_1 = r_2$, which must be neutralized by the local kinetic energy at that point. The exact wave function must therefore feature a discontinuity in its second derivative, the so-called inter-electronic cusp:[19]

$$\left.\frac{\partial \Psi}{\partial r_{12}}\right|_{r_{12}=0} = \left.\frac{1}{2}\Psi\right|_{r_{12}=0} \tag{2.23}$$

This deformation of the wave function caused by the Coulomb repulsion reduces the probability to find two electrons close to each other, independent of their spins. The corresponding effect on the exchange-correlation hole is reflected in $h_{\mathrm{xc}}^{\sigma_1 \neq \sigma_2}$, which is therefore called *Coulomb hole*. It is negative close to the reference electron, where the interaction between the Coulomb hole and the probe electron (see eq 2.18) is largest, and integrates to zero. The resulting decrease in W_{ee} is the source of the negative correlation energy, eq 2.15. It is, however, not the only and often not even the most important contribution to the correlation energy, because the Coulomb correlation changes the density and therefore the kinetic energy and the electron–nuclear interaction energy.[20]

Apart from two-electron systems, the Coulomb correlation contributes also to $h_{\mathrm{xc}}^{\sigma_1 = \sigma_2}$, but in systems that are well represented by the HF determinant, the Fermi hole is strongly dominated by exchange and the correlation contribution to E_{ee} is much smaller than the exchange energy in eq 2.18. This is usually the case in molecular systems close to their equilibrium structure, and the Coulomb correlation is then referred to as "dynamic correlation". The simplest example for dynamic correlation is the He atom,[19,20] where the Coulomb hole reduces the E_{ee} by -2.1 eV. The kinetic energy on the contrary, is increased by +1.1 eV compared to the RHF solution. The total correlation energy of the He atom results in -1.1 eV, which represents a typical value for the correlation energy of electron pairs in molecules. Examples for Coulomb and Fermi holes of ground and excited states of small molecules can be found in Ref.[21].

In situations where the wave function is badly represented by a single Slater determinant, the RHF energy will grossly overestimate the ground-state energy, and the correlation energy, as defined in eq 2.15, will be large. This is generally the case when several determinants or spin-states are degenerate or near degenerate with the lowest one. Typical situations are the breaking of bonds at transition states of a chemical reaction or dissociating radical fragments, or the ground state of open-shell systems or multiply bound transition-metal atoms.[22] The simplest example for a breakdown of RHF, the dissociating H_2 molecule, can be found in many textbooks (see, e.g., Ref.[19]), and has been discussed in terms of Fermi and Coulomb holes.[20,23] The real ground state of H_2 at long bond distances has a density similar to that of two isolated hydrogen atoms. In RHF, the Fermi hole removes the self-interaction of the reference electron from the Hartree potential, hence reduces the interaction of the reference electron with the electron density by $-\frac{1}{2}\rho$. The missing Coulomb hole also removes $-\frac{1}{2}\rho$ from

the conditional probability to find a second electron at the same nuclei where the reference electron resides and adds $\frac{1}{2}\rho$ to the other nuclei. Hence, the reference electron in RHF interacts with two half-shielded nuclei. In the exact calculation, the nucleus where the reference electron resides is unshielded and the other one shielded by the density of the whole second electron. In consequence, the RHF density is much too diffuse and the underestimated electron-nucleus interaction gives rise to the highly overestimated energy. In the exact solution, the Coulomb hole is not produced by a strong electron–electron interaction as in the case of the Helium atom. Therefore, the term "non-dynamic" or static correlation is used in this context.

The breakdown of RHF for dissociating open-shell fragments coincides with the degeneracy of bonding and anti-bonding orbitals, w.r.t. the broken bond, and with the degeneracy of the singlet and triplet ground-state. As the asymptotic energy of the triplet state is correctly described in UHF and restricted open-shell (ROHF), the energy of the RHF singlet state is lowered by breaking the spin symmetry (UHF). The physically correct solution for the singlet state can be obtained both in the framework of Kohn–Sham density functional theory (next section), or multi-configurational SCF (section 3.3.1).

The distinction between dynamic and non-dynamic correlation is to some extent artificial and arbitrary. Other criteria employed to define dynamic correlation are the localization of the Coulomb hole, e.g., in the range of one atom or bond (short vs. long-range correlation), or the computational approach: As the non-dynamic correlation is always recovered in MCSCF (given a sufficiently large active space), the lacking correlation in this approach is often referred to as dynamic. Another term for spacial (Coulomb) correlation that sometimes causes confusion is "left-right correlation", which can refer to the static correlation in H_2 [20,24–26] and open-shell systems[27] as well as to dynamic correlation in atoms or small molecules.[28–30]

2.4 Configuration Interaction, Coupled-Cluster, and Perturbation Theory

The general expansion of the many-body wave function 2.4 for a finite single-particle basis set can be re-written as an expansion based on the HF ground-state wave function $|0\rangle$, which serves as a zeroth-order reference (in the spirit of perturbation theory):

$$|\Psi\rangle = \left\{ \sum_{ia} t_{ia} \hat{E}_{ia} + \sum_{ia,jb} t_{iajb} \hat{E}_{ia} \hat{E}_{jb} + \dots \right\} |0\rangle \,, \tag{2.24}$$

where the excitation operator $\hat{E}_{ia}$ replaces occupied by virtual orbitals in the HF determinant:

$$\hat{E}_{ia} = \sum_{p=1}^{N} |\psi_a(p)\rangle\langle\psi_i(p)| = \hat{a}^\dagger_{a\alpha}\hat{a}_{i\alpha} + \hat{a}^\dagger_{a\beta}\hat{a}_{i\beta} \tag{2.25}$$

The excitation operators can also be used to express the one and two-particle reduced density matrices

$$D_{ij} = \langle\Psi|\hat{E}_{ij}|\Psi\rangle \tag{2.26}$$

$$P_{ijkl} = \langle \Psi | \hat{E}_{ij}\hat{E}_{kl} - \delta_{jk}E_{il} | \Psi \rangle \tag{2.27}$$

The expectation value of the Hamiltonian is then

$$E = \langle \Psi | \hat{H} | \Psi \rangle = \sum_{ij} D_{ij} + \frac{1}{2} \sum_{ijkl} g_{ijkl} P_{ijkl} \tag{2.28}$$

Minimization of the Rayleigh quotient (2.7) under variation of the coefficients $C = \{t_{ia}; t_{ia,jb}; \ldots\}$ with a fixed set of orbitals is called *configuration interaction* (CI), or *full CI*. If the expansion 2.24 is truncated after a certain class of excitations, the method is called configuration interaction singles, doubles, etc. (CISD...). The corresponding secular equation

$$(\mathbf{H} - E_I)C_I = 0 \tag{2.29}$$

can be solved to obtain both ground-state and excited-state energies and wave functions. In particular the CIS method represents the simplest approach to obtain excitation energies, and is still frequently used in combination with semiempirical Hamiltonians.

For the description of electron correlation, the truncated CI methods have several deficiencies and problems:

(i) For their unfortunate scaling with the system size (approximately $\mathcal{O}(N^{2m+2})$, for excitation level m), higher than the CISD level are rarely applied. This is also the lowest level that recovers correlation, as singly-excited configurations do not interact with the reference wave function (Brillouin theorem).

(ii) The convergence of the correlation energy with respect to the dimension of the CI expansion, is very slow.

(iii) Truncated CI methods are not size extensive.

To solve problem (i) in the context of (ii), CI can be replaced (or augmented) by the use of Møller–Plesset (MP) perturbation theory.[31] The second-order perturbation expansion, e.g., employs the same configuration space as CISD, but scales merely $\mathcal{O}(N^5)$ with the system size. The transformation of the two-electron four-center integrals from the AO to the MO basis, which is the bottle neck in the MP2 method, can be replaced by a three-center integral by expanding the density in an auxiliary basis (resolution of the identity), which reduces the scaling to $\mathcal{O}(N^4)$.[32] Furthermore, linear scaling techniques, which employ a localized MO basis, have been implemented (see e.g. Ref.[33] and references therein).

The notion size extensivity (iii), originating from *extensivity* in thermodynamics, denotes that the energy of a homogeneous system is proportional to its size. In the case of finite systems, a method is required to be size extensive in order to correctly describe properties that depend on the system size. A special case is referred to as size consistency: The energy of an ensemble of N well separated identical moieties is N times the energy of that moiety. The correlation energy of CID, e.g., is proportional to $\sqrt{(N)}$, instead. RHF is size extensive, but for open shell moieties, it is not size consistent (see H_2 dissociation problem above). MP perturbation theory is size extensive and it is size consistent when the HF reference is.

Another approach to achieve size extensivity is coupled-cluster theory (CC). Here, an exponential ansatz of the wave function, which can be truncated at some order, guarantees size consistency:

$$|\Psi\rangle = \mathrm{e}^{\hat{T}_1+\hat{T}_2+\cdots}|\Psi_0\rangle\,, \tag{2.30}$$

where $\hat{T}_n$ is a linear combination of all possible n-tuple excitations. In contrast to perturbation theory, the CC expansion will converge to full CI also when the HF configuration is a bad reference. However, in this case, convergence is slow and multireference methods (see section 3.3.2) are considerably more efficient in the description of static correlation. For the recovery of the dynamic correlation (Coulomb hole) on the contrary, CC methods are highly superior to CI. Combining CC theory with a perturbational treatment of the most expensive higher orders terms, methods like CCSD(T) represent the most accurate class of methods that can currently be applied to quantum chemical problems.

A detailed introduction to size-extensive methods with many valuable references and a comparison of PT and CC approaches can be found in Ref.[34]

2.5 Density Functional Theory

The first density functionals[35–37] were designed to replace the nonlocal exchange operator in HF by a simple analytic approximation of the form

$$E_\mathrm{x} = \frac{9}{8}\left(\frac{3}{\pi}\right)^{1/3}\alpha\int\rho(r)^{4/3}\,\mathrm{d}r\,, \tag{2.31}$$

where $\alpha = 2/3\ldots1$ is an empirical parameter. This X_α, or Hartree–Fock–Slater method (α=2/3), does not yield very good results for atoms or molecules, but as the exchange term causes numerical difficulties in periodic systems, it was applied in solid-state physics until the 1980s.

Although density functional theory (DFT) started as an approximation to HF, the introduction of the Hohenberg–Kohn theorems[38] pointed out that its real potential was to introduce electron correlation in a formalism that uses the electron density as basic variable and does not require any information about the many-body wave function or its second-order reduced density matrix. These theorems provide that the exact ground-state energy can be regarded as a functional of ρ, which uniquely determines the external potential v in the Schrödinger equation 2.3 and hence the wave function and all other properties. Further, the variational principle can be applied to this energy functional to obtain the exact ground-state density. With the Levi constraint-search formulation,[39–41] the variation of the density can be performed in the space of all possible N-representable (derived from some antisymmetric N-particle wave function) densities:

$$E_0 = \min_{\rho\to N}\left(F[\rho] + \int\rho(r)v(r)\,\mathrm{d}r\right) \tag{2.32}$$
$$F[\rho] = \min_{\Psi\to\rho}\langle\Psi|\hat{T}+\hat{V}_\mathrm{ee}|\Psi\rangle$$

As the exact functional $F[\rho]$ is not known, this information is of no practical use and the true birth of modern DFT is marked by the first successful approximation to the kinetic

part of $F[\rho]$ by Kohn and Sham in 1965.[42] They considered a hypothetical system of N non-interacting particles in an external potential v_s, for which $F[\rho]$ reduces to a functional of the kinetic energy and is known exactly:

$$T_\mathrm{s}[\rho] = \sum_i^N \langle\psi_i| -\frac{1}{2}\nabla^2|\psi\rangle\,, \qquad \rho(r) = \sum_i^N |\psi_i|^2 \tag{2.33}$$

Analog to HF theory, the orbitals ψ_i are found by solving the corresponding Euler–Lagrange equations

$$\left[-\frac{1}{2}\nabla^2 + v_\mathrm{s}(r)\right]|\psi_i\rangle = \epsilon_i|\psi_i\rangle \tag{2.34}$$

Assuming that a potential v_s exists, which produces the same ground-state density as the system of interacting electrons in the potential v, the total energy of the latter can be written

$$E[\rho] = \int v(r)\rho(r)\,\mathrm{d}r + T_\mathrm{s}[\rho] + J[\rho] + E_\mathrm{xc}[\rho]\,, \tag{2.35}$$

$$E_\mathrm{xc}[\rho] = (T[\rho] - T_\mathrm{s}[\rho]) + (V_\mathrm{ee}[\rho] - J[\rho]) \tag{2.36}$$

The idea behind this notation is to prepare the ground for approximations to the functional $E_\mathrm{xc}[\rho]$ without leaving the framework of the exact theory. In fact, the terms appearing in (2.36) are orders of magnitude smaller than the terms in (2.35) and dominated by the exchange part of the electron–electron interaction. The effective single-particle potential in the Kohn-Sham equation (2.34) then writes

$$v_\mathrm{s} = v(r) + \int \frac{\rho(r')}{|r-r'|}\,\mathrm{d}r' + v_\mathrm{xc}(r) \tag{2.37}$$

The exchange-correlation potential v_xc is the functional derivative of $E_\mathrm{xc}[\rho]$. For an explicit analytic form $E_\mathrm{xc}[\rho] = \int F(\rho, \nabla\rho)\,\mathrm{d}r$, it is

$$v_\mathrm{xc} = \frac{\partial F}{\partial \rho} - \nabla\cdot\frac{\partial F}{\partial \nabla\rho} \tag{2.38}$$

For the uniform electron gas an expressions for T_s can be derived:[43]

$$T_\mathrm{s} = \frac{3}{10}(3\pi)^{2/3}\int \rho(r)^{5/3}\,\mathrm{d}r \tag{2.39}$$

By subtracting this term and Slater's exchange energy from the exact energy, obtained from quantum Monte-Carlo calculations,[44] Vosko, Wilk, and Nusair[45] obtained an analytic expression for the KS correlation energy of the homogeneous electron gas. The resulting SVWN functional is the most prominent example of the local density approximation (LDA) to E_xc.

A major progress in DFT was the generalization of the density functionals to the inhomogeneous case by adding terms depending on the gradient norm of the density. In these generalized gradient approximations (GGA), the choice of the model systems, used to determine free parameters, is not as obvious as in the LDA case. While functionals like PW91[46] and PBE[47] are derived from the properties of the homogeneous and slowly-varying electron gas, Becke's exchange functional[48] contains a parameter that is fitted to six noble gas atoms, and the LYP correlation functional,[49] is derived

from the helium atom.[50] The recent HCTH functional, at the extreme, contains 15 parameters that are fitted to molecular properties of a large training set. Hence, modern density functionals have more or less semi-empirical character and have certain preferences for either solids or molecules. Nonetheless, modern GGA's are remarkably transferable: PW91 and PBE perform reasonably well on molecular properties and Becke's exchange is applicable to semi-conductors.They also have common insufficiencies, as the wrong asymptotic behavior of v_{xc} and the self-interaction error.

It is empirically found and theoretically justified, by the adiabatic connection approach, that admixture of HF exchange to the local KS exchange potential improves the performance of LDA and GGA functionals for molecules as as well as for solid-state applications. The most popular of these "hybrid" functionals, B3LYP, has the form

$$E_{\mathrm{xc}}^{B3LYP} = (1-a)E_{\mathrm{x}}^{\mathrm{LDA}} + aE_{\mathrm{x}}^{\mathrm{HF}} + bE_{\mathrm{x}}^{\mathrm{B88}} + cE_{\mathrm{c}}^{\mathrm{LYP}} + (1-c)E_{\mathrm{c}}^{\mathrm{LDA}}\,, \tag{2.40}$$

with 3 empirical parameters a, b, and c, which are fitted to molecular properties of the G2 data set. The amount of HF exchange a is 20% in B3LYP. Perdew, Ernzerhof, and Burke have argued that 20–25% of HF exchange are optimal for GGA's in general, and suggested the "parameter-free" hybrid functional PBE0, corresponding to the scheme

$$E_{\mathrm{xc}}^{\mathrm{hybrid}} = E_{\mathrm{xc}}^{\mathrm{GGA}} + 0.25(E_{\mathrm{x}}^{\mathrm{HF}} - E_{\mathrm{x}}^{\mathrm{GGA}})\,. \tag{2.41}$$

The correlation described with these local (LDA) and quasi-local (GGA) functionals is clearly of the dynamic type, as introduced in section 2.3,[20,51] although the discrimination from non-dynamic correlation is controversial (see Cremer *et al.*[28,29,52] for the effect of DFT exchange, correlation, and self-interaction on the density). In cases of near-degeneracy of the ground state, where RHF breaks down, also the mentioned DFT functionals fail, although their description in the presence of non-dynamic correlation is somewhat more robust. For example, the point of singlet-triplet instability in dissociating H_2, where the spin-unrestricted description becomes energetically favoured, occurs at larger distance between the nuclei.[52] Interestingly, it is not the single-determinantal form of the KS description which can be blamed for the breakdown of DFT in presence of static correlation: The exact KS potential v_{s} exists also in these situations[23,26,27,53,54] and can be constructed numerically from the exact densities.[55]

2.6 Semiempirical Methods

Another ansatz to incorporate dynamic correlation that avoids the demanding route of wave-function based methods is to empirically parameterize an effective one-particle Hamiltonian and fit the parameters to experimental data (or calculations that treat the correlation explicitly). In this sense, the so-called semiempirical methods go beyond the goal of simply approximating HF, though their original intention was to reduce the computational cost of this method. As noticed in the previous section, the latter applies also to the early development of DFT, but in contrast to DFT, semiempirical methods have not (yet) been considered a general replacement for HF to achieve a higher accuracy.

Semiempirical methods for finite systems usually employ a minimal atomic basis set (LCAO), in which the functions on one center are orthogonal. The non-orthogonality of the basis functions from different atoms can be treated either ex-

plicitly, by solving the generalized eigenvalue problem (2.11), as done in the DFTB method, or approximately, by assuming an orthogonalized basis and then partially repairing the error in the fitting. A third way consists in adding correction terms to the Hamiltonian in the AO basis in order to approximate the transformed Hamiltonian ${}^{\lambda}\mathbf{F} = \mathbf{S}^{-1/2}\mathbf{F}\mathbf{S}^{-1/2}$ in a Löwdin-orthogonalized basis. The effect of this Löwdin transformation on the one- and two-electron integrals and its implication for the calculation of excitation energies will be discussed in section 2.6.1.

In order to reduce the number of required integrals and limit the set of fitting parameters (only atomic parameters are fitted, except for MNDO, in which also atom-pair parameters are used), certain integrals are neglected. Corresponding to which classes of integrals are neglected, semiempirical methods are grouped into CNDO (complete neglect of differential overlap),[56] INDO (intermediate neglect of differential overlap),[57] and NDDO (neglect of differential diatomic overlap) methods.[58] As shown in Table 2.1, the integral classes are defined by the type of orbital product $\mu_A(r)\nu_B(r)$ (differential overlap) over that is integrated.

Table 2.1: NDO Approximations.

Approxomation		Examples
CNDO (ZDO)	$\mu\nu \approx \delta_{\mu\nu}\mu\mu$	
INDO	$\mu_A\nu_B \approx \delta_{AB}\mu\nu$	MINDO/3, ZINDO/S
NDDO	$\mu_A\nu_B \approx \delta_{AB}\mu\nu$	AM1, PM3, MNDO

Due to the NDO approximation, all 3- and 4-center two-electron integrals vanish. Further, all three-center terms in the core Hamiltonian are neglected in conventional NDO methods, and the Fock-matrix elements in the AO basis reduce to the following expressions

$$\mathbf{F} = \mathbf{H} + \mathbf{G} \tag{2.42}$$

$$H^{\mathrm{NDO}}_{\mu\mu} = \langle\mu|T - V_A|\mu\rangle \tag{2.43}$$

$$H^{\mathrm{NDO}}_{\mu\nu} = \langle\mu|T - V_A|\nu\rangle \tag{2.44}$$

$$H^{\mathrm{NDO}}_{\mu\sigma} = \langle\mu|T - V_A - V_B|\sigma\rangle \tag{2.45}$$

$$G^{\mathrm{NDO}}_{\mu\mu} = \sum_{\nu} P_{\nu\nu}\left[(\mu\mu|\nu\nu) - \tfrac{1}{2}(\mu\nu|\mu\nu)\right] + \sum_{B}\sum_{\sigma,\tau} P_{\sigma\tau}(\mu\mu|\sigma\tau) \tag{2.46}$$

$$G^{\mathrm{NDO}}_{\mu\nu} = P_{\mu\nu}\left[\tfrac{3}{2}(\mu\nu|\mu\nu) - \tfrac{1}{2}(\mu\mu|\nu\nu)\right] + \sum_{B}\sum_{\sigma,\tau} P_{\sigma\tau}(\mu\nu|\sigma\tau) \tag{2.47}$$

$$G^{\mathrm{NDO}}_{\mu\sigma} = -\tfrac{1}{2}\sum_{\nu,\tau} P_{\nu\tau}(\mu\nu|\sigma\tau)\,, \tag{2.48}$$

where μ, ν are located on atom A, and σ, τ on atom $B \neq A$. For the remaining required integrals, Table 2.2 summarizes the most common approximations.

The **one-electron integrals** between orbitals on two different centers (core resonance integrals) are not neglected in CNDO, INDO, and MNDO methods (as the NDO

Table 2.2: Integral Approximations in Semiempirical Methods, Parameters in a s-p Valence Basis.

	NDDO	INDO	CNDO
One-electron integrals			
$\langle\mu_A\|T-V_A\|\mu_A\rangle$	U_s, U_p	U_s, U_p	U_s, U_p
$\langle\mu_A\|-V_B\|\mu_A\rangle$	$-\sum_B Z'_B\langle\mu_A s_B\|\mu_A s_B\rangle$	$-\sum_B Z'_B\gamma_{AB}$	$-\sum_B \langle s_A\|V_B\|s_A\rangle$
$\langle\mu_A\|-V_B\|\nu_A\rangle$	$-\sum_B Z'_B\langle\mu_A s_B\|\nu_A s_B\rangle$	0	0
$\langle\mu_A\|T-V_A-V_B\|\sigma_B\rangle$	$\frac{1}{2}S_{\mu\sigma}(\beta_\mu+\beta_\sigma)$	$\frac{1}{2}S_{\mu\sigma}(\beta_\mu+\beta_\sigma)$	$\frac{1}{2}S_{\mu\sigma}(\beta_\mu+\beta_\sigma)$
Two-electron integrals			
$(\mu_A\mu_A\|\mu_A\mu_A)$	g_{ss}, g_{pp}	γ_{AA},F^2	γ_{AA}
$(\mu_A\mu_A\|\nu_A\nu_A)$	$g_{sp}, g_{pp'}$	γ_{AA},F^2	γ_{AA}
$(\mu_A\nu_A\|\mu_A\nu_A)$	$h_{sp}, h_{pp'}$	G^1, F^2	0
$(\mu_A\mu_A\|\sigma_B\sigma_B)$	multipole	γ_{AB}	γ_{AB}
$(\mu_A\mu_A\|\sigma_B\tau_B)$	multipole	0	0
$(\mu_A\nu_A\|\sigma_B\tau_B)$	multipole	0	0

Different indices refer to different orbitals/atoms. Z'_A is the net charge of nucleus A and its core electrons.

approximation would imply), but included within the Mulliken approximation (2.60):

$$\begin{aligned}\langle\mu_A|T-V_A-V_B|\sigma_B\rangle &\approx \frac{1}{2}S_{\mu\sigma}(\langle\mu_A|T-V_A-V_B|\mu_A\rangle+\langle\sigma_B|T-V_A-V_B|\sigma_B\rangle)\\ &\approx \frac{1}{2}S_{\mu\sigma}(\beta_\mu+\beta_\sigma)\end{aligned} \tag{2.49}$$

Instead of using the parameters U_s and U_p, as for the one-center terms, new fitting parameters β_s and β_p are introduced.

In NDDO, all one-center integrals and the overlap matrix $S_{\mu\nu}$ can be calculated analytically by introducing a Slater-type AO basis, whose orbital exponents $\zeta_s, \zeta_p, \ldots$ are the only parameters to be fitted. This procedure would be appropriate when the goal was approximation of the HF method. In the successful "modified" INDO and NDDO implementations (MINDO/3, MNDO, AM1, PM3, etc.), however, the two-electron one-center integrals $g_{\mu\nu}$ (Coulomb type), $h_{\mu\nu}$ (exchange type) and the diagonal elements (core integrals) U_s and U_p are obtained by fitting the energies of different valence states (i.e., occupations n_μ) of the atom to the experimental ionization potentials, electron affinities, and high spin state energies. The HF energy of an atom becomes in the AO basis:

$$E_A = \sum_\mu n_\mu U_\mu + \frac{1}{2}\sum_{\mu\nu}\left[g_{\mu\nu}-\frac{1}{2}h_{\mu\nu}\right] \tag{2.50}$$

Depending on the approximation of the **one-center two-electron integrals** used in the various semiempirical methods (see below), different parameters ($g_{\mu\nu}$, $h_{\mu\nu}$ or G^1 and F^2) appear in the corresponding approximation to (2.50) and are determined in the fitting.[59,60] A common feature of these empirically determined parameters is that they are significantly smaller than the analytically calculated ones. This is essentially the effect of the dynamic correlation of the atomic electrons (Coulomb hole).

In NDDO, and also in MINDO variants, all six one-center two-electron integrals of exchange (h_{sp}, $h_{\mathrm{pp'}}$) and Coulomb type (g_{ss}, g_{pp}, g_{sp}, $g_{\mathrm{pp'}}$) are treated as individual fitting parameters.[60,61] In CNDO, all exchange-type integrals $(\mu\nu|\nu\mu)$ are neglected, and the Coulomb-type integrals are l-independent (spherically averaged) in order to achieve rotational invariance. In INDO, l-dependent onsite corrections

$$(\mathrm{ss}|\mathrm{ss}) = (\mathrm{sp_x}|\mathrm{sp_x}) = \gamma_{AA} \tag{2.51}$$

$$(\mathrm{p_xp_x}|\mathrm{p_xp_x}) = \gamma_{AA} + \frac{4}{25}F^2 \tag{2.52}$$

$$(\mathrm{p_xp_x}|\mathrm{p_yp_y}) = \gamma_{AA} - \frac{2}{25}F^2 \tag{2.53}$$

$$\tag{2.54}$$

are added, as well as one-center exchange terms, using the Slater–Condon parameters:[57]

$$(\mathrm{sp_x}|\mathrm{p_xs}) = \frac{1}{3}G^1 \tag{2.55}$$

$$(\mathrm{p_xp_y}|\mathrm{p_yp_x}) = \frac{3}{25}F^2 \tag{2.56}$$

In NDDO methods, the **two-center two-electron integrals** are approximated by a multipole representation of the orbital products. The multipoles are calculated from the AO's using the same exponent $\zeta_{\mathrm{s}} = \zeta_{\mathrm{p}}$ as used for the calculation of γ_{AB} (see below), but they are mapped onto point charges. The point-charge interactions are then damped for short distances to approach the value of the corresponding onsite two-electron integral for $R_{AB} = 0$. In consequence, the two-center two-electron integrals take smaller values than the exact ones, which again simulates the effect of dynamic correlation.[61]

In CNDO and INDO, all two-center repulsion integrals (electron–electron as well as electron–core) are restricted to the monopole–monopole interactions using a γ function (similar as in the SCC-DFTB method), which interpolates between the point-charge Coulomb potential and the finite value of γ_{AA} in the limit $R_{AB} \to 0$:

$$\gamma_{AB} = (\mathrm{s}_A\mathrm{s}_A|\mathrm{s}_B\mathrm{s}_B) \tag{2.57}$$

The electron–core repulsion integrals in NDDO are modeled with the same s-type valence AO function as the core-core repulsion potential. The different R_{AB}-dependency of the latter is achieved by adding further empiric expressions containing further atomic fitting parameters.

2.6.1 Orthogonalization Effects and OM2

The performance of ground-state parameterized NDDO methods in excited-state CI calculations is limited by systematic errors of the NDDO approximation. In the limit of a full CI calculation, excitation energies are strongly underestimated, the MAE for small organic molecules being larger than 1 eV.[62] This problem can be alleviated by a special parametrization for excited-state properties (e.g., in ZINDO/S[63]) or by exploiting error cancelation between systematic errors in the single-particle spectrum of the Hamiltonian and those of a limited CI expansion (e.g., CIS) of the electronic states.

In both cases, the remaining unsystematic error is considerably higher than on the *ab initio* level of theory, and states with double excitation character cannot be properly described. In the early nineties, Kolb developed a new MNDO-based method, which improved the description of orthogonalization effects[64] both implicitly, by introducing a new semiempirical expression for the resonance integral, and explicitly by adding terms to the core Hamiltonian. It turned out that this new method, called OM1, improved not only problems of MNDO with respect to torsional barriers and configuration energies, but also significantly improved single-particle energies, suggesting its use for excited-state calculations. This work was continued by Weber,[62] who developed OM2.

Weber *et al.* have discussed the principal effects of a Löwdin orthogonalization on the single-particle spectrum in terms a homonuclear two-orbital model, for which the exact analytic expression of the core-Hamiltonian matrix elements in the basis of orthogonalized atomic orbitals (OAO's) can be obtained:

$$^{\lambda}H_{\mu\mu} = H_{\mu\mu} - \frac{S_{\mu\tau}M_{\mu\tau}}{1 - S_{\mu\tau}^2} \tag{2.58}$$

$$^{\lambda}H_{\mu\nu} = \frac{M_{\mu\tau}}{1 - S_{\mu\tau}^2} \tag{2.59}$$

The Mulliken function M is defined as the difference between a two-center matrix element ($\mu \in A$, $\tau \in B$) and its Mulliken approximation:

$$M_{\mu\tau} = H_{\mu\tau} - \frac{1}{2}S_{\mu\tau}\left(H_{\mu\mu} + H_{\tau\tau}\right) \tag{2.60}$$

In case of a negative Mulliken function (which applies to π-bonds but not to σ-bonds[65]), the diagonal element $H_{\mu\mu}$ is shifted up, and the resonance integral $H_{\mu\tau}$ is shifted down in energy, compared to the Elements in the AO basis. This means that the norm of the non-diagonal Fock matrix element $F_{\mu\tau}$ is increased, as is the resulting MO splitting.

Unfortunately, this analysis is *not* applicable to rationalize the effects of the explicit orthogonalization corrections that are introduced in the orthogonalization model 2 (OM2), which are three-center terms. Nonetheless, the single-particle spectrum of the OM2 method does improve dramatically upon the underlying MNDO method (as do some ground state properties as torsional barriers and closed shell repulsion), although no excited state properties are used in the parameter fitting. Therefore, the orthogonalization corrections introduced in OM1 and OM2 shall be briefly revisited here.

The basic idea of OM2[66] is to introduce correction terms to the core Hamiltonian which cover those orthogonalization effects that cannot be implicitly accounted for via the parameterization of the MNDO integrals. These include three-center additions to the resonance integrals and two-center terms in the onsite elements. The correction terms for valence–valence and valence–core orthogonalization are derived from a Taylor expansion of $\mathbf{S}^{-1/2} = (\mathbf{1} + \mathbf{S}')^{-1/2} = \mathbf{1} - \frac{1}{2}\mathbf{S}' + \frac{3}{8}\mathbf{S}'^2 + O(\mathbf{S}'^3)$, where terms of higher than third order in $\mathbf{S}'$ are neglected. Orthogonalization effects on the two-electron integrals, which are empirically found to be smaller than those for the core Hamiltonian, are neglected completely, for the following reasons. In principle, an exact transformation of the one-electron integrals, or the solution of the generalized

eigenvalue problem, as in the case of DFTB, would be feasible. An exact transformation of the two-electron integrals, on the other side, would be accurate only if the original matrix would retain the three- and four-center terms: The latter are significantly smaller in the OAO basis than in the AO basis, and their neglect is much better justified in the approximation of ${}^{\lambda}\mathbf{G}$ rather than $\mathbf{G}$. In order to obtain a balanced treatment of the orthogonalization effects and compensate for the truncation to second order in $\mathbf{S}$, the derived correction terms are scaled, in a semiempiric fashion. The four scaling parameters per atom are determined in the fitting.[2] The correction terms can formally be written as pseudo-potentials:

$$
\begin{aligned}
{}^{\lambda}H_{\mu\mu} &= U_{\mu} + \sum_{B} \left[V^{\mathrm{s}}_{\mu\mu,B} + V^{\mathrm{PI}}_{\mu\mu,B} + V^{\mathrm{ECP}}_{\mu\mu,B} + V^{\mathrm{ORT}}_{\mu\mu,B} \right] && (2.61)\\
{}^{\lambda}H_{\mu\nu} &= \sum_{B} \left[V^{\mathrm{s}}_{\mu\nu,B} + V^{\mathrm{PI}}_{\mu\nu,B} + V^{\mathrm{ECP}}_{\mu\nu,B} + V^{\mathrm{ORT}}_{\mu\nu,B} \right] && (2.62)\\
{}^{\lambda}H_{\mu\tau} &= \beta_{\mu\tau} + \sum_{C} V^{\mathrm{ORT}}_{\mu\tau,C} && (2.63)
\end{aligned}
$$

In (2.63) can be seen that, apart from the sum over three-center terms, the two-center one-electron elements are formally the same as in MNDO. Hence, the only difference in the splitting into bonding and anti-bonding MO's, for the two-orbital example, arises from the new parametric form of the resonance integral β and not from any explicit orthogonalization term. Although the two-center orthogonalization contributions to ${}^{\lambda}H_{\mu\tau}$ are still implicitly treated in OM1 and OM2,

$$
{}^{\lambda}H_{\mu\tau} = M_{\mu\tau} - \frac{1}{2}\sum_{\nu\neq\mu}^{A} H_{\mu\nu}S_{\nu\tau} - \frac{1}{2}\sum_{\kappa\neq\tau}^{B} S_{\mu\kappa}H_{\kappa\tau} + O(S^3) \equiv \beta_{\mu\tau}\,, \tag{2.64}
$$

they are obviously better represented by the suggested functional $\beta_{\mu\tau}$:[65,66]

$$
\begin{aligned}
\beta^{\mathrm{MNDO}}_{\mu\tau} &= \frac{1}{2}(\beta_{\mu} + \beta_{\tau})S_{\mu\tau} && (2.65)\\
\beta^{\mathrm{OM1/OM2}}_{\mu\tau} &= \frac{1}{2}(\beta_{\mu} + \beta_{\tau})\sqrt{R_{AB}}\,\mathrm{e}^{-(\alpha_{\mu}+\alpha_{\tau})R^2_{AB}} && (2.66)\\
& && (2.67)
\end{aligned}
$$

The three-center terms added in OM2 to the MNDO Hamiltonian are:

$$
V^{\mathrm{ORT}}_{\mu\tau,C} = -\frac{1}{2}G_1^{AB}\sum_{\rho\in C}(S_{\mu\rho}\beta_{\rho\tau} + \beta_{\mu\rho}S_{\rho\tau}) + \frac{1}{8}G_2^{AB}\sum_{\rho\in C} S_{\mu\rho}S_{\rho\tau}\,(H_{\mu\mu} + H_{\tau\tau} - 2H_{\rho\rho}) \tag{2.68}
$$

with scaling factor $G_i^{AB} = \frac{1}{2}(G_i^A + G_i^B)$ being the average of the atomic fitting parameters G_i. The AO elements are approximated by

$$
H_{\mu\mu} + H_{\tau\tau} - 2H_{\rho\rho} \approx U_{\mu} + V^{\mathrm{s}}_{\mu\mu,C} + U_{\tau} + V^{\mathrm{s}}_{\tau\tau,C} - 2U_{\rho} - V^{\mathrm{s}}_{\rho\rho,A} - V^{\mathrm{s}}_{\rho\rho,B}\,. \tag{2.69}
$$

In order to analyze, how the new three-center terms in OM2 affect the single-particle spectrum, we consider the splitting of p_{π} OAO levels into bonding and anti-bonding π MO's in an extended, conjugated planar molecule. Since for these orbitals

[2] Note, that the one-center orthogonalization corrections and their scaling parameters[62] are not mentioned in the original article.[66]

Table 2.3: Orthogonalization Effect on Core Integrals.

molecule	μ/i	$F_{\mu\mu}$		$F^*_{ii} - F_{ii}$	
		MNDO	OM2	MNDO	OM2
H_2	s/σ	-5.482	-6.789	19.425	16.962
ethylene	p_z/π	-4.438	-4.124	11.568	13.228
acetylene	p_y, p_z/π_y, π_z	-4.402	-4.255	12.810	14.590
C_2	p_y, p_z/π_y, π_z	-4.826	-5.160	12.435	14.133
N_2	p_y, p_z/π_y, π_z	-7.560	-7.831	17.159	17.694

AO levels and MO gaps before (MNDO) and after (OM2) orthogonalization corrections. All energies in eV.

no s-p hybridization occurs, the magnitude of the level splitting depends essentially on the elements $H_{p_\pi^A p_\pi^B}$ between vicinal carbon atoms C_A and C_B. From the three-center terms in (2.68), only interactions with other p_π orbitals on atoms C_C survive, and since $V^s_{\mu\mu,C} - V^s_{\rho\rho,A} = 0$, the G_2-scaled terms also vanish. The remaining terms $-G_1 S_{p_\pi^{A/B} p_\pi^C} \beta_\pi$ are all positive ($\beta_\pi = -0.22$ a.u.) and of similar (or smaller) magnitude as the resonance integral. Hence, the three-center orthogonalization corrections in OM2 will not increase the gap between π and π^* MO levels. Table 2.3 shows that in absence of the three-center terms, the core Hamiltonian of diatomic molecules are still significantly affected by the resonance integral.

Weber found that vertical and adiabatic excitation energies of small organic molecules from OM1 and OM2 are of the same quality and show similar trends. They reduce the large MAE in ω_{vert} of MNDO, AM1, and PM3 to about 0.33 eV, but still show a systematical underestimation. This may partially be due to double counting of dynamic correlation from the Hamiltonian and the CI calculation, although a full CI on a semiempirical level will add only a small fraction of the exact correlation energy due to the minimal basis and the neglect of three- and four-center two-electron integrals. This issue will be discussed further in section 3.3.5.

Table 2.4 shows the effect of the new resonance integral and the orthogonalization correction on the frontier π MO levels in conjugated molecules. The HOMO–LUMO gap is systematically increased in OM2. Table 2.5 compares vertical excitation energies from AM1, MNDO, OM1, and OM2 for these systems. In these calculations, only the π-system has been included in the CI expansion. The results show that the trends found by Weber *et al.* also apply to aromatic and conjugated systems of larger extent and significantly improve the accuracy of excitation energies with respect to MNDO.

2.6.2 The SCC-DFTB Method

The density-functional based tight-binding method (DFTB) is a semi-empirical method with many similarities as the NDO methods described in this section, but with DFT as starting point, rather then HF. There are excellent reviews on this approach with focus on the derivation and applied approximations,[81–85] on its historic development,[86] its applications,[81,87,88] and performance compared to other semi-empirical methods.[89,90] Therefore, this section shall merely summarize the differences and par-

Table 2.4: Orthogonalization Effect on MO the Levels of Conjugated Molecules

molecule	method	ϵ_i	ϵ_j	ω_{ij}
butadiene	AM1	-9.344	0.459	9.803
	PM3	-9.439	0.251	9.690
	MNDO	-9.160	0.444	9.604
	OM2	-9.317	1.289	10.606
hexatriene	AM1	-8.757	-0.061	8.696
	PM3	-8.868	-0.263	8.605
	MNDO	-8.643	-0.045	8.598
	OM2	-8.589	0.664	9.253
octatetraene	AM1	-8.422	-0.377	8.045
	PM3	-8.540	-0.574	7.966
	MNDO	-8.348	-0.340	8.008
	OM2	-8.161	0.289	8.450
benzene	AM1	-9.673	0.557	10.230
	PM3	-9.740	0.393	10.133
	MNDO	-9.480	0.403	9.883
	OM2	-9.591	1.913	11.504
naphthalene	AM1	-8.718	-0.265	8.453
	PM3	-8.807	-0.426	8.381
	MNDO	-8.605	-0.325	8.280
	OM2	-8.511	0.740	9.251
anthracene	AM1	-8.116	-0.846	7.270
	PM3	-8.210	-0.998	7.212
	MNDO	-8.044	-0.857	7.187
	OM2	-7.805	-0.006	7.799
naphthacene	AM1	-7.726	-1.250	6.476
	PM3	-7.820	-1.393	6.427
	MNDO	-7.679	-1.229	6.450
	OM2	-7.342	-0.503	6.839
azulene	AM1	-7.902	-1.045	6.857
	PM3	-7.985	-1.205	6.780
	MNDO	-7.836	-1.108	6.728
	OM2	-7.537	-0.129	7.408

Table 2.5: Vertical Excitation Energies of Extended π-Systems

molecule	state	AM1/MRCI	MNDO/MRCI	OM2/MRCI	reference
butadiene	1^1B_u	5.22	4.95	6.29	6.23[b]
	2^1A_g	5.95	6.65	6.08	6.27[b]
hexatriene	2^1A_g	3.76	3.37	5.03	5.21[a]
	1^1B_u	4.84	4.65	5.41	4.95–5.13[a]
octatetraene	2^1A_g	3.30	2.98	4.37	3.97[a]
	1^1B_u	4.43	4.30	4.87	4.41[a]
decapentaene	2^1A_g	3.04	2.78	3.96	3.48[a]
	1^1B_u	4.18	4.09	4.50	4.02[a]
benzene	1^1B_{2u}	3.17	2.74	4.53	4.90[c]
	1^1B_{1u}	4.81	4.47	5.95	6.20[c]
naphthalene	1^1B_{2u}	4.04	3.82	4.87	4.66[d]
	1^1B_{3u}	2.28	2.44	3.96	4.13[d]
anthracene	1^1B_{2u}	3.50	3.37	4.05	3.60[d]
	1^1B_{3u}	2.52	2.25	3.53	3.64[d]
naphthacene	1^1B_{2u}	3.14	3.08	3.50	2.88[d]
	1^1B_{3u}	2.43	2.18	3.33	3.39*d*
pentacene	1^1B_{2u}	2.94		3.16	2.37[d]
	1^1B_{3u}	2.43		3.25	3.12[d]
azulene	11^1B_2	1.23	1.05	1.84	1.78[c]
	21^1A_1	2.67	2.41	3.38	3.52[c]
	21^1B_2	2.96	2.61	3.97	4.19[c]
	31^1A_1	3.46	3.05	4.55	4.42[c]

[a]Exp. data from Refs[67–73]. [b]CASPT2 data from Refs[74,75]; the exp. value of the 1^1B_ustate is 5.92 eV[76] and involves valence-Rydberg mixing—the "unperturbed" pure valence state transition energy has been experimentally estimated at 6.25 eV.[77] [c]Exp. data from Refs[78,79]. [d]Derived from exp. 0–0 energies, see[80] and references therein.

ticularities compared to the MNDO schemes.

As in the MNDO's, the Fock matrix (here: KS Hamiltonian) is represented in a minimal LCAO basis of atomic Slater-type orbitals. In DFTB, however, these basis functions are directly used to calculate all integrals, rather than fitting them to experimental data. This makes sense in the context of DFT, as the correlation effects are treated explicitly and do not have to be "smuggled" into the Hamiltonian via the parametrization. This argument is corroborated by the fact that the non-orthogonality of the basis functions on different centers is considered explicitly in DFTB in terms of the overlap matrix $S_{\mu\nu} = \langle\mu|\nu\rangle$ and solution of the generalized KS eigenvalue problem

$$\sum_{\nu}(H_{\mu\nu} - \epsilon_i S_{\mu\nu})c_i^{\nu} = 0\,, \tag{2.70}$$

Like in OM2, the explicit treatment of the non-orthogonality in DFTB leads to improved rotational barriers in molecules compared to conventional MNDO's such as AM1 and PM3.[90]

As all electron–electron interactions in DFT are represented by the effective potential v_s, no two-electron integrals appear in DFTB, and in the "core" Hamiltonian, in addition to the three-center integrals, also the two-center crystal field terms $\langle\mu_A|v_s^B|\nu_A$ are neglected in DFTB. The remaining contributions are:

$$H_{\mu\nu} = \begin{cases} \langle\mu|\hat{T} + v_A + v_B|\nu\rangle & \mu \in A,\ \nu \in B \neq A \\ 0 & \mu \in A,\ \nu \in A,\ \mu \neq \nu \\ \epsilon_\mu^{\text{free atom}} & \mu = \nu \end{cases} \tag{2.71}$$

Obviously, the effective potential must be divided into atomic contributions to apply these approximations. Here, two variants are used: either the effective potentials $v_A = v_\mathrm{s}[\rho_A^0]$ and $v_B = v_\mathrm{s}[\rho_B^0]$ of the isolated atoms are summed, as written in (2.71), or the effective potential is calculated for the superposition of the atomic densities ρ_A^0 and ρ_B^0:

$$H_{\mu\nu} = \langle\mu|\hat{T} + v_\mathrm{s}[\rho_A^0 + \rho_B^0]\rangle\nu \tag{2.72}$$

this is possible in DFTB, because the matrix elements are not calculated on the fly, based on atomic parameters, but can be pre-calculated and tabulated in two-center parameter files (Slater–Koster tables).

In difference to the core Hamiltonian of HF, the KS Hamiltonian depends on the actual density via the Hartree and exchange-correlation parts in the effective potential. In the first non-self-consistent implementations of DFTB, this problem was solved by defining a reference density (indicated by the superscript "0" above), and determining the MO's by diagonalizing the Hamiltonian only once. This approach, first analyzed by Harris in the context of DFT,[91] yields a stationary energy w.r.t. variation of the reference density. As shown by Foulkes and Haydock, the energy can be expanded in a Taylor series around the reference density.[92] This expansion was adopted in the self-consistent charge (SCC) extension of DFTB:

$$\begin{aligned} E[\rho] &= E[\rho^0] + \frac{1}{2}\iint \frac{\Delta\rho(r)\Delta\rho(r')}{|r-r'|}\,\mathrm{d}r\,\mathrm{d}r' \\ &\quad + \frac{1}{2}\iint \left(\frac{\delta^2 E_{xc}}{\delta\rho(r)\delta\rho(r')}\right)_{\rho^0} \Delta\rho(r)\Delta\rho(r')\,\mathrm{d}r\,\mathrm{d}r' \end{aligned}$$

The density fluctuations $\Delta\rho$ are divided into atomic contributions, which are then approximated by spherically-symmetric atom densities. The integral is then represented by the Klopmann–Ohno function $\gamma(R_{AB})$,[93,94] also used for the two-center two-electron integrals in INDO and CNDO (Eq 2.57):

$$\frac{1}{2}\sum_{A,B}\gamma_{AB}(R_{AB})\Delta Q_A \Delta Q_B\,, \tag{2.73}$$

which interpolates between the Coulomb interaction at large distance R_{AB} and the average Hubbard parameter of the two atoms for $R_{AB} \longrightarrow 0$:

$$\gamma_{AA} = U_A = \left.\frac{\partial^2 E_{\text{atom}}}{\partial Q_A^2}\right|_{Q_A=0} \tag{2.74}$$

$$\gamma_{AB} = \left\{R_{AB}^2 + \frac{1}{4}\left(\frac{1}{U_A}+\frac{1}{U_B}\right)^2\right\}^{-1/2} \tag{2.75}$$

The SCC extension to DFTB improves the charge equilibrium in polar organic molecules and is used as by default in all QM/MM applications of DFTB to biologic systems. A third-order correction term was recently introduced into the SCC-DFTB method,[95] but this variant is not applied in this work. In both SCC and non-SCC versions, the atomic densities used to build the reference density for the effective potential and the atomic orbitals used to calculate the reference Hamiltonian matrix elements (but not the onsite energies) are compressed by applying a weak harmonic potential in the DFT calculations.

The repulsive double-counting terms that have to be added in the DFT total energy expression are traditionally used to minimize the deviation between DFT and DFTB total energy differences and vibrational properties. Simplified, the repulsive potential is fitted to obtain

$$E_{\text{rep}} \approx E_{\text{DFT}} - \sum_i \epsilon_i^{\text{DFTB}}\,. \tag{2.76}$$

Chapter 3

Excited-State Quantum Mechanical Methods

3.1 Time-Dependent Density Functional Response Theory

Density functional theory, as described in section 2.5, is limited to the electronic ground-state, or the lowest state of each spin symmetry. A very efficient approach to obtain excited-state properties in the framework of KS theory is to combine the time-dependent generalization of DFT (TDDFT) with linear-response theory.[96] The generalization of the Hohenberg–Kohn theorems and the Kohn–Sham formalism to the time-domain was established by Runge and Gross.[97] This Runge–Gross theorem states that the time-dependent density $\rho(r,t)$ of a system of interacting particles in an time-dependent local external potential $v(r,t)$ determines this potential uniquely up to a purely time-dependent (spatially constant) function. Further, the exact time-dependent density can be obtained from a model system of N noninteracting particles in an effective potential $v_s[r,t,\rho(r,t)]$:

$$\rho(r,t) = \sum_{i=1}^{N} |\psi_i(r,t)|^2 \tag{3.1}$$

$$\left(-\tfrac{1}{2}\nabla^2 + v_s(r,t)\right)\psi_i(r,t) = i\frac{\partial}{\partial t}\psi_i(r,t)\,, \tag{3.2}$$

where

$$v_s(r,t) = v(r,t) + \int \frac{\rho(r',t)}{|\mathbf{r}-\mathbf{r}'|}\,dr' + \underbrace{\frac{\delta A_{xc}[\rho]}{\delta\rho(r,t)}}_{v_{xc}[\rho](r,t)}\,. \tag{3.3}$$

In these time-dependent Kohn–Sham equations (TDKS), the exchange-correlation potential $v_{xc}[\rho](r,t)$ is a nonlocal functional both in time and in space, i.e., it depends on the entire history of the system. Nonetheless, in the most common "adiabatic" approximation, an approximate ground-state functional is simply evaluated with the time-dependent density:

$$v_{xc}^{adia}[\rho](r,t) = v_{xc}[\rho(r,t)] \tag{3.4}$$

There are two efficient approaches based on the TDKS equations to determine excited-state properties. The explicit time-propagation of the density by numerical integration of (3.1) can be used to simulate the dipole response of the electrons to a weak instantaneous perturbation.[98] The latter can be a short electric pulse, or displacement of the KS orbitals by the transformation $\psi_i \longrightarrow \psi_i' = \mathrm{e}^{ikz}\psi_i$. The fourier transform of the resulting time-dependent dipole moment then yields the frequency-dependent dipole-polarizability tensor, which has peaks at the energies of optical excitation. This approach is implemented, e.g., in the octopus code[99] and is most suitable for the calculation of optical spectra that contain a large number of transitions.

For the calculation of individual excited states and their properties, a different approach, based on linear-response theory, has been proposed,[96,100] which is now implemented in many quantum chemistry programs and has become a synonym for "TDDFT". Formally, this approach uses the density-response to a weak, adiabatically switched external potential to determine the poles and residues of the dynamic polarizability. The poles are at the same positions as the peaks in the time-propagation spectrum and the residues can be associated with the oscillator strengths. In practice, this leads to the solution of an eigenvalue problem for the excitation energies ω_I of the KS system:

$$\mathbf{\Omega}\,\mathbf{F}_I = \omega_I^2\,\mathbf{F}_I\,, \tag{3.5}$$

where $\mathbf{\Omega}$ is the response matrix, which is for closed-shell ground states:

$$\Omega_{ia,jb} = \delta_{ij}\delta_{ab}\omega_{jb}^2 + 2\sqrt{(n_i - n_a)\omega_{ia}}\,K_{ia,jb}\,\sqrt{(n_j - n_b)\omega_{jb}}\,. \tag{3.6}$$

The first term contains the KS eigenvalue differences $\omega_{ia} = \epsilon_a - \epsilon_i$. The second term contains the coupling matrix K, which gives a correction to the diagonal terms that causes a singlet–triplet splitting and off-diagonal elements that are responsible for the mixing of the single-particle transitions. For the singlet (S) and triplet (T) case it is given by:

$$K^S_{ia,jb} = \iint \psi_i(r)\psi_a(r)\left(\frac{1}{|r-r'|} + \frac{\delta^2 E_{xc}}{\delta\rho(r)\delta\rho(r')}\right)\psi_j(r')\psi_b(r')\,\mathrm{d}r\mathrm{d}r' \tag{3.7}$$

$$K^T_{ia,jb} = \iint \psi_i(r)\psi_a(r)\,\frac{\delta^2 E_{xc}}{\delta m(r)\delta m(r')}\,\psi_j(r')\psi_b(r')\,\mathrm{d}r\mathrm{d}r'\,, \tag{3.8}$$

with total density $\rho = \rho_\uparrow + \rho_\downarrow$ and magnetization density $m = \rho_\uparrow - \rho_\downarrow$. Oscillator strengths for the singlet states are obtained from the response matrix eigenvectors and the transition-dipole moments $(i|\hat{r}|a)$:

$$f_I = \frac{2}{3}\sum_{i,a}^{n_i>n_a}(n_i - n_a)(\epsilon_a - \epsilon_i)\langle\psi_i|\hat{r}|\psi_a\rangle^2 F_{ia}^2\,. \tag{3.9}$$

As shown by Furche,[101–103] also the exact excited-state density matrix, response properties and analytical derivative of the excitation energy can be obtained.

3.2 Time-Dependent Extension of the SCC-DFTB Scheme

The time-propagation and linear-response formalism has been implemented also in the framework of the SCC-DFTB method by Niehaus.[104–106] For the linear-response

implementation, the required approximations concern only the coupling matrix **K**, which must be expressed in terms of two-center integrals in order to preserve the computational efficiency of the ground-state method. The choice of such an approximation is facilitated by the similarity of the coupling matrix (3.7) with the second-order correction term in SCC-DFTB (2.73). After expanding the KS orbitals in the LCAO basis,

$$K^{S/T}_{ia,jb} = \sum_{ABCD} \sum_{\substack{\mu\in A\\ \nu\in B}} \sum_{\substack{\kappa\in C\\ \tau\in D}} c_i^\mu c_a^\nu c_j^\kappa c_b^\lambda \iint \phi_\mu(r)\phi_\nu(r) V^{S/T}(r,r')\phi_\kappa(r')\phi_\lambda(r')\, dr dr' \tag{3.10}$$

The four-index integrals are approximated by two-index integrals using the Mulliken approximation

$$V^{S/T}_{\mu\nu,\kappa\lambda} \approx \tfrac{1}{4} S_{\mu\nu} S_{\kappa\lambda} \left(V^{S/T}_{\mu\mu\kappa\kappa} + V^{S/T}_{\mu\mu\lambda\lambda} + V^{S/T}_{\nu\nu\kappa\kappa} + V^{S/T}_{\nu\nu\lambda\lambda} \right) \tag{3.11}$$

In a monopole approximation, all functions on an atom are represented by the same spherical density. Introducing the Mulliken transition charges

$$Q^{ij}_A = \sum_{\mu\in A} \sum_B \sum_{\nu\in B} c_i^\mu c_j^\nu S_{\mu\nu}\,, \tag{3.12}$$

the same "γ approximation" as applied for the SCC term yields the coupling matrix

$$K^S_{ia,jb} = \sum_{A,B} \tilde{\gamma}_{AB} Q^{ia}_A Q^{jb}_B \tag{3.13}$$

$$K^T_{ia,jb} = \sum_{A,B} \tilde{m}_{AB} Q^{ia}_A Q^{jb}_B\,. \tag{3.14}$$

It is consistent to employ here the same γ function as in the SCC extension, which contains the Hubbard parameters of the neutral atoms. Here, the actual density, as reflected in the converged MO coefficients, is not the reference density and accordingly, the Hubbard parameters would be charge-dependent. Although such charge-dependency is introduced in the third-order SCC correction,[95] it is neglected in the linear-response implementation.

Due to the short-range character of the function $\tilde{m}_{AB}$, a one-center approximation is used for the coupling matrix of the triplet states:

$$\tilde{m}_{AB} \approx M_A \delta_{AB} = \frac{1}{2} \left(\frac{\partial \epsilon_{\mathrm{HOMO}}}{\partial \rho_\uparrow} - \frac{\partial \epsilon_{\mathrm{HOMO}}}{\partial \rho_\downarrow} \right) \delta_{AB} \tag{3.15}$$

The new parameters M_A are also determined for the reference density and are obtained from atomic DFT calculations.

To obtain the oscillator strengths, the Mulliken approximation is applied to the matrix elements of the dipole operator:

$$\langle \psi_i | \hat{r} | \psi_a \rangle = \sum_{A,B} \sum_{\mu\in A} \sum_{\nu\in B} c_i^\mu c_a^\nu \underbrace{\langle \phi_\mu | \hat{r} | \phi_\nu \rangle}_{\frac{1}{2} S_{\mu\nu}(r_A + r_B)} = \sum_A r_A Q^{ia}_A \tag{3.16}$$

Eq (3.9) then yields:

$$f_I = \frac{2}{3} \sum_{i,a}^{n_i > n_a} \sum_A (n_i - n_a)(\epsilon_a - \epsilon_i) |r_A|^2 (Q^{ia}_A)^2 F^2_{ia}\,. \tag{3.17}$$

The excited-state density matrix and analytic derivatives have been implemented by Heringer *et al.*,[107] based on the formalism of Furche and Ahlrichs[102] and using the same approximations as presented here.

3.3 Multireference Approaches

3.3.1 MCSCF

In difference to single-configurational SCF, the multi-configurational SCF (MCSCF) scheme searches for the total energy minimum of a multi-configurational wave function with respect to both orbital and CI coefficients. MCSCF is therefore the most obvious generalization of HF when the wave function is badly represented by a single Slater determinant, i.e., in cases where non-dynamic correlation becomes important (see section 2.3). A methodological problem of the MCSCF approach is that the optimization of orbital and CI coefficients of a wave function become increasingly redundant the more complete the CI expansion is chosen. In the limit of full CI, the orbital coefficients are completely irrelevant. The most efficient MCSCF approach, the complete active space SCF (CASSCF) method[108,109] therefore separates the molecular orbital space into three subspaces: an inactive space of doubly occupied orbitals, an active space of orbitals that are arbitrarily occupied by a fixed number of (active) electrons, and another inactive space of unoccupied (external) orbitals. The CASSCF wave function is therefore a symmetrized product of a HF and a full CI wave function, which is invariant w.r.t. rotations between orbitals within each of the three subspaces. Correspondingly, the variation of the wave function is expressed in terms of occupied–active, active–virtual, and occupied–virtual rotations, which can be represented by unitary operators $\hat{U} = \mathrm{e}^{\hat{T}}$. The anti-hermitian operators $\hat{T} = \sum_{pq} T_{pq}\hat{E}_{pq}$ contain the variational parameters (orbital-rotation coefficients):

$$T = \begin{pmatrix} 0 & T_{ip} & T_{ia} \\ -T_{ip} & 0 & T_{pa} \\ -T_{ia} & -T_{pa} & 0 \end{pmatrix} \tag{3.18}$$

The variation of the CI coefficients can be represented by unitary rotations $\mathrm{e}^{\hat{S}}$ of the CI vector approximating the state of interest in the chosen CI space. The simultaneous variation of CI and MO coefficients can then be represented by the operators $\mathrm{e}^{\hat{T}}\mathrm{e}^{\hat{S}}$. By expanding the corresponding variation of the energy expectation value

$$E(T,S) = \langle 0|\mathrm{e}^{\hat{T}}\mathrm{e}^{\hat{S}}\,\hat{H}\,\mathrm{e}^{\hat{T}}\mathrm{e}^{\hat{S}}|0\rangle \tag{3.19}$$

up to first or second order in the operators $\hat{S}$ and $\hat{T}$, expressions for the generalized gradient and Hessian are obtained.

All practical MCSCF implementations can be understood as approximations and modifications to the full Newton–Raphson procedure,[109] which searches for the next local energy minimum on the harmonically approximated potential energy surface, i.e., by exploiting the information of the energy gradient and Hessian matrix. For large CI spaces, it is not efficient to calculate the exact Hessian matrix elements. In particular, the elements coupling orbital with CI rotations are too expensive and are

approximated, e.g., in the super-CI procedure.[108] If these matrix elements are completely neglected, the optimizations of CI and MO coefficients are decoupled, but the super-linear convergence of the Newton–Raphson procedure is lost. An efficient alternative to the exact calculation of the Hessian matrix elements is to update the Hessian based on the gradient information of the previous steps.

When the numbers of active orbitals and active electrons are set, the choice of active orbitals is in principle uniquely defined in terms of the variational principle. If a proper initial guess for the active and occupied inactive orbitals is made, it is likely that the global energy minimum in the configuration space is found with state-of-the-art implementations. As initial guess for the ground-state orbitals, RHF or natural orbitals from an UHF, CI, or MP2 calculation can be used. However, it is often necessary, to manually select those orbitals that will yield the lowest energy, using chemical intuition.

The most severe disadvantage of the CASSCF approach is that the computational cost increases factorial with the number of active orbitals (m) and electrons (N). The number of required configurations for a CAS(N,m) wave functions is given by the Weyl formula[110]

$$N_{\mathrm{CSF}} = \frac{2S+1}{m+1}\left(\frac{m+1}{N/2-S}\right)\left(\frac{m+1}{N/2+S+1}\right), \tag{3.20}$$

where S is the total spin. The largest feasible active spaces are CAS(14,14), CAS(12,18) or CAS(18,12), and this will hardly change in future generations of computer hardware. Therefore, the method is limited to very small atoms and molecules or to the description of only a part of the electron correlation, predominantly the non-dynamic one. In this context, non-dynamic correlation is often used as a synonym for the correlation of the π electrons in essentially planar molecules. In practice, the π orbitals all recover more correlation than any n or σ orbital. However, if excited states are requested that are not represented by n$\rightarrow$ π^* transitions, the active space must be extended to include the relevant orbitals.

Apart from problems that involve non-dynamic correlation, CASSCF can also be employed to calculate excitation energies of low-lying states by optimizing the orbital coefficients for higher roots of the CI Hamiltonian. Here, the problem must be addressed that the CASSCF wave functions build with different orbitals will not be orthogonal. To obtain the correct excitation energies and transition properties, the orbitals must be transformed into bi-orthogonal orbitals in the state interaction method.[111] An alternative is to optimize the MO coefficients for several CI roots simultaneously (state averaging), i.e., represent the wave functions of the different states in a common MO basis.

3.3.2 The MRCI method

The idea of MRCI is to incorporate both static and dynamic correlation in an efficient CI expansion to obtain quantitatively accurate results for properties of excited states or highly correlated ground states that are badly described by the HF configuration. The non-dynamic correlation can easily be described using a relatively small set of configurations, which may include highly-excited configurations. In contrast, the description of dynamic correlation, i.e., the Coulomb hole by means of configuration interaction is very inefficient, as the correlation energy is converging extremely slowly

with the size of the CI expansion. To limit the computational cost, the latter has to be truncated at a certain level of excitation. To define a configuration space that is most effective for the description of both kinds of correlation, a minimal CI expansion is chosen that qualitatively describes the states of interest and replaces the HF determinant as a reference in single-reference CI. The dynamic correlation is then recovered by expanding the CI space to the first-order interacting space (FOIS). The FOIS is defined by the set of configurations of the requested spin-symmetry that interact with the reference wave function in second-order perturbation theory:

$$< \Phi_I | \hat{H} | \Psi_{\text{ref}} > \neq 0 \,, \tag{3.21}$$

which involves only determinants that are singly and doubly excited w.r.t. any of the reference configurations (Slater-Condon rules). The CI coefficients are then determined variationally by iterative diagonalization procedures (direct CI) that determine the lowest roots of the Hamiltonian in the FOIS.

The MRCI method allows for a balanced description of dynamic vs. non-dynamic correlation and is therefore suitable to obtain quantitative excitation energies. However, the same limitations as to the truncated single-reference CI, as discussed in section 2.4, apply: Even if a size-consistent reference (e.g., CASSCF) is used, the MR-CISD is not size-consistent. Due to the unfortunate scaling of CISD, MRCI is applicable only to small molecules.

3.3.3 MRPT and the CASPT2 method

The MCSCF approaches described in section 3.3.1 recover usually only a small fraction of the correlation energy, as their focus is to incorporate merely non-dynamic correlation. Hence, their results for systems with negligible static correlation suffer from the same deficiencies as HF. Even worse, dynamic and non-dynamic correlation have often contrary effects on the calculated properties. As will be shown in section 5.3, the bond-length alternation in conjugated molecules are often better described at the HF than at the CASSCF level of theory. The large systematic errors resulting from an unbalanced description of correlation in CASSCF therefore call for a correction to account for the dynamic correlation. Given the enormous size of the FOIS, perturbative schemes are employed much more frequently than the MRCI method described in the previous section. Furthermore, the size-consistency of perturbation theory can be exploited in combination with the size-consistent CAS reference. The combination of CASSCF reference and second order perturbation theory has been implemented in the most effective CASPT2 variant,[112,113] which represents one of the most established methods in excited-state quantum chemistry.

In CASPT2, the zeroth-order Hamiltonian is chosen as a generalization of the single-particle Fock operator used in MP perturbation theory:

$$\hat{H}_0 = \hat{F} = \sum_{pq} f_{pq} \hat{E}_{pq} \,, \tag{3.22}$$

$$f_{pq} = h_{pq} + \sum_{rs} P_{rs} \left[(pq|rs) - \frac{1}{2}(pr|qs) \right] \tag{3.23}$$

For a CASSCF reference, the occupied–external contributions f_{ia} vanish due to the generalized Brillouin theorem. While $\hat{F}$ is diagonal in the canonical orbital basis for a HF

reference, this is not the case for a CASSCF reference. In the CASPT2D approximation, the off-diagonal elements are neglected with small loss of accuracy and computational cost. It is common in current CASPT2 implementations to add a "g3" correction term to the zeroth-order Hamiltonian, which affects only the energies of the active orbitals and leads to some improvement in excitation energies.[114] As in MP theory, the FOIS contains only single and double excitations of the reference configurations, and the first-order wave function Ψ_1 is defined by applying the excitation operators directly on the reference wave function Ψ_0:

$$|\Psi_1\rangle = \sum_{pqrs} C_{pqrs} \hat{E}_{pq} \hat{E}_{rs} |\Psi_0\rangle \tag{3.24}$$

With this "internally contracted" definition of Ψ_1, CASPT2 differs from single or multiconfigurational MP methods, which construct the first-order wave function from the set of configurations included in the FOIS that do not occur in the reference wave function, without any contraction in the coefficients.

The contraction of the CASPT2 first-order wave function brings about that the excitations of Ψ_0 in eq 3.24 are not orthogonal (not even linear independent). Therefore, the equation for the coefficients C_{pqrs} has a more general form, containing the overlap matrix S:

$$(F - E_0 S)C = -V \tag{3.25}$$

$$V_{pqrs} = \langle \Psi_0 | \hat{H} \hat{E}_{pq} \hat{E}_{rs} | \Psi_0 \rangle \tag{3.26}$$

To solve this equation for the coefficients C, the overlap matrix is diagonalized, and a basis transformation to its non-zero eigenvectors is performed. In this new basis, however, the Fock operator is not a single-particle operator anymore, and to calculate F, the first, second, third, and forth order density matrices of Ψ_0 are required. Hence, the calculation of the Fock matrix becomes the bottle neck in CASPT2 calculations if the CAS reference contains more than ten orbitals.

Another problem in MRPT is that individual coefficients C_{pqrs} may become exceedingly large (intruder state). In MP theory, this is prevented by the large energy denominators in the first-order equation if the HF wave function is a good reference. Even if the CAS reference has a high weight in the first-order corrected wave function, a level shift must be added to E_0 to avoid the intruder-state problem in CASPT2.

3.3.4 The SORCI method

The idea of the spectroscopy oriented CI (SORCI) approach, suggested and implemented by Frank Neese,[115,116] is to combine the advantages of MRCI and MRPT: Based on an arbitrary reference space, the FOIS is defined similar as in MRCI (MRCISD) und divided into subspaces of strongly perturbing (selected) and weakly perturbing (unselected) configurations, corresponding to their contribution to the MR-MP2 energy:

$$\frac{|\langle \Psi_I^{(0)} | \hat{H} | \Phi_\mu \rangle|^2}{\langle \Psi_I^{(0)} | \hat{H}_0 | \Psi_I^{(0)} \rangle - \langle \Phi_\mu | \hat{H}_0 | \Phi_\mu \rangle} \geq T_{\text{sel}} \tag{3.27}$$

Here, $\Psi_I^{(0)}$ is the zeroth-order (reference) wave function for state I, and $\hat{H}_0$ the zeroth-order Hamiltonian, which is the same as in the CASPT2D method and includes the g3 correction. In variance to CASPT2, the first-order wave function is uncontracted,

as in the MR-MP approaches of Murphy and Messmer[117] and Grimme and Waletzke,[118] and the CI basis remains orthogonal (see previous section). The amplitudes of the selected configurations are determined variationally, i.e., by diagonalizing the Hamiltonian in the subspace of the reference and strongly perturbing configurations (projectors $\hat{P}_{\text{ref}}$ and $\hat{P}_{\text{sel}}$):

$$(\hat{P}_{\text{ref}} + \hat{P}_{\text{sel}})\hat{H}(\hat{P}_{\text{ref}} + \hat{P}_{\text{sel}})\Psi_I^{(a)} = E_I^{(a)}\Psi_I^{(a)} \tag{3.28}$$

The contributions of the unselected configurations are determined in a relaxed MP2 calculation:

$$E^{\text{unsel}} = \sum_{\mu}^{\text{unsel}} \frac{|\langle\Psi_I^{(a)}|\hat{H}|\Phi_\mu\rangle|^2}{\langle\Psi_I^{(a)}|\hat{H}_0|\Psi_I^{(a)}\rangle - \langle\Phi_\mu|\hat{H}_0|\Phi_\mu\rangle} \tag{3.29}$$

Hence, the convergence of the perturbative treatment is assured and no intruder-states can occur. The size-consistency error of the variational energy contribution is reduced by adding a Davidson-type correction term E_I^{corr}. The total SORCI energy for state I is then:

$$E_I = E_I^{(\text{a})} + E_I^{\text{corr}} + E_I^{\text{unsel}} \tag{3.30}$$

While combining the numeric stability of MRCI, the efficiency and size-consistency of PT is exploited by describing the major part of the dynamic correlation at the MP2 level. The method is applied most effectively by choosing a rather small reference (compared to CASPT2) and increasing T_{sel} until the results are converged to the required level. This can be achieved by using an optimal choice of initial orbitals (vide infra) and pre-selecting the reference configurations from a preliminary CAS or RAS calculation: Configurations with a weight smaller than a second threshold, T_{pre}, in any of the states of interest are excluded from the reference space.

Another important feature of SORCI is the exclusion of certain classes of excitations from the FOIS. Adopting the concept of difference-dedicated CI (DDCI), suggested by Caballol *et al.*, the orbital space is divided into low-lying occupied (internal), high energy virtual (external) orbitals and orbitals that are variably occupied in the reference space for the states of interest (active). The largest class of configurations in the MR-CISD FOIS have two holes in the internal and two electrons in the external orbitals. Since their contribution to the correlation energy is almost the same for different electronic states, they can safely be neglected when calculating excitation energies, which defines DDCI3. In consequence, the scaling with system size is reduced from order N^4 to N^3. A further reduction of the FOIS to DDCI2 excludes configurations with two holes (one particle) or one hole (two particles) in the internal (external) orbitals, respectively. DDCI2 still yields excitation energies of acceptable accuracy but the deviations from MRCI and DDCI3 are usually in the order of several hundred meV. In SORCI, DDCI2 is used in a preliminary calculation to generate approximate state-averaged natural orbitals for the actual DDCI3 calculation.

The use of natural orbitals makes the results less dependent on the choice of the initial MO basis (RHF, UHF, DFT, CASSCF), which is of particular importance when the canonical HF or DFT orbitals are inappropriate for the description of the excited states of interest. They result in most compact wave functions in which already a small reference is sufficient to achieve a high weight in the final CI vectors. In addition, natural orbitals with occupation numbers close to zero or two (within a threshold T_{nat}) can be frozen, i.e., excluded from the CI space, without loss of accuracy. This leads to

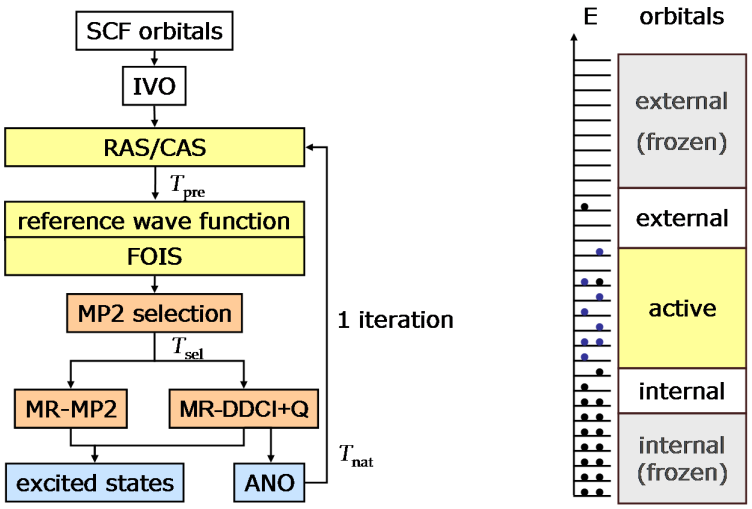

Figure 3.1: Default procedure of a SORCI calculation (left). Orbitals involved in the final DDCI3 step (right).

a considerable increase of efficiency when using larger basis sets. The disadvantage of the use of approximate natural orbitals consists in the arbitrariness of their generation. This important practical aspect shall be investigated in some detail in the following section.

Figure 3.1 sketches the procedure of a standard SORCI calculation: The MO basis for the preliminary CI calculation is provided by a SCF or MC-SCF calculation. In case of HF, the virtual orbitals can be improved for the application in CI by an additional SCF step where one electron is removed from the system. These "improved virtual orbitals" (IVO's) are more compact and their energy levels more comparable with quasi-particle or KS levels. At this level, some MO's can already be discarded from proceeding CI calculations in terms of an energy criterion. This option is intended to freeze the core levels of heavy atoms but can also be used to limit the memory consumption in the following integral transformation by excluding virtual orbitals of high energy. The Hamiltonian is diagonalized in the defined RAS/CAS space and the reference configurations are selected corresponding to the T_{pre} criterion (vide supra). The RAS/CAS definition also determines the orbitals considered as "active" in the DDCI2 and DDCI3 calculations. The FOIS of DDCI2 is then generated based on the reference and the internal/active/external orbital ranges. The MP2 selection criterion (3.27) is applied to the generated FOIS configurations to select the configurations for the DDCI2 calculation. After the DDCI2 calculation, the density matrices of the states of interest are averaged and diagonalized to obtain the ANO's and their occupation numbers. ANO's are frozen corresponding to the T_{nat} threshold and the hole procedure is repeated with the ANO's and DDCI3. After the latter, the Davidson correction is applied and the contributions of the unselected configurations are calculated in a relaxed MP2 calculation to obtain the final energies. Electronic properties are calculated directly from the DDCI3 density matrices.

The convergence of excitation energies and electrostatically-induced shifts with respect to the thresholds T_{pre}, T_{sel}, and T_{nat}, and the basis set are considered in Appendices 9.1 and 9.1, respectively, for a protonated Schiff base model. With the target

accuracy of 0.1 eV, safe thresholds are defined, and these thresholds are employed throughout this work if not noted otherwise. Convergence with respect to T_{pre} is certainly not complete, as the converged value would be the full-CI result. Corresponding to the experience gained within this work, values between 10^{-3} and $10^{-}4$ represent an optimal choice, both with respect to efficiency and accuracy. Further, the threshold T_{sel} determines the ratio between the perturbational and the variational evaluation of the configurational contribution to the correlation energy. While the "error" of the perturbational treatment with respect to the CI expansion can be reduced by using smaller values of T_{sel}, the size-consistency error contained in the MR-CISD treatment will increase. As MP2 is size-extensive in contrast to CISD, it will be superior if the perturbation is sufficiently small, i.e., the reference is of sufficient quality. There is little to no experience about the effect of the MRCI size-inconsistency error on excitation energies of large molecules and the performance of the Davidson and other empirical size-consistency corrections. It is therefore not clear whether the fully converged MR-DDCI3+Q result will outperform the SORCI one with finite T_{sel}. In practice, however, T_{sel} provides the strongest control on the computational cost of the SORCI calculation, and it is an essential advantage of the method that it achieves an attractive efficiency/accuracy ratio for a wide range of T_{sel}.

SORCI owes both its flexibility and its largest drawback to the use of individual selection: total energies are less well defined as excitation energies and potential energy surfaces are not microscopically smooth. For the prediction of very small shifts in the excitation energy, the physical effects may compete with numerical fluctuations due to changes in the reference and the configuration selection. The implemented perturbational correction for the internal–external doubles configurations, which are excluded from the DDCI3 FOIS, was not successful in the prediction of total energies in the context of polarizable-MM calculations (chapter 6). Apart from the numerical fluctuations, satisfying excited-state total energies can be obtained by adding the SORCI excitation energies to the ground-state total energies obtained with the single-reference correlation module in ORCA.

Generation of Approximate Natural Orbitals

Apart from the thresholds described in the previous section, the result of a SORCI calculation depends on the procedure used to obtain the approximate natural orbitals (ANO) that are used in the final DDCI3 calculation. There are many ways to obtain ANO's and little to no publications that consider the problem. The "default" procedure implemented in ORCA performs one (or several) DDCI2 calculation(s), preferentially using IVO's and canonical orbitals as starting point. The same definition of active orbitals and reference configuration is used as for the final DDCI3. The advantage is that no user interaction is needed to select the active orbitals for the DDCI2, as simply the frontier orbitals are used. The latter represents also the greatest disadvantage, because the frontier orbitals are usually not the optimum choice and, more important, can contain orbitals of different type when performing several calculations. For example, the 8 frontier orbitals of octatetraene may contain 4 π orbitals in one calculation and 5 in another, which gives rise to artificial shifts in the excitation energies.

In the course of this work, alternatives have been tested, which of the most promising procedures are:

Iterative DDCI The DDCI2 or DDCI3 calculation and ANO generation can be iter-

ated until a certain convergence in the calculated properties is achieved. In practice, the convergence is slow and the final result is of purer quality than without the ANO iterations. In general, the excitation energies will be close to DDCI3 calculations performed with CASSCF orbitals and systematically overestimated compared to CASPT2 calculations using the same orbitals and CAS reference. It is not guaranteed that the ANO's converge to the "right" orbitals: If the system contains weakly interacting subsystems with π orbitals, the latter may achieve higher natural orbital occupation numbers than those of the chromophore even when excited states of the chromophore are used in state-averaging.

Manual Selection By choosing manually the canonical/IVO orbitals that are most similar to the ANO's of the DDCI2 calculation (those that are required for the considered states), a more or less unique set of ANO's can be produced. In practice however, the desired orbitals are more or less mixed up with orbitals that do not contribute to the correlation or excited-state transitions. The level of mixing may change from one calculation to another, which may affect the calculation of spectral shifts. To remedy this problem, the selected orbitals can be de-mixed manually by specifying rotation angles for the input MO's. This procedure is the most tedious one, but also yields the best results. The arbitrariness of the rotation angles usually translates to an arbitrariness in the excitation energy of ca. 0.01 eV. In some cases, however, fluctuations of up to 0.03 eV were found for varying choices of the rotation angles.

Minimal CI ANO's As a compromise between the two previous approaches, the MO's for the ANO-generating DDCI2 calculation can be obtained as ANO's from a minimal CI calculation on canonical orbitals. Also canonical MO's from an UHF, or minimal MCSCF [e.g., CAS(2,2)] are possible, but do not always produce the same order, i.e., frontier orbitals as the ANO's from multi-state CI calculations. In practice, ANO's from a 3-root CAS(2,2) calculation containing the HOMO and LUMO *pi* orbitals reliably produces frontier orbitals that contain the entire π system. The resulting excitation energies are systematically higher than with *manual selection*, but the difference is small (e.g., 0.05–0.17 eV for S_1 in retinal in rhodopsins) and can reduced significantly by freezing orbitals, i.e., limiting the orbitals in the CI using the *ewin* threshold.

3.3.5 Semiempirical MRCI

In section 2.6.1, it was shown that the semiempirical OM2 Hamiltonian is well suited for excited-state calculations in extended MRCI expansions. While other semiempirical Hamiltonians, such as AM1, PM3, MNDO, yield full CI excitation energies that are dramatically underestimated, OM2 does not suffer from this systematic error and in combination with MRCI yields accurate results for both ground and excited-state applications. Thus far, two implementations of OM2/MRCI exist. In the group of Paul Tavan,[119,120] an individual selecting MRCI has been developed, which is very effective for large systems and applications where many active orbitals must be included in the MRCI. The development of OM2/MRCI in the group of Walter Thiel has focused on the implementation of analytical gradients for molecular dynamics applications based on the graphical unitary group approach (GUGA).[121] The latter implementation (MNDO program package) was extensively applied in this work and some

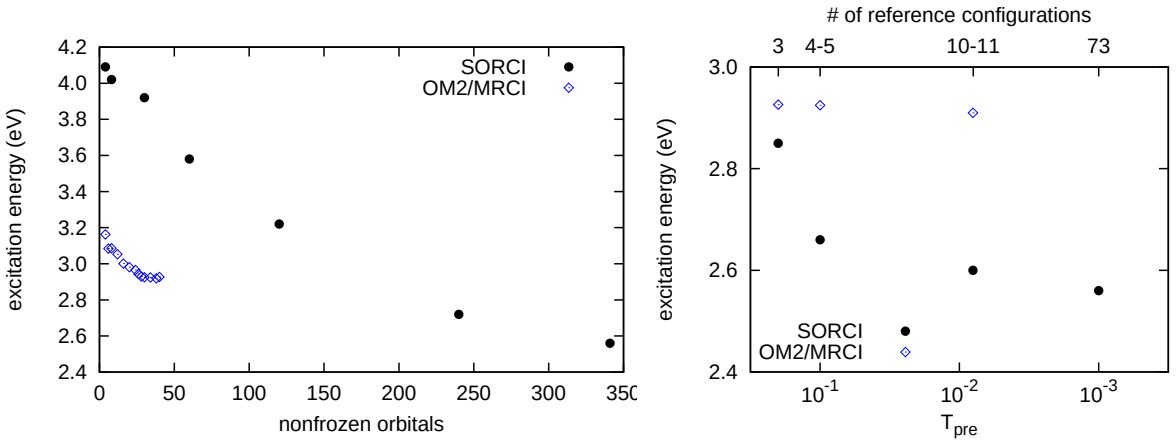

Figure 3.2: Convergence of the lowest excitation energy of pharaonis sensory rhodopsin II (psRII) w.r.t. the number of active MO's (left) and number of reference configurations (right).

technical details of this method shall be given in this section. Further, some general aspects of semiempirical MRCI will be discussed.

As the GUGA implementation of MRCI does not allow for an individual selection of the configurations included in the CI expansion, it is mandatory to limit the number of active, i.e., unfrozen orbitals for the MRCI. To gain one order of magnitude in computational efficiency compared to CASPT2 or SORCI, it is necessary to reduce the number of active orbitals to ca. 30–40. In contrast to *ab initio* MRCI, this is already sufficient to obtain converged excitation energies (see Figure 3.2, left). The reason for the fast convergence is that dynamic correlation is included already in the semiempirical Hamiltonian. Whereas at the *ab initio* level, the incorporation of dynamic correlation converges extremely slowly with the size of the CI expansion, as the latter is very inefficient to produce the Coulomb hole in the two-particle reduced density. The same fast convergence is inherent to the DFT/MRCI method of Grimme and Waletzke,[122] which employs integrals from hybrid DFT and CI matrix elements that are empirically scaled, depending on the CSF energy. It is interesting, that the same fast convergence is found also for the size of the reference (Figure 3.2, right). This shows that for the incorporation of the purely non-dynamic correlation, which is not included in semiempirical Hamiltonians or local density functionals, merely a very small CI expansion is required. This finding makes the development of methods highly desirable that combine the respective efficiencies of implicit and explicit treatments of correlation.

The MNDO program features several criteria to select the active MO's and reference configurations. From the experience gained in this work, the best (in terms of energy lowering) selection of active orbitals for the description of $\pi \rightarrow \pi^*$ excitations is obtained by choosing the MO's with the most *pi* character. As a manual selection involves some arbitrariness and is to time-consuming, the best option for the S_1 state is to perform consecutive minimal CAS(2,2) calculations which include HOMO and one virtual orbital, or LUMO and one occupied orbital. The S_1 energy is calculated for all "second" MO's and the n_{occ} occupied and n_{virt} virtual MO's with the lowest S_1 energies are defined as active. This algorithm is not very efficient in selecting the most important (e.g., π)orbitals, but outperforms a simple frontier-orbital active space. Based on this experience, a more efficient selection criterion for $\pi \rightarrow \pi^*$ excitations is

currently implemented by Tom Keal, which considers directly the π character of the MO's in terms of the "out-of-plane" contributions of the p-shell AO's, where the "out-of-plane" direction is defined for each atom based on the nearest neighbor positions.

The reference configurations are determined by performing a preliminary single-reference CISD calculation and then adding the configurations with the largest weight in the calculated CI roots, such that the total weight of the reference is above a threshold *CISELT* for all roots. This threshold can easily be chosen sufficiently tight to assure converged excitation energies, which usually results in 1-3 configurations per state.

Chapter 4

Molecular Mechanics Force Fields and Combined Quantum Mechanical/Molecular Mechanical Schemes

4.1 Conventional Force Fields

The great majority of current molecular mechanics (MM) applications employs an two-body additive potential for the description of the total energy of the system as a function of the nuclear coordinates R_n, which commonly is of the analytic form

$$\begin{aligned} E_{\text{tot}}[r] &= E_{\text{bonded}} + E_{\text{nonbonded}} \\ E_{\text{bonded}} &= \sum_{\text{bonds}} K_d(d-d_0)^2 + \sum_{\text{angles}} K_\theta(\theta-\theta_0)^2 + \sum_{\text{dihedrals}} K_\phi\left[1+\cos(n\phi-\phi_0)\right] \\ E_{\text{nonbonded}} &= \sum_{m<n}\left\{\epsilon_{mn}\left[\left(\frac{\sigma_{mn}}{R_{mn}}\right)^{12}-\left(\frac{\sigma_{mn}}{R_{mn}}\right)^{6}\right]+\frac{Q_mQ_n}{R_{mn}}\right\}. \end{aligned} \tag{4.1}$$

The empirical parametrization of this potential function, in terms of force constants K_d, K_θ, K_{phi}, equilibrium coordinates d_0, θ_0, ϕ_0, Lennard–Jones parameter σ and ϵ, and atomic charges Q, defines the force field (FF). The bond-torsion term is often complemented by an out-of-plane displacement potential (improper dihedrals), and some FF's contain an additional harmonic potential for the hydrogen–hydrogen distance in certain H-C-H bonds (Urey–Bradley term) to improve the description of vibrational modes.[123,124] In $E_{\text{nonbonded}}$, 1–2 and 1–3 interactions (pairs of atoms that are covalently connected via one or two bonds) are excluded, and 1–4 interactions are often evaluated with special parameters. The notion "two-body additive" means that the potential contains sums over atom pairs and single three- and four-center coordinates, only. This implies that the number terms scales with the second order of the number of atoms, and can be reduced to a linear scaling by introducing suitable distance thresholds for the nonbonded terms. Then, the only computational step which is not (trivially) linear-scaling is the generation of the list of interacting atom pairs. Many-body effects, such as electronic polarization, are described only implicitly in these "class I"-type FF's via their parametrization. For reviews on popular FF and their performance

in describing structural, energetic, and spectroscopic properties of biomolecules the reader is referred to the rich literature on this topic.[123,125–135]

4.2 Polarizable Force Fields

Despite the early integration of explicit polarization models into molecular mechanics (MM) force fields (FF) by Warshel and Levitt,[136] the development of FF's for macromolecules was long based on additive models of the nonbonded interactions, in which the charge distribution is represented by fixed atomic point charges. It was not before the 1990s that a broad consensus formed on that the additive FF's were approaching their limit and that further development should include the cooperative (or many-body) effects arising from intra- and intermolecular polarization.[129] This was accompanied by a number of publications that addressed the importance of an explicit microscopic treatment of polarizability and a consistent dielectric embedding (see Ref.[128] for a recent review). Examples where the incorporation of polarization was essential include the calculating solvation free energies of divalent ions,[128] pK_a's of titratable groups inside proteins,[137] redox potentials,[138] and the correct description of macrodipoles (see Ref.[128] and references therein). Besides augmentation of the nuclear point charges by additional charge sites (in particular, lone pairs) or multipoles, to improve the electrostatic near field, polarization models were also considered as a key to overcome known weaknesses of water models,[126,139–148] and to improve the structural reliability and accuracy of conformational energies[149–153] and protein–ligand interaction energies.[145,154–156] There are two different classes of empirical polarization models, which where originally developed to predict molecular polarizability tensors.

The fluctuating charge models assign a chemical potential to the atomic sites, which consists of the electrostatic potential (ESP) and a charge-dependent term, which simulates the chemical hardness of the atom. Polarization in response to an external field is then modeled by redistributing the charge among the sites to equalize the chemical potential. In extended systems, this redistribution must in general be limited to molecules or subgroups because the model does not preserve the correct macroscopic scaling behavior of the polarizability increasing linearly with the system size. This failure arises, on the one hand, from the principal inability to describe out-of-plane polarizability of planar molecules and on the other hand from the charge transfer between dissociating or non-interacting moieties, which violates the known derivative discontinuity of the total energy with respect to the particle number. Hence, appropriate parameters must be found for each molecule or subgroup to reproduce gas-phase charge distribution and polarizability. Efforts have been made to overcome the charge-transfer problem, but remain at a qualitative level.[157] Promising concepts to remedy both problems and derive transferable parameters have been studied by Chelli and coworkers.[150] Besides atomic dipoles for out-of-plane polarization, they introduced an additional restraint on the charges to moderate the polarizability contribution from intra-molecular charge transfer.

A more common approach to model polarization empirically is the use of atomic linear polarizabilities. In 1972, Applequist[158] showed that the mean polarizability and anisotropy of molecules can be reproduced simultaneously, using just one transferable atomic polarizability per element, when the mutual interactions between the induced dipoles are included in the model. The anisotropies of his model, however, were sys-

tematically overestimated. This problem was addressed by Thole[159] who proposed a short-range damping of the dipole–dipole interaction, which can be motivated physically as to mend the short-range breakdown of the point-multipole approximation by replacing the constituting point charges on one site by an appropriate spherically symmetric charge density distribution $\rho(r)$. With the resulting modified dipole–dipole interaction, he could reproduce molecular polarizability components with remarkable accuracy using only one additional parameter. For several functional forms of ρ, he proposed damping parameters and atomic polarizabilities for the elements H, C, N, and O.

For efficiency reasons, it is appealing to eliminate the dipole–dipole interaction and apply a fully additive atomic polarizability model. In general, additive models need smaller atomic polarizabilities than interactive ones. Warshel *et al.* proposed a scaling of the dipole–charge interaction to mimic the average charge-screening effect of the other dipoles on the local field. This essentially allows to use the same parameters for the additive[136] and the interactive model.[160] To retain anisotropies in the additive model, anisotropic site polarizabilities are required which are hybridization- and thus structure-dependent.[161] More parameters are needed, and the conformational transferability must be considered. Despite their complexity, such models are valid at least for small molecules, where, apart from the hybridization-dependent modification of atomic polarizabilities, molecular polarization is essentially an additive effect.[162,163] A limitation of additive models is that in extended systems (liquid phase or macromolecules), cooperative effects between the individual molecules or parameter groups, e.g., amino acid residues (AA), are neglected. As a compromise between additive and interactive models, the self-consistency of the latter can be abandoned and the interaction energy between the initial dipoles can be added to the additive energy expression. For water clusters, e.g., this approach already yields a fair estimate of the interactive polarization (induction) energy.[164]

A special variant of the atomic induced dipole model is based on the classical Drude oscillator.[165,166] It represents the induced dipole by introducing a fixed virtual charge q, borrowed from the host atom and attached harmonically to the latter. The atomic polarizability is expressed as $\alpha = q^2/k$, with force constant k. By assigning a mass to the virtual charge (Drude particle), a straightforward time integration for molecular dynamics simulation can be established. In the limit of infinite charge and spring constant, the model is identical to the point-dipole model. It has been implemented into CHARMM,[167] but no protein FF parameters are available yet.

Although early QM/MM studies on enzymes already introduced polarization into the MM model,[136,160,176] polarizable FF's are still not common use in protein modeling[177–182] and QM/MM studies.[136,147,160,181,183–199] The efforts of many groups, mainly during this decade, have led to a first generation of polarizable protein FF's (see Table 4.1), which are currently under development or assessment. In this context, the interactive polarization model of Thole has been implemented in this work and Thole's original parametrization for small organic molecules was extended and benchmarked for the application to peptides. The results are presented in chapter 6, which also illuminates the relevance of an explicit protein polarization treatment for the calculation of optical absorption energies in rhodopsins. Rhodopsins represent an ideal test system for this issue, because the absorption maximum of their chromophore, the protonated Schiff base of retinal (PSB) is highly sensitive to the electrostatic environment

Table 4.1: Polarizable Protein FF's.

name	refs	perm. multipoles	polarization model
ff02 (AMBER)	142,158	point charges[a]	interactive, undamped ind. dipoles, atomtype-based α, no groups
AMOEBAPRO (TINKER)	126,140,168	DMA	interactive, damped (Thole) ind. dipoles, element-based α from Ref.[159], groups
CPE	150	—	fluct. charges and dipoles (s-/p-type Gaussians), atomtype-based η_s, η_p, and χ
DRF90	169–171	point charges	interactive, damped (Thole) ind. dipoles, element-based α, molecular groups
ENZYMIX	136	point charges	ind. dipoles, element-/row-based α
FQ (CHARMM)	172,173	point charges	fluct. charges, atomtype-based η and χ
PFF	152,174	point charges,[a] dipoles	interactive, undamped,[b] ind. dipoles, atom-based α, no groups
SIBFA	145,175	DMA	distributed, anisotropic, damped ind. multipoles, molecular groups

Model parameters: α: polarizability, χ:electronegativity, η: chemical hardness. [a]Including lone pair sites. [b]Excluding 1-2, 1-3 interactions.

due to the extended charge transfer upon S_1 excitation.

4.3 Quantum Mechanical/Molecular Mechanical Approaches

Despite the success of MM force fields in modeling structural and dynamical properties of large biomolecules at room temperature, their validity or accuracy is essentially limited to structures close to their equilibrium geometry. For the description of chemical reactions (bond-breaking), accurate evaluation of conformation, binding, and transition energies, excited-state processes, or properties of co-factors for which no FF parameters are available, parts of the system must be described with quantum mechanical (QM) methods. One approach, which is still often applied, is to consider a subsystem (active site) which contains the residues directly involved in the reaction or strongly interact (e.g., via salt bridges) with the reactive fragments and neglect the influence of the protein/solvent environment. Such gas phase models are useful to study the "intrinsic" properties of the reactant species with high level methods. In order to make quantitative predictions for bioenergetic processes and study the catalytic action of the protein, it is essential to include at least the electrostatic potential of the protein environment in the model. This is the main motivation to combine QM with MM methods in a hybrid QM/MM model. This powerful approach exploits the computational efficiency of MM FF's to describe the major part of the system and the more general applicability of QM methods to describe the structure and energetics of a small chemically active region.

In contrast to solid-state systems, the splitting of biologic macromolecules into a chemically active QM region and a MM region that is well described by classical FF is in most cases straight-forward and does not involve any severe approximations: Only

few covalent bonds have to be cut between the QM/MM frontier atoms, and these can be chosen sufficiently separated from the reactive part. Moreover, un-polar bonds in saturated fragments can often be chosen, e.g., between the backbone C_α and side chain C_β atom. The QM system is saturated with a link atom, usually a hydrogen atom, although numerous more sophisticated schemes have been developed, such as the local self-consistent field (LSCF) method,[200,201] the generalized hybrid-orbital (GHO),[202,203] the frozen orbital,[204] frozen-core orbital (FCO),[205] the pseudobond,[206,207] quantum-capping potential (QCP),[206,208] effective group potential (EGP),[209,210] optimized effective Hamiltonian,[211] or the semiempirical connection-atom (CA)[212] approach (see Ref.[199] for an overview). In order to avoid artificially strong polarization of the QM link atom by the MM frontier atom, various schemes have been suggested to delete the charge of the MM frontier atom while minimizing artifacts in the QM system or the global electrostatics.[213–217] For DFTB as the QM method, different schemes have been tested by König *et al.*[218], which of the "divided frontier charge" scheme (DIV) has shown best results and is used also in the current work. The DIV scheme consists of a simple manipulation of the standard atomic charges of the FF: The charge of the MM frontier atom is deleted and re-distributed equally on the remaining atoms of the "host group". The latter is a pre-defined subunit of the residue, which contains the frontier atom. In the CHARMM implementation it corresponds to a "charge group", which carries an integer total charge.

Two different types of QM/MM approaches can be distinguished: In **additive schemes**, the total energy is decomposed of the total energy of the isolated QM subsystem E_{QM}, the FF energy of the MM part E_{MM}, and the QM/MM interaction term E_{QMMM}:

$$E_{\mathrm{tot}} = E_{\mathrm{QM}} + E_{\mathrm{QMMM}} + E_{\mathrm{MM}} \tag{4.2}$$

As most of the QM codes support external charges in the definition of the external potential in the QM Hamiltonian, the electrostatic part of E_{QMMM} is commonly evaluated at the QM level (electrostatic embedding). The bonded and Van-der-Waals interactions in E_{QMMM} are described by the FF. As the optimal choice for the Van-der-Waals parameter depends on the electrostatic model, alternative parameters for the QM/MM interactions may be used. For the SCC-DFTB/CHARMM combination, however, little improvement was found.[219] The link atoms interact only with the QM atoms but are constrained along the cut bond.

In **subtractive schemes**, like Morokuma's ONIOM scheme,[220] the total energy is defined in terms of the FF energy of the entire system (without link atoms) $E_{\mathrm{MM}}^{\mathrm{all}}$, the total energy of the isolated QM subsystem (including link atoms) $E_{\mathrm{QM}}^{\mathrm{subsystem}}$, and the MM energy of the same subsystem $E_{\mathrm{MM}}^{\mathrm{subsystem}}$:

$$E_{\mathrm{tot}} = E_{\mathrm{MM}}^{\mathrm{all}} + E_{\mathrm{QM}}^{\mathrm{subsystem}} - E_{\mathrm{MM}}^{\mathrm{subsystem}} \tag{4.3}$$

The subtractive scheme requires therefore a FF parametrization of the QM region and describes all QM/MM interactions at the MM level (mechanical embedding). The obvious drawback of this approach is that the QM subsystem is not polarized by MM charges and geometry-dependent changes in the QM charge density are not reflected in the QM/MM interaction energy. This approximation is inadequate to describe properties of the QM moiety that depend on the electrostatic environment. In this case, the scheme must be generalized by including the electrostatic potential of MM charges in the QM Hamiltonian (electronic embedding). Then, the subtractive scheme

becomes equivalent to the additive one, except for the treatment of the link atom interactions.

4.4 QM/QM Interfaces and Link Atom Schemes for Polarizable Force Fields

When a multi-scale model combines several methods that describe a variable, e.g., polarizable charge distribution, it is essential to treat electrostatic interactions in a consistent way to ensure that the total energy is variational with respect to all degrees of freedom. In an additive integration scheme, this can be achieved by two conditions: (1) the methods applied to different parts of the system provide a variational energy, and (2) the interactions between the subsystems that enter the Hamiltonians of the corresponding subsystems are identical. As an example, consider two QM moieties that are described by different methods and mutually polarize each other. If the two Hamiltonians contain different approximations to the mutual Coulomb interaction, the total energy of the system will in general not be stationary with respect to variation in the wave function coefficients when the total energies of the subsystems are stationary.

In case of a QM/QM interface, the two QM Hamiltonians must contain the Coulomb potential of the exact density of the other subsystem. This can be achieved by calculating the ESP of one subsystem on a grid that samples the density of the other. If the other QM code does not support the definition of an external potential on a grid, ESP-fitted atomic charges represent a satisfying approximation. Also here, the grid points for the ESP fit have to sample the density of the other subsystem to achieve the smallest error in the interaction energy. In the case of semiempirical methods, Mulliken (or Löwdin) charges may represent a valid approximation. For SCC-DFTB, e.g., the use of Mulliken charges is consistent with the internal representation of Coulomb interactions within the method and hence implies no further approximation. No mapping of the ESP is required for interfaces between QM and MM, or QM and dipole-polarization models. Here, the ESP of the QM density and its finite-difference derivative (electric field) at the positions of the point charges or dipoles can be used to calculate the exact Coulomb interaction.

The optimal treatment of electrostatic interactions at the frontier between two QM regions in an additive scheme is not obvious. If the cut between the two QM regions cannot be avoided, more sophisticated link approaches, such as the constrained-density KS approach,[221,222] may be required. Subtractive schemes avoid this problem but exclude a "divide-and-conquer" strategy, in which the system is divided into subsystems that are all described at the same level of theory. A classical link atom scheme between two QM moieties will in general lead to a non-variational total energy, but the error in energy differences may cancel if the geometry of the link region is fixed and the density does not change (or is constrained).

For the interface between a QM and a polarizable MM model, a variational energy can be achieved by applying a conventional link atom scheme to the MM frontier charges and defining zero polarizabilities on the MM frontier atoms within an appropriate distance from the link atom to avoid artificially high polarization of the polarizable MM atoms. The induced dipoles can then interact with the exact QM density, i.e., the total energies of the QM method and the polarization model contain the same

Coulomb interaction. In the current work this approach is implemented and applied to calculate excitation energies of a chromophore in a polarizable environment (see chapter 6). The QM density is mapped onto ESP charges, and the grid for the ESP fit samples the region of all polarizable MM atoms. In the QM Hamiltonian, the permanent charges and induced dipoles are represented by point charge pairs centered at the nuclei with a fixed separation of 0.1 Å.

Chapter 5

Spectral Tuning of the Protonated Schiff Base of Retinal

Rhodopsins can modulate the optical properties of their chromophores over a wide range of wavelengths. The mechanism for this spectral tuning is based on the response of the retinal chromophore to external stress and the interaction with the charged, polar, and polarizable amino acids of the protein environment and is connected to its large change in dipole moment upon excitation, its large electronic polarizability, and its structural flexibility. In this chapter, these intrinsic response properties of the retinal chromophore are investigated, and a wide spectrum of computational approaches is tested for the accuracy in modeling changes in the electronic excitation energies with respect to changes in the geometry and applied external electric fields. The methodological requirements for a quantitative prediction of absorption energies and shifts in rhodopsins represent a considerable challenge for current quantum chemical methods. Problematic are the high sensitivity of absorption energies on the ground-state structure of the chromophore, which varies significantly with the computational method used for geometry optimization, and the response to external fields, which is not properly represented by previously used methods, such as time-dependent density functional theory (TDDFT), complete active space self-consistent field (CASSCF), and Hartree-Fock (HF) or semiempirical configuration interaction singles (CIS). This is discussed in detail for bacteriorhodopsin (bR), a protein which blue-shifts retinal's gas-phase excitation energy by ca. 0.5 eV. Based on the results of this study, a procedure for quantitative studies of spectral tuning is proposed, which combines several semiempirical and *ab initio* methods with QM/MM techniques.

5.1 Introduction

Retinal proteins, rhodopsins, are located in the cell membrane and contain the chromophore retinal (Figure 5.1), which triggers the response of the cell to light. For example, in bacteriorhodopsin (bR) absorption of a photon leads to an all-*trans* $\rightarrow$ 13-*cis* isomerization of the retinal, which induces a proton transfer from the cytoplasmic to the extracellular side of the cell membrane (see, e.g., the recent review of Neutze *et al.*[223]). The resulting pH gradient is used for synthesizing ATP. In rhodopsin, a member of the superfamily of G-protein coupled receptors, photoabsorption leads to an

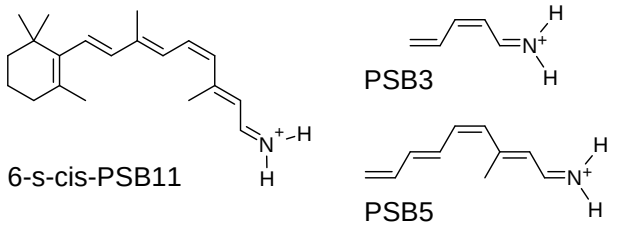

Figure 5.1: 6-s-*cis*-11-*cis* PSB of retinal (PSB11) and model systems.

11-*cis* → all-*trans* isomerization which induces the signaling state of the protein.[224]

In these photoreceptors, the retinal is covalently linked to the apoprotein via a protonated Schiff base to a lysine residue. The protein environment drastically modulates the absorption maximum of the chromophore: While it is at about 450 nm in organic solvents,[225] it varies from 360 to 635 nm in the light sensitive cone pigments,[226] which are responsible for color vision. Retinal responds to its protein environment in a twofold manner, due to its high electronic polarizability and its structural flexibility. In various protein structures it is found to be highly twisted. Both, the electrostatic field and mechanical strain exerted by the protein environment can therefore change the optical properties considerably. In return, the chromophore changes its protonation state during the photocycle and, in its charged state, its electric dipole moment changes strongly due to $S_0 \rightarrow S_1$ excitation, which again causes changes in the polarization of the protein environment.

These strong and variable interactions between the chromophore and its environment implicates particular difficulties in the theoretical modeling of spectroscopic features of rhodopsins. Previous studies on the spectral tuning, i.e., the ability of distinct protein environments to regulate the absorption maximum, employed a wide range of different models and quantum chemical approaches. They have pointed out several prerequisites to be important for the calculation of accurate absorption spectra:

1. Highly accurate methods, such as MRMP2 or CASPT2, must be used.[1,9,10]

2. The geometrical parameters of the chromophore must be properly described,[1,10] as the spectrum is highly sensitive to the chromophore geometry.[227]

3. The interaction of the chromophore with the charge distribution of the protein environment must be incorporated. Here, a simple approximation consists of representing the environment by fixed point charges at the atomic sites, as it is usually done in combined quantum mechanical/molecular mechanical (QM/MM) calculations.[9,183,228–233] In this approach, the polarization of the chromophore by the environment is included, whereas the polarization of the environment by the chromophore is neglected. Yet, the latter might have an important effect, especially in the case of the protonated Schiff base (PSB) of retinal which changes its dipole moment by 12 debye (Cl^- salt) when being excited into the S_1 state.[234]

4. The polarizability of the protein must be accounted for by polarizable force fields[179,183,187,235,236] or implicit solvent models.[237] These studies emphasize the effect of polarization on the optical spectra, and according to them, any study not

Table 5.1: Vertical S_1 Excitation Energies (eV), Oscillator Strengths (in parentheses) of CASSCF-Optimized *cis* Ground-State Structures.

structure	TD-DFTB	BP86	B3LYP	SORCI	CASPT2
PSB3 model					
	3.89	3.94	4.10	4.06	4.02[a]
	(0.43)	(0.42)	(0.51)	(0.65)	
PSB5 model					
	2.57	2.73	2.91	2.79	2.58[b]
	(0.57)	(0.79)	(1.05)	(1.28)	(0.83)
11-*cis*-6-s-*cis* PSB of retinal (PSB11)					
	1.22	1.39	1.91	2.26	2.41
	(0.09)	(0.14)	(0.25)	(1.03)	
11-*cis*-6-s-*cis* dimethyl PSB, PBE0 geometry					
	1.97	2.07	2.30	2.00	
	(0.53)	(0.75)	(1.21)	(1.37)	

SORCI and TDDFT calculations were performed with Dunning's Aug-cc-pVTZ (PSB3),[239] Aug-TZVP (augmented with diffuse functions from the Aug-cc-pVDZ basis set; PSB5) and SV(P)[240] (PSB11) basis sets on CASSCF-optimized ground-state geometries. [a]Ref.[3]. [b]Ref.[241].

including this effect might miss an important contribution to retinal absorption energies.

5. The effects of dispersion have been taken into account by Birge and coworkers.[227,238] They included a large set of the surrounding amino acids in the excited-state calculations using *partial single and double configuration interaction* (MNDO/PSDCI): Dispersion is reflected in the CI double excitations across the chromophore and the aromatic residues. The authors use a large QM region for their calculations, not treating the full protein and solvation.

6. Most approaches rely on geometry optimization, evaluating the spectrum at a single point in configuration space. However, this may not lead necessarily to representative structures. Therefore, conformational sampling using MD[183,187] or MC[232] techniques is necessary to calculate absorption energies and spectra that are directly comparable to experimental ones.

Each theoretical approach followed this far in the literature stresses the importance of a few of these aspects, while ignoring the others. However, as will become evident in this chapter, the requirements (i)–(vi) are highly interdependent. This is because different quantum methods predict very different electronic and energetic properties of the chromophore in the ground and excited states and are in quantitative or even qualitative disagreement concerning the response to changes in the chromophore geometry and electrostatic environment. Therefore, the use of different quantum methods makes it hard to directly compare the results of these approaches and can lead to contradicting conclusions. As an example, Table 5.1 shows excitation energies for retinal

chromophores in the gas phase. Although all methods predict red shifts when extending the polyene chain, the results are quantitatively very different for the CASSCF optimized geometries. Using the PBE0 optimized structure, a completely different picture emerges: Now both SORCI and the pure GGA functional BP86 are in excellent agreement with the experimental value of 2.03 eV.[242] To interpret these discrepancies and consider the emerging errors in previous and forthcoming theoretical studies, it is necessary to understand and, if possible, quantify the intrinsic errors for each method, which is the main purpose of this work.

The current chapter focusses on the effects of (i)–(iii), i.e., the capability of different methods to accurately describe:

1. The vertical excitation energies for different geometries. This is particularly important for rhodopsins, where the protein environment exerts mechanical stress on the chromophore, thereby tuning its absorption wavelength.

2. The effect of the environment represented by point charges on absorption energies. Here, it will be shown that many commonly used methods should not be applied in this context. This concerns not only the accuracy of the QM method itself, but also the way it is integrated in a QM/MM scheme, in particular the values of the point charges.

The effects of (iv)–(vi) shall be considered in chapters 6 and 7, based on a proper treatment of (i)–(iii). This imposes additional constraints to the computational efficiency of the approach, as MD sampling and self-consistent coupling to polarizable force field methods require a large number of single-point calculations, and the computational cost is further increased by the use of large QM regions. High level *ab initio* methods, such as CASPT2 and MRMP2, are not suited for this task due to their exceedingly high computational cost. Therefore, the goal is to find a feasible computational strategy for the proper treatment of all the effects that are important for reliable calculation of retinal absorption energies in various protein environments. In this respect, high-level methods provide reliable benchmark data for more approximate methods, such as HF/CIS, TDDFT, and semiempirical methods.

5.2 Computational Details

As the highest level method that is applicable to the systems being studied, the *Spectroscopy ORiented Configuration Interaction* (SORCI) method[115] is employed, which is part of the ORCA quantum chemical package.[243] This method is described in detail in section 3.3.4. In appendix 9.1, the convergence behaviour of all the thresholds used in SORCI are determined individually. The thresholds used throughout this work are chosen to achieve excitation energies that are converged within 0.1 eV of the method's limit. They are as follows: $E_{\mathrm{win}} = 3,3$, $T_{\mathrm{pre}} = 10^{-3}$, $T_{\mathrm{nat}} = 10^{-6}$, and $T_{\mathrm{sel}} = 10^{-6}$. Ahlrich's SV(P) basis set is used for the complete chromophore and the TZVP set, augmented with diffuse functions from Dunning's Aug-cc-pVDZ set, for calculations on the PSB5 model. The basis set convergency is tested in appendix 9.2.

In addition to CASPT2 calculations from the literature, the presented SORCI results can be considered a reliable benchmark for evaluating the accuracy of lower level methods. This applies especially to the assessment of the semiempirical OM2

Hamiltonian[62,66] for providing matrix elements for an MRCI expansion[121] of ground- and excited-state wave functions. As is explained in sections 2.6.1 and 3.3.5, the usage of an OM2 Hamiltonian in extended CI treatments of excited states is expected to be superior to traditional semiempirical Hamiltonians like MNDO or AM1. The HOMO–LUMO gap is significantly underestimated by the latter methods because they neglect the non-orthogonality between the atomic orbital basis functions, leading to underestimated excitation energies in extended CI calculations (for case studies see Refs.[120,244]). By applying orthogonalization corrections to the Fock matrix, OM2 is able to overcome this problem and thus yields improved excitation energies, without the need for re-parametrization. This has been shown in Ref.[120] for butadiene. All OM2/MRCI calculations have been performed with the GUGA implementation in version 6.1 of the MNDO99 program. An active orbital window of 19 occupied and 19 virtual orbitals has been used, which have been selected from a preliminary CI run. No configuration selection has been applied.

TDDFT, HF/CIS, MP2, and CC2 calculations have been performed with the turbomole program package,[245] which features analytical gradients for excited-state geometry optimization. If not denoted otherwise, the employed basis set is Ahlrich's TZVP,[240] which has been augmented in calculations of the PSB5 model with the diffuse functions from the Aug-cc-pVDZ set.[246] In the MP2 and CC2 calculations, the resolution of the identity approximation (RI) was employed with the default auxiliary basis for TZVP.[247]

Ground-state geometry optimization for molecules the size of the protonated Schiff base (51 atoms) is today routine with most commercial and academic quantum chemistry packages. QM/MM optimizations, however, are much more involved, since the slowly converging optimization of the MM region with its thousands of degrees of freedom is coupled to the time-consuming energy and gradient calculation of the QM region. Techniques such as "micro iterations" may help overcome this bottleneck[229,233] but are not available in many QM/MM packages. Long timescale MD or MC simulations, however, are not feasible at the *ab initio* or DFT level of theory; more approximate or semiempirical methods have to be used for these applications. An alternative to the traditional well-established semiempirical methods, such as MNDO, AM1, or PM3, is the approximate DFT method SCC-DFTB[88] (called DFTB in the following), which has been applied in numerous QM/MM MD studies before.[248] DFTB has been shown to describe the ground-state properties of the PSB (bond length alternation of the polyene chain, torsional barriers etc.) with an accuracy comparable to that of full DFT methods about three orders of magnitude faster.[90] Therefore, DFTB is an ideal tool for producing QM/MM optimized geometries and MD trajectories, which can then be used in subsequent calculations of absorption energies. The time-dependent generalization of DFTB (TD-DFTB[105]) is used in this work to supplement the results of TDDFT.

QM/MM optimizations of the chromophore in the bR structure are based on the x-ray structure of Luecke *et al.*[249] (PDB code 1C3W). Missing hydrogen atoms were added with the *HBuild* module of the CHARMM software.[131] Default protonation states were assumed except for Asp96, Asp115, and Glu204, which were protonated. The SCC-DFTB/CHARMM QM/MM implementation was used with a hydrogen link atom, and MM frontier charges corresponding to the DIV scheme.[218,250] During the minimization, all C_α atoms with a distance to the chromophore larger than 12 Å were harmonically restrained to their original positions. No cutoffs were used for

the QM/MM non-bonded interactions.

5.3 Impact of Geometry and Conformation on the Absorption Maximum

To achieve reliable excitation energies, high-level *ab initio* methods, such as CASPT2 or MRCI, have to be used, while for the geometry relaxation of the whole retinal and MD simulations, this level of theory is not feasible. Therefore, in practice, lower-level methods have been used for relaxation of the chromophore either in the gas phase, or in the protein environment using combined QM/MM methods. However, the various lower-level QM methods, such as CASSCF,[9,231] HF,[229,230], PM3,[227] DFT,[233] or SCC-DFTB,[10] provide considerably varying descriptions of the electronic and geometrical structure of the chromophore in its ground state. The main structural differences occur in the bond length alternation of the conjugated chain and the dihedral twist angle of the β-ionone ring.

5.3.1 Bond Length Alternation

This section investigates how the bond length alternation (BLA) is reflected in the vertical excitation energy in the case of the all-*trans* PSB gas phase structure. It is a general feature of HF and of those post HF methods that incorporate primarily static correlation to overestimate the BLA of conjugated systems. The inclusion of dynamic correlation (e.g., in a PT2 correction to a CASSCF reference) reduces the BLA. This has been shown explicitly for the PSB3 and PSB5 models of retinal.[7] On the other hand, pure DFT methods based on the local density or generalized gradient approximation (LDA or GGA) render primarily the effect of dynamic correlation and therefore tend to underestimate the BLA. These general trends apply perfectly to the retinal case, as Table 5.2 reveals. Moreover, hybrid functionals profit from error cancelation between the deficiencies of DFT (LDA) and HF, providing a balanced description of single and double bonds. In fact, B3LYP and PBE0 ground-state bond lengths of retinal models are found in excellent agreement with those of the CASPT2 method, which incorporates static and dynamic correlation in a balanced manner, whereas MP2 yields a slightly higher (0.007 Å) BLA.[7] When considering geometries of the full chromophore, MP2 features a BLA 0.007-0.010 Å higher than B3LYP.[251] Thus, it can be expected, that the performance of hybrid functionals like B3LYP and PBE0 is as high for the complete chromophore as for the PSB3 and PSB5 model systems.[7]

The BLA of retinal and other conjugated systems has a significant impact on the S_1 vertical excitation energy because the S_1 gradient at the FC point is almost collinear to the C–C double-bond stretching mode (PSB11: 1556 cm^{-1}), which is responsible for the strongest peak in the RR spectrum. A displacement along the S_1 gradient reduces the BLA of the polyene chain.[253] Hence, the absorption maximum is blue-shifted if the structure features an increased BLA. As can be seen in Table 5.2, this applies to all HF-based methods (and OM2), whose S_1 energies can be "tuned" within a range of 0.16 eV (SORCI), or 0.38 eV (HF/CIS) by the choice of the method used for geometry optimization. A deviation between MRCI and CIS can be found for the CASSCF geometry, which features the highest BLA: While both *ab initio* and semiempirical MRCI

Table 5.2: Excitation Energies (eV) of All-*trans* PSB (NH_2 terminus) for Various Geometries. Geometry Optimization of the Full Chromophore in Vacuo Using a 6-31G* Basis Set.

	geometry optimized with						
	CASSCF[a]	HF	BH-LYP	MP2	B3LYP	DFTB	BLYP
BLA[b] (Å)	0.100	0.069	0.035	0.036	0.028	0.025	0.023
average bond length (Å)	1.397	1.388	1.378	1.399	1.396	1.399	1.406
TD-BP86	2.00	2.16	2.37	2.28	2.33	2.29	2.31
TD-DFTB	1.76	1.95	2.22	2.14	2.19	2.18	2.18
TD-B3LYP	2.21	2.36	2.49	2.40	2.43	2.40	2.40
OM2/CIS	2.59	2.53	2.40	2.31	2.32	2.28	2.27
HF/CIS	3.25	3.18	3.04	2.93	2.94	2.89	2.87
OM2/MRCI	2.16	2.22	2.15	2.05	2.07	2.03	2.01
SORCI[c]	2.01	2.07	2.04	1.95	1.96	1.93	1.91
HF/CIS (S_2)	5.09	5.05	4.97	4.85	4.86	4.75	4.78
SORCI[c] (S_2)	2.77	2.61	2.45	2.32	2.30	2.20	2.22
$\lvert\Delta_{S_1-S_0}\mu\rvert$ (debye)							
TD-B3LYP	5.4	4.5	2.5	2.4	2.1	2.1	1.9
OM2/MRCI	16.8	12.0	8.1	8.4	7.2	7.0	6.7
SORCI	14.0	9.5	5.2	5.9	4.7	4.5	4.4

[a]CAS(12,12)/6-31G* calculation (Gaussian03[252]) including all π orbitals in the active space; during geometry optimization the β-ionone ring twist angle was held fixed at the HF value of 165°. [b]Difference between mean bond lengths of formal double bonds (six, including N=C) and single bonds (five). [c]RAS(12,12,4) pre-selected reference.

calculations predict the highest excitation energy for the HF structure, CIS yields the largest blue shift for the CASSCF one. For the S_2 state, in contrast, SORCI predicts much larger shifts than CIS, and both methods find the largest one for the CASSCF geometry.

In addition to the blue-shifted excitation energies, increasing the BLA also drastically enhances the charge transfer due to S_1 excitation, as measured by the difference dipole moment in Table 5.2. As will be discussed below, this has important consequences for the calculation of excitation energies in protein QM/MM models.

DFT-based methods show deviating behavior. By comparing their excitation energies on GGA-, HF-, and CASSCF-optimized structures, a general red shift with increasing BLA can be found, which is reduced by admixture of HF-X in the functional. As will be discussed in section 5.4.2, this reflects the feature of TDDFT to increase the BLA upon S_1 relaxation, in contrast to post-HF methods.[254] Among the DFT structures of different hybrid functionals, a second effect must be taken into account to rationalize this slightly broken trend: the average C–C bond length along the conjugated chain increases with the amount of HF-X, whereas the HF structure again features a value close to that of the B3LYP structure. S_1 relaxation on the TDDFT level increases both the BLA and average bond length. If the BH-LYP structure is modified to adopt the average bond length of the BLYP structure, the S_1 energy of BP86 drops to 2.27 eV showing the isolated effect of the BLA.

The good agreement of the B3LYP structures with those from CASPT2[7] and

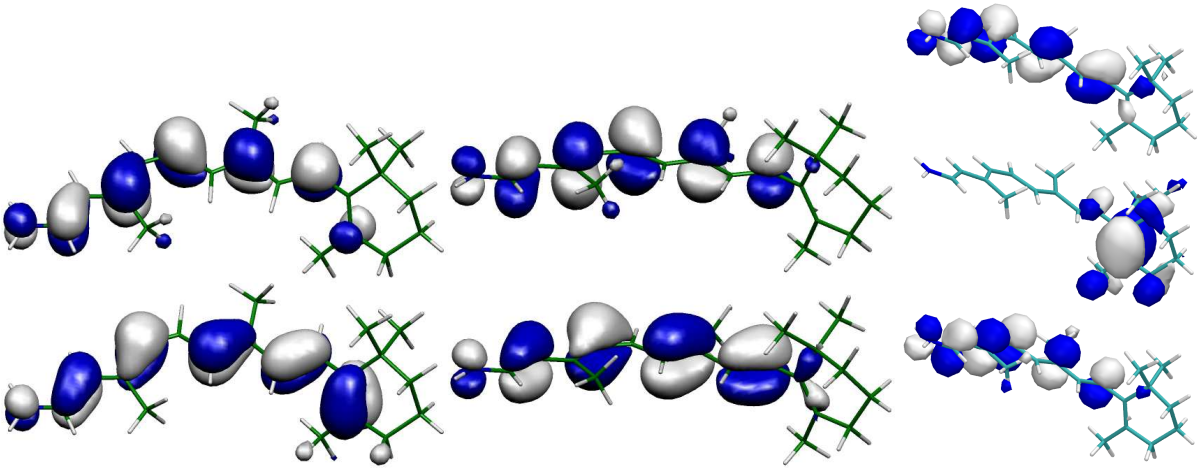

Figure 5.2: SORCI frontier averaged (S_0, S_1, S_2) natural orbitals for the B3LYP optimized PSB11 (left) and for the 90°-twisted-ring structure (middle). B3LYP orbitals for the latter (right): HOMO-1, HOMO, and LUMO.

MP2,[251,255] and the large impact of the BLA on the absorption energy leads to the conclusion, that for calculations of absorption energies hybrid DFT geometries should be used. The results in Table 5.2 also recommend SCC-DFTB geometries as a very cheap alternative, as the deviations from the B3LYP ones are small and do not bias the excitation energies significantly (0.04 eV at the SORCI level). This is attractive, as it allows for long QM/MM MD simulations for proper sampling of the conformational space of retinal, where excitation energies can be calculated for snapshots along the trajectory in order to obtain a realistic absorption spectrum.

5.3.2 Planarity of the β-Ionone Ring: The Problem of CT States in TDDFT

Another important geometrical parameter is the C5–C6–C7–C8 dihedral twist angle of the β-ionone ring. For 6-s-*cis*-11-*cis* PSB *in vacuo*, CASSCF predicts a value of 65° (HF: 56°) whereas DFT yields 37° (35°) using B3LYP (BP86). For the all-*trans* isomer, DFT and HF predict almost planar structures (171° and 165°, respectively), whereas CASSCF relaxes into a 6-s-*cis* minimum when starting from the 6-s-*trans* HF geometry. The first is often assumed as the more stable configuration (1 kcal/mol in MP2), although the barrier might be very small, and both isomers may coexist in samples used for absorption measurements.

For a vanishing twist angle, the planar arrangement of all six double bonds, allows the strongly correlated π-system (i.e., the photoactive region of the chromophore) to extend over the whole conjugated chain. A highly twisted C6–C7 single bond disrupts the π-system, which is reflected in a localization of the frontier natural orbitals on the shortened polyene chain (see Figure 5.2, left and middle). Thus, effectively, only five double bonds contribute to the excitation, which should lead to a hypsochromic shift versus the planar structure, according to the particle-in-a-box model (compare Table 5.1).

As shown in Table 5.3, this behavior is indeed found with all *ab initio* and semiempirical methods that employ HF exchange. The hypsochromic shift from the 6-s-*cis*-11-

Table 5.3: Dependence of the S_1 Excitation Energy (eV) on the Twist Angle of the β-Ionone Ring.[a]

	37°	60°	90°	171°
TD-DFTB	2.05	1.68	0.96	2.17
BP86	2.10	1.74	0.88	2.29
B3LYP	2.31	2.11	1.55	2.40
BH-LYP	2.52	2.55	2.62	2.52
AM1/CIS	1.98	2.05	2.16	1.93
OM2/CIS	2.38	2.45	2.58	2.33
HF/CIS	3.01	3.13	3.27	2.94
CC2	2.12	2.14	2.39	2.13
OM2/MRCI	2.18	2.23	2.40	2.06
SORCI	1.96	1.99	2.28	1.95

[a] The C5-C6-C7-C8 dihedral angle of the 6-s-*cis*-11-*cis* B3LYP/TZVP gas phase structure (37°) has been altered without further relaxation. 171° is the fully relaxed s-*trans* B3LYP structure.
The applied basis set is TZVP[240] for HF and DFT-based methods and CC2, and SV(P) for SORCI. In the latter case, a RAS(6,6,4) pre-selected reference was employed.

cis ground-state minimum structure to the 90°-twisted one (0.18–0.32 eV) is comparable to the experimentally observed shift in Rh when replacing the native chromophore by an acyclic 5-double-bond analog that lacks the ring (0.22 eV).[256]

Interestingly, with pure DFT (BP86) and TD-DFTB, the effect is reversed, leading to a dramatic underestimation of the S_1 excitation energy for the perpendicular orientation. Partially replacing DFT exchange by HF exchange in the B3LYP and BH-LYP methods reduces the error, depending on the amount of HF exchange. In combination with the fact that HF/CIS and CC2 provide shifts similar to those of the multireference methods (including OM2/MRCI), this suggests that nonlocal exchange rather than strong static correlation causes the weak performance of the local GGA XC-functional and linear-response kernel. To further investigate this matter, the electronic nature of the S_1 and S_2 transitions shall be considered.

As can be seem in Figure 5.2, the HOMO of the ground-state B3LYP calculation is strongly localized on the ring-internal double bond, whereas the second highest occupied orbital "HOMO-1" and the LUMO are delocalized over the remainder of the conjugated chain. The response eigenvector of the S_1 state in TDDFT is strongly dominated by a HOMO–LUMO transition (BP86: 99.7 %, B3LYP: 98.0 %), i.e., describes a pure charge-transfer (CT) state between two orbitals with vanishing overlap. In this situation, the non-diagonal elements in the ALDA response matrix can in fact be neglected, and the diagonal elements of the singlet coupling matrix are given by:

$$K^S_{ia,ia} = (ia|ia) + (1 - c_{\mathrm{HF}})(ia|f_{\mathrm{xc}}|ia) + c_{\mathrm{HF}}(ii|aa)\,,$$

where f_{xc} denotes the local part of the ALDA XC kernel, and c_{HF} denotes the fraction of HF exchange in the hybrid functional. In consequence of the local/semi-local approximation to the exchange potential and its density derivative ($f_{\mathrm{xc}}(r, r') = f_{\mathrm{xc}}(r)\delta(r - r')$), the first two terms vanish with vanishing overlap of the orbitals ψ_i and ψ_a, which leaves an effective Coulomb interaction between the two orbital densities,

Table 5.4: Dependence of Excitation-Induced CT on the Twist Angle of the β-Ionone Ring.

	$\lvert\Delta_{S_1-S_0}\mu\rvert$ (debye)			$\lvert\Delta_{S_2-S_0}\mu\rvert$ (debye)		
	37	60	90	37	60	90
SORCI	6.1	8.0	3.8	6.4	15.1	25.6
OM2/MRCI	7.6	8.6	5.8	4.7	9.9	23.2
CC2	8.7	11.1	19.1	10.0	13.0	10.3
B3LYP	3.9	8.5	18.9	4.5	4.1	2.8

The same geometries as in Table 5.3 have been used.

scaled by the factor c_{HF}. If the latter is zero (pure LDA/GGA/meta-GGA functionals), the excitation energy is identical to the KS orbital energy difference $\epsilon_a - \epsilon_i$. This means that in the ALDA, there is no particle–hole interaction for pure CT states.

In the present case of the PSB with 90-twisted β-ionone ring, the TD-BP86 excitation energy is indeed close the HOMO and LUMO gap (0.86 eV), while the scaled Coulomb term in eq 5.3.2 gives rise to a red shift of ca. 0.57 eV for B3LYP ($c_{\mathrm{HF}} = 0.2$, HOMO–LUMO gap: 2.12 eV). Hence, the reduced error in the B3LYP excitation energy compared to the BP86 one is due to the larger difference in the KS energy levels.

The Problem of the underestimation of CT states in TDDFT has first been addressed by Casida *et al.*[96,257] and noticed in benchmark calculations by Tozer *et al.*[258] The case of intermolecular CT states has been discussed nicely in the papers of Dreuw *et al.*.[259–261] If the donor and acceptor orbitals for the excited electron are located on different molecules A and B, respectively, and the molecules are infinitely separated, the exact excitation energy for the CT state A$\longrightarrow$B is given by the difference of the electron affinity of B and the ionization potential of A. While the occupied and virtual energy levels in HF theory are approximations to the ionization potential and electron affinities (Koopman's theorem), this applies only for the HOMO in exact KS theory. The virtual KS levels, in contrast, are calculated with the same effective potential as the occupied ones, i.e., represent a particle that interacts with N-1 electrons rather than N, as required for the calculation of electron affinities. More precisely, v_{KS} contains the Coulomb interaction with all N electrons. While in HF, the orbital-dependent exchange operator cancels the self-interaction of each particle (occupied states) exactly, the virtual states are not exposed to any exchange hole, i.e., they interact with all N electrons. In KS theory, the self-interaction is not exactly canceled for each electron. Instead, all electrons are exposed to the same "averaged" exchange potential, whether they are delocalized over the system or not. On the one hand, this leads to an underestimation of delocalized versus localized states, as an exchange hole that contains the self-interaction cancelation would be localized/delocalized likewise. On the other hand, as argued by Dreuw *et al.*,[260] an electron which is excited from molecule A to molecule B is still interacting "with itself" on A when it occupies the acceptor state on B, rather than interacting with the hole generated on A. This lacking particle–hole interaction then causes a wrong shape of the PES along the A–B separating coordinate. In the present case, the two errors are additive, as the donor level is localized on the ring-internal double bond and the acceptor level is delocalized over the polyene chain. In the opposite case, however, some error-cancelation can be expected.

The preceding discussion explains why TDDFT methods underestimate the S_1 ex-

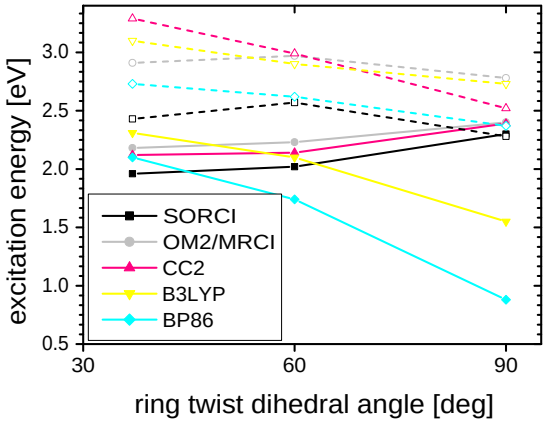

Figure 5.3: Dependence of S_1 and S_2 (dashed) Excitation Energies (eV) on the Ring-Twist Angle.

citation energy of retinal chromophores with strongly twisted β-ionone ring. It remains to clarify whether S_1 is actually transforming into a CT state with increasing twist-angle, or whether this is also an artifact of TDDFT. This question is most relevant, since the amount of CT is correlated with the spectral shift induced by the protein electrostatics. Table 5.4 shows the changes in the difference dipole moment $|\Delta_{S_n-S_0}\mu|$ with increasing twist angle. The multireference calculations predict an decrease for the S_1 excitation and a strong increase for S_2. TDDFT describes the opposite trend, since in B3LYP (and GGA) calculations, S_2 is a locally excited (LE) state, dominated by the HOMO-1 $\longrightarrow$ LUMO transition. In fact, the S_1 state of the MR methods and the S_2 state in TDDFT have the same electronic structure and properties. Interestingly, the CC2 method, which does not suffer from the self-interaction error (SIE) as TDDFT but incorporates predominantly dynamic correlation, predicts S_1 and S_2 to be mixtures of CT and LE states. This mixture does not originate from the HF orbitals but from the weights for the CT and the LE singles configurations, which are 0.57 and 0.38 for the S_1 state, respectively.

Despite this difference in the CC2 and the MR wavefunctions, both describe the same energetics in the S_1 and S_2 state. As shown in Figure 5.3, all methods agree in a bathochromic shift of the higher S_2, and CC2 agrees with the MR methods that the gap between S_1 and S_2 is reduced with increasing twist angle. Merely the TDDFT methods predict an increasing gap due to the artificial bathochromic shift in S_1.

As the results in Table 5.3 show, the shift of the S_1 and S_2 excitation energies due to external fields will depend drastically on the C5-C6-C7-C8 dihedral angle of the ground-state structure. This applies to the S_1 state in TDDFT as well as to the S_2 state in MR approaches. If this angle is, e.g., underestimated by the method used for geometry optimization, TDDFT will severely underestimate this shift for the S_1 state, while MR methods will underestimate the S_2 excitation energy in presence of a counterion located close to the Schiff base.

Table 5.5: Absolute Energies (eV) of the 6-s-*cis*-11-*cis* Retinal in Rhodopsin (**1**) and its Batho Structure (**2**) from Ref.[1]; Shift in the Vertical Excitation Energy.[a]

	state	CASSCF[b]	CASPT2[b]	SORCI	B3LYP	OM2/MRCI
1	S_0	0.00	0.00	0.00	0.00	0.00
	S_1	2.64	1.88	1.93	2.20	2.15
2	S_0	1.35	0.94	1.12	0.90	1.00
	S_1	3.39	2.65	2.82	3.14	2.94
S_1 shift		-0.60	-0.17	-0.23	0.04	-0.21

[a]Energies were calculated without MM point charges. [b]Ref.[1].

5.3.3 Isomerization of Retinal

Recently, two QM/MM models of retinal in rhodopsin, one representing the 11-*cis* ground state (structure **1**), the other its isomerized (all-*trans*) conformation in the so-called batho state (structure **2**) have been used to calculate absorption energies of the isolated chromophore (without point charges) at the CASSCF and CASPT2 level of theory.[1] Structure **1** had been optimized with DFTB using a QM/MM implementation, thereby including the whole protein during the optimization. Structure **2** was taken as the mirror image of that from Ref.[262], which was optimized with DFT (BP86). Table 5.5 shows the absorption energies for the two chromophore structures at various levels of theory. It is very encouraging, that CASPT2, SORCI and OM2/MRCI predict very similar shifts in absolute and excitation energies. DFT on the other hand agrees for the ground state, but fails to reproduce the spectroscopic shift. Obviously, also CASSCF is inadequate for quantifying spectral shifts due to geometrical changes, in this case overestimating the effect by 0.4 eV compared to CASPT2 or SORCI.

In the same paper,[1] Schreiber and Buß decompose the structural changes between **1** and **2** into seven intermediates (omitting the β-ionone ring) in order to analyze the effect of bond lengths, bond angles, and dihedral angles separately. As can be seen in Figure 5.4, the agreement of the MR methods is not punctual but also reproduced for the shifts between the intermediate structures: the standard deviation between SORCI and CASPT2 is 0.05 eV, OM2/MRCI values are 0.14 eV too high compared with CASPT2, but exhibit shifts that agree within 0.08 eV on average.

Considering the results of this section, it is evident that geometrical changes, as they are caused by the protein environment and photoisomerization, are able to shift the absorption maximum considerably. However, it appears that TDDFT and CASSCF are not appropriate methods to quantify these shifts, whereas CASPT2, SORCI, and OM2/MRCI display the same trends. Furthermore, the level of accuracy needed for geometry optimization to not introduce artificial shifts is provided by the B3LYP and SCC-DFTB methods but not by pure GGA functionals, HF or CASSCF, which yield extreme values for the BLA and the C5–C6–C7–C8 dihedral angle.

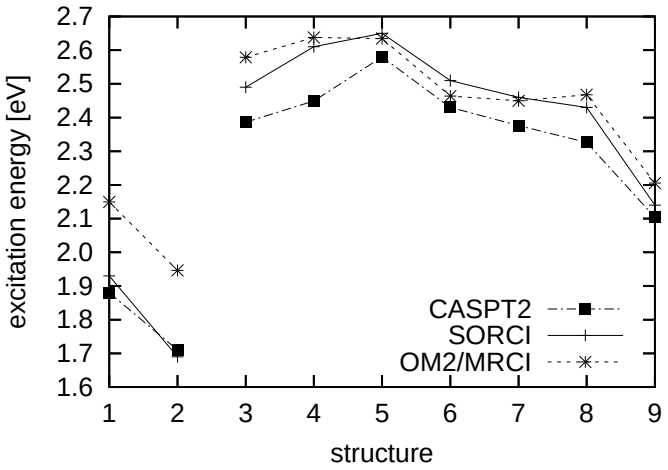

Figure 5.4: Influence of conformational changes on S_1 excitation energies. Labels 1–9 refer to the structures described in Ref.[1]: PSB of retinal (**1**, **2**) and PSB5 analogs of the Rh (11-*cis*) and batho (11-*trans*) chromophore (**3** and **9** respectively), the fully-optimized, planar PSB5 analogs (**4**, **5**). From 5 to 8 the internal coordinates of 9 are stepwise imposed: bond lengths (**6**), bond angles (**7**), dihedral angles about formal single bonds (**8**), and double bonds (**9**).

5.4 Excited-State Potential Energy Surface

In the previous section, the response of the vertical excitation energy to individual geometric deformations of the PSB of retinal were analyzed using single-point calculations of modified ground-state structures. Although this procedure reveals already some information about the excited-state potential energy surface (PES), it is insufficient to obtain a picture of the ultrafast excited-state photoreaction and test the methods ability to correctly describe the features of the PES that are relevant for the excited-state dynamics, the nonadiabatic decay to the ground state, and product formation. To achieve this, the topology of the PES's of the involved states must be considered in terms of minimum energy pathways (MEP), local minima, transition states, conical intersections, and intersection seams. In this section, the PES's of DFT-based methods will be compared with those of multireference approaches for the reduced PSB3 and PSB5 models (see Figure 5.1).

5.4.1 Cross Sections of the PES

A limited, but quite common approach for investigating the PES of excited states is to simply displace the optimized ground-state structure along a single coordinate that is representable for the expected reaction path and plot the vertical excitation energies along this path. In the present case, the isomerization path can be approximated by twisting the molecule around the corresponding double bond while all other internal coordinates are kept fixed to their ground-state values. In this way, different computational approaches can easily be compared by performing single point calculations. However, as will be demonstrated in the following, the information obtained from such cross sections of the adiabatic surfaces can be misleading.

In Figure 5.5 (left), the cross sections of PSB5 along the twist coordinate of the

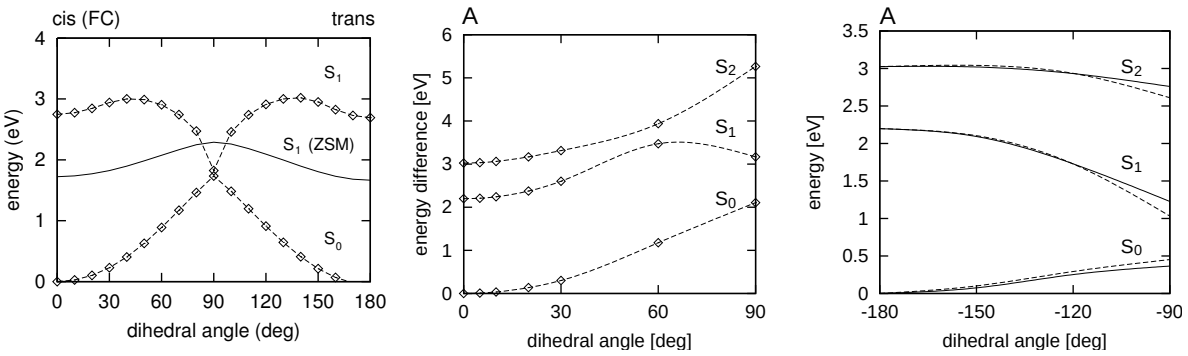

Figure 5.5: Energy profiles of PSB5. Left: the DFTB ground-state minimum structure (FC) is twisted around the central double bond, S_1 energies from TD-DFTB and ΔSCF-DFTB (Ziegler's sum method). Alternatively, starting from the TD-DFTB planar S_1 minimum (A), the structure is twisted around the central double bond (center) or vicinal single bonds (right) keeping all other degrees of freedom fixed.

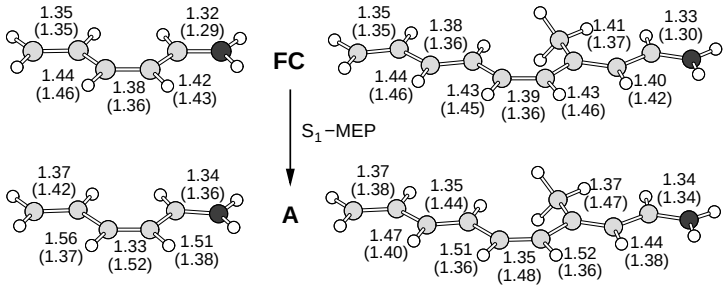

Figure 5.6: Initial S_1 relaxation of PSB3 (left) and PSB5 (right) in TD-DFTB. Above: ground-state minimum geometry (FC-point), below: S_1 C_s minimum (structure A). CASSCF values[2–4] of FC point and S_1 C_s minimum in parentheses.

central double bond are compared, as described by TD-DFTB and ΔSCF-DFTB (based on Ziegler's sum method[263]). While TD-DFTB predicts a S_1/S_0 conical intersection at a 90° twisted structure, ΔSCF-DFTB features a gap of 0.56 eV. In the TD-DFTB S_1 cross section a barrier occurs between FC point and CI of 0.25 eV. In contrast to this, the S_1 cross section of ΔSCF-DFTB shows a barrier at the 90° twisted avoided crossing point, which is 0.57 eV above the S_1 energy at the FC point.

At this stage, it is not clear whether the observed barriers correspond to real transition states on the global PES, or if these "barriers" vanish when the path is fully optimized in the excited state. Further, the question arises if the gap in the ΔSCF-DFTB cross section will disappear along the relaxed S_1 path. However, the same qualitative properties of the ΔSCF S_1 PES have been found in a plane-wave study[264] of the PSB, in which the transition structure was fully relaxed (constraining only the twist angle of 90°).

5.4.2 Initial Relaxation from the FC Point

In all models and in PSB11, the gradient of TD-DFTB and TDDFT (GGA and hybrid functionals) differs qualitatively from that of CASSCF/CASPT2. During the initial

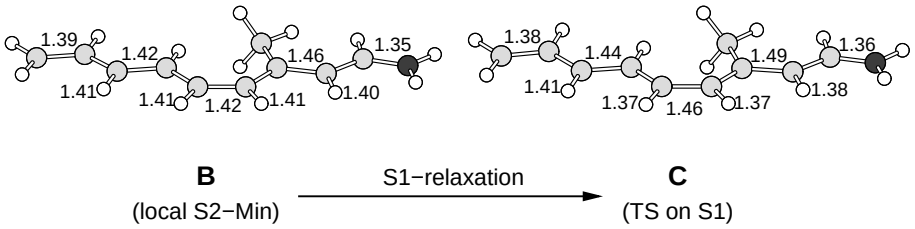

Figure 5.7: PSB5 TD-DFTB geometries of S_2 C_s-minimum (B) and local S_1 C_s-minimum (C) obtained by S_1 relaxation of structure B. TDDFT values (BP86/6-311++G**) in parentheses. CASSCF values[4,5] of S_2 (left) and S_1 (right) C_s-minimum in square brackets.

relaxation along the S_1 SD path starting at the FC point, the BLA is not inverted as in CASSCF[2,3,5,6,253] but increased, approaching a stationary point in the model systems (TS of second order), which I will refer to as structure A (see Figure 5.6). Due to the tightening of double bonds, the torsional barrier in the cross section of the unrelaxed path (Figure 5.5 left) does not disappear but increases in energy (Figure 5.5, center). This means that the expected isomerization of the central double bond of PSB3, PSB5 and C_{11}=C_{12} of PSB11, respectively, is not predicted by TD-DFTB/TDDFT to be a relevant reaction path. Instead, barrierless isomerization paths around single bonds are opened for the two vicinal single bonds in PSB5 (Figure 5.5 right). A CASPT2 calculation of structure A (PSB5) yields an energy 0.36 eV above the CASSCF stationary point, which is another strong clue that this structure is merely an artifact of TD-DFTB/TDDFT.

In agreement with CASSCF, the S_2 gradient of all TDDFT methods in the FC point decreases the BLA in all three systems. In the context of the high $S_0 \rightarrow S_2$ oscillator strength (which even increases along the S_1 relaxation coordinate) and the small energy separation between S_1 and S_2, it is important to clarify if an avoided crossing occurs along the relaxation path and if the two states are not simply exchanged in TDDFT. In an analysis of KS orbitals and single-particle properties (see Appendix 9.3), there is no indication of any S_1/S_2 state crossings, neither between the excited-state structures nor along the double-bond isomerization path. Thus, the wrong S_1 gradient of TDDFT methods at the FC point cannot be ascribed to a wrong order of states.

On the TD-DFTB S_1 PES of PSB5, there exists also a stationary point of inverted BLA in agreement with the CASSCF geometry,[2,5,6] which is labeled structure C in the following (see Figure 5.7). The Hessian at this point (local minimum within planar subspace) has two negative eigenvalues corresponding to double-bond twisting modes. Nonetheless, structure C is located energetically above FC point and structure A in TD-DFTB (Table 5.6), and no significant barrier divides structure C from the lower energy region around A. From the A $\leftrightarrow$ C TS (within the C_s subspace), which is very close to C, we calculated a SD path for PSB5 (Figure 5.8). In TDDFT we did not find a stationary point of inverted bond alternation at all, neither with GGA nor with hybrid functionals. Although the PES of TDDFT resembles closely that of TD-DFTB (at structure C the TDDFT surface is also very flat) and single point calculations (Figure 5.8) indicate qualitative agreement with TD-DFTB, the inverted BLA can only be stabilized by twisting the structure around the central double bond by at least 40°.

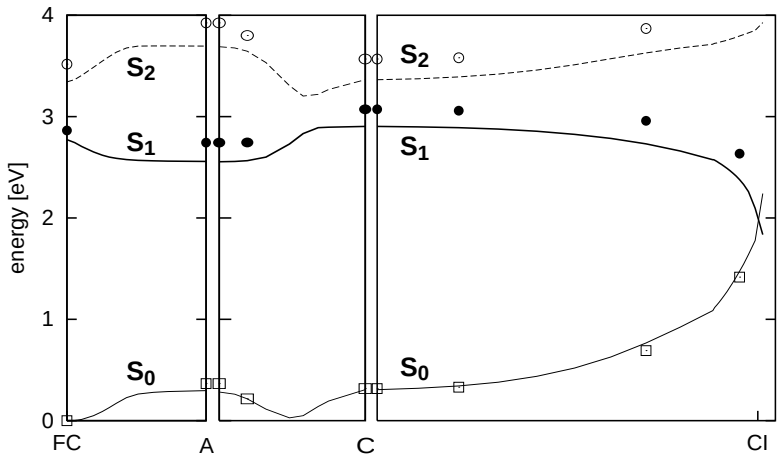

Figure 5.8: PSB5 potential energy profile along the S_1 SD paths of TD-DFTB described in the text. TDDFT single-point energies based on TD-DFTB geometries are represented by circles/squares.

5.4.3 Double-Bond Isomerization Path to Conical Intersection

Starting from structure C of PSB5 and breaking the C_s symmetry along the vibrational mode of the lowest Hessian eigenvalue, I calculated a S_1 SD path with TD-DFTB. This path describes a double-bond isomerization and agrees both energetically (Table 5.6) and structurally (Figure 5.9) with the reported CASSCF/CASPT2 path,[2,5,6] ending up in a nearly perpendicular CI structure (TICT state). In agreement with CASSCF/CASPT2, the HOMO $\rightarrow$ LUMO single excitation character of S_1 is preserved along the isomerization path.

Although the correct description of *cis-trans*-isomerization paths may appear encouraging, it is evident at this point that a correct dynamical description of PSB11 photochemistry in vacuum following excitation into the spectroscopic S_1 state will not be delivered by TDDFT, since the steep gradient at the FC point will drive the system into the valley of structure A.

5.4.4 Reasons for the Erroneous S_1 Gradient in TD-DFTB/TDDFT

In section 5.3.2, it was shown that TDDFT using GGA functionals dramatically underestimates the S_1 excitation energy when the β-ionone ring is twisted out of the molecular plane of the conjugated chain. This example also shows, that the CT problem in TDDFT can lead to artifacts in the excited-state PES. In fact, when all-*trans* PSB is relaxed in the S_1 state with TD-BP86, a rotation of the C6–C7 bond can be observed. Therefore, the question arises, in how far the erroneous S_1 gradient of TDDFT, i.e., the increase of the BLA, is related to the local exchange approximation in the employed density functionals and linear response kernels.

First, the charge distribution of the PSB5 model in the S_0, S_1, and S_2 states shall be compared for TD-DFTB and CASSCF/CASPT2. According to the latter,[4] the positive charge is located predominantly on the SB side of the molecule in the ground state. In S_1 a CT to the opposite side occurs, whereas the S_2 charge distribution again resembles

Table 5.6: Energies of stationary points (eV).

structure	state	TD-DFTB	BP86	B3LYP	CASPT2
PSB3 model					
FC	S_0	0.00	0.00	0.00	0.00
	S_1	3.90	4.03	4.17	4.02
	S_2	5.00	5.32	5.87	5.37
A	S_1	3.70	3.73	3.97	-
	S_2	5.24	5.67	5.94	-
PSB5 model					
FC	S_0	0.00	0.00	0.00	0.00
	S_1	2.77	2.89	3.01	2.58
	S_2	3.34	3.49	4.05	3.61
A	S_1	2.56	2.73	2.92	2.75
	S_2	3.70	3.78	4.16	-
C	S_0	0.33	-	-	0.33
	S_1	2.89	-	-	2.39
	S_2	3.38	-	-	3.04
68°	S_0	1.44	-	-	1.24
	S_1	2.39	-	-	1.92
CI	S_0	1.80	1.72	1.82	1.64
	S_1	2.07	1.94	1.92	1.59
	S_2	3.86	4.06	4.33	4.20

Structure A energies are compared to CASPT2 energies of the TD-DFTB geometry; structure C energies are compared to CASPT2 energies of the CASSCF planar S_1 SP. "68°" refers to a S_1 SD path/MEP intermediate of the corresponding method, "CI" refers to the last point of this path where SCF convergency is reached (except CASPT2: optimized CI structure using state averaged orbitals).

that of the ground state. The corresponding change of dipole moment on S_1 excitation is consistent with experimental data on all-*trans*-N-butyl retinal PSB. To simplify the analysis, the atomic charges have been summed over all atoms right to the central double bond. The TD-DFTB results are compared to CASSCF data from refs[3,4,6] in Figure 5.9. As can be seen, TD-DFTB does not describe any significant CT at all: The charge is already delocalized over the molecule in the ground state and nearly equal distributions are found for S_1 and S_2. The trend of increased charge separation toward the CI, observed at the CASSCF level, is completely missing; instead some 20% of the positive charge is transferred across the central bond in all three states. The same trend is found for TDDFT when comparing the difference of the dipole moment $|\Delta\mu|$ between $S_0 \leftrightarrow S_1$ and $S_0 \leftrightarrow S_2$: For the 68° twisted intermediate, CASSCF[4] yields a $|\Delta\mu|$ of 13.9 debye ($S_0 \leftrightarrow S_1$) and 3.9 debye ($S_0 \leftrightarrow S_2$), whereas TD-DFTB and TD-DFT (BP86/6-31G* calculation on TD-DFTB geometry) both yield 1.2 debye ($S_0 \leftrightarrow S_1$) and less than 1 debye for the $S_0 \leftrightarrow S_2$ transition. Although this lacking CT in TDDFT has important implications for the calculation of electrostatically induced shifts, as will be discussed in the next section, it means that the CT problem of the ALDA linear response kernel is not the source of the wrong S_1 gradient.

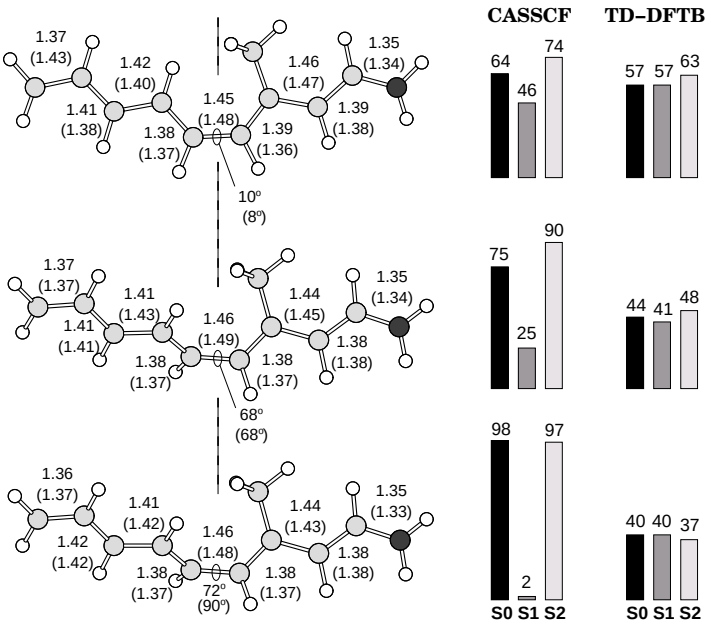

Figure 5.9: Geometries and CT along the S_1 isomerization path of PSB5. Upper: 10°/8° twisted intermediate, middle: 68° twisted intermediate, lower: conical intersection (the CASSCF CI geometry was optimized using state averaged orbitals). On the left side are shown geometries of TD-DFTB and CASSCF (values in parentheses). Beside them, on the right is presented the amount of positive net charge (percent of 1 e) corresponding to the right half of the molecule (sum of all Mulliken net charges over atoms right to the dotted line). All CASSCF values from Refs.[3,4,6].

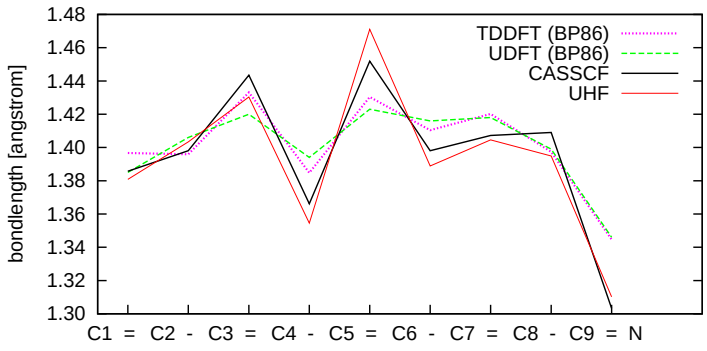

Figure 5.10: Bond lengths of T_1-relaxed retinal PSB5 (planar minimum) from TDDFT, UDFT (both with GGA functional) and CASSCF.

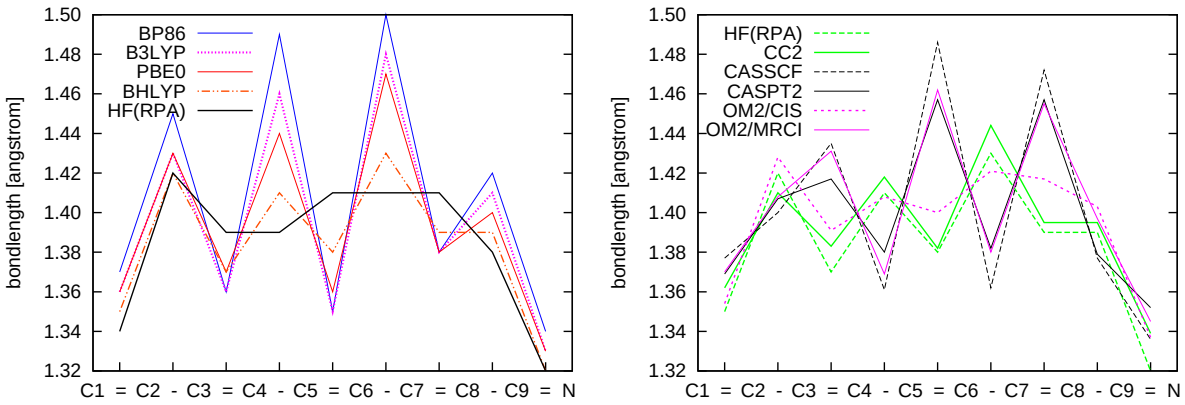

Figure 5.11: Bond lengths of S_1-relaxed retinal PSB5 (planar minimum, i.e., structure A). Left: effect of HF exchange in TDDFT. Right: effect of dynamic and static correlation. CASPT2 data from Ref.[7].

Further evidence comes from a comparison of the T_1 (triplet) planar minimum-energy structure. Like S_1, this state is dominated by the HOMO–LUMO transition. In case of a CT state, the missing particle–hole term from the exchange part of the response kernel would be even more important than for the singlet state, as the kernel for triplet states does not contain the Coulomb part. Therefore, linear response should describe the T_1 gradient even worse than the S_1 gradient. Instead, the T_1 linear-response gradient is in agreement with the gradient of an spin-unrestricted DFT (UDFT) treatment of the T_1 state, inverting the BLA on planar relaxation (Figure 5.10). Nonetheless, the inversion is less pronounced than at the UHF or CASSCF level. Like UDFT, also the restricted open shell KS approach (ROKS) does not suffer from the CT problem and yields a singlet-triplet mixed state that inverts the BLA upon relaxation. Thus, ΔSCF methods, such as Ziegler's sum method, provide a way to obtain the correct energies and gradients of the lowest singlet and triplet state, independent of the level of CT. However, these approaches introduce new problems as the missing S_1/S_0 intersection, described in section 5.4.1.

Also TDHF (RPA) places structure A energetically 0.25 eV above structure C, which is close to the corresponding CASSCF value of 0.32 eV. Moreover, the S_1 BLA changes changes drastically when HF exchange is added in hybrid functionals. As Figure 5.11 (left) shows, the change is proportional to the amount of HF exchange until the BLA is completely removed in the HF/RPA structure. This trend is the mirror image of the increase of BLA with HF exchange in the ground state, as described in section 5.3.1. It appears therefore that the electronic structure of the ground state is closely correlated with the properties of the excited state, which applies both to the CT and the minimum geometry.

When local exchange is replaced by HF exchange, this reduces on the one hand the self-interaction error but simultaneously reduces the incorporation of dynamic correlation. Hence, it is important to understand, whether GGA favours a S_1 geometry with increased BLA due to errors in the treatment of exchange, or wether an unbalanced description of correlation is the reason. To decide this, one can either add dynamic correlation to the HF or CASSCF calculation or reduce the non-dynamic correlation in methods that already incorporate both dynamic and non-dynamic correlation. In the discussion of the ground-state BLA in section 5.3.1, we observed an increase due to

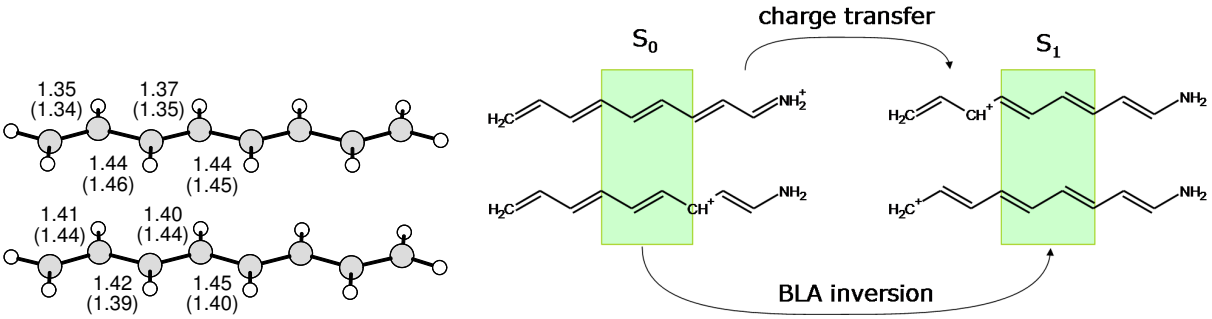

Figure 5.12: Left: octatetraene, planar ground-state (upper) and 2^1A_g (lower) minimum from BP86; CASSCF values (in parentheses) from Ref.[8]. Right: PSB model resonance structures.

correlation of the π electrons (CASSCF in comparison with HF), as well as an reduction due to dynamic correlation (CASPT2 vs. CASSCF and MP2 vs. HF). Figure 5.11 (right) shows that the inversion of the BLA in S_1 shows the same characteristic. The complete inversion of the BLA at the CASSCF level is considerably moderated when adding dynamic correlation in CASPT2. The EOM coupled cluster methods (here approximated by the CC2 method) add predominantly dynamic correlation to the HF RPA calculation. In contrast to the HF/RPA S_1 minimum geometry, the CC2 S_1 minimum does not feature any significant reduction of the BLA compared to the ground state. In the semiempirical OM2/MRCI, dynamic correlation is incorporated already in the Hamiltonian, and the correlation energy resulting from the MRCI is essentially converged when the entire π system is included in the CI space. If the π orbitals are separated by symmetry in the planar model, an active orbital space of 10 electrons in the 10 π orbitals, OM2/MRCI(10,10), is therefore sufficient and reproduces the S_1 BLA of CASPT2 with remarkable accuracy. If the active space is extended by adding 22 σ orbitals, the effect on the geometry is negligible: as the largest deviation, the central double bond is elongated by 0.006 Å. When the CI expansion is truncated to CIS, a similar pattern as that of TDHF (RPA) is produced. This shows that an important part of the π correlation is introduced by the doubles and higher-excited configurations. When, on the other hand, the active space for the OM2/MRCI is further reduced to 8, 6, 4, or 2 frontier π orbitals, two stable S_1 planar minima of similar energy arise: In addition to the C-type minimum, an A-type structure becomes stable, which does not exist on the OM2/MRCI(10,10) PES.

In summary, correlation of the π electron system leads to an enhancement of the BLA in the ground state and strong inversion in the excited state. Dynamic correlation, in general, has the opposite effect, reducing the difference between the ground and excited state. This phenomenon is more general, and can be observed also in neutral polyenes: Figure 5.12 (left) compares ground and excited-state geometries (optimization within subspace of C_{2v} symmetry) of octatetraene. The CASSCF geometry (from Ref.[8]) features a stronger BLA in the ground state and a more pronounced inversion in the 2^1A_g excited state than TDDFT (BP86/6-311++G**) optimized structures. The common discrimination between dynamic and non-dynamic correlation (e.g., in MP2 or DFT and CASSCF) is somewhat misleading in this context, because the main effect of the π correlation here is to produce the Coulomb hole in the two-particle density of the π-electrons. This reduces the Coulomb repulsion of paired π-electrons, i.e., strengthens the double bonds. The dynamic correlation introduced by MP or CC

methods does not discriminate between σ and π electrons, and stabilizes all paired electrons in the bonding regions. As the comparison between HF and MP2 geometries shows, this moderates the effect of the fermi-hole in conjugated systems, i.e., favours single vs. double bonds. Local density functionals mimic and exaggerate this effect by replacing the localized fermi-hole by an averaged effective potential, while hybrid functionals yield a more balanced description. For ground-state geometries, the correlated single reference methods (MP2, CC2) are in good agreement with the multireference methods (CASPT2, MRCI). For the excited state of retinal chromophores, this is no longer the case, as CC2 does not reduce the BLA in the S_1 state. As multireference approaches describe ground and excited states in a more balanced way, they can be considered as more trustworthy. Moreover, the photoisomerization process suggested by CASSCF-based studies on the excited-state PES[2,4,6,265–267] and the nonadiabatic dynamics[220,268,269] of rhodopsin are in qualitative agreement with the information obtained from time-resolved spectroscopic measurements, despite the unbalanced treatment of correlation in CASSCF and the use of small model chromophores.

The relation between the BLA and the charge localization/transfer in the PSB can be rationalized in terms of a valence bond analysis of the ground and excited-state wave function. Figure 5.12 (right) sketches resonance structures that are dominating S_0 and S_1. Complete BLA and strong localization of the excess charge on the Schiff base side are described by the same resonances. Ionic resonances that shift the excess charges to the allyl fragment also invert the bonding pattern in the central region of the molecule. Indeed, an analysis of the S_0 and S_1 CASSCF wave function using localized orbitals shows that the leading configuration in S_0 locates the positive charge on the carbon next to the Schiff base nitrogen and establishes the spin-pairing of the π-bonds. The leading S_1 configuration charges the allyl carbon and features the spin paring corresponding to the inverted bond pattern (ionic resonance structure, lower right in Figure 5.12). The S_2 state, in contrast, is dominated by covalent (dot–dot) structures, which also invert the alternation pattern but do not transfer the charge.

This rationale explains why wave-function based methods including only π correlation overestimate the BLA and the localization of the excess charge in the ground state, whereas methods lacking these correlations (e.g., RPA, CIS) underestimate it. Although the same correlation is found for DFT (Table 5.2), the argument is not straightforward for LDA/GGA functionals, as correlation is introduced implicitly in the XC functional. Here, the substitution of the localized fermi hole by the averaged exchange potential, i.e., the self-interaction error, is causing a strong delocalization of the excess charge (see Figure 5.9). This is a general problem of conventional functionals, and has been observed in other contexts. In addition, the effect of the π correlation might be underestimated, which is related to the fact that energies of ionic states in neutral conjugated systems are underestimated by GGA, and that the error increases with system size (e.g., in polyenes and polyacenes[80]) and decreasing gap between the covalent states (e.g., along the excited-state isomerization pathway of neutral polyenes). The consequences of the over- or underestimated CT for the spectral tuning of retinal will be analyzed in the following section.

Table 5.7: Shifts of the S_1 Vertical Excitation Energy (eV) Caused by Geometry Rearrangement[a] (column "charge = 0.0") and Point Charges of Different Amount.

method	charge = 0.0	charge = -0.5	charge = -1.1
TD-DFTB	-0.09	0.00	0.11
ΔSCF-DFTB	0.08	0.13	0.19
BP86	-0.07	-0.01	0.08
B3LYP	-0.03	0.04	0.16
BH-LYP	0.02	0.13	0.27
AM1/CIS	0.06	0.24	0.47
OM2/CIS	0.07	0.22	0.41
HF/CIS	0.09	0.22	0.37
CC2	0.01	0.22	0.51
CASSCF[b]	0.13	0.96	1.59
SORCI	0.03	0.28	0.58
OM2/MRCI	0.07	0.39	0.73

[a] All shifts incorporate already the geometry change due to switching on the full point charge of -1.1 e (see text). [b] State-averaged CASSCF(10,10)/6-31G* calculation (Gaussian98[252]); at charge -0.5 a S_1/S_2 crossing occurs at which the two states are mixing their diabatic components.

5.5 Spectral Tuning Due to the Electrostatic Environment

Corresponding to several recent QM/MM studies, the most important contribution to the electrostatic environment of the retinal chromophore in rhodopsins comes from negatively charged groups within the binding pocket, which cause a significant hypsochromic shift in the S_1 excitation energy.[9,228,229] The latter has been explained[9,10] by the CT associated with $S_0 \rightarrow S_1$ excitation, which transports a part of the positive net charge from the SB fragment to the allyl fragment, causing a large change in the dipole moment.[234] If the counter ion is located closer to the SB than to the allyl fragment, the CT works against the electric field of the counter ion and the resulting shift is hypsochromic.

In almost all current QM/MM techniques, the electrostatic environment constituted by the MM atoms is represented in the QM system by atomic point charges (though also induced atomic dipole models exist[183,187]), which are usually taken from the MM force field. Therefore, it is interesting to evaluate whether the various QM methods respond similarly to this type of external perturbation.

As a simple model for an unscreened counterion, a point charge is placed at 2.22 Å distance to the SB proton of a PSB5 model. The geometry was then re-optimized (DFTB) using a point charge of -1.1 a.u., and the spectral shifts for charges of 0, -0.5, and -1.1 a.u. were calculated with various methods. The results are shown in Table 5.7.

In the presence of this single point charge, the optimized DFTB geometry features an increased BLA, as Schreiber *et al.* found also in their QM/MM model of Rh.[10] The resulting spectroscopic shift (column 'Charge = 0.0') is small and negative for TDDFT

Table 5.8: Change of Dipole Moment $|\Delta\mu|$ (debye) Due to $S_0 \rightarrow S_1$ Excitation.

method	charge = 0.0	charge = -0.5	charge = -1.1
TD-DFTB	2.9	3.4	3.8
ΔSCF-DFTB	2.2	1.9	1.4
BP86	1.7	2.2	2.9
B3LYP	2.3	2.9	3.4
BH-LYP	3.3	3.8	4.0
AM1/CIS	1.5	1.4	1.3
OM2/CIS	1.4	1.7	1.9
HF/CIS	4.3	4.2	3.8
CC2	7.5	8.7	9.2
CASSCF[a]	14.7	—[b]	14.1
SORCI	6.0	6.6	6.7
OM2/MRCI	8.5	10.3	10.6

[a]State-averaged CASSCF(10,10)/6-31G* calculation (Gaussian98[252]). [b]S_1/S_2 crossing causes arbitrary mixing of the two states and no reasonable dipole moments can be obtained.

but positive for HF-based methods, consistent with the considerations in section 5.3.1. In presence of the -1.1 charge, the excitation energy is blue-shifted by 0.6 eV at the SORCI level. This value may serve as a reference for the other methods (further justification for this is given later in this section).

As shown in Ref.[254], TDDFT with pure LDA/GGA functionals does not feature a strong S_0–S_1 CT and underestimates the corresponding change in the dipole moment because of its local exchange kernel. Thus, the magnitude of $|\Delta\mu|$ (Table 5.8) and the blue shift in TDDFT with hybrid functionals increases with the portion of HF exchange. In any case, the TDDFT methods underestimate the shift by more than a factor of two. This is also true for the single reference CIS methods, regardless of whether the HF or a semiempirical Hamiltonian is used. In both cases, $|\Delta\mu|$ and the S_1 shift are increased when extending the CI space to MRCI (i.e., replacing HF/CIS by SORCI, or OM2/CIS by OM2/MRCI). CASSCF on the other hand displays the largest value for $|\Delta\mu|$, and largely overestimates the shift. OM2/MRCI slightly overshoots the SORCI values for both $|\Delta\mu|$ and the shift. CC2 lacks the shift due to the increased BLA at 'Charge = 0.0', but predicts $|\Delta\mu|$ and charge-induced shifts that are similar to the multireference methods.

In summary, the CT associated with $|\Delta\mu|$ is not reduced by the polarizing external point charge and provides a qualitative explanation for the large deviations among the various methods, following the above argument. Although the relationship is not strictly quantitative, the predicted hypsochromic shifts of the S_1 excitation energy increase with the extent of CT described by the corresponding method. The amount of this CT is related to the way correlation is treated in the methods (see section 5.4.4): it is overestimated by CASSCF, which incorporates primarily static correlation, and underestimated by CIS methods (and TDDFT), which cover primarily dynamic correlation.

Above, the results from SORCI were used as a reference for the other methods.

Table 5.9: Shifts of the S_1 Vertical Excitation Energy (eV) for the Rh Model of Ref.[10] in Presence of the Principal Counterion.[a]

model	CASPT2[b]		OM2/MRCI		SORCI	
	S_1	shift	S_1	shift	S_1	shift
3	2.39	0.00	2.58	0.00	2.48	0.00
3a-MM1	2.73	0.34	2.98	0.40	2.84	0.36
3a-MM2	2.79	0.40	3.04	0.46	2.92	0.44
3a-QM	2.95	0.56	3.21	0.63	3.03	0.55

[a]The latter is represented by Mulliken (MM1) or natural population analysis (MM2) charges from a DFT ground-state calculation, or included as QM atoms. [b]Ref.[10].

In the following, SORCI shifts with respect to external point charges shall be compared with CASPT2 results from Schreiber and Buß.[10] They used a QM/MM optimized chromophore geometry, as proposed for the Rh protein structure. Then, they eliminated the β-ionone ring and the C-terminal double bond, and calculated CASPT2 excitation energies for the resulting PSB5 model, without the MM point charges of the protein environment. This model is labeled as "**3**". To estimate the separate influence of the counter ion (Glu181), they included partial charges of the glutamate, represented by a formate ion, as external point charges in the calculation. For a set of Mulliken charges resulting from a DFT ground-state calculation (oxygen -0.62 and -0.52, carbon 0.4, and hydrogen 0.05), labeled "**3a-MM1**", they obtained a slightly smaller shift than using charges coming from a natural population analysis (oxygen -0.83 and -0.71, carbon 0.62, and hydrogen 0.12), labeled "**3a-MM2**".

The SORCI and OM2/MRCI results for these models, together with the CASPT2 data from Ref.[10], are shown in Table 5.9. SORCI and CASPT2 are in excellent agreement, indicating a higher accuracy for the shifts than for the absolute values. This applies also to OM2/MRCI, which systematically overestimates the S_1 excitation energies, but reproduces the shift of the high-level methods. OM2/MRCI gives a slightly higher shift than SORCI, as observed above in the case of the simple point-charge model.

5.6 QM/MM Models of bR and Rh

5.6.1 Modeling the Electrostatic Tuning of Retinal

In recent years, several groups have calculated the maximum absorption energy of retinal in the bR ground-state structure using QM/MM methods at various QM levels. A compilation of these results together with own data (SORCI, OM2/MRCI, and OM2/CIS) is given in Table 5.10. At first glance, the large deviations of the values for the bare chromophore and the spectral shifts due to electrostatic interaction with the protein environment may appear disappointing. However, these have many reasons which must be understood before a comparison between the various approaches and their predictions can be made. In the following, the main factors that lead to the observed differences shall be discussed, in an attempt to extract the common trends and statements. Of course, this is possible only up to a certain level, as considering

Table 5.10: S_1 Excitation Energy and Spectral Shift (eV) Due to the Electrostatic Environment as Predicted by Various Approaches for bR (experimental value: 2.18 eV[11]).

	HF/CIS[a]	B3LYP[a]	CASSCF[b]	MRMP[b]	PSDCI[c]	INDO/S[d]	HF/CIS[e]	CI[f]	SORCI[g]	OM2/MRCI[g]	OM2/CIS[g]
vacuum[h]	3.38	2.42	2.87	2.06	1.64	2.37		2.50	1.85	2.13	2.34
bR	3.64	2.53	3.94	2.75	2.49	2.69		2.76	2.32	2.53	2.54
shift	0.26	0.11	1.08	0.70	0.85	0.32	0.16	0.26	0.47	0.40	0.20

[a]Vreven *et al.*:[233] HF/CIS for ONIOM(HF:AMBER) geometry; TD-B3LYP for ONIOM(B3LYP:AMBER) geometry. [b]Hayashi *et al.*:[229] CAS(12,9) calculation and MRMP correction on HF/AMBER geometry. [c]Ren *et al.*:[227] partial CISD (PSDCI) on PM3 ground-state wave function and PM3 optimized geometry. [d]Houjou *et al.*:[228] INDO/S on exp. geometry. [e]Rajamani *et al.*:[232] MD-averaged shift with respect to gas-phase optimized HF structure. [f]Warshel *et al.*:[187] modified QCFF/PI CI on QM/MM MD structures. [g]This work: excitation energies on DFTB/CHARMM geometry. [h]Bare chromophore (QM/MM-optimized bR geometry) without point charges.

all the differences in the underlying protein structures and QM/MM setups would go beyond the scope of a comprehensive analysis. Although some of the studies investigated also the effect of the protein polarizability,[187,227] only results obtained with static external charges shall be considered here. The role of polarization and dispersion is addressed in chapters 6 and 7, respectively.

The SORCI, OM2/MRCI, and OM2/CIS energies have been calculated on a chromophore geometry obtained by QM/MM optimization using SCC-DFTB/CHARMM. As discussed in section 5.3.1, DFTB structures feature a BLA close to B3LYP and CASPT2. Furthermore, it has been found that the stiffness of the chromophore is accurately rendered by SCC-DFTB: ground-state torsional barriers for rotations of double and single bonds agree very well with B3LYP.[90] Hence, SCC-DFTB geometries are sufficiently accurate to enable unbiased spectroscopic calculations, if one accounts for a systematic artificial red shift of ca. 0.05-0.10 eV due to the underestimated BLA of the DFTB structure. As CASPT2 values are not yet available for the full chromophore in bR, the SORCI values will serve as a reference for the discussion of the other data. The OM2/MRCI absolute values are about 0.23 eV too high, which supports the preceding observations concerning this method, while the OM2/CIS shift is too small, as expected.

Vreven and Morokuma[233] used the ONIOM method to optimize the bR structure in a QM/MM framework. They had already pointed out the importance of the proper quantum level for geometry optimization and used B3LYP for this task. Concerning the excitation of the bare chromophore, their TD-B3LYP value is close to the TD-B3LYP//B3LYP calculation for all-*trans* PSB in the gas phase (see Table 5.2). This is consistent with the present SORCI//DFTB results, which also indicate that the net shift of the absorption maximum due to geometrical distortion in bR is rather small. The same comparison for the HF/CIS//HF values gives a blue shift of 0.20 eV, but

this is rather an effect of the lysine side chain than due to structural differences in the conjugated part: If the all-*trans* PSB model (Table 5.2) is terminated by n-butyl, the HF/CIS//HF excitation energy (3.32 eV) agrees with the bR result of Vreven and Morokuma (Table 5.10). As can be expected from the results of section 5.5, TDDFT and CIS underestimate the electrostatically induced spectral shifts, and therefore, Vreven's shifts are much lower than the MRMP ones from Hayashi and coworkers.[229] The same applies to TD-DFTB, which yields a shift of 0.13 eV.

Hayashi *et al.*[229] used HF as the QM method for geometry optimization and calculated the absorption energies at the CASSCF and MRMP levels of theory. As expected, the CASSCF shift is much larger (by 0.38 eV) than the MRMP one. In a later publication,[231] an even higher value (2.96 eV, 4.26 eV, and 1.30 eV for vacuum, bR, and shift, respectively) was obtained using a larger active space. The MRMP excitation energy for the bare chromophore is only 0.20 eV higher than the corresponding SORCI value. As will be shown in the next section, the SORCI value for Hayashi's geometry is not lower, but 0.14 eV higher than the MRMP value and the total deviation due to the geometry (0.34 eV) is primarily the effect of the high BLA produced by the HF method; the same applies to the electrostatically induced shift.

Ren and coworkers[227] relaxed only the chromophore and hydrogen atoms of a bR crystal structure using PM3. In contrast to all other work referenced here, they included a large part of the protein (binding site) in the ground-state SCF calculation and performed CISD, including all π orbitals localized on the chromophore (PM3/PSDCI). It is interesting that their vacuum value for the bare chromophore is much lower than that of all other methods. According to own calculations,[1] this is not—as could be guessed—a consequence of the employed QM method for calculating the excitation energy. A plausible reason for this low energy can be found (again) in the method used for geometry optimization: As shown earlier by Zhou *et al.*,[90] AM1 and PM3 underestimate torsional barriers in the protonated Schiff base considerably, thereby describing the chromophore much too flexible. This might cause too much distortion in the carbon skeleton when external stress is exerted by the binding pocket. As has been shown by Schreiber *et al.*,[1] dihedral twisting of the conjugated chain, whether around single or double bonds, lowers the S_1 excitation energy. Starting from this low energy, it is that they come closest to the experimental value of 2.18 eV for bR.[11] One reason for their larger shift, compared to the MRMP or SORCI values, is the CT between the chromophore and the complex counter ion, which they incorporate using the extended QM zone. It has been shown earlier[10,229] that inclusion of the counter ion in the QM region enhances the hypsochromic shift when compared with the purely electrostatic interaction with point charges: Schreiber and Buß[10] found an additional shift of about 0.2 eV in the case of Rh (see Table 5.9), whereas the CASSCF shift of Hayashi *et al.*[229] is increased by another 0.55 eV when treating the counterion and one water quantum mechanically. In the latter example also geometry optimization was carried out with the counterion complex included in the QM region, which led to significant changes in the hydrogen bonded network of the complex. As will be shown in section 7.3, the CT does not significantly change upon excitation, and its effect is therefore included in the small CI calculation of Ren *et al.*

[1] PM3 excitation energies for the current bR QM/MM setup using CIS, CISD (with frozen σ orbitals), and MRCI. Due to the PM3 Hamiltonian S_1 energies (1.96, 2.12, and 1.78 eV, respectively) are 0.34–0.38 eV lower than their OM2 counterparts, but the lack of triple excitations in CISD compensates for this, yielding a PM3/CISD value close to the OM2/MRCI one (2.16 eV).

Houjou and coworkers[228] obtained an excitation energy for the bare chromophore in its bR structure that is 0.73 eV higher than Ren's[227] result using INDO/S. Their value of 2.37 eV is close to the OM2/CIS result. On the other hand, own ZINDO/S calculations, based on the DFTB/CHARMM bR setup, yield an excitation energy of 2.25 eV (using a 20 eV orbital window). This suggests that their geometry (although directly derived from the 2BRD X-ray structure) only slightly biases the absorption maximum to higher energies (in contrast to that of Ren *et al.*). Compared to our SORCI benchmark, the vacuum value of Houjou *et al.* is too high by at least 0.4 eV, whereas their electrostatic shift is underestimated by the CIS calculation, which partially compensates for this error in the final result for bR.

Rajamani and Gao[232] performed statistical Monte Carlo (MC) simulations with the chromophore in a methanol solution (6-s-*cis* configuration) and MD simulations in bR (all-*trans*) to set the stage for a decomposition of the experimentally observed opsin shift into several spectroscopic effects. Here, we will consider only the last step of their analysis, the spectroscopic shift from all-*trans* PSB in the gas phase to bR. In the basis of 50 MD structures, they calculated an averaged hypsochromic shift of 0.16 eV, using HF/CIS and a 3-21G basis set within a QM/MM model. Their shift is considerably smaller than the HF/CIS shift of Vreven and Morokuma,[233] but there are several possible reasons for this: Rajamani and Gao's shift includes the steric distortion of the chromophore in the binding site (their reference is the gas-phase structure), they use the AM1 Hamiltonian during the MD simulation, which might cause dihedral distortions of the polyene chain that are too strong (see above), and dynamic effects which are not included in the other studies reviewed above. Gao has shown[270] that CIS also underestimates the solvatochromic shift of the lowest n$\rightarrow\pi^*$ state of acetone in polar solvents with respect to a full CI treatment. Thus, an extension of his approach to larger CI spaces (e.g., MRCI) would change his decomposition but presumably not his overall estimate for the opsin shift, which is already close to the experimental value.

Warshel *et al.*[187] presented another study that incorporates dynamic effects by MD sampling. They use a semiempirical QCFF/PI Hamiltonian and represent the excited state in a limited CI space (including only $\pi \rightarrow \pi^*$ singles and the most relevant doubles). The CI matrix is modified, introducing geometry-dependent parameters which are fitted to match the CASSCF reaction coordinate of Ref.[6]. Thus, the high absorption maximum of 2.50 eV for the bare chromophore partially reflects the overestimation of this value at the CASSCF level of theory. The hypsochromic shift of 0.26 eV induced by the electrostatic environment (excluding induced dipoles on the protein) is comparable to the results of CIS methods, but it is not clear whether this is due to the small CI space, the used Hamiltonian, structural differences, or dynamic effects.

5.6.2 Role of Bond Length Alternation in the Protein

To estimate the influence of the BLA inside the protein, the HF QM/MM optimized structures published by Hayashi *et al.* shall be used here for comparative calculations.[229] The chromophore was re-optimized in the fixed protein structure, using SCC-DFTB in a QM/MM implementation with the CHARMM force field. Then absorption energies were calculated using OM2/MRCI and SORCI for both, Hayashi's original HF geometry and the SCC-DFTB one. The results are shown in Table 5.11.

For the HF/AMBER structure, SORCI yields an excitation energy for the bare chro-

Table 5.11: Vertical S_1 Excitation Energies for Different bR QM/MM Setups.[a]

	SORCI	OM2/MRCI
HF/AMBER	2.89 (2.20)	3.15 (2.40)
SCC-DFTB/CHARMM[b]	2.52 (1.91)	2.70 (2.13)
shift	0.37 (0.29)	0.45 (0.27)

[a]Values for the bare chromophore (omitting the MM point charges) are given in parentheses. [b]Chromophore optimized, protein fixed to original structure.

Table 5.12: Vertical S_1 Excitation Energies for Different Rh QM/MM Setups.

	SORCI	OM2/MRCI
CASSCF/AMBER	3.23	3.34
SCC-DFTB/CHARMM[a]	2.94	3.05
shift	0.29	0.29

[a]Chromophore optimized, protein fixed to original structure.

mophore of 2.20 eV (0.14 eV lower than Hayashi's MRMP result) and an electrostatically induced shift of 0.69 eV, which is in excellent agreement with Hayashi's calculation (Table 5.10). Due to relaxation with DFTB/CHARMM, the BLA is reduced from 0.120 to 0.059 Å, and the vertical excitation energy, corresponding to SORCI, is red-shifted by 0.37 eV (0.45 eV on the OM2/MRCI level). As can be seen from the corresponding energies for the bare chromophore, the major part of this shift (0.29 eV) arises directly from the geometrical change in the chromophore, but is enhanced by the electrostatic environment. This is consistent with the observation in section 5.3.1 that CT on the chromophore, in terms of the difference dipole moment $|\Delta_{S_1-S_0}\mu|$, increases with the BLA of the underlying chromophore geometry. When compared to the situation in the gas phase (Table 5.2), the BLA is approximately doubled in the protein at both levels of theory. As explained in section 5.5, this effect is induced primarily by the field of the counter ion.

Note, that the bR excitation energy for the DFTB/CHARMM relaxed chromophore still differs by 0.2 eV from the SORCI//DFTB/CHARMM value given in Table 5.10, which is caused by using different protein structures. Hayashi's structure was constructed primarily from the X-ray structure by Luecke *et al.*[271] (PDB code: 1BRX). The RMSD from the DFTB/CHARMM structure amounts to 1.39 Å (backbone only).

In contrast to bR, there are only few investigations of Rh including a large part of the binding pocket around the chromophore or using QM/MM techniques up to now. However, an investigation of the structure provided by Ferre *et al.*[9] shows the same trend that was found for bR. Relaxation of the PSB5 chromophore model within the fixed protein structure at the DFTB/CHARMM level reduces the BLA from 0.112 to 0.070 Å and yields excitation energies that are red-shifted by 0.29 eV at the SORCI (or OM2/MRCI) level of theory as shown in Table 5.12.

These results demonstrate that BLA (among other geometrical parameters) plays a decisive role in spectral tuning within the protein environment. The variations in the excitation energy caused by inaccurate description of the chromophore geometry are even larger than in the gas phase, studied in section 5.3.1, and are of the same order

of magnitude as effects discussed for explaining the gap between experimental and theoretical results (e.g., protein polarization and dispersion).

5.7 Conclusions

The calculation of accurate retinal absorption energies remains a great challenge, since they depend sensitively on many factors, as outlined in this chapter. In general, all approaches are deficient in describing the spectral shifts for retinal in different environments (different proteins, solutions). A comparison to experimental results is not straightforward, since good agreement with experiment can result for the wrong reasons or from a fortunate error cancelation. To test theoretical methods for every individual factor, a comparison to the experiment is not always possible. Therefore, this investigation was based on comparison with high-level *ab initio* methods for ground-state and excited-state properties. Among these, CASPT2 may be regarded as the best established one; for ionic 1^1B_2-like states of linear conjugated systems akin to retinal, average deviations to experiment below 0.1 eV have been achieved.[272–274] The recently developed SORCI method agrees with CASPT2 quite well: for the 16 S_1 excitation energies presented in this chapter (Tables 5.1, 5.5, and 5.9 and Figure 5.4), the standard deviation between the two methods amounts to only 0.08 eV.

Vertical excitation energies are very sensitive to the ground-state geometry, in particular to the bond length alternation (BLA) of the retinal chromophore, and thereby, to the method used for geometry optimization. CASSCF and HF methods tend to exaggerate the BLA of PSB's, leading to overly high excitation energies, while the opposite applies to pure LDA/GGA density functionals. The resulting error is more significant in the protein (0.3-0.4 eV) or solution than in the gas phase because the CT associated with excitation into S_1 increases with increasing BLA. The S_2 state is even more affected than S_1, which complicates the quantitative prediction of the S_1–S_2 energy gap. Hybrid DFT methods and MP2 obtain the most accurate ground-state geometries, BLA's in particular, when taking the CASPT2 geometries of Page *et al.* as a reference.[7,275] As a fast alternative, SCC-DFTB geometries can be used without a significant loss of accuracy in excitation energies, causing an estimated red shift of 0.05–0.10 eV in the gas phase and 0.10–0.20 eV in the protein, due to the smaller BLA. Further, SCC-DFTB has been shown to give good agreement also for other geometrical and energetic properties of retinal.[90]

OM2/MRCI performs very well for excited-state energies for all tests performed so far. It describes the dependence of the excitation energy with respect to geometrical and external field perturbations very accurately, when compared to the SORCI and CASPT2 results. However, OM2/MRCI excitation energies for the PSB are systematically overestimated: the mean deviation from SORCI amounts to 0.12 eV. By subtracting this value from all OM2/MRCI results in an *a posteriori* correction, one obtains accurate excitation energies with a standard deviation of 0.09 eV from SORCI. This is the level of precision that can be expected from OM2/MRCI for predicting spectroscopic shifts of retinal proteins. Therefore, it is a very powerful tool in combination with SCC-DFTB (for ground-state optimization, MD trajectories), since both methods are several orders of magnitude faster than their *ab initio* counterparts. This, in turn, makes studies of spectral tuning feasible that incorporate dynamic effects by calculating spectra along ground-state MD trajectories.

Surprisingly, neither CASSCF nor CIS (HF or semiempirical) is very reliable for the systems studied here. CIS methods systematically underestimate shifts in excitation energies with respect to external charges, while CASSCF overestimates this effect. In CASSCF, additionally, the response to geometrical effects is overestimated.

The performance of TDDFT for excited-state properties of retinal, despite promising excitation energies for planar geometries, is very poor. For both, geometrical and external field perturbations of excited-state energies, TDDFT fails dramatically due to different reasons: The wrong topology of the S_1 PES at the FC region affects the response to changes in the BLA (1). The underestimation of CT states causes artificial low-energy minima on the S_1 PES at structures with highly twisted β-ionone ring (2). The same problem might occur in hydroretinals, where the conjugated chain is interrupted by saturated segments. For structures with fully conjugated retinal (co-planar $\beta - ionone$ring), the CT upon S_1 excitation is drastically underestimated (3), explaining the weak response to electrostatic perturbations (counter ion). In structures with twisted ring and/or high BLA, error cancelation may "cure" this deficiency of TDDFT. As argued in section 5.4.4, the deficiencies can be associated with an unbalanced description of correlation (1), the local response kernel in the ALDA approximation (2), and the delocalization of excess charges due to the averaged fermi-hole, i.e., the self-interaction error (3), respectively.

To summarize, calculating CASPT2 or SORCI spectra for MP2 or hybrid DFT (B3LYP, PBE0) retinal geometries will lead to accurate results. A similar accuracy is obtained by the combination of OM2/MRCI with SCC-DFTB, when taking into account the systematic error of OM2 a posteriori. The latter approach is several orders of magnitude faster than the *ab initio* procedure. The resulting "best estimate" for the absorption maximum of bR at the SORCI//DFTB/MM level of theory is 2.34 eV. Although this value lies only 0.1-0.2 eV above the experimental result, the proposed approach still neglects several effects, which have been estimated to be of the same order of magnitude as the spectroscopic shifts that are actually under investigation. First, the effect of charge transfer (CT) between chromophore and complex counter ion has been addressed in the case of rhodopsin (Table 5.9), where it gives rise to a blue shift of ca 0.15-0.20 eV, depending on the value of the point charges used for comparison. Second, the effects of polarization and dispersion on the absorption maximum have been considered explicitly in several different models[187,227,236] suggesting hypsochromic shifts on the order of magnitude of 0.2–0.3 eV. In chapters 6 and 7, the current QM/MM model will be extended to include and investigate these effects and allow for more quantitative predictions of the optical properties of retinal proteins.

Chapter 6

The Effect of Protein Polarization on the Opsin Shift in Rhodopsins

6.1 Introduction

In chapter 5, the high sensitivity of retinal's spectroscopic properties to the chromophore geometry, electrostatic environment, and hydrogen-bond formation were demonstrated. This sensitivity allows rhodopsins to be photoactive in a range between 345 and 630 nm,[276,277] whereas their common chromophore absorbs at 610 nm in the gas phase.[278] On the other hand, this feature can be exploited by using the chromophore as a sensitive probe for structural changes in the opsin. Spectroscopic information can be used to detect transitions between intermediates along the photocycle and determine their lifetimes under specific conditions.

An important implication of this sensitivity for the computational investigation of these proteins is that the theoretical prediction of spectral features can in principle be used to judge the plausibility of proposed structural and models for intermediates that are difficult to resolve via crystallographic techniques but are well characterized from a spectroscopical point of view. However, despite the progress in the computational modeling and the increasing resolution of available crystallographic 3D structures, it remains difficult to achieve the required accuracy in both absolute absorption maximum and spectral shifts. As an example, the individual significance of tuning mechanisms to the shift between bacteriorhodopsin (bR, 568 nm[11]) and the structurally very similar pharaonis sensory rhodopsin II (psRII, 497 nm[279]) has long been debated (see Ref.[280] and references therein).

As discussed in chapter 5, calculated absorption energies and spectral shifts of retinal proteins depend severely on the methods used to obtain the chromophore geometry and excitation energies, and the dominating source of error in most previous theoretical studies on opsin shifts was the approximate QM treatment of the chromophore. The computational strategy developed in the previous sections achieves an accuracy in the prediction of the chromophore absorption maximum that is sufficient for quantitative analyses of the opsin shift in different rhodopsins, mutants, and intermediates. When comparing the absorption maxima of different proteins, the dominant error might therefore arise from uncertainties in the employed QM/MM model. This may concern conformational alternatives, protonation states, but not least, the electrostatic representation of the protein environment in the QM Hamiltonian. The point-

charge models of common protein force fields (FF) are coordinated with the remaining nonbonded parameters to reproduce interaction energies and structural features, but the point charges of the amino acids do not necessarily provide a good representation of the electrostatic potential (ESP) in their vicinity.

Apart from the employed charge model, the accuracy of the calculated optical properties is affected by the limitations of the QM/MM approach itself. Even when the light-absorbing π system of the chromophore is well separated from the covalent link between the QM and the MM region, significant charge transfer across the QM/MM border can occur, e.g., via the hydrogen-bonded network connecting Schiff base and counter ion, which is suppressed if the QM region contains only the chromophore. In fact, theoretical studies have observed blue shifts of the excitation energy of the rhodopsin chromophore of 0.2–0.5 eV when including the counter ion in the QM region instead of using a point charge model,[10,229] which result essentially from the charge transfer.[281] Moreover, the fixed-charge model of the MM region neglects the effects of static polarization and inter-residual charge transfer. Further, the vicinity of several aromatic side chains to the chromophore has given rise to the assumption that differential dispersion may red-shift the absorption.[227]

Among the former theoretical works on the optical absorption properties of retinal proteins, there are only few that explicitly included polarizability in their protein model.[179,187,236] These emphasized the necessity of a polarizable protein model to correctly describe the solvation of the chromophore[187] and arrive at quantitative results for absorption maxima and spectral shifts.[179,236] On the other hand, numerous theoretical studies[9,10,228,229,280,282–284] reproduced experimental absorption energies using fixed-charge models for the protein or binding-pocket residues. Such agreement, however, does not implicate any information about the magnitude or relevance of dielectric and other neglected effects, since the calculated absorption maximum depends on many details of the computational approach and can easily result from error-cancelation.[281] Therefore, it is necessary to quantify the isolated effect of the environment polarizability on the absorption maximum, independent from other sources of error.

The importance of polarization in solvation models for the retinal chromophore embedded in a host protein has been discussed for some time.[187,236] Some theoretical studies on the spectral shifts between different rhodopsins[179,236] have proposed that quantitative results can be expected only from models that include the polarization response of the protein to the charge relocation on the chromophore upon excitation. For the spectral shift between bR and ppR (0.32 eV in experiment[11,279]), Matsuura *et al.* suggested a contribution of 0.23 eV (70%) due to polarization.[285] On the other hand, a number of theoretical studies[9,10,228,229,280,282–284] reproduced experimental results using non-polarizable FF's. In the preceding chapter, however, it was demonstrated that many factors and details of the computational approach influence the calculated absorption energies, and that such agreements can easily result from error-cancelation. Therefore, it is highly desirable to quantify the isolated effect of the environment polarizability on the absorption maximum, which is not directly accessible in experiment, independent from other sources of error.

The developments and investigations described in this chapter are dedicated to examine the influence of protein polarization at the atomic level on the excitation energy of an embedded chromophore, using retinal as a prototype system, and to quantify the errors caused by the fixed charge representation of the electrostatic environment

in common FF's. At a first stage, I consider the electrostatic interaction between the chromophore in its electronic ground and first excited state and the immediate protein environment, i.e., the amino acid side chains within retinal's binding pocket. By substituting the CHARMM27 fixed point charges in this region by an explicit quantum mechanical treatment, a self-consistent mutual polarization between chromophore and binding pocket is achieved, which incorporates (1) the inter-residual polarization and charge transfer in the binding pocket and (b) the instantaneous response of the binding pocket to the charge relocation associated with the $S_1 \leftarrow S_0$ excitation. At the second stage, empirical polarization models are implemented and parameterized for polypeptides and integrated in the QM/MM interface for excited-state calculations. The results of the first stage will then be used to assess empirical polarization models on the binding pockets of bacteriorhodopsin (bR) and pharaonis sensory rhodopsin II (psRII). In the last stage, the effect of polarization on long-range interactions is investigated: The empirical polarization models are applied to the entire protein and are combined with continuum-electrostatics methods to describe the embedding in a solvent/membrane environment. Here, the effect on the calculated excitation energies is studied on the systems bR, psRII, and two different rhodopsin (Rh) models.

6.2 Development of a QM/QM/MM model

The methods that appropriately describe the excited state of the chromophore are computationally too demanding to be applicable to a larger part of the protein binding site. To describe the state-dependent polarization of the molecular environment, the range of active orbitals must span the entire system. Even semiempirical MRCI methods are therefore limited to regions that cover the whole chromophore and few surrounding amino acids. On the other hand, the quantum mechanical description of the chromophore and the protein fragment have to meet quite different demands. While the latter must merely provide an accurate ground-state charge distribution for a system of several hundred atoms, the first must quantify the response of retinal's absorption maximum to subtle changes in the electrostatic environment. For this reason, it is necessary to split the quantum mechanical region into two weakly coupled subsystems: the chromophore, on which the excitation is localized and the protein fragment. In the following, these are referred to as QM1 and QM2, respectively. The resulting QM1/QM2/MM model will be developed below, its implementation and computational details are described in section 6.4. The model is then applied to bR and psRII (section 6.5.1).

6.2.1 Variational Ground-State Energy

In the following, the variational energy expression for the ground state of a QM1/QM2/MM model is derived, starting with the common QM/MM Hamiltonian

$$H = H_{\mathrm{QM}} + H_{\mathrm{QMMM}} + H_{\mathrm{MM}} \,. \tag{6.1}$$

Here, H_{QM} refers to the non-relativistic, Born–Oppenheimer Hamiltonian of the QM subsystem,

$$H_{\mathrm{QM}} = -\frac{1}{2}\sum_i \nabla_i^2 + \frac{1}{2}\sum_i \sum_{j\neq i} \frac{1}{r_{ij}} - \sum_{i,m} \frac{Z_m}{r_{im}} + \frac{1}{2}\sum_m \sum_{n\neq m} \frac{Z_m Z_n}{R_{mn}} \,. \tag{6.2}$$

H_{QMMM} contains the electrostatic ($H^{\mathrm{el}}_{\mathrm{QMMM}}$) and the charge-independent (bonded and van der Waals $H^{\mathrm{b+vdW}}_{\mathrm{QMMM}}$) interactions between the QM and MM parts. H_{MM} is the usual MM Hamiltonian. Since the QM1/QM2/MM model shall describe only the classical Coulomb interaction between two moieties of the QM subsystem, i.e., the static mutual polarization, the electronic wave function can be written as a single (non-symmetrized) product $|\Psi^{(1)}\rangle|\Psi^{(2)}\rangle$ of two normalized vectors of the N_{QM1}- and N_{QM2}-particle Hilbert spaces. This ansatz neglects charge transfer, exchange, and correlation (e.g., dispersion) between the two subsystems and leads to the total energy

$$\begin{aligned} E &= \langle\Psi^{(1)}|H^1_{\mathrm{QM}} + H^{1,\mathrm{el}}_{\mathrm{QMMM}}|\Psi^{(1)}\rangle + \langle\Psi^{(2)}|H^2_{\mathrm{QM}} + H^{2,\mathrm{el}}_{\mathrm{QMMM}}|\Psi^{(2)}\rangle + \langle\Psi|H^{12}_{\mathrm{QM}}|\Psi\rangle \\ &\quad + H^{1,\mathrm{b+vdW}}_{\mathrm{QMMM}} + H^{2,\mathrm{b+vdW}}_{\mathrm{QMMM}} + H_{\mathrm{MM}}\,, \end{aligned} \tag{6.3}$$

where H^1_{QM} and H^2_{QM} have the form of eq 6.2 with the sums restricted to the particles of the corresponding subsystem. The third term in eq 6.3 is the Coulomb interaction between QM1 and QM2. For any states $\Psi^{(1)}$ and $\Psi^{(2)}$ it can be written in two equivalent ways:

$$\begin{aligned} \langle\Psi|H^{12}_{QM}|\Psi\rangle &= -\langle\Psi^{(1)}|V^2_{\mathrm{ES}}|\Psi^{(1)}\rangle + \sum_m^{\mathrm{QM1}} Z_m V^2_{\mathrm{ES}}(R_m) \\ &= -\langle\Psi^{(2)}|V^1_{\mathrm{ES}}|\Psi^{(2)}\rangle + \sum_n^{\mathrm{QM2}} Z_n V^1_{\mathrm{ES}}(R_n)\,, \end{aligned} \tag{6.4}$$

where $V^1_{\mathrm{ES}} = V_{\mathrm{ES}}[\Psi^{(1)}]$ and $V^2_{\mathrm{ES}} = V_{\mathrm{ES}}[\Psi^{(2)}]$ are the electrostatic potentials created by the electrons and nuclei of moiety QM1 and QM2, respectively, and Z_m and R_m refer to charges and positions of the QM nuclei.

The wave functions $\Psi^{(1)}$ and $\Psi^{(2)}$ can be obtained by applying the variational principle. Variation of eq 6.3 with respect to $\Psi^{(1)}$ and $\Psi^{(2)}$ yield, respectively,

$$\left\{H^1_{\mathrm{QM}} + H^{1,\mathrm{el}}_{\mathrm{QMMM}} - V^2_{\mathrm{ES}}\right\}|\Psi^{(1)}\rangle = \varepsilon_{\mathrm{QM1}}|\Psi^{(1)}\rangle \tag{6.5}$$

$$\left\{H^2_{\mathrm{QM}} + H^{2,\mathrm{el}}_{\mathrm{QMMM}} - V^1_{\mathrm{ES}}\right\}|\Psi^{(2)}\rangle = \varepsilon_{\mathrm{QM2}}|\Psi^{(2)}\rangle\,. \tag{6.6}$$

The QM subsystems can now be treated separately by different quantum methods using different levels of approximation to eq 6.5 and 6.6. The two equations are coupled via the potentials V^1_{ES} and V^2_{ES} and must be solved iteratively, till self-consistency is achieved. Introducing the total energies of QM1 and QM2 (as commonly given by the QM programs),

$$\begin{aligned} E_{\mathrm{QM1}} &= \varepsilon_{\mathrm{QM1}} + \sum_m^{\mathrm{QM1}} Z_m V^2_{\mathrm{ES}}(R_m) \\ E_{\mathrm{QM2}} &= \varepsilon_{\mathrm{QM2}} + \sum_n^{\mathrm{QM2}} Z_n V^1_{\mathrm{ES}}(R_n)\,, \end{aligned} \tag{6.7}$$

the total energy of the system results in

$$\begin{aligned} E &= E_{\mathrm{QM1}} + E_{\mathrm{QM2}} - \langle\Psi|H^{12}_{\mathrm{QM}}|\Psi\rangle \\ &\quad + H^{1,\mathrm{b+vdW}}_{\mathrm{QMMM}} + H^{2,\mathrm{b+vdW}}_{\mathrm{QMMM}} + H_{\mathrm{MM}}\,. \end{aligned} \tag{6.8}$$

Only the first three terms of the right hand side depend on the electronic state and have to be considered when calculating excitation energies.

6.2.2 Vertical Transition Energies

Corresponding to the Franck–Condon principle, the nuclei can be considered as frozen when calculating vertical transition energies for, e.g., the QM1 subsystem (solute/chromophore), hence excluding the orientational, or "inertial", response of the QM2 subsystem (solvent/protein) to the solute's electronic excitation. The electronic degrees of freedom of the solvent, however, respond to the change of the electron distribution on the solute within the time-scale of the transition. If neglecting the effect of differential dispersion, this latter response can be considered adiabatically, i.e., as instantaneous polarization.

Based on the scheme presented in the last subsection, the effect of instantaneous polarization on the transition energy can be approximated by two different approaches. Apart from the ground state $\Psi_0^{(1)}$ of QM1, the iterative solution of eq 6.5 and 6.6 can be performed for any stationary state $\Psi_I^{(1)}$ to obtain a self-consistent charge distribution and total energy. In approach (i), the transition energy is approximated simply by the total energy difference of two such solutions. As noted by Luzhkov and Warshel[183] and Thompson and Schenter,[177] the excited-state wave function of a fully self-consistent QM/QM or QM/MMpol system is not orthogonal to the corresponding ground state (although both wave functions satisfy the variational principle) because of the different external potential contained in the QM Hamiltonian for the ground- and excited-state calculation. This problem is well known in the context of multi-configurational self consistent field (MCSCF) theory, where the correct calculation of excitation energies and other transition properties can be achieved by the state-interaction method.[111] To avoid this problem, Luzhkov and Warshel proposed to use another approach (ii) to evaluate the excitation energy, which has been adopted also by others.[177,286]

The idea of approach (ii) is to preserve the orthogonality between the initial and the final state by obtaining both solute states as eigenstates I and J of the same Hamiltonian which contains the interaction with the solute in the initial state $\Psi^{(2),\mathrm{i}}$. The initial state is hence defined as fully self-consistent solution $|\Psi_I^{(1),\mathrm{i}}\Psi^{(2),\mathrm{i}}\rangle$ of eq 6.5 and 6.6. In the final state $|\Psi_J^{(1),\mathrm{i}}\Psi^{(2),\mathrm{f}}\rangle$, only $\Psi^{(2),\mathrm{f}}$ is varied and allowed to relax in presence of the "frozen" QM1 state $\Psi_J^{(1),\mathrm{i}}$ which is some eigenstate of the initial QM1 Hamiltonian containing the potential of the initial state $V_{\mathrm{ES}}[\Psi^{(2),\mathrm{i}}]$:

$$\left\{H^1_{\mathrm{QM}} + H^{1,\mathrm{el}}_{\mathrm{QMMM}} - V_{\mathrm{ES}}[\Psi^{(2),\mathrm{i}}]\right\}|\Psi_J^{(1),\mathrm{i}}\rangle = \varepsilon^{\mathrm{i}}_{\mathrm{QM1},J}|\Psi_J^{(1),\mathrm{i}}\rangle\,. \tag{6.9}$$

Approach (ii), however, neglects the response of the excited QM1 state to the change in the charge distribution in QM2, in contrast to approach (i). As it is not clear, a priori, which approach is superior, calculations with both approaches will be performed.

The total energy of the final state in approach (ii) associated with the solute transi-

tion $J \leftarrow I$ is

$$\begin{aligned} E^{\mathrm{f}} &= \langle \Psi_J^{(1),\mathrm{i}} | H_{\mathrm{QM}}^1 + H_{\mathrm{QMMM}}^{1,\mathrm{el}} | \Psi_J^{(1),\mathrm{i}} \rangle + \langle \Psi^{(2),\mathrm{f}} | H_{\mathrm{QM}}^2 + H_{\mathrm{QMMM}}^{2,\mathrm{el}} | \Psi^{(2),\mathrm{f}} \rangle \\ &\quad - \langle \Psi^{(2),\mathrm{f}} | V_{\mathrm{ES}}[\Psi_J^{(1),\mathrm{i}}] | \Psi^{(2),\mathrm{f}} \rangle + \sum_n^{\mathrm{QM2}} Z_n V_{\mathrm{ES}}[\Psi_J^{(1),\mathrm{i}}] \\ &\quad + H_{\mathrm{QMMM}}^{1,\mathrm{b+vdW}} + H_{\mathrm{QMMM}}^{2,\mathrm{b+vdW}} + H_{\mathrm{MM}} \,. \end{aligned} \tag{6.10}$$

Variation of this energy with respect to $\Psi^{(2),\mathrm{f}}$ yields

$$\left\{ H_{\mathrm{QM}}^2 + H_{\mathrm{QMMM}}^{2,\mathrm{el}} - V_{\mathrm{ES}}[\Psi_J^{(1),\mathrm{i}}] \right\} |\Psi^{(2),\mathrm{f}}\rangle = \varepsilon_{\mathrm{QM2}}^{\mathrm{f}} |\Psi^{(2),\mathrm{f}}\rangle \,. \tag{6.11}$$

Employing eq 6.4, 6.9, and 6.11, eq 6.10 can be written[1]

$$\begin{aligned} E^{\mathrm{f}} &= E_{\mathrm{QM1},J}^{\mathrm{i}} + E_{\mathrm{QM2}}^{\mathrm{f}} + \langle \Psi^{(2),\mathrm{i}} | V_{\mathrm{ES}}[\Psi_J^{(1),\mathrm{i}}] | \Psi^{(2),\mathrm{i}} \rangle - \sum_n^{\mathrm{QM2}} Z_n V_{\mathrm{ES}}[\Psi_J^{(1),\mathrm{i}}] \\ &\quad + H_{\mathrm{QMMM}}^{1,\mathrm{b+vdW}} + H_{\mathrm{QMMM}}^{2,\mathrm{b+vdW}} + H_{\mathrm{MM}} \,. \end{aligned} \tag{6.12}$$

This leads to the following expression for the transition energy of approach (ii):

$$\Delta E_{IJ}^{(\mathrm{ii})} = \Delta E_{IJ}^{\mathrm{QM1}} + \Delta E_{IJ}^{\mathrm{pol(ii)}} \tag{6.13}$$

$$\begin{aligned} \Delta E_{IJ}^{\mathrm{QM1}} &= E_{\mathrm{QM1},J}^{\mathrm{i}} - E_{\mathrm{QM1},I}^{\mathrm{i}} \\ \Delta E_{IJ}^{\mathrm{pol(ii)}} &= E_{\mathrm{QM2}}^{\mathrm{f}} - E_{\mathrm{QM2}}^{\mathrm{i}} \\ &\quad + \langle \Psi^{(2),\mathrm{i}} | V_{\mathrm{ES}}[\Psi_J^{(1),\mathrm{i}}] - V_{\mathrm{ES}}[\Psi_I^{(1),\mathrm{i}}] | \Psi^{(2),\mathrm{i}} \rangle \\ &\quad - \sum_n^{\mathrm{QM2}} Z_n \left(V_{\mathrm{ES}}[\Psi_J^{(1),\mathrm{i}}] - V_{\mathrm{ES}}[\Psi_I^{(1),\mathrm{i}}] \right) \,. \end{aligned} \tag{6.14}$$

The polarization energy $\Delta E_{IJ}^{\mathrm{pol(ii)}}$ represents the energy gain when relaxing adiabatically the QM2 density from the initial state (adapted to $\Psi_I^{(1),\mathrm{i}}$) to the final state (adapted to $\Psi_J^{(1),\mathrm{i}}$) in the presence of the QM1 system in state $\Psi_J^{(1),\mathrm{i}}$. This is obtained by taking the total-energy difference of the two QM2 calculations (first two terms in 6.14) and correcting it for the altered QM1–QM2 Coulomb interaction of the constrained initial state.

If the methods used for the QM1 and the QM2 subsystem provide total energies that are fully variational w.r.t. to their own parameter spaces, then approach (ii) can be used to obtain an upper and a lower bound for the approach (i) excitation energy: If the ground state is chosen as the fully-relaxed initial state, then $\Delta E^{(\mathrm{ii})} \geq \Delta E^{(\mathrm{i})}$, and if the excited state is chosen as the initial state, $\Delta \widetilde{E}^{(\mathrm{ii})} \leq \Delta E^{(\mathrm{i})}$ (see Figure 6.1).

The calculation of $\Delta E^{(\mathrm{i})}$ requires the QM1 ground-state energy difference between the two calculations with QM2 being ground-state or excited-state polarized. This

[1] Here, the QM1 and QM2 total energies $E_{\mathrm{QM1},J}^{\mathrm{i}}$, $E_{\mathrm{QM2}}^{\mathrm{i}}$, and $E_{\mathrm{QM2}}^{\mathrm{f}}$ are defined as in eq 6.7.

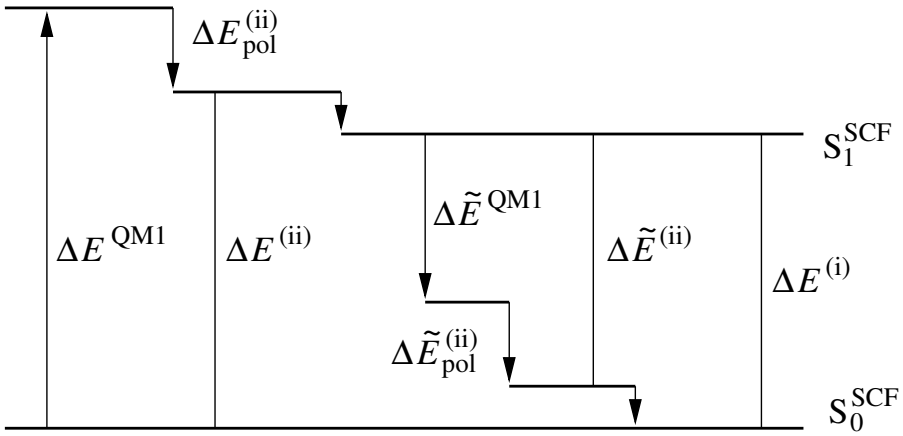

Figure 6.1: Scheme of the states and transition energies defined in the text. When the charge density in a subsystem is constrained to the initial state, arrows point from the initial to the final state, i.e., in the direction in which the constraints are applied or released.

total energy difference must be calculated with the same accuracy as the vertical excitation energies. Both MRCI variants, however, are predominantly designed to yield accurate excitation energies rather than absolute energies. Fluctuations in the total energy can arise when changing the electrostatic environment. In the case of SORCI, these are caused by changes in the reference and the restriction of the FOIS to a difference-dedicated CI with three degrees of freedom (DDCI3). Also in the GUGA implementation of OM2/MRCI, the effective FOIS can change due to the limitation to 30 non-frozen orbitals, whose character may change with the electrostatic environment. For this orbital window, excitation energies are sufficiently converged whereas total energies are not.

To overcome these problems, the ground-state energy of SORCI is substituted by the corresponding CISD energy. The ORCA CISD calculation spans the full set of canonical valence orbitals and uses the same perturbation treatment for weakly interacting configurations with the same perturbation selection threshold ($T_{\mathrm{Sel}} = 10^{-6}\ \mathrm{E_h}$) as used in the SORCI calculation. In the case of GUGACI, a full-valence CISD calculation is not feasible, and calculations with orbital windows including up to 72 orbitals still shows fluctuations in the total-energy difference in some cases. Hence, in the applications, only $\Delta E^{(\mathrm{ii})}$ excitation energies are considered for OM2/MRCI, for which no total energy differences are required.

For the calculation of the Coulomb interaction energy, eq 6.4, it is convenient to map the ESP's V^1_{ES} and V^2_{ES} onto some set of point charges, as quantum chemical programs usually do not support the definition of external potentials on a grid. In the implementation, the RESP program[287] is used to fit atom-centered point charges to reproduce the ESP of one QM zone in the range of the other. For the mapping of V^1_{ES}, e.g., a grid is generated which fills the volume inside overlapping spheres of 1–1.5 Å radius around the QM2 atoms, excluding points within 1.4 Å of the QM1 atoms. As a useful measure for the error of the mapping, the numerical difference between left- and right-hand side of eq 6.4 can be considered. In the calculations presented below, this difference is very systematic and affects the excitation energies by less than 0.005 eV. Test calculations have shown that Mulliken and Löwdin charges, which may be well justified for representing the charge distribution of semiempirical methods,

are insufficient at the *ab initio* level of theory.

For the communication between the different QM codes, the calculation of resp charges, the analysis of the output, and the control of the iterative calculation, an interface was written, which currently supports SCC-DFTB (NG branch), MNDO99, Turbomole, and ORCA.

6.3 Atomic Polarization Models for Peptides

The QM/QM/MM model developed in the last section has obvious limitations: When the QM2 region is treated at an *ab initio* level, a severe compromise between basis-set convergency and size of the polarizable QM2 zone must be made. But even at the semiempirical level, linear-scaling techniques must to be applied to realize a QM2 zone that is large enough to obtain a converged electrostatics in the active QM1 region. Moreover, when the QM2 charge density is mapped onto charges at atomic sites, out-of-plane polarization can be rendered only via inter-molecular charge-relocations, which is possible only if the QM2 layer is sufficiently thick. Therefore, empirical polarization models are more appropriate to achieve an accurate and efficient description of polarization in the protein environment of the active region.

As discussed in section 4.2, atomic induced-dipole models are very attractive for this task, because they can accurately reproduce experimental polarizability tensors of organic molecules with a small set of parameters. In this section, the transferability of such models to peptides will be investigated taking Thole's interactive isotropic polarization model[159] as a representative example. Special attention is paid to the anisotropy of aromatic amino acid side chains, which exist in the hydrophobic binding pocket of rhodopsins and are likely to influence the ESP at the chromophore with their high polarizability.

6.3.1 Revisiting Thole's Interactive Model

Thole's polarization models feature a short-range damping scheme that follows physical intuition: The Coulomb interaction between two multipoles is modified by replacing the constituting point charges of one multipole by a spherical charge distribution ρ. From the different variants of Thole's damping models, the same exponential charge distribution ρ is chosen here that has been adopted also into the AMOEBA FF:[140,168]

$$\rho = \frac{3a}{4\pi} \exp\left(-au^3\right) , \tag{6.15}$$

where a is a dimensionless damping parameter and $u = R_{AB}/(\alpha_A \alpha_B)^{1/6}$ an effective distance normalized using the atomic polarizabilities α_A and α_B of the two interacting centers.

The dipole at atom A is induced by the field ξ_A of permanent charges q_B and in-

duced dipoles μ_B of other sites corresponding to its isotropic polarizability α_A:[2]

$$\begin{aligned} \mu_A &= \alpha_A \left(\xi_A^{\text{perm}} + \xi_A^{\text{ind}} \right) \\ &= \alpha_A \left(\sum_B \underline{\mathbf{T}}_{AB} q_B + \sum_C \underline{\underline{\mathbf{T}}}_{AC} \mu_C \right) . \end{aligned} \tag{6.16}$$

The first- and second-rank interaction tensors, $\underline{\mathbf{T}}$ and $\underline{\underline{\mathbf{T}}}$, mediate the damped Coulomb interaction between a point multipole and a multipole composed of the smeared charge distributions ρ (eq 6.15), their spatial components ($\alpha = x, y, z$) are given by:[140]

$$\begin{aligned} T_{AB}^{\alpha} &= -\lambda_3 \frac{R_{AB}^{\alpha}}{R_{AB}^3} \\ T_{AB}^{\alpha\beta} &= \nabla_\beta T_{AB}^{\alpha} = \lambda_5 \frac{3 R_{AB}^{\alpha} R_{AB}^{\beta}}{R_{AB}^5} - \lambda_3 \frac{\delta_{\alpha\beta}}{R_{AB}^3} , \end{aligned} \tag{6.17}$$

with the damping coefficients

$$\lambda_3 = 1 - \exp(-au^3) \tag{6.18}$$

$$\lambda_5 = 1 - (1 + au^3) \exp(-au^3) \tag{6.19}$$

Eq 6.16 can be derived by applying the variational principle to the following energy expression:[159]

$$\begin{aligned} E^{\text{pol}} &= -\sum_A \mu_A \cdot \xi_A^{\text{perm}} - \frac{1}{2} \sum_{A,B} \mu_B \underline{\underline{\mathbf{T}}}_{AB} \mu_A \\ &\quad + \frac{1}{2} \sum_A \frac{|\mu_A|^2}{\alpha_A} . \end{aligned} \tag{6.20}$$

Using eq 6.16 in eq 6.20 yields the simple (non-variational) form of the polarization (induction) energy

$$E^{\text{pol}} = -\frac{1}{2} \sum_A \mu_A \cdot \xi_A^{\text{perm}} . \tag{6.21}$$

For small systems, the induced dipoles can be calculated by matrix inversion[289]

$$\mu = \left(\underline{\underline{\alpha}}^{-1} - \underline{\underline{\mathbf{T}}} \right)^{-1} \xi^{\text{perm}} , \tag{6.22}$$

whereas for larger systems, an iterative solution of eq 6.16 is more efficient. The number of iterations needed to achieve self-consistent dipoles depends on the damping.

[2]Note, that $R_{AB}^{\alpha}, (\alpha = x, y, z)$ is defined here as $R_B^{\alpha} - R_A^{\alpha}$. Some publications[288,289] use a different sign convention, resulting in an opposite sign in $\underline{\mathbf{T}}_{AB}$.

6.3.2 A Polarization-free Charge Model for Peptides

As the polarization model describes only the linear response to external fields, it can be parameterized independently from the representation of the permanent (fixed) charge distribution. The latter, on the contrary, must be conform with the polarization model to avoid double counting of polarization and yield the correct gas phase charge distribution. For the permanent charge distribution, ESP derived point charges are chosen, which can easily be employed in existing FF programs and QM/MM schemes. This requires a division of the peptides into groups suitable for fitting to *ab initio* ESP's, minimizing conformational variance and avoiding buried atoms. In multipole models of the permanent charge distribution, the induced moments can be subtracted from the total moments during the fitting of the permanent moments.[152,168] In the case of a point charge model, it is more suitable to exclude induced dipoles in the fit of the permanent charges. Then the interaction between permanent charges and induced dipoles within each group must be omitted also in the application of the polarization model. Ren and Ponder have shown that also in a multipole model, the use of polarization groups can be advantageous over all-atom intramolecular polarization, and suggested to define groups with little conformational flexibilities and small net charges.[168] Here, AA side chains and backbone fragments are chosen as groups which are parameterized independently. The mutual polarization of the groups via fixed point charges and induced dipoles is modeled corresponding to eq 6.16.

For the fitting of the permanent charges for side chains and backbone, a similar strategy is followed here as used in the AMBER ff02 parameterization[142]: A multi-stage restraint electrostatic potential (RESP)[287] fit to B3LYP/6-311G(2d,2p) gas-phase calculations is performed using the RESP program.[287] No diffuse functions are added to the basis set, in order to mimic the confining effect of Pauli repulsion on the density in a condensed-phase environment. In a first stage fit, weak hyperbolic charge restraints are set on all non-hydrogen atoms. In a second stage fit, the charges of polar groups are frozen, while a stronger restraint is set on the non-polar groups, and equivalent hydrogens are constraint to identical charges. Finally, the link atom charge is summed into its host atom.

For the backbone charges, multiconfigurational fits for different peptide models resulted in charges that were almost identical to the CHARMM charges. Therefore, the original CHARMM backbone charges are adopted in this model.

6.3.3 Parametrization for Peptides

In a first parameterization of the model, referred to as "polar.t", Thole's original parameters for damping ($a = 0.572$) and polarizabilities for the elements H, C, O, and N are used, which were fitted to the 48 experimental polarizability components of 16 molecules. These parameters are completed with an atomic polarizability for sulfur, which is fitted to reproduce the MP2/cc-pVQZ mean polarizabilities of the Cys and Met side chains. In a second parameterization, "polar.t", the stronger damping ($a = 0.39$) proposed by Ren and Ponder[140] and Burnham *et al.* was employed.[146] Following their argument, polarization energies are more sensitive to a than the molecular polarizabilities, and hence they fitted a to water-cluster energies. This fit may depend to some exten on their chosen partial charges and FF parameters and may not

Table 6.1: RESP Charge Model

Arg	
CB	-0.091259
HB1	0.058981
HB2	0.058981
CG	0.082165
HG1	0.030309
HG2	0.030309
CD	0.067198
HD1	0.059947
HD2	0.059947
NE	-0.546562
HE	0.313712
CZ	0.882852
NH1	-0.878518
HH11	0.437614
HH12	0.437614
NH2	-0.878518
HH21	0.437614
HH22	0.437614
Asn	
CB	-0.237659
HB1	0.087965
HB2	0.087965
CG	0.764005
OD1	-0.567382
ND2	-0.890390
HD21	0.377748
HD22	0.377748
Asp	
CB	-0.184907
HB1	-0.025446
HB2	-0.025446
CG	0.768485
OD1	-0.766343
OD2	-0.766343
Asp (prot.)	
CB	-0.181861
HB1	0.094127
HB2	0.094127
CG	0.687815
OD1	-0.526744
OD2	-0.558211
HD2	0.390747
Cys	
CB	0.021971
HB1	0.058275
HB2	0.058275
SG	-0.304190
HG1	0.165669

Gln	
CB	-0.071849
HB1	0.027291
HB2	0.030597
CG	-0.029200
HG1	0.030597
HG2	0.030597
CD	0.645544
OE1	-0.560968
NE2	-0.828467
HE21	0.347412
HE22	0.378446
Glu	
CB	-0.014740
HB1	-0.049590
HB2	-0.049590
CG	0.114892
HG1	-0.091433
HG2	-0.091433
CD	0.662866
OE1	-0.740486
OE2	-0.740486
Glu (prot.)	
CB	-0.086897
HB1	0.038416
HB2	0.038416
CG	0.059269
HG1	0.013887
HG2	0.013887
CD	0.610456
OE1	-0.537332
OE2	-0.553740
HE2	0.403638
Ile	
CB	0.083042
HB	-0.034285
CG2	-0.113416
HG21	0.021553
HG22	0.021553
HG23	0.021553
CG1	0.117328
HG11	-0.034285
HG12	-0.034285
CD	-0.113417
HD1	0.021553
HD2	0.021553
HD3	0.021553

Leu	
CB	-0.241614
HB1	0.055079
HB2	0.055079
CG	0.482057
HG	-0.088579
CD1	-0.294481
HD11	0.054490
HD12	0.054490
HD13	0.054490
CD2	-0.294481
HD21	0.054490
HD22	0.054490
HD23	0.054490
Lys	
CB	-0.091267
HB1	0.055870
HB2	0.055870
CG	0.123006
HG1	0.002773
HG2	0.002773
CD	-0.121724
HD1	0.057483
HD2	0.057483
CE	0.094388
HE1	0.085525
HE2	0.085525
NZ	-0.433444
HZ1	0.341913
HZ2	0.341913
HZ3	0.341913
Met	
CB	0.014040
HB1	0.013682
HB2	0.013682
CG	0.051640
HG1	0.024059
HG2	0.024059
SD	-0.276451
CE	0.014473
HE1	0.040272
HE2	0.040272
HE3	0.040272

Phe	
CB	-0.153711
HB1	0.059959
HB2	0.059959
CG	0.201608
CD1	-0.202142
HD1	0.106824
CE1	-0.053166
HE1	0.080578
CZ	-0.119109
HZ	0.087106
CD2	-0.202142
HD2	0.106824
CE2	-0.053166
HE2	0.080578
Ser	
CB	0.160706
HB1	0.012394
HB2	0.012394
OG	-0.508922
HG1	0.323428
Thr	
CB	0.345872
HB	-0.030639
OG1	-0.578925
HG1	0.340240
CG2	-0.228528
HG21	0.050660
HG22	0.050660
HG23	0.050660
Trp	
CB	0.067293
HB1	-0.005378
HB2	-0.005378
CG	-0.108368
CD1	-0.128934
HD1	0.152212
NE1	-0.403386
HE1	0.340902
CE2	0.194085
CD2	0.116714
CE3	-0.204382
HE3	0.125009
CZ3	-0.121452
HZ3	0.086155
CZ2	-0.227737
HZ2	0.113620
CH2	-0.075155
HH2	0.084180

Tyr	
CB	-0.137471
HB1	0.054141
HB2	0.054141
CG	0.146392
CD1	-0.168924
HD1	0.116950
CE1	-0.204959
HE1	0.135950
CZ	0.284942
OH	-0.455788
HH	0.323678
CD2	-0.168924
HD2	0.106542
CE2	-0.204959
HE2	0.118289
Val	
CB	0.219820
HB	-0.053736
CG1	-0.201518
HG11	0.039492
HG12	0.039492
HG13	0.039492
CG2	-0.201518
HG21	0.039492
HG22	0.039492
HG23	0.039492
water	
OH2	-0.674280
H1	0.337140
H2	0.337140

The atom names follow the default CHARMM nomenclature.

Table 6.2: Polarizability (Å^3) and Damping Parameters

parameter	polar.t	polar.h	polar.h[a]	fitting set
$\alpha(\mathrm{H})$	0.496	0.496	0.496	Ref.[159]
$\alpha(\mathrm{C})$	1.334	1.334	1.334	Ref.[159]
$\alpha(\mathrm{C_{sp2}})$	—	1.897	1.720	Trp, Tyr, Phe
$\alpha(\mathrm{N})$	1.073	1.073	1.073	Ref.[159]
$\alpha(\mathrm{O})$	0.837	0.837	0.837	Ref.[159]
$\alpha(\mathrm{S})$	2.368	2.877	2.440	Cys, Met
a	0.572	0.390	0.390	Refs.[140,159]

[a] Fitting to MP2/cc-pVTZ instead of MP2/cc-pVQZ.

be the optimum for other systems. However, as will be shown below, the combination of stronger damping with Thole's original polarizabilities results in too small polarizabilities for aromatic and sulfur-containing AA side chains, while other side chains are represented well. Indeed, the performance of Thole's original parameters can easily be surpassed by re-fitting merely the polarizabilities for sulfur and sp2-hybridized carbon atoms. Therefore, an alternative parameter set, "polar.h", is defined with the stronger damping (see Table 6.2), to test the influence of the damping parameter on the final results.

6.3.4 The QM/polar Interface

The QM/MM integration and application to multi-state problems requires further considerations, some of which have been treated already in the context of the QM/QM/MM scheme: The two approaches for the calculation of excitation energies (section 6.2) can be adopted here. The QM2 zone is replaced by a polarizable MM zone, which will in most cases span the entire protein. The self-consistent charge distributions for the ground and excited states must be obtained iteratively. In ground-state SCF calculations, the induced moments of the polarizable MM zone can in principle be determined in each SCF cycle to reduce the computational cost.[199] For excited-state calculations based on small CI expansions, the polarization energy can be calculated for each configuration before diagonalizing the CI matrix. This however, will only be efficient if the polarization response can be integrated efficiently in the calculation of the configuration energies and the off-diagonal corrections are neglected. On the other hand, practical experience shows that a self-consistent charge distribution is already achieved within some 3–5 iterations.

In the applications presented below, the QM density is mapped onto atomic point charges, using the same RESP-fit approach as for the QM/QM/MM scheme. The MM permanent charges Q_{perm} and induced dipoles μ_{ind} are represented by a pair of point charges

$$q_1 + q_2 = Q_{\mathrm{perm}}\,, \quad \mu_{\mathrm{ind}} = (q_1 - q_2)R_{12}\,, \quad \|R_{12}\| = d\,, \tag{6.23}$$

centered at the host atom with a fixed distance of $d = 0.1$ Å. The grid points for the RESP fit of the QM charges include the positions of these MM charges and their host atoms. To enhance the numeric stability of the fit, additional grid points within a 0.2 Å sphere around all polarizable MM atoms are added. The ESP values at the host atoms

and dipole charge pairs are used to calculate the exact Coulomb interaction between the permanent or induced moments and the QM charge density.

It is not obvious, how charges and polarizabilities at the QM/MM frontier should best be treated. The ideal link scheme should pursue three aims: (1) exclude over-polarization of the frontier atoms (2) obtain a meaningful charge distribution in the border region and, (3) minimize modifications to the RESP charges and induced MM moments,[3] so that both the QM and the polarization-model Hamiltonian contain the same QM/MM Coulomb interaction energy. The first two points apply also to conventional QM/MM applications. The last point is important to preserve a variational total energy and yield reliable excitation energies. Link-atom schemes for conventional QM/MM applications can be adopted, such as the excluded group (EXGR)[176] or the divided frontier charge (DIV) scheme[218]. In the DIV scheme, which is also used in this work, the charge of the MM frontier atom is deleted and redistributed among the remainder of its host group. In addition, the polarizability of the MM frontier atom must be deleted to avoid artificially large induced dipoles on the MM frontier atom. The latter is also limited by the short-range damping of the polarization model, but the MM frontier atom would still be polarized by the permanent MM charges, and the induced dipole would strongly interact with the QM charge density. Further, the density–dipole interaction will deviate from the damped interaction between the dipole and the RESP fitted point charges, in disaccord with aim (3). To avoid these problems, independent of the applied short-range damping scheme/parameter, the polarizabilities of the entire MM host group are set to zero and the coordinate of the MM frontier atom is excluded from the list of grid points for the RESP fit. In case of a link atom between C_β (QM frontier atom) and C_α (MM frontier atom), the MM host group is comprised of the H_α, N, and H_N backbone atoms.

6.3.5 Assessment

The polarization model provides two quantities: the MM contribution to the polarization energy and the self-consistent charge distribution of the MM moiety, which polarizes the QM fragment. In this section, the accuracy of the models regarding both quantities are evaluated by comparing polarizabilities, polarization energies, and ESP's to QM calculations with various methods, which are performed with Turbomole.[245]

Table 6.3 gives the calculated mean polarizabilities of all 17 AA side chains (except Ala and Gly) that are present in rhodopsins. The good agreement between the polarizabilities obtained with MP2 and the PBE0 hybrid-DFT functional (1.6% RMS deviation) indicates that these methods can be used as a reliable reference for the considered test systems. Note, that DFT in general overestimates polarizabilities and hyperpolarizabilities of extended conjugated systems.[290–293] For the aromatic residue side chains however, the hybrid functional PBE0 still yields accurate polarizabilities. More important than the QM method is the impact of the applied basis set. QM calculations in the basis-set limit are approximating gas-phase polarizabilities, and may not be appropriate as a reference or fitting target for a polarization model that shall describe condensed-phase systems. In fact, models parameterized to reproduce gas-phase data may cause over-polarization in condensed-phase simulations.[172,294] Using basis sets without diffuse augmentation is a pragmatic way to mimic the confining effect of intermolecular exchange repulsion, but it is unclear to which level the basis set should

[3] Also the permanent MM charges should be the same in both Hamiltonians.

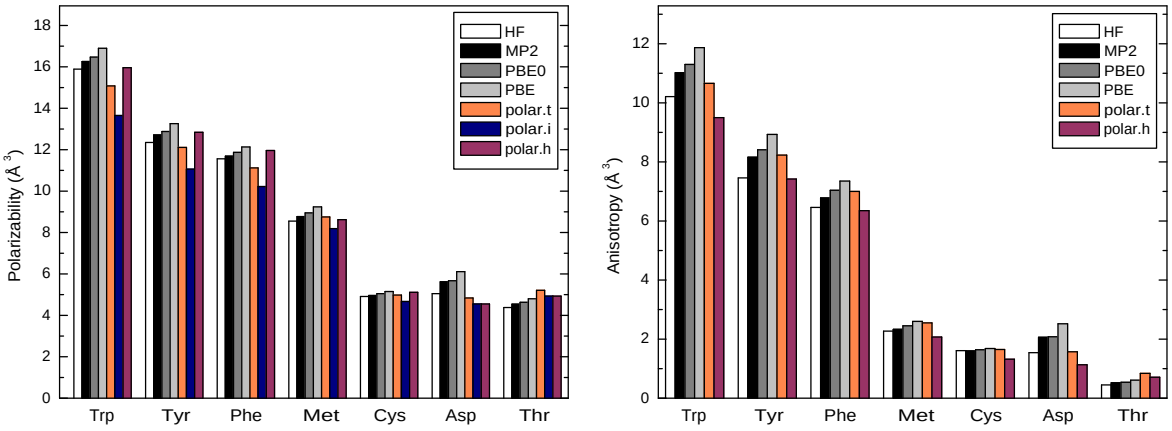

Figure 6.2: Mean polarizabilities (left) and anisotropies (right) of some AA side chains. For all QM methods, the employed basis set was cc-pVQZ. Results from the polarization model were obtained using Thole's original parameters (polar.t), our hybridization-dependent parameters (polar.h), and Thole's polarizabilities combined with $a = 0.39$ (polar.i).

be converged. As Table 6.3 shows, mean polarizabilities of AA side chains from MP2 calculations are almost 5% higher when using a cc-pVQZ basis set rather than a cc-pVTZ one. A first augmentation of the cc-pVQZ set with uncontracted [spdfg] diffuse functions leads to a further increase of 1.5–20% (see Table 6.4), depending on the AA. In the lack of an experimental reference, it is interesting to note that Thole used experimental data of small molecules in the gas phase and in solution and of pure liquids to fit polarizabilities and damping parameters. Hence, bulk polarizabilities may be slightly overestimated by his parameterization. In fact, the polar.t polarizabilities for the 17 AA side chains are in average 3.3% larger than the MP2/cc-pVQZ results, which indicates that this basis set is suitable for reference calculations.

When the damping is increased by reducing the parameter to $a = 0.39$ (without changing the other parameters of the polar.t model), the polarizabilities are significantly lowered (see "polar.i" data in Table 6.3 and Figure 6.2), and particularly the polarizabilities of the aromatic residues are severely underestimated. The hybridization-dependent polar.h model, using the same damping, does not deviate systematically from the MP2/cc-pVQZ results. When the sulfur and sp2-carbon parameters are fitted against MP2/cc-pVTZ, the polarizabilities are lowered by 1.4%, in average, as compared with the MP2/cc-pVQZ fit.

The general agreement of both parameterizations with the MP2 or PBE0 results is surprisingly good. The mean relative RMS deviation from MP2 (17 AA side chains) is 9.5% for polar.t and 7.3% for polar.h, which is close to the *ab initio* fit of van Duijnen and Swart[288] (6%) to 58 molecules using different Thole damping schemes. The largest deviations occur for the cations Lys and Arg, whose mean polarizabilities are overestimated (polar.h: +12% and +6%, respectively) and for anions Asp and Glu with the error on the opposite side (up to -19% for polar.h). This is clearly an effect of the different charge states rather than poor nitrogen or oxygen parameters (Ser and

Table 6.3: Mean Polarizabilities of AA Side Chains (Å^3).

AA	HF	MP2	MP2[a]	PBE0	PBE	pol.t	pol.i	pol.h	pol.h[a]
Arg	9.94	10.59	10.27	10.63	11.00	12.16	11.24	11.24	11.24
Asn	5.10	5.47	5.17	5.51	5.77	5.75	5.40	5.40	5.40
Asp	5.05	5.62	5.07	5.67	6.11	4.84	4.55	4.55	4.55
Cys	4.91	4.96	4.60	5.05	5.15	4.98	4.67	5.11	4.73
Gln	6.84	7.30	6.96	7.36	7.68	7.70	7.19	7.19	7.19
Glu	6.82	7.49	6.91	7.58	8.14	6.82	6.34	6.34	6.34
Ile	7.52	7.73	7.57	7.90	8.16	8.26	7.76	7.76	7.76
Leu	7.54	7.77	7.55	7.96	8.23	8.24	7.75	7.75	7.75
Lys	8.15	8.42	8.27	8.58	8.87	10.13	9.45	9.45	9.45
Met	8.55	8.77	8.36	8.95	9.24	8.75	8.19	8.62	8.25
Phe	11.56	11.69	11.22	11.87	12.13	11.12	10.22	11.96	11.43
Pro	9.60	10.12	9.74	10.30	10.82	10.73	9.94	9.94	9.94
Ser	2.84	2.95	2.77	2.99	3.10	3.36	3.20	3.20	3.20
Thr	4.54	4.74	4.54	4.84	5.04	5.21	4.93	4.93	4.93
Trp	15.89	16.26	15.54	16.47	16.90	15.08	13.65	15.96	15.26
Tyr	12.35	12.71	12.15	12.88	13.26	12.11	11.06	12.84	12.30
Val	5.81	5.96	5.82	6.09	6.29	6.38	6.01	6.01	6.01
RMSD[b] MP2	5.0	0.0	5.1	1.6	5.7	9.5	9.5	7.3	7.6
RMSD[b] MP2[a]	2.4	5.4	0.0	6.8	11.3	11.5	8.2	7.9	7.1
MSD[c] MP2	-4.3	0.0	-4.6	1.5	5.5	3.3	-3.6	-0.3	-1.7
MSD[c] MP2[a]	0.4	4.9	0.0	6.5	10.7	8.2	1.0	4.5	3.0

QM results (without footnote) were obtained with the cc-pVQZ basis set. The polarization model was applied using Thole's original parameters (pol.t), Thole's polarizabilities combined with $a = 0.39$ (pol.i), and our hybridization-dependent parameters (pol.h). [a] MP2/cc-pVTZ data or fit (pol.h). [b] RMS relative deviation (%). [c] Mean (signed) relative deviation (%).

Thr polarizabilities are overestimated) and hence a principal limitation of the model. The obvious solution, to introduce charge-dependent polarizabilities, has been implemented recently, by Giese and York.[295] Excluding the charged AA, the relative RMSD from MP2/cc-pVQZ drops to 6.9% and 3.0% for polar.t and polar.h, respectively. The latter error is even below the 3.8% deviation in Thole's original fitting and smaller than the (rather systematic) errors of HF or PBE.

As Figure 6.2 (right) shows, the two models reproduce also the anisotropy of molecular polarizabilities with remarkable agreement with the QM calculations. The dipole–dipole interactions correctly model the gain of in-plane polarization in the aromatic peptides. The signed mean deviations show that anisotropies are sensitive to the damping parameter: while they are 0.37 Å^3 too high in the polar.t model, they are underestimated by 0.21 Å^3 in polar.h. More important, the large anisotropies of the aromatic AA's are systematically underestimated, whereas they are overestimated for the saturated side chains of Leu, Ile, Ser, and Thr. Here, apparently, is space for improvement of the damping scheme, although the accuracy achieved by both models is more than sufficient for the purpose of this study.

Table 6.4: Basis Set Convergence: Polarizabilities and Anisotropies (Å^3) of Different Side Chains

		Thr		Val		Leu	
	basis set	α (MP2)	α (PBE0)	α (MP2)	α (PBE0)	α (MP2)	α (PBE0)
A	6-31G*	25.69	26.39	32.90	33.92	43.06	44.53
B	cc-pVTZ	30.69	31.26	39.28	39.92	50.98	52.24
C	cc-pVQZ	32.02	32.64	40.22	41.12	52.39	53.70
D	aug-cc-pVTZ	33.55	34.12	41.19	42.02	53.52	54.67
E	aug-cc-pVQZ	33.35	34.14	40.81	42.02	53.45	54.66
	C/B	1.043	1.044	1.024	1.030	1.028	1.028
	E/C	1.042	1.046	1.015	1.022	1.020	1.018
	C/A	1.246	1.237	1.222	1.212	1.217	1.206

To assess the performance of the presented polarization models for polypeptides, in which cooperative effects may occur, the polarizability tensor of a protein fragment, the retinal binding pocket in bR, has been calculated. It contains the 24 side chains and three waters within 4 Å of the chromophore. QM calculations at the PBE0/6-31G* level shall serve as a reference. To consider the effect of the unconverged basis set, a simple scaling factor can be derived from the gas-phase polarizabilities of the AA (see Table 6.4):

$$f = 1/24 \sum_i \alpha_i^{\mathrm{cc-pVQZ}} / \alpha_{\mathrm{i}}^{6-31\mathrm{G}^*} , \tag{6.24}$$

where the sum is over all 24 AA in the bR binding pocket model. The scaled value can be considered as an upper bound because of the basis set superposition present in the binding pocket QM calculation. The results of both models for the polarizability components (Table 6.6) are in between the unscaled and the scaled PBE0 values and slightly closer to the latter. This result is encouraging as it does not indicates any severe over-polarization of the models in the protein environment. As for the individual side chains, the anisotropy is underestimated, but also here, basis-set superposition effects might cause the scaled QM anisotropies to be overestimated.

The polarization energies $E_{\mathrm{pol}}^{\mathrm{MM}}$ obtained by the three polarization models are tested against *ab initio* data using a probe charge, which is arranged at different in-plane and out-of-plane positions around the test molecule. The cc-pVQZ basis set was employed. The polarization energy at *ab initio* level was obtained as

$$E_{\mathrm{pol}} = E_{\mathrm{tot}} - (E_{\mathrm{tot}}^{\mathrm{vac}} + E_{\mathrm{coul}}^{\mathrm{vac}}) , \tag{6.25}$$

where E_{tot} and $E_{\mathrm{tot}}^{\mathrm{vac}}$ are the total energy of the molecule in presence and absence of the probe charge, respectively, and $E_{\mathrm{coul}}^{\mathrm{vac}}$ is the Coulomb interaction between the unrelaxed QM density and the probe charge, which is evaluated as product of charge and ESP of the density (in vacuo) at the probe charge position. Figure 6.3 shows results for the side chains of Trp and Tyr. Both polar.t and polar.h agree closely with the PBE0/cc-pVQZ data, the out-of-plane arrangements show that the anisotropy of Tyr is accurately reproduced, while it is slightly underestimated for Trp. When the dipole–dipole interactions are neglected (polar.a), the lacking anisotropy causes large deviations from the QM data. The combination of a damping parameter $a = 0.39$

Table 6.5: Anisotropies of AA Side Chains (Å^3).

AA	HF	MP2	MP2[a]	PBE0	PBE	pol.t	pol.i	pol.h	pol.h[a]
Arg	4.24	5.00	5.00	5.09	5.47	6.79	5.22	5.22	5.22
Asn	1.71	2.04	2.09	2.07	2.30	2.35	1.75	1.75	1.75
Asp	1.54	2.06	1.88	2.08	2.52	1.57	1.13	1.13	1.13
Cys	1.61	1.60	1.77	1.64	1.68	1.65	1.15	1.32	1.17
Gln	1.68	2.05	2.07	2.12	2.39	2.60	1.95	1.95	1.95
Glu	1.77	2.37	2.20	2.42	2.97	2.18	1.60	1.60	1.60
Ile	1.08	1.17	1.16	1.26	1.34	1.81	1.47	1.47	1.47
Leu	0.84	0.94	0.87	1.00	1.07	1.40	1.19	1.19	1.19
Lys	2.12	2.43	2.36	2.60	2.87	3.90	3.14	3.14	3.14
Met	2.27	2.33	2.48	2.45	2.60	2.55	1.89	2.07	1.92
Phe	6.46	6.78	7.30	7.04	7.35	7.00	5.19	6.35	6.01
Pro	2.36	2.50	2.41	2.71	3.04	2.92	2.22	2.22	2.22
Ser	0.49	0.50	0.51	0.50	0.51	0.91	0.66	0.66	0.66
Thr	0.45	0.52	0.49	0.54	0.61	0.84	0.71	0.71	0.71
Trp	10.21	11.02	11.48	11.30	11.87	10.66	7.79	9.50	9.01
Tyr	7.46	8.16	8.59	8.41	8.93	8.23	6.05	7.42	7.02
Val	0.82	0.91	0.88	0.98	1.05	1.35	1.11	1.11	1.11
RMSD[b] MP2	0.41	0.00	0.22	0.14	0.44	0.67	1.09	0.58	0.72
RMSD[b] MP2[a]	0.54	0.22	0.00	0.16	0.38	0.70	1.27	0.71	0.87
MSD[c] MP2	-0.31	0.00	0.07	0.11	0.36	0.37	-0.48	-0.21	-0.30
MSD[c] MP2[a]	-0.38	-0.07	0.00	0.04	0.30	0.30	-0.55	-0.28	-0.37

QM results (without footnote) were obtained with the cc-pVQZ basis set. The polarization model was applied using Thole's original parameters (pol.t), Thole's polarizabilities combined with $a = 0.39$ (pol.i), and our hybridization-dependent parameters (pol.h). [a] MP2/cc-pVTZ data or fit (pol.h). [b] RMS deviation. [c] Mean (signed) deviation.

Table 6.6: Polarizability of the Binding Pocket of bR (Å^3)

method	α_{xx}	α_{yy}	α_{zz}	$\frac{1}{3}\mathrm{tr}(\mathrm{ff})$	anisotropy
HF	169.0	188.0	162.7	173.3	43.3
PBE0	177.8	197.3	170.9	182.0	47.3
PBE	183.3	203.6	176.4	187.8	50.3
polar.t	204.5	223.5	201.0	209.7	45.6
polar.h	203.2	220.0	202.0	208.4	42.2
polar.h[a]	198.1	214.4	197.2	203.2	39.9
scaled PBE0[b]	218.5	242.4	210.0	223.6	58.1

For all QM methods, the employed basis set was 6-31G* (see text). The polarization model was applied using Thole's original parameters (polar.t) and our hybridization-dependent parameters (polar.h). [a] $\alpha(\mathrm{C_{sp2}})$, α(S) fitted to MP2/cc-pVTZ instead of MP2/cc-pVQZ. [b] Simple extrapolation to PBE0/cc-pVQZ (see text).

and Thole's original polarizabilities (polar.i) systematically underestimates the polar-

ization energy of both AA.

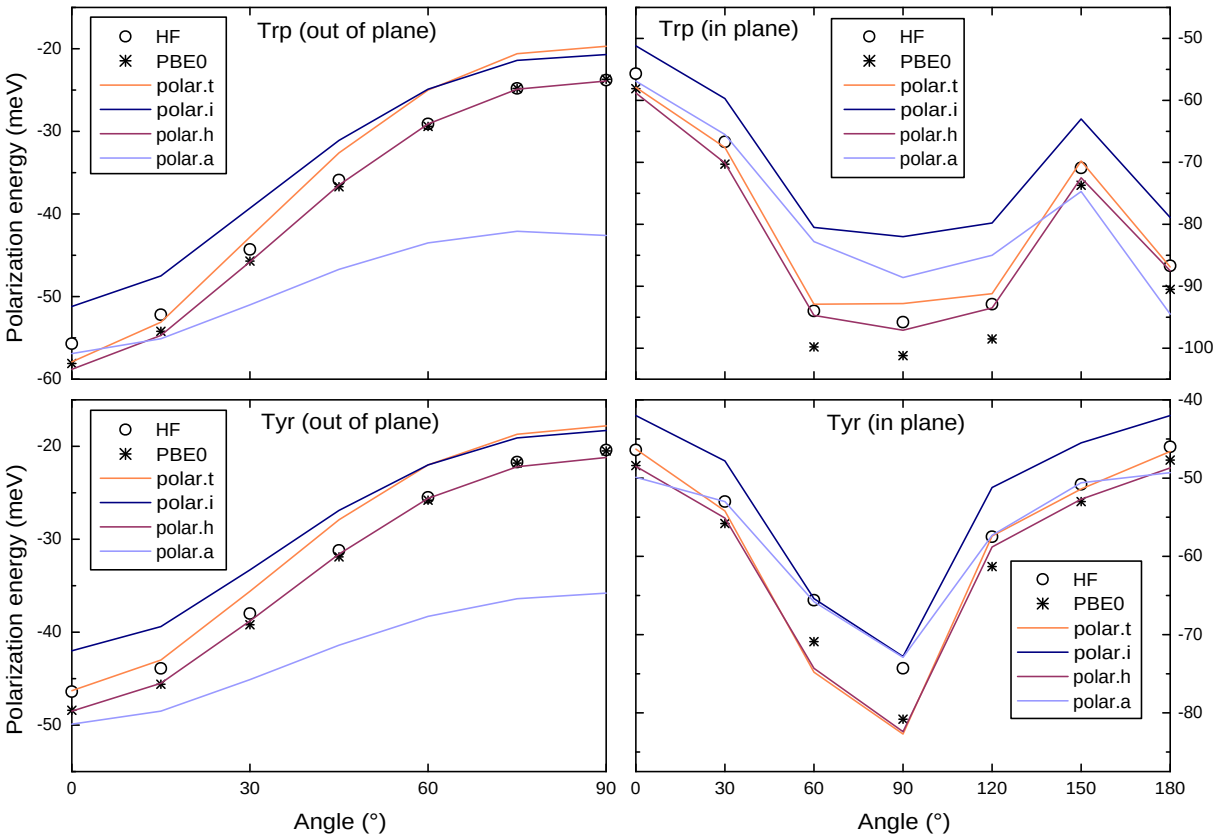

Figure 6.3: Polarization energy with respect to position of probe charge for Trp (upper) and Tyr (lower). Left: out-of-plane angle, right: in-plane orientational angle. QM calculations employed the cc-pVQZ basis set. The polarization model was applied using Thole's original parameters (polar.t), the hybridization-dependent parameters (polar.h), and Thole's polarizabilities combined with $a = 0.39$ (polar.i) and $a = 0$ (polar.a), which corresponds to an additive model).

6.4 Computational Details

The general computational strategy and the choice of QM methods for structure generation and excited-state calculations was developed and justified in chapter 5. The QM/QM/MM and QM/polar schemes introduced above are applied to the same QM/MM structural models as used in Refs.[280,296] Excitation energies and charge distribution of the QM (or QM1) region, in its ground and excited states, were obtained using the *ab initio* SORCI method[115] included in the ORCA program package[297] and the semiempirical OM2/MRCI method.[121]

In the QM/QM/MM models, the QM2 regions contain the side chains of all amino acids with at least one atom within 4 Å of any QM1 atom, excluding proline. This results in 27 side chains (301 atoms) in the bR and 25 side chains (283 atoms) in the psRII QM2 zone. The QM2 electron density is calculated with Turbomole[245] using the PBE0 functional[47,298] and the SV(P) basis set.[240]

The QM1 and QM2 charges, where required, were obtained as RESP[287] charges from the corresponding QM density (SORCI, DFT), as described above, or as Mulliken charges (OM2/MRCI). The optimal parameters and thresholds for the CI calculations were determined in benchmark calculations (chapters 5 and 5). From the improved virtual orbitals, the π MO's were manually selected to define the reference space for the MRDDCI2 calculation, whose NO's are used in the SORCI calculation. In the SORCI calculations, only core orbitals are frozen. The OM2/MRCISD calculations use the full first-order interaction space (FOIS) within a window of 15 occupied and 15 virtual non-frozen orbitals, and no configuration selection is used.

The models of Rh, bR, and psRII, are based on the X-ray crystallographic structures of Okada *et al.*[299] (PDB code 1U19), Luecke *et al.*[249] (PDB code 1C3W), and Royant *et al.*[300] (PDB code 1H68), respectively. Default protonation states were assumed except for Asp96, Asp115, and Glu204 in bR, which were protonated, as were Asp83 and Glu122 in Rh. Based on the published experimental and theoretical evidence, the protonation state of Glu181 in Rh cannot be determined with certainty (see discussion in Ref.[296]). Therefore, two different Rh models are employed which are both consistent with the 1U19 structure and other experimental data. The Rh(u) and Rh(p) models assume Glu181 to be unprotonated and protonated, respectively, and differ in the orientation of Ser186 and in the adjacent hydrogen-bonded network. QM/MM molecular dynamics, simulated annealing, and subsequent geometry optimization have been carried out using SCC-DFTB (mio parameter set)[88] for the QM1 region. The latter contains the chromophore and the Lys side chain to which it is covalently bound. At the QM/MM frontier between C_α and C_β of the Lys residue, the QM region is saturated by a hydrogen link atom, the MM charges at the frontier are modified corresponding to the divided frontier charge (DIV) scheme.[218]. The CHARMM27 FF[123] was employed for the remainder of the protein. All water molecules resolved in the crystal structure are included. The screening effect of bulk solvent on surface exposed charges was considered using the Poisson-Boltzmann (PB) charge-scaling scheme proposed by Dinner et al.[301] MM atoms with a distance greater than 14 Å (15 Å in the Rh setups) from the QM atoms were harmonically constrained to their crystallographic positions. In the bR and psRII setups, only C_α atoms were constrained, in the case of Rh, the constraints were also applied to the side chain atoms, with force constants that reflect the temperature b-factors of the crystal structure.

For the embedding of the system in a solvent/membrane environment, continuum electrostatics calculations were performed using the PBEQ module in CHARMM. The boundary conditions were defined iteratively using the *focus* option with a final grid spacing of 0.4 Å. RESP charges fitted to the SORCI ESP are used for the QM atoms. The induced dipoles from the polarization model are included as pair charges on cloned segments. The pair charges have a fixed separation of 0.05 Å from their host atoms, and their Born radii are set to zero in the Poisson–Boltzmann calculations. The latter is important to preserve the cavity in the calculations for different states/induced dipoles. The solvation energy was found stable and independent of the grid spacing over a wide range of values.

Table 6.7: S_1 Excitation Energies and Polarization Shifts (eV).

QM2	MM	ΔE^{QM1}	$\Delta\langle H^{12}\rangle$		$\Delta E^{(\mathrm{ii})}$	$\Delta E^{\mathrm{pol(ii)}}$	$\Delta E^{(\mathrm{i})}$	$\Delta E^{\mathrm{pol(i)}}$
bR, QM1: SORCI								
crm	crm	2.32	0.61					
ff03[a]	crm	2.26	0.53					
ff03	ff03	2.32	0.52					
PBE0	crm	2.27	0.55	(0.69)	2.24	-0.03	2.23	-0.04
bR, QM1: OM2/MRCI								
crm	crm	2.65	0.72					
PBE0	crm	2.59	0.64	(0.85)	2.54	-0.05	2.55	-0.04
DFTB	crm	2.57	0.69	(0.80)	2.52	-0.04	2.52	-0.05
psRII, QM1: SORCI								
crm	crm	2.56	0.59					
ff03[a]	crm	2.50	0.56					
ff03	ff03	2.49	0.55					
PBE0	crm	2.50	0.59	(0.77)	2.48	-0.02	2.49	-0.01
psRII, QM1: OM2/MRCI								
crm	crm	2.93	0.69					
PBE0	crm	2.85	0.74	(0.94)	2.81	-0.05	2.78	-0.07
DFTB	crm	2.82	0.65	(0.81)	2.79	-0.03	2.76	-0.06

QM1, QM2, and MM are the employed methods for the treatment of the chromophore, the binding pocket residues, and the remainder of the protein. "crm" denotes the CHARMM27, "ff03" the AMBER-ff03 fixed charge model. ΔE^{QM1} is the vertical QM1 excitation energy within a fixed (force field or ground-state polarized) QM2 environment. $\Delta\langle H^{12}\rangle$ is the QM1–QM2 Coulomb contribution to ΔE^{QM1} or (in parentheses) to the excitation energy $\Delta E^{(\mathrm{i})}$ corresponding to approach (i). The excitation energies $\Delta E^{(\mathrm{ii})}$ and $\Delta E^{(\mathrm{i})}$ are based on approach (ii) and (i), respectively. [a] Including also the backbone of the QM2 residues for charge integrity.

6.5 Results and Discussion

6.5.1 Polarization and Charge Transfer in the Retinal Binding Pockets of Bacteriorhodopsin and Pharaonis Sensory Rhodopsin II. A QM/QM/MM Model

In this section, the QM/QM/MM model introduced in section 6.2 is applied to investigate polarization and inter-residual charge transfer in the binding pocket of the retinal chromophore and their effects on vertical excitation energies. The details of the setup have been described in section 6.4.

Table 6.7 shows the $S_1 \leftarrow S_0$ excitation energies as calculated at different levels. In all cases, a bathochromic shift is predicted when substituting the CHARMM point charge model of the binding pocket residues by a quantum mechanical treatment. When introducing the ground-state polarized charge distribution, the vertical excita-

Table 6.8: PBE0/SV(P) NPA Net Charges on Individual QM2 Residues in bR[a]

residue	S_0	S_1	S_0 (QM1+2)[b]	S_0 (HF)
		donors of negative charge		
Asp85	-0.861	-0.863	-0.852	-0.901
Asp212	-0.879	-0.879	-0.870	-0.916
W18	0.033	0.033	0.033	0.019
Tyr83	0.017	0.018	0.016	0.011
W19	0.006	0.006	0.008	0.003
Met20	0.005	0.005	0.010	0.006
Ser141	0.005	0.005	0.015	0.002
Phe219	0.002	0.001	0.002	0.002
Thr142	0.001	0.001	0.009	0.000
Thr90	0.001	0.001	-0.001	0.000
		acceptors of negative charge		
retinal	—	—	0.843	—
W2	-0.088	-0.086	-0.039	-0.071
Tyr185	-0.069	-0.070	-0.061	-0.051
Thr89	-0.049	-0.049	-0.042	-0.035
Trp86	-0.034	-0.034	-0.018	-0.020
Trp182	-0.023	-0.023	-0.019	-0.014
Ala53	-0.014	-0.014	-0.012	-0.008
Trp189	-0.013	-0.013	-0.007	-0.008
Leu93	-0.009	-0.008	-0.006	-0.004
Val49	-0.007	-0.007	-0.009	-0.004
Trp138	-0.004	-0.005	-0.005	-0.002
Ala215	-0.004	-0.004	-0.004	-0.002
Val217	-0.004	-0.004	-0.004	-0.002
Met145	-0.003	-0.004	0.008	-0.003
Met118	-0.002	-0.002	0.009	0.000
Ile119	-0.002	-0.002	-0.002	-0.000
Phe208	-0.001	-0.001	-0.001	-0.001
Val213	-0.001	-0.001	-0.001	-0.001

[a] The remainder of the protein is represented by CHARMM charges, the chromophore by SORCI (S_0) RESP charges. [b] From PBE0 calculation on the joined retinal (QM1) and QM2 system in presence of CHARMM charges on the remaining atoms of the protein.

tion energy of the QM1 system ΔE^{QM1} is already red-shifted. This shift is small and of same magnitude in bR and psRII (0.05–0.06 eV at the SORCI, 0.06–0.08 eV at the OM2/MRCI level of theory), although it contains several effects that are neglected in the fixed charge model: An effective screening of the counter ion complex by the surrounding polarizable medium can be expected, although this effect is not completely recovered here, due to the limited size of the QM2 region.

Apart from the intra-molecular refinement of the charge distribution and explicit polarization by the chromophore in its ground state, also charge transfer between individual residues can be observed. The ESP-derived charges incorporate this charge transfer by reproducing the ESP of the QM2 density, but they are inappropriate to

Table 6.9: PBE0/SV(P) NPA Net Charges on Individual QM2 Residues in psRII[a]

residue	S_0	S_1	S_0 (QM1+2)[b]	S_0 (HF)
		donors of negative charge		
Asp75	-0.861	-0.863	-0.854	-0.902
Asp201	-0.878	-0.877	-0.870	-0.916
Met15	0.010	0.010	0.015	0.009
Met109	0.007	0.006	0.008	0.005
Trp178	0.004	0.004	0.008	0.002
Thr80	0.004	0.004	0.003	0.002
Phe208	0.002	0.002	0.002	0.002
Trp171	0.001	0.001	0.004	-0.000
		acceptors of negative charge		
retinal	—	—	0.874	—
W3	-0.093	-0.091	-0.039	-0.075
Tyr174	-0.063	-0.064	-0.054	-0.045
Thr79	-0.052	-0.052	-0.045	-0.037
Trp76	-0.040	-0.040	-0.023	-0.024
Ala47	-0.014	-0.014	-0.012	-0.007
Val206	-0.006	-0.006	-0.006	-0.004
Phe127	-0.005	-0.005	-0.005	-0.002
Leu202	-0.004	-0.004	-0.004	-0.003
Thr204	-0.004	-0.003	0.003	-0.002
Val108	-0.003	-0.003	-0.002	-0.002
Ile83	-0.001	-0.001	0.000	-0.000
Tyr73	-0.001	-0.001	-0.001	-0.000
Ile43	-0.001	-0.001	-0.003	0.000
Ser44	-0.001	-0.001	-0.001	-0.000
Phe134	-0.000	-0.000	0.000	0.000
Ala131	-0.000	-0.000	-0.000	-0.000

[a] The remainder of the protein is represented by CHARMM charges, the chromophore by SORCI (S_0) RESP charges. [b] From PBE0 calculation on the joined retinal (QM1) and QM2 system in presence of CHARMM charges on the remaining atoms of the protein.

define the net charges on the QM2 residues in terms of a summation over the corresponding atoms. Therefore, we consider here the atomic charges from a natural population analysis (NPA) of the QM2 density, summed over the atoms of each residue (Tables 6.8 and 6.9).

In bR, the two counter ion residues Asp85 and Asp212 donate each ca. 13% of their negative charge. Main charge acceptors are water 2, Thr89, Tyr185, Trp86, and Trp182. This corresponds to a redistribution of negative charge from the counter ion towards the center of the binding pocket. The same applies to psRII, where negative charge is carried from Asp75 and Asp201 to water 3, Tyr174, Thr79, and Trp76. This charge redistribution is essentially independent from whether the chromophore is in its ground or first excited state. It is also qualitatively preserved when the charge exchange with the chromophore is added, in a DFT calculation that spans both QM regions. When the hybrid DFT method is replaced by HF, the same trends occur, merely the extent

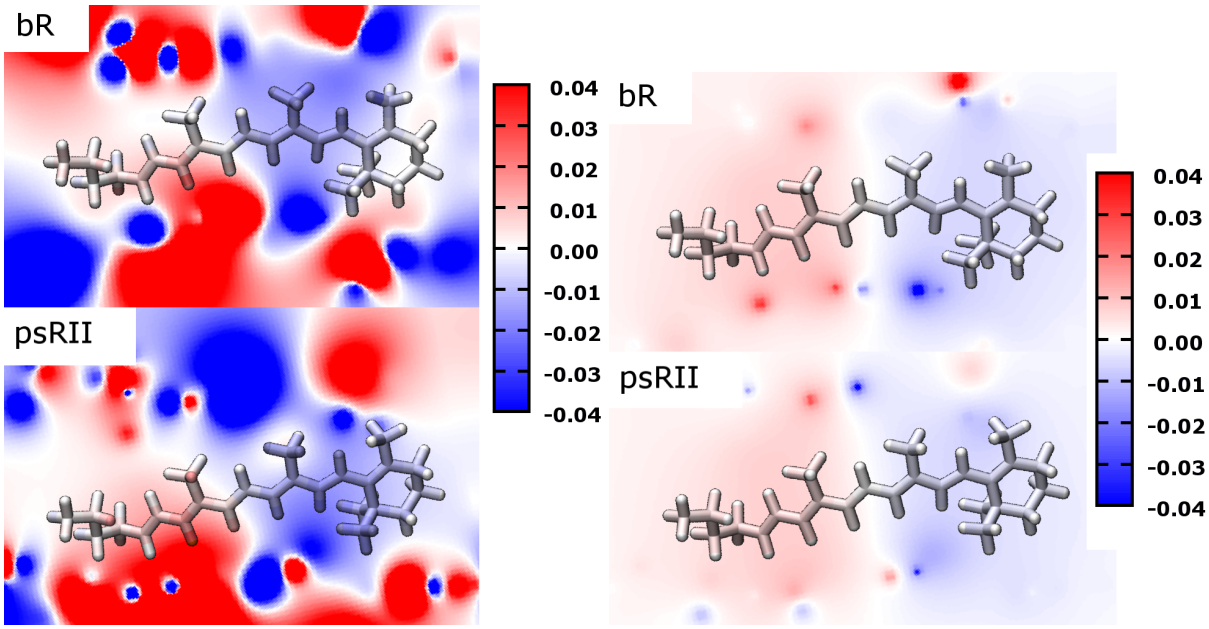

Figure 6.4: Left: changes in the ESP (a.u.) due to exchange of the CHARMM27 point charges in QM2 by the (ground-state adapted) PBE0 charge distribution in bR (top) and psRII (bottom). Right: Changes in the ESP (a.u.) of the QM2 moiety in bR (top) and psRII (bottom) due to substitution of the ground-state adopted PBE0 charge distribution by the S_1 adopted one. The difference ESP's are plotted in the molecular plane of the chromophore and at its nuclear positions.

of the charge transfer is reduced by ca. 30%. These results are consistent with previous studies of the charge delocalization of phosphate anions in aqueous solution (see Ref.[302] and references therein).

The origin of the bathochromic shift in ΔE^{QM1} relative to the excitation energy of the conventional QM/MM model can be rationalized by considering the fluctuation in V^2_{ES} (the ESP that the chromophore is exposed to) caused by the change in the QM2 charge distribution. Figure 6.4 (left) shows an increase of the ESP at the Schiff base side and a decrease in the central and β-ionone ring region of the chromophore, which is very similar in the two proteins and follows the same pattern as the inter-residual charge transfer. Given the direction of the excitation-induced charge transfer towards the β-ionone ring, the observed change in the ESP should cause a relative stabilization of the excited versus the ground state, resulting in a bathochromic shift.

This conclusion, however, is only valid if the magnitude of the excitation-induced charge transfer does not change. This is indeed the case in bR, and the red-shifted excitation energy is accompanied by a lowering of the electrostatic interaction energy $\Delta\langle H_{12}\rangle$ (see Table 6.7). In psRII, the situation is more complicated because the excitation-induced charge transfer, as measured in the norm of the difference dipole moment $\Delta\mu_{S_1-S_0}$ of the QM1 subsystem, is increased in the presence of the DFT-treated binding pocket (see Table 6.10). In consequence, $\Delta\langle H_{12}\rangle$ is unchanged (or even increased in the OM2/MRCI calculation), and the electrostatic analysis cannot explain the bathochromic shift in psRII. In fact, the real cause is found when considering the polarization of the PSB in the different electrostatic environments. Table 6.12 shows the difference dipole moments $\Delta\mu^{\mathrm{QM1}}_{\mathrm{prot-vac}}$ between unpolarized (vacuum) and

Table 6.10: Excitation-Induced Charge Transfer on the PSB—the QM1 Difference Dipole Moment $\Delta\mu^{\mathrm{QM1}}_{\mathrm{S_1-S_0}}$ (debye)

	x	y	z	norm
bR,vacuo	0.43	7.55	-6.32	9.85
bR,CHARMM	0.76	8.03	-5.86	9.97
bR,PBE0	0.71	7.95	-5.89	9.93
psRII,vacuo	0.89	9.21	-6.17	11.12
psRII,CHARMM	1.08	6.72	-4.05	7.92
psRII,PBE0	1.14	7.71	-4.66	9.09

As a measure for the excitation-induced charge transfer on the chromophore, the difference between the excited-state and the ground-state dipole moment, which is origin-independent and hence can be compared between different proteins is shown. While in bR the charge transfer hardly changes when the protein electrostatic environment is changed (CHARMM27 charges or PBE0 density) or switched off (vacuo), substantial changes occur in psRII. In the latter case, the slightly increased bond length alternation of the retinal molecule causes an increased charge transfer *in vacuo*, whereas the inclusion of the protein electrostatics reduces it to the level found in bR. The charge transfer in the DFT-calculated binding pocket, however, is larger than in the CHARMM-modeled one and closer to the vacuum value.

Table 6.11: Change of the Coulomb Interaction Energies (eV) between QM1 and MM Region due to $S_1 \leftarrow S_0$ Excitation

protein	QM1	QM2	$\Delta(E^{1,\mathrm{el}}_{\mathrm{QMMM}})_{\mathrm{S_1-S_0}}$
bR	SORCI	PBE0	-0.210
	SORCI	CHARMM27	-0.212
psRII	SORCI	PBE0	-0.116
	SORCI	CHARMM27	-0.101

polarized chromophore. In both proteins, the polarization is considerably reduced when replacing CHARMM27 charges by the DFT charge density. This leads to a reduced QM1 onsite energy (E_{QM1} less QM/QM and QM/MM interactions, also called electronic reorganization energy E^{ERO}), whereas changes in the Coulomb interaction energy between the QM1 and the MM region are within 0.01 eV (see Table 6.11). In psRII, this effect is more pronounced in the highly polarized S_1 state than in S_0, which leads to a bathochromic shift. The opposite applies to bR, where the ground state is slightly more polarized than S_1.

When the charge distribution in the QM2 region is allowed to relax in response to the excitation-induced charge transfer on the chromophore, approach (ii) yields another bathochromic shift ($\Delta E^{\mathrm{pol(ii)}}$, see Table 6.7) of 0.02–0.03 eV (SORCI). In total, compared with ΔE from the conventional (CHARMM27) QM/MM calculation, the excitation energy is lowered in both proteins by ca. 0.08 eV (SORCI) due to the polarizability of the binding pocket side chains. OM2/MRCI slightly overestimates the shifts in ΔE^{QM1} and ΔE^{pol} yielding excitation energies that are red-shifted by ca.

Table 6.12: QM1 Polarization by the QM2/MM Environment: $|\Delta\mu^{\mathrm{QM1}}_{\mathrm{prot-vac}}|$ (debye).

protein	QM2	S_0	S_1	$\Delta_{S_1-S_0}$
bR	CHARMM	6.87	6.27	-0.60
bR	PBE0	5.72	5.38	-0.34
psRII	CHARMM	10.03	12.96	+2.93
psRII	PBE0	9.05	10.78	+1.73

0.12 eV with respect to the QM/MM calculation. Similar results are produced also with SCC-DFTB as the QM2 method (Table 6.7).

Incorporating the response of the QM1 S_1 density to the changed QM2 charge distribution in approach (i), the excitation energies ($\Delta E^{(\mathrm{i})}$) do not change significantly. In the case of psRII (SORCI) and bR (OM2/MRCI in PBE0), $\Delta E^{(\mathrm{i})}$ slightly exceeds $\Delta E^{\mathrm{pol(ii)}}$, which is physically uncorrect, assuming a variational total energy. In the first case, the error might arise from a slightly inconsistent treatment of the Coulomb interaction energy between the QM1 and QM2 moieties: while the QM2 density is relaxed with respect to the MRCI density, the SORCI and CISD energies incorporate a PT2 correction from the unselected configurations. In the case of OM2/MRCI, the dominating error is the OM2/CISD ground-state total energy difference, which is not fully converged with respect to the number of active orbitals.

To investigate the error made in approach (ii) when neglecting the response of the QM1 system to the changed QM2 charge distribution in the final state, the reference state, which is determined fully self-consistently, can be changed: Starting from the variational S_1 state, the QM1 system is de-excited to the ground state (with frozen QM2 moiety), which yields the vertical excitation energy $\Delta\widetilde{E}^{\mathrm{QM1}}$ in Table 6.13 (see Figure 6.1). Keeping the resulting S_0 charge density in QM1 fixed, the QM2 density is relaxed, yielding $\Delta\widetilde{E}^{\mathrm{pol(ii)}}$. The total "de-excitation" energy corresponding to approach (ii) is then obtained as

$$\Delta\widetilde{E}^{(\mathrm{ii})} = \Delta\widetilde{E}^{\mathrm{QM1}} - \Delta\widetilde{E}^{\mathrm{pol(ii)}} \,. \tag{6.26}$$

In contrast to $\Delta E^{(\mathrm{i})}$, which fluctuates, the energies $\Delta E^{(\mathrm{ii})}$ and $\Delta\widetilde{E}^{(\mathrm{ii})}$ are always in the right order, deviating by 0.00–0.02 eV (Table 6.13). Furthermore, the polarization energies $\Delta E^{\mathrm{pol(ii)}}$ are widely unaffected from the choice of the initial state. This suggests, to use the average of $\Delta E^{(\mathrm{ii})}$ and $\Delta\widetilde{E}^{(\mathrm{ii})}$ as transition energy, which is numerically more stable than $\Delta E^{(\mathrm{i})}$ and eliminates any systematic error from the approach (ii) excitation energy due to the asymmetric treatment of ground and excited state.

6.5.2 Polarization in the Retinal Binding Pocket: A Test Case for Empirical Polarization Models

As in the QM/QM/MM approach described in the previous section, the effects of the explicit polarization treatment on the excitation will be analyzed in a two-step procedure. First, a self-consistent ground-state charge distribution is generated by iteratively relaxing the QM density and the induced dipoles of the polarization model.

Table 6.13: S_0–S_1 Transition Energies and Polarization Shifts (eV).

QM2	ΔE^{QM1}	$\Delta E^{\mathrm{pol(ii)}}$	$\Delta E^{(\mathrm{ii})}$	$\Delta E^{(\mathrm{i})}$	$\Delta \widetilde{E}^{\mathrm{QM1}}$	$\Delta \widetilde{E}^{\mathrm{pol(ii)}}$	$\Delta \widetilde{E}^{(\mathrm{ii})}$
bR, QM1: SORCI							
PBE0	2.27	-0.03	2.24	2.23	2.19	-0.03	2.22
bR, QM1: OM2/MRCI							
PBE0	2.59	-0.05	2.54	2.55	2.47	-0.05	2.52
DFTB	2.57	-0.04	2.52	2.52	2.48	-0.04	2.53
psRII, QM1: SORCI							
PBE0	2.50	-0.02	2.48	2.49	2.45	-0.02	2.47
psRII, QM1: OM2/MRCI							
PBE0	2.85	-0.05	2.81	2.78	2.77	-0.04	2.81
DFTB	2.82	-0.03	2.79	2.76	2.75	-0.03	2.78

The methods for the QM1 and QM2 zones are indicated. CHARMM27 charges represent the remainder of the protein. $\Delta \widetilde{E}^{\mathrm{QM1}}$ is the vertical QM1 transition energy within a fixed (excited-state polarized) QM2 environment, $\Delta \widetilde{E}^{\mathrm{pol(ii)}}$ and $\Delta \widetilde{E}^{(\mathrm{ii})}$ are the approach (ii) polarization and transition energy, respectively, with S_1 as the initial state. Other quantities are defined in Table 6.7.

Keeping these ground-state adapted induced dipoles fixed, a "vertical" excitation energy ΔE^{QM1} is calculated. Then, the induced dipoles are allowed to adapt to the excited-state charge distribution, and the excitation energy $\Delta E^{(\mathrm{ii})}$ of the complex is evaluated corresponding to the orthogonality-preserving approach (ii), as described in section 6.2.2. Analogously, the transition energy $\Delta \widetilde{E}^{(\mathrm{ii})}$ is obtained by starting with the induced dipoles adopted to the excited state. In approach (i), the excitation energy $\Delta E^{(\mathrm{i})}$ is defined by directly comparing the total energies of the complex in the two fully relaxed variational states.

At first, the two polarization models are applied to the chromophore binding-pocket side chains in bR and psRII while including the remainder of the protein as CHARMM charges. This allows for a direct comparison of the energetics and electrostatics with the quantum mechanical treatment presented above, where the same atoms constituted the "QM2" (hybrid DFT) layer of the QM/QM/MM model. The two approaches are very different in their description of the charge distribution. While the QM treatment will underestimate polarization due to the employed SV(P) basis set, it incorporates inter-residual charge transfer, which is missing in the polarization models. Nonetheless, the resulting excitation energies are very similar (see Table 6.15) showing the same bathochromic shifts in the vertical excitation energy ΔE^{QM1} relative to the QM/MM model (CHARMM charges in QM2 and MM, see Table 6.14). Also the polarization shifts due to relaxation of the QM2 charge distribution in response to the QM1 excitation are in close agreement when considering the $\Delta E^{(\mathrm{ii})}$ excitation energies.

The $\Delta E^{(\mathrm{i})}$ excitation energies, which arise from the fully self-consistent ground and excited-state charge distributions, show the same problem as in the QM/QM/MM model: in some cases they are higher than $\Delta E^{(\mathrm{ii})}$ or lower than $\Delta \widetilde{E}^{(\mathrm{ii})}$, in violation of the variation principle. In contrast, the $\Delta \widetilde{E}^{(\mathrm{ii})}$ energies, obtained with the excited state as the initial (self-consistent) state, are systematically 0.00–0.03 eV below the $\Delta E^{(\mathrm{ii})}$

Table 6.14: Conventional QM/MM S_1 Excitation Energies (eV).

QM1	QM2	MM	bR	psRII	Rh(u)	Rh(p)
SORCI	CHARMM27	CHARMM27	2.32	2.56	2.53	2.42
OM2/MRCI	CHARMM27	CHARMM27	2.65	2.93	2.82	2.68
SORCI	AMBER-ff03	AMBER-ff03	2.32	2.49	2.61	2.45
SORCI	AMBER-ff03[a]	CHARMM27	2.26	2.50		
SORCI	CHARMM27[b]	CHARMM27[b]	2.28	2.62	2.50	2.34

The QM zone contains the chromophore and Lys side chain (63 atoms). The remainder of the protein is represented by the fixed FF charges. [a] Including the backbone of QM2 residues. [b] No charge scaling applied to solvent exposed charged AA's.

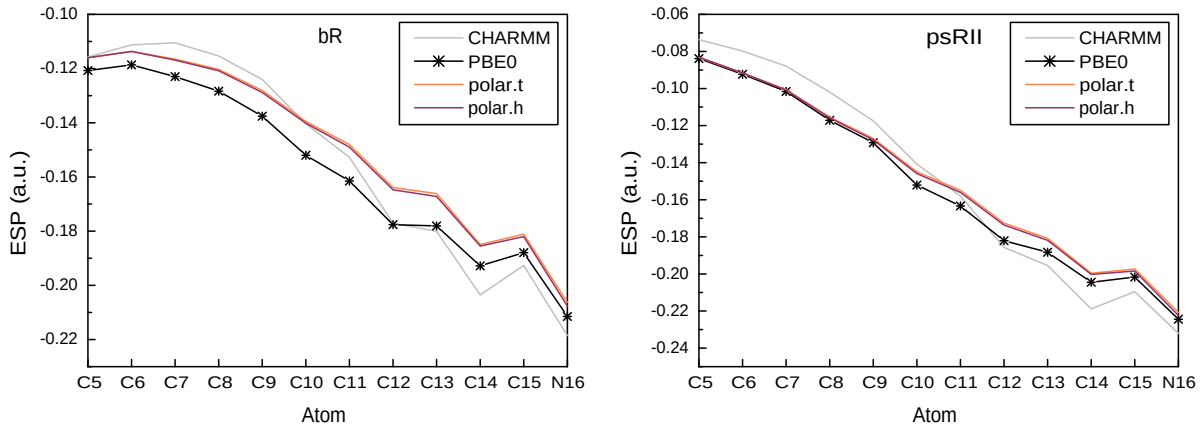

Figure 6.5: ESP (a.u.) at the nuclear positions along the PSB backbone in bR (top) and psRII (bottom) as generated by the fixed CHARMM or ground-state adapted QM2 charge distribution and the CHARMM charges in the MM moiety.

values, as it should be.

The agreement in excitation energies is encouraging but not sufficient to judge the general accuracy of the empirical polarization models for the studied systems. Therefore, I consider the ESP as produced by the polar.h and polar.t models and the QM density, and compare them with the ESP as generated by the CHARMM charges in the conventional QM/MM setup. Figure 6.5 shows the ESP at the nuclear positions of the chromophore along the conjugated carbon chain. The differences in ΔE^{QM1} between the QM/MM and the QM/polar/MM model indeed correlate with the differences in the ESP. The empirical models, whose ESP curves are almost indistinguishable in Figure 6.5, show the same trends as the QM/QM/MM model: Due to the explicit polarization treatment, the ESP is increased on the Schiff-base side of the C11–C12 double bond and lowered on the opposite side. The gradient, i.e., the electric field, is reduced in just the region where the maximum charge flux occurs upon excitation. The essential difference between the QM and the two empirical polarization models, besides a global shift in the case of bR (which does not affect the field at the chromophore site), consists in a slight downshift of the PBE0 potential relative to the polar.h/polar.t potential, in a region around C12. This effect can clearly be ascribed to the inter-residual

Table 6.15: Polarizable Binding Pocket: S_1 Excitation Energies and Polarization Shifts (eV).

	QM1	QM2	ΔE^{QM1}	$\Delta E^{(\mathrm{ii})}$	$\Delta\widetilde{E}^{(\mathrm{ii})}$	$\Delta E^{\mathrm{pol(ii)}a}$	$\Delta E^{(\mathrm{i})}$
bR	SORCI	polar.t	2.26	2.23	2.20	-0.05	2.23
	SORCI	polar.h	2.26	2.22	2.20	-0.04	2.23
	SORCI	PBE0	2.27	2.24	2.22	-0.04	2.23
	OM2/MRCI	polar.t	2.58	2.52	2.51	-0.07	2.54
	OM2/MRCI	polar.h	2.58	2.51	2.52	-0.06	2.55
	OM2/MRCI	PBE0	2.59	2.54	2.52	-0.06	2.55
psRII	SORCI	polar.t	2.52	2.49	2.47	-0.04	2.48
	SORCI	polar.h	2.51	2.47	2.46	-0.04	2.48
	SORCI	PBE0	2.50	2.48	2.47	-0.02	2.49
	OM2/MRCI	polar.t	2.86	2.82	2.81	-0.05	2.81
	OM2/MRCI	polar.h	2.85	2.81	2.80	-0.05	2.81
	OM2/MRCI	PBE0	2.85	2.81	2.81	-0.04	2.78

QM1 and QM2 refer to the two QM level zones introduced in Ref.[303], which contain the chromophore and the binding-pocket side chains, respectively. The remainder of the protein is described by the fixed CHARMM27 charges. "polar.t" denotes the polarization model with Thole's original parameters ($a = 0.572$), and "polar.h" the hybridization-dependent model with $a = 0.390$. ΔE^{QM1} is the vertical QM1 excitation energy with the frozen (ground-state adapted) QM2 density/dipoles. [a] The polarization shift $\Delta E^{\mathrm{pol(ii)}}$ is defined as the difference between approach (ii) excitation energy (average of $\Delta E^{(\mathrm{ii})}$ and $\Delta\widetilde{E}^{(\mathrm{ii})}$) and the vertical excitation energy ΔEQM1.

transfer of negative charge from the counter ions towards Tyr185/Tyr174 in the center of the binding pocket, which was observed and discussed in section 6.5.1. Figure 6.6 shows plots of difference ESP's on a planar grid in the molecular plane, which visualize further details of the "refinement" of the ESP by the polarization treatment (left) and its response to the excitation-induced charge transfer (right). When comparing to the QM/QM/MM models (Figure 6.4), it is remarkable, that polar.h generates similar gradients in the difference ESP's in the range of the chromophore, despite the fact that the difference is produced by monopoles in one case and by dipoles in the other.

6.5.3 Polarization in Rhodopsin, Bacteriorhodopsin, and Pharaonis Sensory Rhodopsin II

In this section, the dielectric effect of long-range electrostatic interactions will be investigated and the effect of the polarizability of the entire (protein/solvent) system on the excitation energy will be quantified for bR, psRII, and the Rh models Rh(u) and Rh(p).

First, the question shall be answered at which range the polarization response of the environment on the excitation-induced charge transfer can contribute significantly to the excitation energy. Therefore, the charge transfer can be associated with the creation of an additional dipole moment of $\mu \approx 10$ D and Onsager's formula[304] can be applied to obtain the solvation energy of the dipole in a spherical cavity (radius R_c)

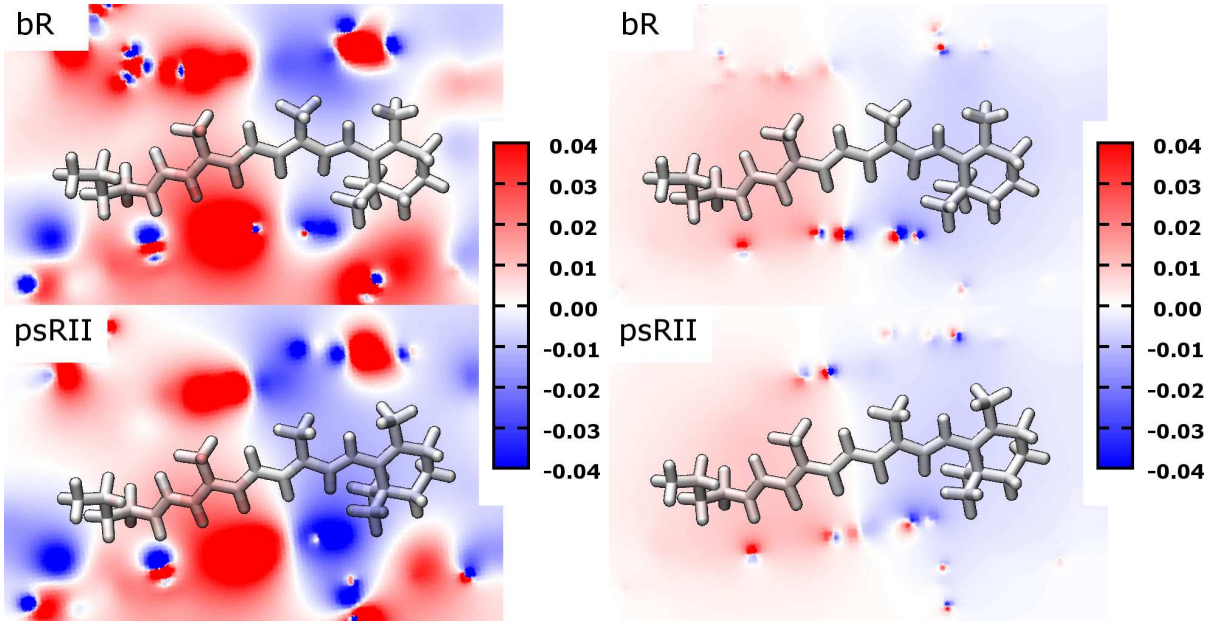

Figure 6.6: Left: Changes in the ESP (a.u.) due to exchange of the CHARMM27 point charges in the QM2 zone by the ground-state adapted polar.h multipoles in bR (top) and psRII (bottom). Right: Changes in the ESP (a.u.) of the QM2 zone (polar.h) in bR (top) and psRII (bottom) due to the substitution of the ground-state adapted moments by the S_1 adopted ones. The difference ESP's are plotted in the molecular plane of the chromophore and at its nuclear positions.

surrounded by a dielectric medium:

$$\Delta E^{\mathrm{pol}} = -\frac{\epsilon - 1}{2\epsilon + 1}\frac{\mu^2}{R_c^3} \tag{6.27}$$

Assuming a dielectric constant of $\epsilon = 2$, we obtain -0.10, -0.06, and -0.01 eV for R_c = 5, 6, and 10 angstrom, respectively. Since the diameter of the QM2 zone perpendicular to retinal's molecular axis is in the range of 10–12 angstrom, the polarizability of the remainder of the protein can significantly contribute to the excitation energy.

Table 6.16 shows the excitation energies and polarization shifts for bR, psRII, and the two Rh setups, where the polar.t and polar.h models are applied to the entire protein. Although the polarization shifts $\Delta E^{(\mathrm{ii})}_{\mathrm{pol}}$ are still within 0.10 eV, they are larger, almost doubled for psRII, compared to the polarizable-binding pocket model. Also the vertical excitation energies ΔE^{QM1} are reduced by ca. 0.03 eV. This means that the polarizable-binding pocket model is not appropriate to quantify the total dielectric effect of the protein on the excitation energy.

For all four setups, very similar values are obtained for $\Delta E^{(\mathrm{ii})}_{\mathrm{pol}}$, ranging from 0.06 eV in the Rh(p) model (SORCI/polar.h) to 0.08 eV in bR (SORCI/polar.h). This correlates with the observation that the excitation-induced charge transfer, in terms of the difference dipole moment $|\Delta\mu_{S_1-S_0}|$, is comparable in the four cases (bR: 10.0 D, psRII: 9.6 D, Rh(u): 8.1 D, Rh(p): 8.4 D). Note, that OM2/MRCI predicts ΔE_{pol} in the same order as $|\Delta\mu_{S_1-S_0}|$, while the SORCI results only partially resolve this subtle trend. If we instead consider the S_0–S_2 excitations at the SORCI level, which are accompanied by a much smaller charge transfer (bR: 4.7 D, psRII: 3.9 D, Rh(u): 2.9 D, Rh(p): 3.3 D),

Table 6.16: Excitation Energies and Polarization Shifts (eV).

	QM	MM	ΔE^{QM1}	$\Delta E^{(\mathrm{ii})}$	$\Delta \widetilde{E}^{(\mathrm{ii})}$	$\Delta E^{(\mathrm{i})}$	$\Delta E^{\mathrm{pol(ii)}\,a}$
bR	SORCI	polar.t	2.23	2.18	2.15	2.20	-0.07
	SORCI	polar.h	2.24	2.19	2.13	2.17	-0.08
	SORCI (S_2)	polar.h	2.47	2.45			-0.01
	OM2/MRCI	polar.t	2.54	2.46	2.45	2.50	-0.09
	OM2/MRCI	polar.h	2.55	2.46	2.44	2.48	-0.10
psRII	SORCI	polar.t	2.49	2.44	2.39	2.43	-0.07
	SORCI	polar.h	2.48	2.44	2.39	2.42	-0.07
	SORCI (S_2)	polar.h	2.53	2.52			-0.01
	OM2/MRCI	polar.t	2.82	2.75	2.71	2.73	-0.09
	OM2/MRCI	polar.h	2.82	2.75	2.71	2.73	-0.09
Rh(u)	SORCI	polar.t	2.45	2.41	2.36	2.37	-0.07
	SORCI	polar.h	2.43	2.38	2.33	2.35	-0.07
	SORCI (S_2)	polar.h	2.60	2.60			-0.01
	OM2/MRCI	polar.t	2.76	2.70	2.69	2.71	-0.06
	OM2/MRCI	polar.h	2.75	2.69	2.69	2.70	-0.06
Rh(p)	SORCI	polar.t	2.32	2.27	2.23	2.27	-0.07
	SORCI	polar.h	2.32	2.28	2.25	2.28	-0.06
	SORCI (S_2)	polar.h	2.58	2.57			-0.01
	OM2/MRCI	polar.t	2.70	2.64	2.58	2.64	-0.09
	OM2/MRCI	polar.h	2.68	2.61	2.58	2.64	-0.08

"polar.t" denotes the polarization model with Thole's original parameters ($a = 0.572$), "polar.h" the hybridization-dependent model with $a = 0.390$. ΔE^{QM} is the vertical QM excitation energy with frozen (ground-state adapted) induced dipoles. [a] The polarization shift $\Delta E^{\mathrm{pol(ii)}}$ is defined as the difference between approach (ii) excitation energy (average of $\Delta E^{(\mathrm{ii})}$ and $\Delta \widetilde{E}^{(\mathrm{ii})}$) and the vertical excitation energy ΔE^{QM}.

the corresponding values for $\Delta E^{(\mathrm{ii})}_{\mathrm{pol}}$ are reduced likewise. Further, no significant differences are found between the polar.t and polar.h parametrization when considering the results of approach (ii).

With the polarization energy $\Delta E^{\mathrm{pol(ii)}}$, also the deviation between $\Delta E^{(\mathrm{ii})}$ and $\Delta \widetilde{E}^{(\mathrm{ii})}$ increases when extending the polarizable region. However, it remains rather systematic, varying between 0.03 and 0.06 eV in the SORCI calculations. The excitation energies obtained with approach (i) mostly agree with the approach (ii) results, but the $\Delta E^{(\mathrm{i})}_{\mathrm{pol}}$ values show larger fluctuations in some cases that are not present in $\Delta E^{(\mathrm{ii})}_{\mathrm{pol}}$. In the case of bR, $\Delta E^{(\mathrm{i})}$ significantly exceeds $\Delta E^{(\mathrm{ii})}$ (both SORCI and OM2/MRCI), in violation of the variational principle.

By adding the shifts in ΔE^{QM1} to the polarization shifts, the resulting excitation energies are found shifted by -0.14 to -0.17 eV compared to the conventional QM/MM results based on CHARMM27 MM charges (Table 6.14). This result, however, might depend on the fixed-charge model used for comparison. To test the influence of the particular charge parameterization in the conventional QM/MM calculations, I substituted the CHARMM27 charges by those of the amber ff03 FF.[130] The charge model

of the amber ff03 FF is designed to incorporate a mean polarization in the liquid phase (similar to the CHARMM27 one, which anticipates an aqueous environment). This is achieved by performing the QM calculations to whose ESP the ff03 charges are fitted in a dielectric medium using a continuum electrostatic model. In contrast, the CHARMM27 charges are chosen more empirically to reproduce solute–water interactions in combination with the TIP3P water model and form small integer charge groups on each AA.[123]

When replacing the CHARMM27 charges by the ff03 ones only for those AA's occurring in the QM2 zone, the SORCI excitation energy (Table 6.14) is lowered by ca. 0.06 eV in bR and psRII. A complete substitution, on the contrary, results in shifts of -0.07 eV (psRII) to +0.08 eV [Rh(u)]. When comparing the SORCI/polar.h results for $\Delta E^{(\mathrm{ii})}$ with the SORCI/ff03 excitation energies, the resulting shifts range from -0.07 eV (psRII) to -0.25 eV [Rh(u)]. These considerations show that the overall effect of the explicit treatment of polarization strongly depends on the "unpolarized" model chosen as reference. Different charge models that implicitly contain condensed-phase polarization yield different excitation energies. Merely within one explicit polarization model, a unique polarization *shift* ΔE^{pol} can be defined, e.g., based on the fully relaxed ground- (or initial-) state charge configuration as point of reference.

To complete the discussion of polarization effects, I consider the dielectric effect of a solvent/membrane environment on the excitation energy. The dominant effect here is the effective shielding of the solvent-exposed charged AA's at the protein surface, which is explicitly calculated with the Poisson–Boltzmann (PB) equation solver in CHARMM. The resulting change of the potential at the active site is approximated, for each charged solvent-exposed AA, by scaling its permanent charges to reproduce the potential in presence of the corresponding solvent reaction field. This approach, suggested by Dinner *et al.*,[301,305] leads to scaling factors between 0.2 and 0.001 in the four considered models. With the scaled charges, the excitation energy ΔE^{QM1} is shifted by -0.06 to +0.08 eV (see Table 6.14). While geometry optimization, polarization and excited-state calculations are performed with the scaled charges to obtain more realistic structures and induced dipoles, this procedure only crudely approximates the protein–solvent interaction energy. It also neglects the interaction between the excitation-induced charge transfer and the (state-dependent) reaction field induced by the non-scaled permanent and induced charges inside the protein. This can be corrected in a similar manner as the reaction profiles in Ref.[301] by substituting the interaction with the scaled charges by the interaction with the reaction field. The latter is obtained from solving the PB equations with the unscaled charges and the same geometry, induced moments, and QM density as before. The reaction-field correction to the excitation energy obtained with the scaled charges is then obtained as

$$\Delta\Delta E^{\mathrm{rf}} = \Delta\Delta E^{\mathrm{QM/MM}} + \Delta\Delta E^{\mathrm{pol/MM}} + \Delta\Delta E^{\mathrm{solv}} \tag{6.28}$$

$$\Delta\Delta E^{\mathrm{QM/MM}} = \sum_A (1-\lambda_A) q_A \Delta V_A^{\mathrm{ES}}\left[\rho^{\mathrm{QM}}\right] \tag{6.29}$$

$$\Delta\Delta E^{\mathrm{pol/MM}} = \sum_{A,B\notin A} (1-\lambda_A) q_A \underline{\mathbf{T}}_{AB} \Delta\mu_B \tag{6.30}$$

$$\Delta\Delta E^{\mathrm{solv}} = \Delta E_{\mathrm{solv}}\left[\rho^{\mathrm{QM}}_{\mathrm{S}_1}, \mu_A^{\mathrm{S}_1}, q_A\right] - \Delta E_{\mathrm{solv}}\left[\rho^{\mathrm{QM}}_{\mathrm{S}_0}, \mu_A^{\mathrm{S}_0}, q_A\right] . \tag{6.31}$$

The first two terms, $\Delta\Delta E^{\mathrm{QM/MM}}$ and $\Delta\Delta E^{\mathrm{pol/MM}}$, restore the full Coulomb interaction energies with the unscaled charges, for the QM density and the induced dipoles,

Table 6.17: Solvent Reaction Field Corrections to the SORCI Excitation Energy (eV).

	$\Delta\Delta E^{\mathrm{QM/MM}}$	$\Delta\Delta E^{\mathrm{pol/MM}}$	$\Delta\Delta E^{\mathrm{solv}}$	$\Delta\Delta E^{\mathrm{rf}}$
bR	-0.028	+0.002	+0.018	-0.008
psRII	+0.021	-0.023	+0.009	+0.007
Rh(u)	-0.010	+0.026	-0.004	+0.012
Rh(p)	-0.012	+0.024	-0.019	-0.007

respectively. The (outer) sum in eq 6.29 and 6.30 runs over all permanent charges q_A that are scaled by corresponding scaling factors λ_A. The inner sum in eq 6.30 runs over all induced dipoles μ_B excluding the polarization group to which atom A belongs (side chain of the corresponding AA). ΔV_A^{ES} is the difference ($S_1 - S_0$) in the ESP of the QM density at the position of atom A, $\Delta\mu_B$ are the difference dipole moments ($S_1 - S_0$) of the polarization model. ΔE_{solv} is the solvation free energy of the protein in solution compared to the gas phase, where the protein charge distribution is represented by the QM density (RESP charges), induced dipoles, and unscaled permanent charges. This approximate correction to the charge-scaling procedure is based on the assumption that the geometry, QM density, and induced moments would not significantly change if they would be determined self-consistently with the exact solvent reaction field. As Table 6.17 shows, the reaction field corrections to the excitation energy are in the order of 0.01 eV for the four protein models. As they are much smaller than the shifts resulting from the charge-scaling, the level of approximation appears well justified.

Several previous studies reported bathochromic shifts in the excitation energy which were associated with the polarizability of the protein. When quantifying such shifts, it is important to clearly define the reference model in which the associated effect is excluded. For bR, Warshel *et al.*[187] found a hypsochromic shift of 0.19 eV (semiempirical QCFF/PI CI) when *omitting* the induced dipoles, i.e., their polarization shift relates to the fixed charge model of the ENZYMIX[306] FF. The employed CI Hamiltonian was state-independent, including only the ground-state adapted permanent and induced dipoles. Hence, their shift can be compared to the -0.13 eV (SORCI) or -0.19 eV (OM2/MRCI) that we obtain by considering $\Delta E^{(\mathrm{ii})}$ and the CHARMM point charge environment as a reference. This comparison certainly ignores the fact that different fixed charge models were employed. In the studies of Houjou *et al.*[236] and Matsuura *et al.*,[285] the reference for the polarization shift in bR (-0.34 and -0.41 eV, respectively) contains a self-consistent ground-state charge distribution, where the protein is polarized by the chromophore in its ground state. According to eq 20 in Ref.[236] and eq 14 in Ref.[285], the CI (or response) matrix contains configuration- (or orbital-) dependent induced dipoles. Hence, their polarization shifts can best be compared to our polarization shift $\Delta E^{\mathrm{pol(i)}}$ of -0.07 eV (SORCI/polar.t) to -0.08 eV (SORCI/polar.h). Following this assignment, our semiempirical results compare quite well with the model of Warshel *et al.*, whereas both semiempirical and *ab initio* results disagree clearly with the large polarization shifts found by Houjou *et al.*[236] and Matsuura *et al.*[285] for bR and with the strong variations of this shift for different rhodopsins (only -0.18 eV for Rh and psRII) reported in the latter article.

6.6 Conclusions

In this chapter, I developed and applied two different extensions of the conventional QM/MM scheme to improve the electrostatic representation of polypeptides in multi-scale calculations of excitation energies and to explicitly introduce nonadditive polarization effects and inter-residual charge transfer across hydrogen-bonded networks. Both achieve (iteratively) a self-consistent mutual polarization of the optically active region, which is described by high-level multi-state QM methods, and the surrounding molecular environment. Concerning the latter, they are complementary in the description of the charge distribution using either the QM electron density mapped onto ESP fitted atomic charges (QM/QM/MM model) or atomic induced dipoles (empirical polarization models).

I tested two different approaches to calculate the excitation energy of a quantum system embedded in a polarizable medium. The fully self-consistent approach (i) requires the total energy difference between the initial and the final state and therefore proved to be less numerically stable in connection with the employed MRCI schemes (in particular OM2/MRCI) and should be abandoned in favour of approach (ii). The latter requires only the difference in the vertical excitation energy of the inner QM region and in the polarization energy of the polarizable environment. Initial and final state are not treated symmetrically in approach (ii), but the resulting systematic error can be eliminated by combining the results of two calculations where either the ground or the excited state is defined as the initial (fully variational) state. For excited-state methods that provide fully variational absolute energies and corresponding density matrices, like CASSCF, TDDFT, or EOM-CC, approach (i) might be applicable without this limitation.

Two parameterizations of Thole's interactive empirical polarization model were calibrated and tested for peptides using MP2/cc-pVQZ calculations as a reference. I have shown that Thole's original parameterization for small organic molecules is transferable to amino acids. The polar.h model, adding polarizabilities for sulfur and sp2-carbon to Thole's 5-parameter model, reproduces the *ab initio* mean polarizabilities of 13 neutral amino acid side chains with a relative RMSD of 3%. For ionic side chains, considerably larger deviations were found, indicating space for improvement by explicitly charge-dependent parameters.

The effects of polarization and charge relocation within the binding pocket of the retinal chromophore on the vertical excitation energy of bR and psRII were studied using a three-layer QM/QM/MM model. For the S_1 absorption maximum of bR and psRII, bathochromic shifts were found in all employed QM/QM/MM models. These shifts, as well as the changes in the ESP, were accurately reproduced with both empirical polarization models (polar.t and polar.h) substituting the hybrid DFT description in the outer QM2 region, although they exclude inter-residual charge transfer. Therefore, both models agree that polarization and charge transfer within the binding pocket have only a moderate influence on the absorption maximum in bR and psRII, and do not contribute to the observed spectral shift between these two structurally similar proteins. In fact, the refinement of the charge distribution within the binding pocket of bR and psRII leads to excitation energies that are within the range obtained by employing different MM charge models. While this result appears to corroborate previous gas-phase and QM/MM models,[9,10,228,229,280,282–284] the incompleteness of the polarizable-binding pocket model must be emphasized, which is found when ex-

tending the polarizable region to the entire system. In bR and psRII, the remainder of the protein contributes nearly equally to the overall dielectric effect. Also the reaction field induced in the solvent/membrane environment contributes to the excitation energy, but the predominant effect here is the shielding of solvent exposed charged groups, which can efficiently be incorporated using Dinner's charge scaling procedure: When the SORCI/polar.h calculations are performed with the scaled exposed charges, the solvent/membrane contribution to the excitation energy is reproduced within 0.01 eV. This comforting result might certainly be transferable only to systems where the chromophore is deeply embedded in the protein. Otherwise, a layer of explicit solvent and the proposed reaction–field corrections can be applied to achieve a consistent description of the solvation.

When discussing the effects of the protein polarizability, it is important to distinguish between two aspects: (1) the substitution of a fixed charge model for the protein (e.g., point charges from a particular FF) by a self-consistent ground-state charge distribution of the polarizable protein–ligand complex and (2) the instantaneous polarization response of the protein to the excitation-induced charge relocation on the ligand. The refinement of the electrostatic interactions associated with (1) and the related effect on calculated properties (e.g. ΔE^{QM1}) depends on the initial charge model taken as reference and on the specific arrangement of charged and polar groups, which induce screening moments in their vicinity. On the contrary, the impact of (2) on, e.g., the excitation energy $\Delta E^{(\mathrm{ii})}$ depends essentially on the polarizability of the chromophore environment and on the extent of charge relocation due to the excitation, as measured, e.g., in the difference dipole moment $|\Delta\mu_{\mathrm{S}_1-\mathrm{S}_0}|$.

As the excitation energies obtained with different FF charge models deviate in an unsystematic manner, the corresponding refinements of ΔE^{QM1} in the polarizable models range from -0.01 to -0.18 eV for the four considered models bR, psRII, Rh(p), and Rh(u). This shows that the calculation of spectral shifts between different proteins can be improved by an explicit treatment of polarization. For the prediction of absolute absorption energies, an additional bathochromic shift of ca. 0.06–0.08 eV due to the instantaneous response of the medium to the excitation-induced charge transfer should be taken into account, which was found to be rather similar in the different rhodopsins. The magnitude of this polarization shift certainly depends on the employed quantum method to obtain the ground- and excited-state energies and densities for the QM region. E.g., the OM2/MRCI method tends to overestimate the shifts when compared with SORCI, as it overestimates the difference dipole moment due to excitation.[281] However, the SORCI/polar.h calculations represent the first accurate quantification of the polarization shift for rhodopsins that is based on a well calibrated polarization model and a QM method that reliably reproduces the experimental opsin shifts between the protonated and unprotonated Schiff base *in vacuo* and in different rhodopsins.

With OM2/MRCI and SCC-DFTB, the QM/QM/MM model can be used also at a semiempirical level with satisfying agreement to the high level *ab initio* results. This allows the extension of the model to larger QM zones, but the incorporation of the entire protein environment at the QM2 level remains computationally demanding, even if linear-scaling techniques are employed. In contrast, the empirical polarization models can easily be applied also to larger proteins with negligible computational demands.

It is not the purpose of the calculations presented above to provide a best possible

estimate for the vertical excitation energy of the four considered structural models. When compared to experiment, the SORCI/polar.h results for $\Delta E^{(\mathrm{ii})}$ coincide with the experimental absorption maxima of bR (2.18 eV[11]) and psRII (2.50 eV[279]), whereas the Rh absorption energy (2.49 eV[307]) is underestimated by 0.11 eV (0.21 eV) in the Rh(u) and Rh(p) models. A rigorous comparison with experiment, which could be used as a criterion for the quality of the structural model itself (e.g., the protonation state of Glu181 in Rh), should eliminate two remaining short-comings of the presented QM/MMpol ansatz: the neglect of charge transfer between the chromophore and the complex counter ion via a hydrogen-bonded network and the neglect of dispersion interactions between the chromophore and the vicinal highly polarizable aromatic side chains. Both effects can be included by extending the QM region to the relevant fragments, which is the subject of the final chapter.

Chapter 7

The Effect of Charge Transfer and Dispersive Interactions on the Optical Excitation in Rhodopsins

7.1 Introduction

The QM/MM calculations presented in the previous chapters all employed a QM zone that was restricted to the chromophore, i.e., the photoactive part of the system, in which the wave function changes significantly upon excitation. In the previous chapter, this model was extended to incorporate the response of the polarizable protein/solvent environment to the excitation-induced charge transfer (CT) on the chromophore, in terms of static polarization. The resulting QM/polar.h approach accounts for all classical chromophore–environment interactions, but neglects CT and dispersion between the two moieties. A non-empirical treatment of both effects requires the extension of the QM region to parts of the environment that contribute the charge exchange with the chromophore, or the dispersive interactions. The purpose of this chapter is to quantify the overall contribution of both interactions on the excitation energy and suggest effective ways to determine, which parts of the environment should be included in the QM part of the model.

7.2 Computational Details

When comparing the results of QM calculations using different QM regions, it is essential to consider the possible size-consistency errors of the quantum approach. This concerns the basis-set superposition error (BSSE) when using local basis sets, the intrinsic size-consistency error of truncated CI methods, and the effect of employed thresholds for which the results are not fully converged. An example for the latter is the limited number of active (non-frozen) MO's in the OM2/MRCI method. To limit the memory requirements, it is necessary to restrict the CI calculations to a window of 30-40 active orbitals. If the QM region comprises merely the chromophore, this window is sufficiently large to cover the entire π system, and excitation energies are nearly converged (see chapter 2.6). If, on the contrary, the QM region is extended, the canonical chromophore orbitals are mixing with orbitals from other fragments. With

a fixed number of active MO's, this leads to an effective shrinking of the active space, i.e., the fraction of the π-correlation energy recovered in the GUGA-CI calculation. For this reason, the OM2/MRCI approach will not be used in this chapter.

In the *ab initio* SORCI calculations presented below, the following strategy is followed to minimize size-consistency errors: The net CT between chromophore and environment is essentially state-independent and well described already at the SCF level (*vide infra*). Dispersion interactions are reasonably well described at the MP2 level. Therefore, the reference wave function in the SORCI calculation shall contain only excitations that are well localized on the chromophore. This is achieved by performing the preliminary DDCI2 with either manually selected/de-mixed canonical MO's (and IVO's) of π character, or with natural orbitals of a minimal CI calculation (see section 3.3.4). The frontier natural orbitals of such a DDCI2 calculation are strongly localized (on the chromophore) π orbitals and are used in the DDCI3 and relaxed MP2 steps with the same parameters as used in the SORCI calculations of the previous chapters. The individual configuration selection with the first-order perturbation threshold of $T_{\mathrm{sel}} = 10^{-6}$ ensures that the major part of the dynamical correlation energy, and hence the dispersion contribution, is incorporated at the MP2 level. In this way, the size-extensivity of the MP2 method is exploited, and the results depend only marginally on the size-consistency correction of the MRCI-Q energy (here: Davidson correction).

Atomic charges obtained from natural population analysis[308] (NPA) of HF, MP2, and hybrid DFT densities have been calculated using Gaussian03.[309] Mulliken and Löwdin population analyses and electrostatic potentials (ESP) were computed from the densities of SORCI, CISD, and HF, using ORCA,[297] and from HF and DFT densities, using Turbomole.[245] In particular, full selection-free CISD density matrices were computed with the newly implemented MDCI module in ORCA.[310] If not noted otherwise, molecular charges are obtained from NPA of the HF density matrix.

The same structural models have been used for bR, psRII, and Rh as in chapter 6, where they are explained in detail. For re-optimizations of the chromophore at the PBE0/CHARMM level, the turbomole[245] modules have been used. The employed basis set is TZVP.[240] Scleronomic constraints and van-der-Waals forces are applied in an own application that interfaces with turbomole's jobex script. The MM atoms, the QM link atom, and its host atom are fixed during the optimization. The same van-der-Waals parameter are applied as in the DFTB/CHARMM QM/MM optimization.

7.3 Inter-Residual Charge Transfer and the Proper Choice of the QM Zone

7.3.1 CT in Different QM Methods: Derivative Discontinuity, Dynamic Correlation

Before investigating the convergence of the CT and related properties with respect to the extent of the QM zone, the performance of different QM methods in predicting inter-molecular CT shall be clarified. Therefore, a small model system (see Figure 7.1) is derived from the QM/MM structure of bR, which contains the truncated chromophore (dimethyl-pentadieniminium cation), the saturated Asp85 and Asp212 side

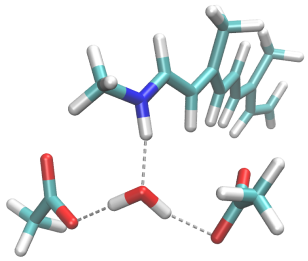

Figure 7.1: Model system used for comparative calculations of HBN mediated CT.

Table 7.1: Population Analysis of HF Density: W2 Net Charge (au).

oxygen	non-oxygen	Mulliken	Löwdin	NPA
SV(P)	SV(P)	-0.039	-0.071	-0.037
SV(P)+	SV(P)	0.154	0.076	-0.036
SV(P)+	SV(P)+	-0.015	-0.002	-0.032

chains, and the bridging water molecule (W2). In the following, molecular charges refer to the sum of their atomic net charges as obtained from some population analysis. AO-based population analysis provides reasonable molecular charges only for small and compact basis sets. They break down if diffuse functions are present. Natural population analysis[308] (NPA) provides a convenient way to avoid this problem and define meaningful molecular charges that are independent from the applied basis set. As shown in Table 7.1, the NPA derived net charge on W2 is hardly affected when diffuse functions are added to the carboxyl oxygen atoms. Mulliken and Löwdin charges, in contrast, deviate already with the SV(P) basis and change drastically with augmentation. Therefore, NPA charges should be considered when analyzing inter-molecular CT.

As the charge density on the carboxyl groups of the two anions is much more diffuse than on the cation, it is an obvious choice to augment the basis set by diffuse functions on the carbonyl oxygens. However, when applying different basis sets to different parts of the system, it should be ensured that no unbalance arises from this procedure. The HF NPA charges in Table 7.2 indicate that the CT is slightly reduced when adding the diffuse functions on the oxygens only. When augmenting the sets on every heavy atom, this change is partially undone. However, the molecular charges obtained with the SV(P) set and diffuse sp functions on the oxygen atoms agree fairly well with those obtained with Pople's 6-311++G** set and will be adopted in all following calculations.

Table 7.3 shows the inter-molecular CT as it is represented in different QM methods. Mulliken charges are compared here because they are available in all QM codes. All methods show a delocalization of the negative excess charge from the anions across the HBN, depositing ca. -0.04 au on the water molecule, which is the same result as found with HF NPA charges (Table 7.1). At the HF level, the cation's excess charge reduced by 0.17 au. While dynamic correlation at the MP2 level slightly increases the extent of this CT (0.24 au), the CISD and MR-DDCI3 results are again in good agreement with HF. In the case of MR-DDCI3, this may be due to the applied configuration se-

Table 7.2: HF NPA Charges (au): Effect of Diffuse Functions.

oxygen	non-oxygen	Ret	Asp85	Asp212
SV(P)	SV(P)	0.931	-0.932	-0.962
SV(P)+	SV(P)	0.951	-0.944	-0.971
SV(P)+	SV(P)+	0.939	-0.940	-0.967
6-311++G(d,p)	6-311++G(d,p)	0.947	-0.941	-0.967

SV(P)+ specifies Ahlrich's SV(P) basis set[240] augmented (heavy atoms) with diffuse sp functions[311] optimized for Pople's sets.[312]

Table 7.3: Summed Mulliken Charges (au) on Model Residues.

	HF	MP2	PBE0	PBE	CISD[a]	CISD[b]	MR-DDCI3[a]		
							S_0	S_1	S_2
Ret	0.834	0.761	0.614	0.430	0.826	0.829	0.835	0.803	0.815
Asp85	-0.874	-0.827	-0.804	-0.731	-0.871	-0.870	-0.875	-0.874	-0.874
Asp212	-0.921	-0.893	-0.765	-0.663	-0.917	-0.919	-0.923	-0.891	-0.903
W2	-0.039	-0.041	-0.044	-0.036	-0.038	-0.040	-0.038	-0.039	-0.039

The used basis set is SV(P). [a] Using a configuration selection threshold of $T_{\text{sel}} = 10^{-6}$. [b] Full CISD calculation, no configuration selection.

lection ($T_{\text{sel}} = 10^{-6}$), which considerably reduces the amount of dynamic correlation recovered in the CI wave functions. The full CISD calculation, however, performed without any configuration selection, shows little difference to the CISD calculation with selection and hence corroborates the HF and MR-DDCI3 results rather than the MP2 one. Finally, the MR-DDCI3 results show that the amount of CT hardly changes upon excitation into the S_1 or S_2 state.

DFT (LDA/GGA) grossly overestimates the CT, due to the obligatory underestimation of the integer derivative discontinuity of the total energy w.r.t. the particle number. This well known deficiency of DFT is appreciably alleviated using hybrid functionals, but the PBE0 functional, using 25% of HF exchange, gives still a much more pronounced CT than MP2.

The important conclusion that may be drawn from these results is that HF NPA charges provide a very efficient and reliable estimate of the CT between the chromophore and the complex counterion, and is representable also for the ground- and excited-state wave functions of MRCI calculations.

7.3.2 Convergence of CT

Figure 7.2 shows the topology of the HBN's in bR, psRII, and the two Rh setups Rh(u) and Rh(p). The network is traced starting from the PSB, following all strong hydrogen bonds, until a hydrogen-bond donor or acceptor is reached that belongs to the backbone, or to a side chain with no further hydrogen bonds. In the two Rh models, also the continuation of the HBN via the backbone of Cys187 to the network around Glu181 is considered. The number of traced hydrogen bonds ("level" in Figure 7.2) defines a selection of residues, which again defines a corresponding QM zone. "hbn3"

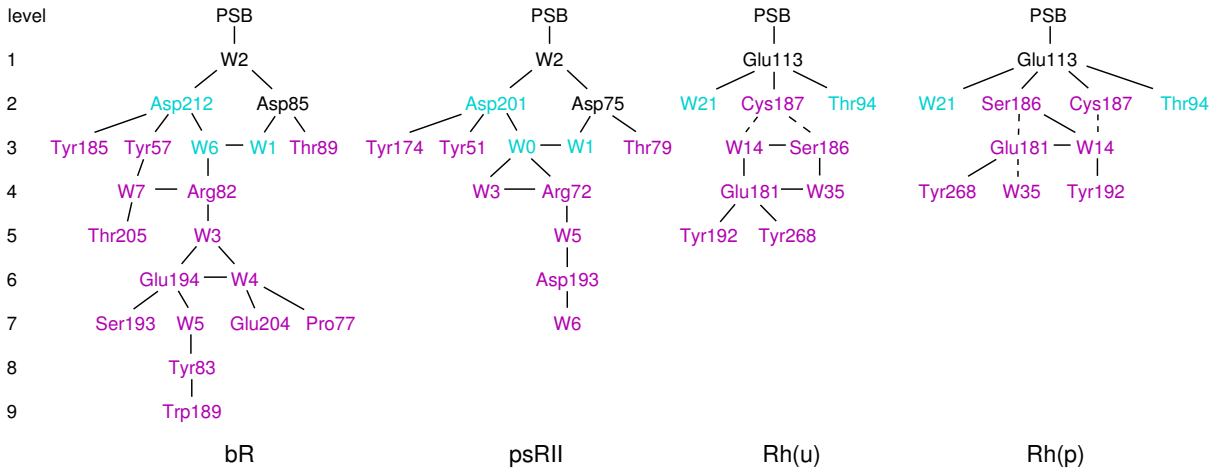

Figure 7.2: Topology of the HBN in different rhodopsin setups. QM zones, as defined in the text, are color-coded: black (qm2), cyan (qm4), purple (hbn2–hbn9). Water labels refer to the last two digits in the residue number of the corresponding x-ray structure.

in bR, e.g., contains the chromophore (qm1), the side chains of Asp85, Asp212, Tyr185, Tyr57, Thr89, and the water molecules W2, W6, and W1.

When the primary counterion, Asp85 (bR), Asp75 (psRII), and Glu113 (Rh) is included in the "qm2" QM zone, a charge exchange between the PSB and the counterion of ca. 0.05 au occurs. The extent of this CT is does hardly change when the QM zone is further extended. In particular, the inclusion of the second counterion and the bridging water molecules of the complex counterion in the archaeal rhodopsins ("qm4" in Tables 7.4 and 7.5) does not affect the net charge on the chromophore. Merely the charge distribution on the complex counterion changes when the QM zone is further extended.

The inter-molecular CT is dominated by the delocalization of the excess charge of ionic groups. This behavior is more pronounced for the anions (unprotonated Asp and Glu side chains), which donate negative charge (0.10–0.15 au in total) to all neighbouring hydrogen-bond partners, in particular water molecules. Water molecules connecting anionic with cationic groups (e.g., W402, W406/400, and W403/405 in bR/psRII) all carry a significant negative charge. Apart from the cation Arg82, the aromatic side chains of Tyr185 and Tyr57 (bR) act as acceptors of negative charge. For the charge delocalization of the complex counterion, they are more important than Arg82: While the total charge of the qm4 zone is hardly reduced with the extension towards the proton-release group (PRG) in "qm5" (adding Arg82) and "qm6" (adding W403, Glu194, W404, W405), it is reduced by 0.14 au when the side chains of Tyr57, Tyr185, and Thr89 are added in "hbn3". Note, that in the extension to qm6, the positive charge of Arg82 is delocalizing via W403 (negative) towards the PRG, but the charge distribution on the qm4 residues remains exactly the same as in the qm5 calculation. The same trends are found for the "total qm4" charge in psRII (Table 7.5), which is converged likewise with the extension to hbn3.

The CT mediating role of water salt bridges between donor and acceptor groups can be observed elsewhere: (1) In the qm2 calculations, the CT between PSB and primary counterion is nearly the same in Rh (Tables 7.6 and 7.7) and in the archaeal

Table 7.4: HF NPA Charges (au) for Different QM Zones in bR.

	qm2	qm4	qm5	qm6	hbn3	hbn9	hbn9[a]
qm4 residues							
Ret	0.956	0.949	0.950	0.949	0.946	0.942	0.942
Asp85	-0.936	-0.890	-0.889	-0.889	-0.854	-0.854	-0.854
Asp212		-0.934	-0.933	-0.933	-0.838	-0.836	-0.836
W402	-0.020	-0.039	-0.039	-0.039	-0.035	-0.035	-0.035
W406		-0.063	-0.027	-0.027	-0.060	-0.026	-0.025
W401		-0.023	-0.021	-0.021	-0.020	-0.019	-0.019
qm4 total		-1.000	-0.960	-0.961	-0.860	-0.827	-0.826
level 6-9				-0.912		-0.908	-0.989
donors of negative charge							
Glu194				-0.863		-0.814	-0.843
Thr205						0.020	0.020
Pro77						0.018	0.018
acceptors of neg. charge							
Arg82			0.960	0.909		0.877	0.921
Tyr185					-0.047	-0.047	-0.047
Tyr57					-0.059	-0.040	-0.040
Glu204 (prot)						-0.041	-0.043
W403				-0.038		-0.036	
Thr89					-0.034	-0.033	-0.033
Tyr83						-0.022	-0.022
Ser193						-0.019	-0.020
W404				-0.011		-0.020	-0.049
W407						-0.006	-0.006
W405				-0.038		-0.005	0.001
Trp189						-0.004	-0.004

The employed basis set is SV(P). [a] Excluding W403.

rhodopsins, despite the direct hydrogen bond in the latter. (2) If W403 is removed from the hbn9 QM zone (and replaced by MM water), the CT between the counterion region and the PRG is suppressed (see "level 6-9" charge in Table 7.4).

In the Rh(u) setup, the charges of the "qm4" residues (PSB, Glu113, Thr94, and W2021) are well converged already in the qm4 calculation. Cys187 receives a negative charge of merely 0.024 au, when treated quantum mechanically in the "hbn2" calculation. Any further extensions of the QM region, including the vicinal Ser186 (backbone and side chain), and following the salt bridges from the backbone of Cys187, do not affect the charges in the qm4 region. This is in difference to the Rh(p) setup, where the side chain of Ser186 forms a direct salt bridge to Glu113 and drains another fraction of negative charge (0.043 au) when added to the QM region (compare 4th and 5th columns in Table 7.7). This indicates that the backbone does not mediate CT between donor and acceptor groups, neither between neighbouring residues nor between the

Table 7.5: HF NPA Charges (au) of qm4 Residues for Different QM Zones in psRII.

	qm2	qm4	qm5	qm6	hbn3
Ret	0.954	0.948	0.949	0.949	0.943
Asp75	-0.938	-0.896	-0.895	-0.895	-0.859
Asp201		-0.936	-0.935	-0.935	-0.849
W402	-0.016	-0.039	-0.039	-0.039	-0.036
W400		-0.061	-0.034	-0.034	-0.057
W401		-0.017	-0.015	-0.015	-0.015
qm4 total	0.000	-1.000	-0.969	-0.969	-0.873

The employed basis set is SV(P).

Table 7.6: HF NPA Charges (au) of qm4 Residues for Different QM Zones in Rh(u).

	qm2	qm4	hbn2	hbn3	hbn4	hbn5
Ret	0.944	0.946	0.945	0.946	0.947	0.946
Ret[a]	0.933	0.937	0.937	0.938	0.938	0.938
Glu113	-0.944	-0.894	-0.869	-0.867	-0.867	-0.867
Thr94		-0.034	-0.033	-0.035	-0.034	-0.034
W2021		-0.019	-0.019	-0.019	-0.019	-0.018
qm4 total	0.000	0.000	0.024	0.026	0.027	0.027

The SV(P) basis set is augmented with diffuse sp functions on Glu113 and Glu181 carboxyl oxygens, except: [a] No diffuse augmentation.

side chain and any groups forming a salt bridge to the backbone of the same AA residue.

7.3.3 Changes in the ESP

In section 6.5.1 of the previous chapter, some effects of inter-residual CT on the ESP were discussed, i.e., the changes in the electrostatic environment of the chromophore that result when substituting the CHARMM fixed point charges by the QM density (PBE0 in that case) for all side chains in the binding pocket. The observed trends in the CT for bR and psRII were rather independent whether the chromophore was in-

Table 7.7: HF NPA Charges (au) of qm4 Residues for Different QM Zones in Rh(p).

	qm2	qm4	hbn2[a]	hbn2	hbn3	hbn4
Ret	0.948	0.949	0.948	0.948	0.949	0.948
Glu113	-0.948	-0.902	-0.879	-0.836	-0.834	-0.834
Thr94		-0.030	-0.030	-0.030	-0.030	-0.030
W2021		-0.017	-0.017	-0.017	-0.016	-0.016
qm4 total	0.000	0.000	0.023	0.066	0.069	0.068

[a] Excluding Ser186; this corresponds to hbn2 in Rh(u). The employed basis set is SV(P) augmented with diffuse sp functions on Glu113 carboxyl oxygens.

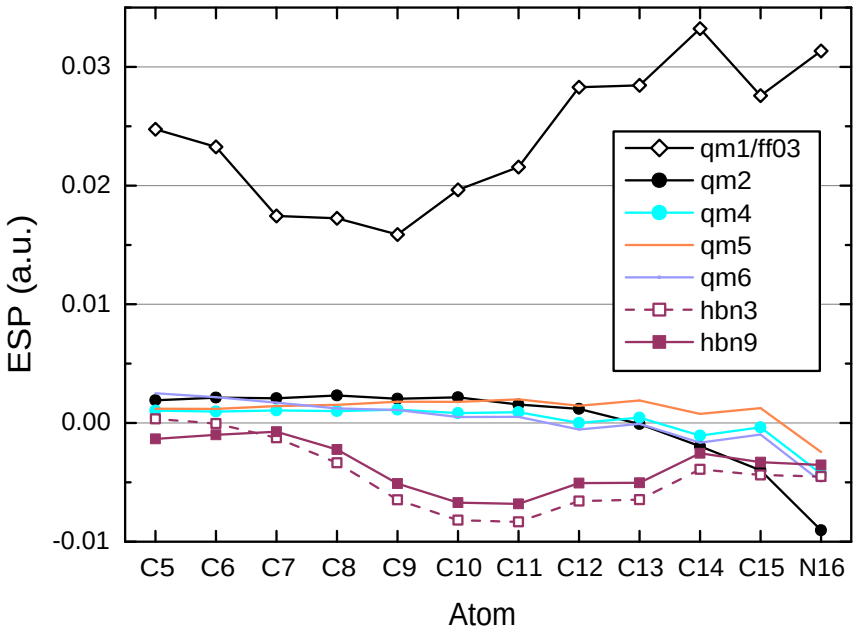

Figure 7.3: Difference ESP w.r.t. qm1/CHARMM27 Model at Retinal Atom Positions in bR.

cluded in the SCF calculation or not. Hence, CT in the binding pocket can essentially incorporated in a QM/QM/MM model, and its influence on the ESP is partially recovered in the empirical polar.h polarization model. Therefore, I will analyze here merely the changes in the ESP due to the extensions of the QM zone that were introduced in the previous subsection. The aim is to distinguish between the effects of charge injection to the chromophore and purely electrostatic interactions, when considering the dependency of excitation energies on the QM zone in section 7.3.4.

For various QM zones, the ESP was calculated along the conjugated chain of the chromophore, counting the contributions from the MM atoms (CHARMM27 or AMBER ff03 charges) and the HF NPA charges of those atoms that are not part of the qm1 zone. The resulting values can directly be compared with the ESP generated by the MM atoms in the qm1 models. Figures 7.3 to 7.6 show the difference in the ESP w.r.t. the latter.

Compared to the ESP gradient caused by the protein electrostatics, i.e., the ESP difference between Schiff base and β-ionone ring (ca. 0.08–0.14 hartree), the changes in the ESP are small when the QM zone is extended to qm2–qm6. Merely with the qm2 zone, the ESP is lowered by ca 0.01 hartree. In contrast to the net CT from the chromophore, the ESP is not converged w.r.t. extension of the QM zone. When including, e.g., the next level of the HBN (hbn3 and hbn2 in the archaeal and visual rhodopsins), the ESP is significantly lowered at the central part (bR, psRII) or around C12/C13 (Rh). This feature is found also in the QM/QM/MM models, as discussed in section 6.5.1. The changes in ESP remain also small compared to the changes that occur when the CHARMM charge model is exchanged by the AMBER ff03 one.

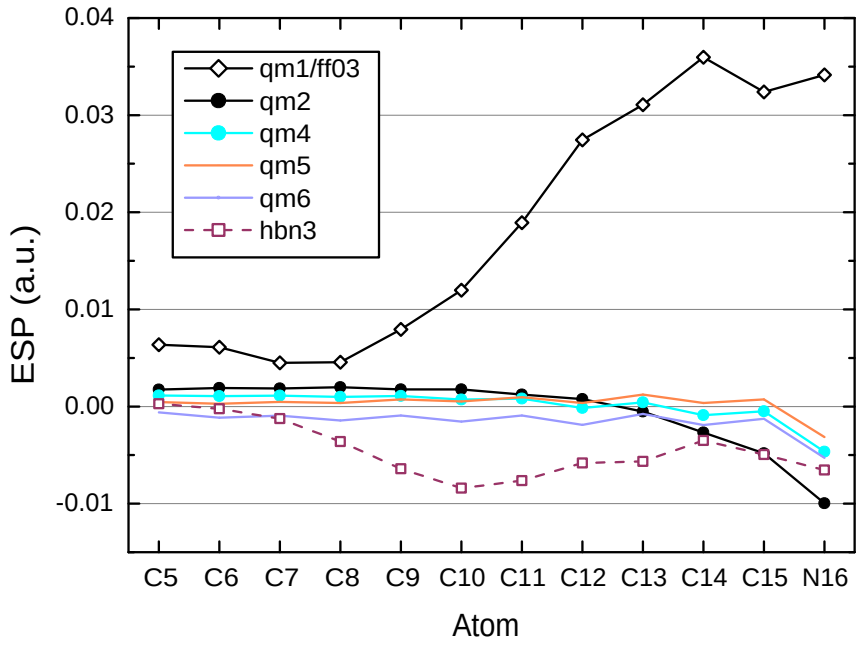

Figure 7.4: Difference ESP w.r.t. qm1/CHARMM27 Model at Retinal Atom Positions in psRII.

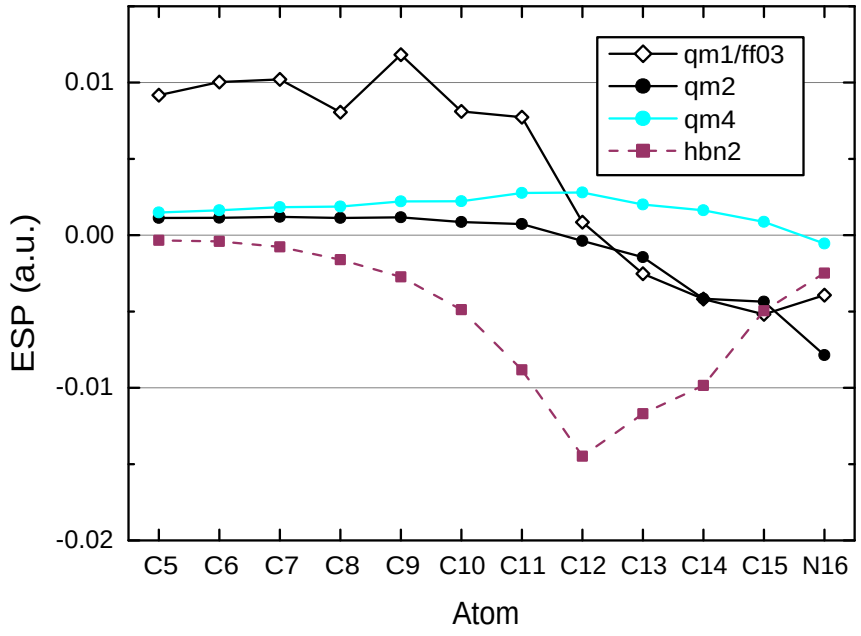

Figure 7.5: Difference ESP w.r.t. qm1/CHARMM27 Model at Retinal Atom Positions in Rh(u).

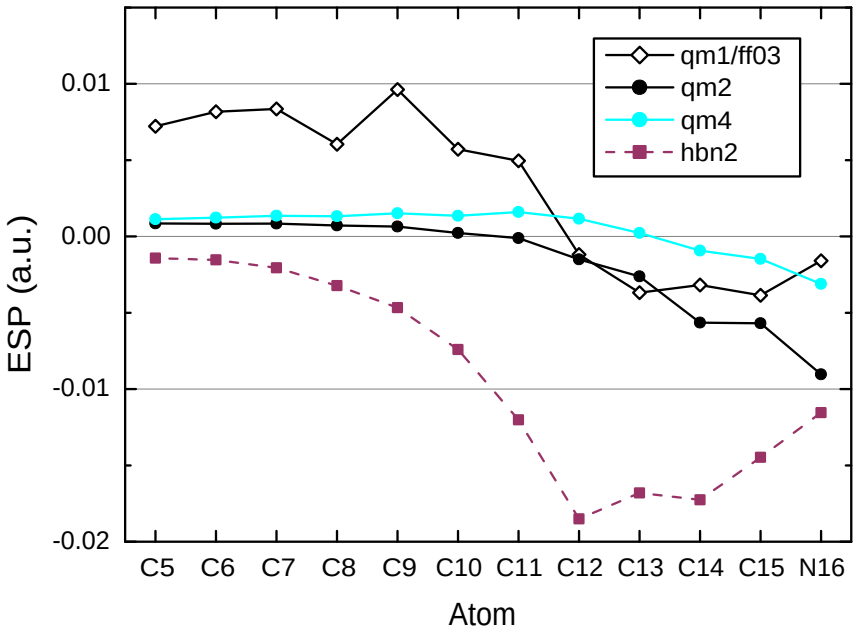

Figure 7.6: Difference ESP w.r.t. qm1/CHARMM27 Model at Retinal Atom Positions in Rh(p).

7.3.4 Convergence of Excitation Energies

Table 7.8 shows the SORCI S_1 excitation energies obtained with the various QM zones. The important trends are illustrated in Figure 7.7. All four models show significant blue shifts (0.05–0.14 eV) when extending the QM zone from qm1 to qm4, and the shifts are higher in the archaeal rhodopsins than in the bR models. These shifts are even considerably higher without a diffuse augmentation of the basis on the anionic carboxyl oxygen atoms (0.12 and 0.17 eV in br and psRII, respectively). Since the ESP along conjugated part of the chromophore is essentially unchanged (vide supra), the blue shifts can be associated with the observed CT. Note, that basis-set superposition, which is not corrected here, would stabilize the electron density only in the Schiff base region, where the electron population is increased in the S_1 state w.r.t. the ground state. Therefore, a potential BSSE due to the considered extensions of the QM zone would cause a redshift, i.e., counter-act the observed shift. Similar to the CT, also the shift in the excitation energies is already complete using the qm2 zone. However, the lowering of the ESP at N16 (Schiff base) may contribute to this quick convergence. Furthermore, in Rh(u) the excitation energy is less well converged with the qm2 zone, while also the corresponding change in the ESP is slightly less expressed.

All previous calculations presented in the chapter were using the same geometry for each setup. As Figure 7.7 (right) shows, the extent of the QM zone is also relevant for the QM/MM structure optimization. If the structure is optimized with the same QM zone as used for the excited-state calculation, the resulting shifts can be appreciably different. This is shown for the example of bR, where the excitation energy with the qm4 and qm5 zones is lowered by ca 0.04 eV.

Another interesting feature shown in Figure 7.7 (right) is the distinct bathochromic

Table 7.8: SORCI S_1 Excitation Energies (eV) Using Different QM Zones.

	qm1	qm2	qm4	qm5	qm6	hbn3[a]	qm1/ff03
bR	2.32	2.44	2.44	2.44	2.48	2.35	2.30
bR[b]	2.32	2.45	2.41	2.40	2.47		2.30
bR[c]	2.32	2.39	2.39				2.30
psRII	2.56	2.73	2.73				2.49
psRII[c]	2.56	2.71	2.70				2.49
Rh(u)[c]	2.53	2.58	2.58			2.56	2.61
Rh(p)[c]	2.42	2.43	2.47			2.48	2.45

The applied basis set is SV(P). [a] hbn3 for bR and psRII, hbn2 for Rh(u) and Rh(p). [b] Geometry was re-optimized with the corresponding QM zone. [c] Diffuse sp functions were added on the carbonyl oxygen atoms.

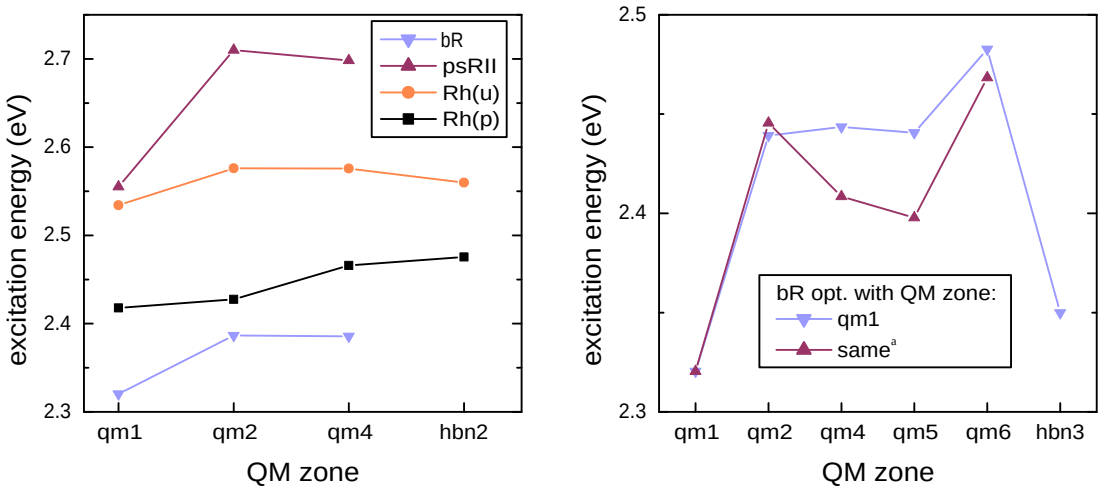

Figure 7.7: SORCI S_1 Excitation Energies (eV) Using Different QM zones.

shift in bR when including Trp185 in the QM zone (hbn3). This effect can neither be explained in terms of CT (Ret charge does not change) nor from the change in the ESP (would indicate rather a hypsochromic shift). In fact, polarization and dispersion interactions are responsible, as will be shown in the following section.

7.4 Dispersion Bathochromic Shifts in Rhodopsins

The influence of dispersive interactions on the absorption maximum of molecules in a condensed-phase environment is well known from the solvent shifts of nonpolar solutes in nonpolar solvents. Theoretical works in the 1950's have provided a rigorous understanding and derived approximate formulas from perturbation theory to predict these solvent shifts. As will be discussed in section 7.4.1, the results from such formulas are subject to some arbitrariness, due to the applied approximations and the required parameters. Problematic in the present case are the point-dipole approximation of transition densities and the isotropic averaging of their Coulomb interaction, which is not justified in context of a chromophore and the surrounding

polarizable groups that are of similar, or larger, dimensions than the distance between them. Therefore, explicit, non-statistical approaches are required to reliably quantify the dispersive redshift to the retinal absorption in rhodopsins.

As the leading term in the dispersion interaction decays like $1/R^6$ with the intermolecular distance, it is sufficient to consider only the interactions with highly polarizable groups in the immediate environment of the chromophore. In the case of the archaeal rhodopsins this includes three aromatic side chains, Trp86, Trp182, and Tyr185 in bR (psRII), respectively. In Rh, only two such residues ... $\Rightarrow$ expension of QM zone is acheavable $\Rightarrow$ do MRCI

7.4.1 Empirical Formulas

There exist various derivations of the solvation-induced dispersion redshift, emphasizing different physical aspects, such as the interaction of the transition dipole with an adiabatically or non-adiabatically induced reaction field due to the presence of a polarizable solvent molecule, or with an environment of a certain refractive index. Most start from the sum-over-states (SOS) representation of the 2nd order perturbation correction for the solute molecule interacting with the solvent. To eliminate the SOS, the energy differences in the denominators are replaced by "average excitation energies". Here, merely the simple and instructive derivation of Longuet-Higgins and Pople shall be summarized.[313]

The wave function of the solute–solvent system is written as a sum of products $|\Psi_J^{(1)}\Psi_K^{(2)}\rangle$ of the Fock states of the unperturbed solute (1), in state I, and solvent (2) molecule. In the following, the abbreviation $|JK\rangle$ will we used. Neglecting exchange, the wave function is not symmetrized. Adding the Coulomb interaction between the moieties as a perturbation of the reference state $|\Psi_0\rangle = |I0\rangle$, the correction to the total energy can be expanded in a perturbation series:

$$\begin{aligned}\Delta E_{I0} &= \langle I0|H'|I0\rangle - \sum_{J\neq I}\frac{\langle I0|H'|J0\rangle^2}{\Delta E_J^{(1)}} - \sum_{K>0}\frac{\langle I0|H'|IK\rangle^2}{\Delta E_K^{(2)}} \\ &- \sum_{J\neq I}\sum_{K>0}\frac{\langle I0|H'|JK\rangle^2}{\Delta E_J^{(1)} + \Delta E_K^{(2)}} - \dots \end{aligned} \tag{7.1}$$

The first term (first-order correction) is the Coulomb interaction between the unperturbed charge densities, as it is part of the usual QM/MM Hamiltonian for mechanical embedding. The second term adds the response of the solute to the field of the (unperturbed) solvent, which is contained in the electronically-embedded QM/MM Hamiltonian. The third term adds the response of the solvent to the charge density of the solute, and is accounted for only in QM/MM models with explicit polarization treatment, as the QM/polar.h model proposed in section 6.3. The fourth term, finally, describes the dispersion interactions at the lowest order, and is used to approximate the dispersion redshift:

$$\Delta E^{\text{disp}} \approx \sum_{J\neq K}\sum_{K>0}\frac{\langle I0|H'|JK\rangle}{\Delta E_J^{(1)} + \Delta E_K^{(2)} - \Delta E_I^{(1)}} - \sum_{J>0}\sum_{K>0}\frac{\langle 00|H'|JK\rangle}{\Delta E_J^{(1)} + \Delta E_K^{(2)}} \tag{7.2}$$

The nominators representing Coulomb interactions between transition densities

(mixed indices) are usually approximated by point (transition) dipole moment interactions:

$$\langle 00|H'|JK\rangle \approx \underline{\mathbf{M}}_{0J}^{(1)}\underline{\underline{\mathbf{T}}}\,\underline{\mathbf{M}}_{0K}^{(2)}, \tag{7.3}$$

where $\underline{\underline{\mathbf{T}}}$ is the second rank multipole interaction tensor (see section 6.3.1).

The obvious problem with the SOS expression (7.2) is the summation over the entire spectra of the solute and solvent Hamiltonians. It is solved by applying to approximations, (1) the averaging of the denominators and (2) the isotropic averaging of the transition dipole moments. (1) introduces effective "average excitation energies" $\Delta\overline{E}$, and (2) replaces (7.3) by $\frac{2}{3}M_{0J}^{(1)\,2}M_{0K}^{(2)\,2}R^{-6}$, where R is the effective distance between the interacting moments. Further, the assumption of neutral and nonpolar solute and solvent means that the lowest moment of the molecules (in both ground and excited-states) is the quadrupole moment and that their interactions can be neglected. Under this assumption, the sums can be extended to the full range. This leads to the following expression:

$$\begin{aligned}
\Delta E^{\text{disp}} \approx\ & \frac{2}{3}R^{-6}\left\{\frac{1}{\Delta\overline{E}^{(1)}+\Delta\overline{E}^{(2)}-\Delta E_I^{(1)}}\sum_J\sum_K M_{IJ}^{(1)\,2}M_{0K}^{(2)\,2}\right. && (7.4)\\
& -\frac{1}{\Delta\overline{E}^{(1)}+\Delta\overline{E}^{(2)}}\sum_J\sum_K M_{0J}^{(1)\,2}M_{0K}^{(2)\,2} && (7.5)\\
& \left.+\frac{\Delta\overline{E}^{(1)}}{(\Delta\overline{E}^{(2)}-\Delta E_I^{(1)})(\Delta\overline{E}^{(1)}+\Delta\overline{E}^{(2)}-\Delta E_I^{(1)})}M_{0I}^{(1)\,2}\sum_K M_{0K}^{(2)\,2}\right\} && (7.6)
\end{aligned}$$

Here, the SOS expressions can be associated with the static polarizabilities:

$$\alpha_I \approx \frac{2}{\Delta\overline{E}-\Delta E_I}\langle I|M^2|I\rangle = \frac{2}{\Delta\overline{E}-\Delta E_I}\sum_K M_{IK}^2 \tag{7.7}$$

Substituting the oscillator strength $f_{0I}=\frac{2E_I}{3}M_{0I}^2$, we arrive at

$$\begin{aligned}
\Delta E^{\text{disp}} \approx \frac{1}{3}\frac{\Delta\overline{E}^{(2)}\alpha^{(2)}}{R^6}&\left\{\frac{1}{2}\frac{\Delta\overline{E}^{(1)}-\Delta E_I^{(1)}}{\Delta\overline{E}^{(1)}+\Delta\overline{E}^{(2)}-\Delta E_I^{(1)}}\alpha_I^{(1)}-\frac{1}{2}\frac{\Delta\overline{E}^{(1)}}{\Delta\overline{E}^{(1)}+\Delta\overline{E}^{(2)}}\alpha_0^{(1)}\right.\\
&\left.+\frac{3}{2}\frac{\Delta\overline{E}^{(1)}}{\Delta E_I^{(1)}(\Delta\overline{E}^{(1)}+\Delta\overline{E}^{(2)}-\Delta E_I^{(1)})(\Delta\overline{E}^{(2)}-\Delta E_I^{(1)})}f_{0I}\right\}
\end{aligned} \tag{7.8}$$

Longuet-Higgins and Pople further assumed $\alpha_I^{(1)}=\alpha_0^{(1)}=\alpha^{(1)}$, which results in

$$\begin{aligned}
\Delta E^{\text{disp}} \approx \frac{1}{3}\frac{\Delta\overline{E}^{(1)}\Delta\overline{E}^{(2)}\alpha^{(2)}}{\Delta\overline{E}^{(1)}+\Delta\overline{E}^{(2)}-\Delta E_I^{(1)}}R^{-6}&\left\{\frac{1}{2}\frac{\Delta E_I^{(1)}}{\Delta\overline{E}^{(1)}+\Delta\overline{E}^{(2)}}\alpha^{(1)}\right.\\
&\left.+\frac{3}{2}\frac{1}{\Delta E_I^{(1)}(\Delta\overline{E}^{(2)}-\Delta E_I^{(1)})}f_{0I}\right\}
\end{aligned} \tag{7.9}$$

Table 7.9: Empirical Dispersion Red Shifts of the S_1 Excitation (eV).

system	residue	R (Å)		$\Delta\Delta E^a_{\text{disp}}$ (eV)		$\Delta\Delta E^b_{\text{disp}}$ (eV)	
bR	Trp86	4.80	(3.84)	-0.036	-(0.135)	-0.022	-(0.084)
	Trp182	6.04	(5.52)	-0.009	-(0.015)	-0.006	-(0.010)
	Tyr185	4.46	(3.64)	-0.041	-(0.138)	-0.027	-(0.091)
	Phe208	8.20	(7.60)	-0.001	-(0.001)	-0.001	-(0.001)
	total			-0.086	-(0.289)	-0.055	-(0.184)
psRII	Trp76	4.76	(3.77)	-0.039	-(0.158)	-0.025	-(0.101)
	Trp171	5.98	(5.33)	-0.010	-(0.020)	-0.006	-(0.013)
	Tyr174	4.54	(3.85)	-0.039	-(0.104)	-0.026	-(0.070)
	Phe134	7.02	(7.94)	-0.003	-(0.001)	-0.002	-(0.001)
	total			-0.088	-(0.282)	-0.057	-(0.183)
Rh(u)	Trp265	5.39	(5.56)	-0.016	-(0.013)	-0.009	-(0.007)
	Tyr268	4.95	(4.12)	-0.019	-(0.058)	-0.011	-(0.033)
	Tyr191	6.98	(7.84)	-0.002	-(0.001)	-0.001	-(0.001)
	Tyr178	7.70	(8.02)	-0.001	-(0.001)	-0.001	-(0.001)
	total			-0.035	-(0.071)	-0.020	-(0.040)
Rh(p)	Trp265	5.37	(5.50)	-0.015	-(0.013)	-0.008	-(0.007)
	Tyr268	4.94	(4.94)	-0.019	-(0.053)	-0.011	-(0.030)
	Tyr191	6.93	(7.89)	-0.002	-(0.001)	-0.001	-(0.001)
	Tyr178	7.56	(7.87)	-0.001	-(0.001)	-0.001	-(0.001)
	total			-0.034	-(0.066)	-0.019	-(0.037)

The effective intermolecular distance R is calculated as average over all atoms of the conjugated part of the molecules either weighted by $1/R^6$ or simply taken as center of coordinates (values in parentheses). [a] Using the formula of Longuet-Higgins and Pople[313], eq (7.9). [b] Using eq (7.10) from Ren *et al.*[227]. Average excitation energies are evaluated as first ionization potential from HF (in eV: 9.54, 9.54, 9.89, 9.85 for retinal in bR, psRII, Rh(u), Rh(p), Trp 7.55, Tyr 8.29, Phe 8.74); polarizabilities from MP2/cc-pVQZ (in Å^3: retinal 84, Trp 16.3, Tyr 12.7, Phe 11.7); experimental S_1 excitation energies; oscillator strength of bR (0.80)[227] was extrapolated using SORCI results for psRII (0.84), Rh(u) (0.63), Rh(p) (0.60).

Another empirical formula was considered by Ren *et al.* in the context of dispersion red shifts in bR and psRII:

$$\Delta E^{\text{disp}} \approx -\frac{\pi}{4}\frac{\alpha^{(2)} f}{R^6}\frac{2\Delta\overline{E}^{(1)} - \Delta E_I^{(1)}}{\Delta\overline{E}^{(1)}(\Delta\overline{E}^{(1)} - \Delta E_I^{(1)})} \tag{7.10}$$

This formula describes only the f_I-dependent part of the shift, i.e., the interaction between the transition dipole moment of the solute and its reaction field from the induced moments in the solvent. It yields quite similar results as the first term in eq (7.9). Ren *et al.* considered also an additional term for the excitation coupling, which is dominating when the excitations of solute and solvent are close to resonance. In the case Trp75 in psRII, it increased the shift of eq (7.10) by ca. 30%.

Table 7.9 shows dispersion shifts calculated with the empirical formulas for all

Table 7.10: Charge Transfer to Aromatic Residues: HF/SV(P) NPA Charges (au).

	bR	Rh(u)
Ret	0.981	0.992
Trp86/Trp265	0.012	0.007
Trp182/Tyr268	0.003	0.001
Tyr185/—	0.004	

The QM zone contains the side chains of the listed residues, the remainder of the protein is represented by CHARMM27 charges.

aromatic residues in bR, psRII, and the Rh(u) and Rh(p) models within 8 Åof the chromophore π system. The results demonstrate the strong dependence on the intermolecular distance parameter R. Moreover, the way this parameter is evaluated, e.g., using either the centroid of each π system, or the average $\langle R^{-6} \rangle$ over the same set of atoms, determines the result more than the actual choice of any other parameter. This fact simply reflects the break-down of the point-dipole approximation and emphasizes the need to evaluate the interaction of the transition densities more accurately. However, some qualitative insights can be obtained from the empirical formulas: (1) only polarizable groups within ca. 5.5 Å from the chromophore contribute significantly to the dispersion redshift. (2) the latter is much smaller in Rh than in the archaeal rhodopsins.

7.4.2 Differential Dispersion Calculations on the MRMP2 Level

The empirical calculations of the last section have been used to select the relevant residues for a quantitative analysis of the dispersion redshift at the SORCI level of theory. Due to the structural similarity, the dispersion redshifts will be similar between bR and psRII as well as for the two Rh models. This assumption is corroborated by the empirical calculations. Therefore, the SORCI calculations were performed for bR and the Rh(u) model only. In order to separate the effect of differential dispersion from the effects of CT and classical polarization, the latter two have to be considered individually. As Table 7.10 shows, intermolecular CT is negligible and will therefore not influence the excitation energy. The effect of polarization is obtained from QM/QM/MM and QM/polar.h/MM calculations in which only those residues are polarized that are added to the qm1 QM zone in the dispersion calculations. In the case of bR, these are Trp86, Trp182, and Tyr185; in the Rh(u) model, Tyr268 and Tyr191 are included in the supermolecular dispersion calculations. In contrast to chapter 6, the second QM region, which comprises the aromatic side chains, is calculated on the HF/SV(P) level here, rather than PBE0/SV(P).

In Table 7.11 are presented the SORCI excitation energies for the QM/MM, QM/QM/MM, QM/polar.h/MM, and the supermolecular QM/MM calculations. With respect to the qm1 QM/MM model, which treats only the chromophore quantum mechanically, significant bathochromic shifts result when extending the QM zone to include Trp86 or Tyr185 in bR and Trp265 or Tyr268 in Rh. The largest shift (Trp86 in bR) amounts to 0.13 eV. Trp182 in bR causes no net shift when included in the SORCI calculation. Including all three (two) aromatic residues simultaneously, the resulting

Table 7.11: SORCI S_1 Excitation Energies (eV) for Extended QM Zones.

QM zone	bR	shift	Rh(u)	shift
Ret	2.32		2.53	
Ret+Trp86/Trp265	2.19	-0.13	2.44	-0.09
Ret+Trp182/Tyr268	2.32	-0.00	2.47	-0.06
Ret+Tyr185/−	2.22	-0.10		
Ret+all 3/2	2.12	-0.20	2.40	-0.13
QM/polar.h/MM	2.19	-0.13	2.41	-0.12
QM/QM/MM	2.20	-0.12		

In the QM/polar.h/MM and QM/QM/MM calculations, the retinal chromophore (Ret) is treated with SORCI, all three (bR) or two (Rh) aromatic residues are polarized at the polar.h or HF/SV(P) level. The charge distributions are obtained fully self-consistently, excitation energies are calculated corresponding to approach (ii). CHARMM27 charges are used for the remainder of the protein.

shift amounts to -0.20 eV in bR and -0.13 eV in the Rh(u) model, which indicates that the shifts are almost additive. The results for bR are comparable to the shifts obtained by Ren *et al.*[227] using semiempirical (MNDO) CISD (-0.09, -0.02, and -0.05 eV for Trp86, Trp182, and Tyr185, respectively). However, this comparison must be considered with care, as the shifts might depend on the charge model employed in the conventional QM/MM calculation. Moreover, Ren *et al.* correlated merely a part of the π system of the chromophore and aromatic side chains.

Interestingly, similar bathochromic shifts are obtained also in the QM/QM/MM and QM/polar.h/MM models, where the charge distribution on the aromatic residues is refined but only classical (static) polarization is incorporated. Here, the excitation energies were evaluated corresponding to approach(ii) with initial-state averaging (see chapter 6). The SORCI/polar.h/MM model reproduces the result from the SORCI/HF/MM model. When the excitation energies of the supermolecular SORCI calculations are compared with these hybrid models, the effect of the additional electron correlation that is responsible for the dispersive redshift becomes visible. In the case of bR, the supermolecular calculation yields a significantly lower excitation energy (by 0.07–0.08 eV), while the difference is negligible for Rh.

7.5 Towards Absolute Excitation Energies of Retinal Proteins

In this section, the systematic improvements of the QM/MM model for biologic chromophores introduced in chapters 6 and 7 shall be combined to arrive at a realistic prediction of the vertical excitation energy of different rhodopsins. The new model incorporates the CT effects discussed in section 7.3 by extending the QM zone to include the complex counterion ("qm4" zone), as well as the improved protein electrostatics (ESP charge model) with an explicit treatment of polarization using the polar.h model. Due to its additive character, the contribution of differential dispersion interactions to the excitation energy can be included in an *a posteriori* correction. They are obtained as the excitation-energy difference between the SORCI/polar.h/CHARMM model and

Table 7.12: Geometry Parameters of DFTB vs. PBE0/TZVP QM/MM Structures.

		ABL[a] (Å)	BLA (Å)	H bond[b] (Å)	C5-C6-C7-C8 (°)
bR	DFTB	1.396	0.056	1.79	167
	PBE0	1.386	0.069	1.84	170
psRII	DFTB	1.397	0.065	1.82	171
	PBE0	1.386	0.079	1.76	173
Rh(u)	DFTB	1.397	0.066	1.73	-42
	PBE0	1.388	0.080	1.67	-45
Rh(p)	DFTB	1.397	0.062	1.72	-41
	PBE0	1.387	0.076	1.66	-44
Rh(E181A)	DFTB			1.61	-41
	PBE0			1.62	-44
Rh(E181Q)	DFTB			1.58	-41
	PBE0			1.31	-44

[a] Average bond length of the conjugated chain. [b] Length of the hydrogen bond between the Schiff base proton and the acceptor oxygen atom.

the supermolecular SORCI/CHARMM model (see Table 7.11). As argued in the previous chapter, the structural similarities between bR and psRII as well as between the Rh models justify to assume the same dispersive shifts in the respective models.

Finally, the error made by using SCC-DFTB for the QM/MM geometry optimization is accounted for. The chromophore (qm1 QM zone) has been re-optimized in the fixed binding pocket, starting from the SCC-DFTB QM/MM geometry. The PBE0 hybrid functional and TZVP basis are applied in the QM zone, while the same CHARMM point charges and Van-der-Waals interactions are applied as in the DFTB QM/MM optimization.

The main structural changes are given in Table 7.12. PBE0 predicts slightly larger bond lengths (+0.010 Å) and an increased BLA (+0.014 Å). Corresponding to the analysis of geometry-induced optical shifts, presented in chapter 5, both modifications will cause a blue shift. Further, the ring-twist dihedral angle (C5–C6–C7–C8), which is also strongly dependent on the method, is slightly modified by the PBE0 optimization. The trend is opposite in the all-*trans* configurations in bR and psRII (coplanarization) and in the Rh 6-s-*cis* configurations, but the differences are too small to have a pronounced impact on the absorption maximum. Finally, the strength of the salt bridge between the Schiff base and the direct counter ion shows some variance, if considering the NH$\cdots$O distance. The latter, however, is not a very profound measure for the actual interaction between the two moieties and the effect on the excitation energy cannot be deduced reliably.

The resulting shifts in the excitation energy are considerable, ranging from +0.13 to +0.21 eV (see Table 7.13), although SCC-DFTB underestimates the BLA of the conjugated chain much less than DFT/GGA.

Adding the corrections for dispersive interactions and the chromophore geometry to the qm4 SORCI/polar.h results, a "best estimate" is obtained for the excitation energy of each structural model (Table 7.13), which can directly be compared to ex-

Table 7.13: SORCI S_1 Excitation Energies (eV) for Different Protein Setups and Models.

QM zone	MM model	bR	psRII	Rh(u)	Rh(p)	Rh(E181A)	Rh(E181Q)
qm1	CHARMM	2.32	2.56	2.53	2.42	2.34	2.35
qm1	polar.h	2.16	2.42	2.36	2.26		
qm4	polar.h	2.23	2.47	2.49	2.30	2.36	2.41
dispersion shift		-0.07	-0.07	-0.01	-0.01	-0.01	-0.01
geometry correction[a]		+0.13	+0.21	+0.16	+0.16	+0.18	+0.17
best estimate		2.29	2.61	2.64	2.45	2.53	2.57
exp.		2.18[b]	2.50[c]	2.47[d]	2.47[d]	2.48[d]	2.44[d]/2.46[d,e]

[a] Absorption shift between the DFTB and the PBE0 QM/MM optimized (qm1 zone) geometry. [b] Ref.[11]. [c] Ref.[279]. [d] Ref.[314]. [e] In presence of 200 mM NaCl.

periment. The remaining difference between the theoretical excitation energies and experimental absorption maxima is dominated by the error arising from the structural model itself and the applied SORCI method. The first may also contain effects of the different environments (crystal vs. buffer solution).

In comparison with the experiment, the theoretical estimates for the absorption maxima of bR and psRII are 0.11 eV (24 nm) too high, whereas the shift bR vs. psRII of 0.32 eV is exactly matched. This is an improvement to the conventional QM/MM result, where the shift is underestimated by 0.08 eV. The shift is essentially altered by the PBE0 geometry optimization, whereas the other model advancements are affecting merely the absolute values. In the two considered Rh mutants E181A and E181Q, Glu181 is replaced by a neutral alanine or glutamine AA. The lack of any significant shift in the absorption maximum compared to the wildtype was interpreted as a proof for a protonated Glu181 in the latter.[314] The theoretical estimates for the mutants are slightly higher in energy than the experimental values, as in the case of the archaeal rhodopsins. Neither of the two wildtype Rh models yields the same excitation energy as the mutants, the Rh(u) result is 0.1 eV too high, whereas the Rh(p) one is 0.1 eV too low. This situation does not allow a clear assignment of the protonation state of Glu181, but it shows that the underlying assumption of the experimental assignment might be wrong: a change of the protonation state of Glu181 does not cause a dramatic shift of the excitation energy, and both the Rh(u) and the Rh(p) model are equally consistent with the experimental absorption data. This conclusion is not affected by the applied corrections for the chromophore geometry or the dispersive shift, but depends on the representation of the protein electrostatic model: In the conventional QM/MM model based on CHARMM27 charges, the mutant excitation energies are significantly too low and are in better agreement with the Rh(p) model. Other charge models might give different results. In all cases, the Rh(u) model yields a better agreement for the shifts to bR and psRII.

7.6 Conclusions

In this chapter, the impact of inter-molecular and inter-residual charge transfer (CT) and dispersion interactions on the excitation energy was studied by varying the extent of the QM zone in the QM/MM approach and analyzing the resulting changes in charge distribution, ESP, and energetics.

In the case of CT, it was shown that HF SCF calculations and natural population analysis can be used to estimate accurately and efficiently the CT that occurs in the excited-state calculations, and therefore facilitate the definition of an appropriate QM zone. Concerning the latter, it was found that the net CT from the PSB of retinal to the surrounding HBN can be completely incorporated in the excited-state calculations when the QM zone includes the immediate counter ion, bridging water molecules, and direct hydrogen-bond partners of the Schiff base. Additional changes in the ESP that occur substituting the MM point charges by a QM density cannot be incorporated in an excited-state QM/MM approach, due to their slow convergence. Here, other strategies must be followed to improve the electrostatic representation of the protein environment, like the QM/QM/MM or QM/polar.h models introduced in chapter 6. It is important to augment the basis set with diffuse functions on the anionic groups to obtain realistic CT and avoid artificial blue shifts in the excitation energy. Furthermore, the QM zone should be extended also during the geometry optimization, implying that the QM method yields more accurate structures of HBN's.

The SORCI/HF/MM and SORCI/polar.h/MM calculations have shown that a significant redshift results when the CHARMM27 point charge model for the aromatic residues in the binding pocket is substituted by a more accurate, polarizable charge representation. The additional dispersion redshift that is incorporated in the supermolecular SORCI calculations is merely of the order of 0.07–0.08 eV in bR and negligible in Rh. The comparison with empirical dispersion calculations suggests that the evaluation of the inter–molecular distance is more important than the actual approximation for the dispersion redshift. The formula of Longuet-Higgins and Polple[313] yields the correct order of magnitude, but only if the inter–molecular distance parameter is evaluated based on an effective atomic average $\langle 1/R^{-6} \rangle$. It was shown that significant contributions (>0.01 eV) to the dispersion redshift arise only from highly polarizable groups with an effective distance of ca. 6 Å or less from the conjugated part of the chromophore.

The largest remaining uncertainty of the computational model consists in the strong effect of the geometry of the chromophore and the HBN of the complex counter ion. This is reflected, e.g., by the shifts of up to 0.21 eV when re-optimizing the chromophore using PBE0/TZVP. In total, the applied enhancements and corrections to the conventional QM/MM scheme are partially canceling, but in an unsystematic way. For bR and psRII, the incorporation of CT, protein polarization, and differential dispersion leads to small net shifts, whereas for the considered Rh models, the predicted excitation energies are significantly blue-shifted by up to 0.22 eV.

Chapter 8

Summary, Conclusions, and Outlook

The aim of this work is to establish new multi-scale computational schemes for theoretical spectroscopy on biologic systems, with focus on the most challenging field: the quantitative prediction of the optical properties of chromophores and their dependence on structural changes in their molecular environment. These changes may be associated with mutation experiments of proteins, different configuration states (e.g., intermediates along a photocycle), or comparison between theoretical structure models, e.g., derived from homology modeling, and the "real" system in vivo, for which only spectroscopic data is available experimentally.

Assessment of QM Methods for Spectral Tuning Applications

The PSB of retinal represents an ideal test case which reveals many of the computational difficulties that may arise when studying excited states of biologic chromophores. This work has discussed, for the first time, the problem of intramolecular charge-transfer states TDDFT, and the qualitatively wrong excited-state gradient in a conjugated polyenic system. These errors have important implications for the applicability of TDDFT in the context of spectral tuning and excited-state dynamics, which explain short-comings of this method in recent applications: The underestimation of electrostatically induced shifts in the S_1 absorption,[233,315,316] the prediction of high barriers in the excited-state photoisomerization pathway,[317] and artificial excited-state intermediates and radiationless decay via single-bond isomerization.[318] Furthermore, it was shown that the bond-length alternation of the chromophore strongly depends on the method used for geometry optimization and drastically affects the calculated excitation energies and charge distribution on the chromophore, in particular, in the protein environment.

The positive outcome of this methodological analysis can be summarized as follows:

- The chromophore geometry in the electronic ground state can be described in close agreement with reference CASPT2 calculations[7] using much more efficient MP2 and hybrid DFT methods. Furthermore, the approximate DFT method SCC-DFTB yields chromophore structures of similar quality at even lower computational cost.
- All post-HF approaches that include both dynamic and non-dynamic correlation yield comparable results for the excited-state properties. In particular, CASPT2,

SORCI, and the semiempirical OM2/MRCI method are in close quantitative agreement. The latter approach is suggested as the QM method of choice for optical calculations on large ensembles of structures, as required for configurational sampling or perturbation analysis.[280]

Based on these findings, a combination of hybrid DFT and multireference methods for structure optimization/MD simulations and excited-state calculations was suggested and applied to different rhodopsins. This approach was recently adopted in studies on Rh mutants and cytochrome.[319,320]

Polarizable Protein Electrostatics

While the development of polarizable protein force fields is a field of active research and has not yet reached the level of routine application, the current work has shown that substantial improvements in the electrostatic interactions in proteins can be achieved with simple polarization models. These can be applied in accurate single-point QM/MM calculations based on the structures obtained with conventional, well tested force fields. The presented polar.h model requires a minimum of parameters and reproduces polarizabilities of neutral amino-acid side chains within 3% of MP2 reference calculations.

A new approach for the calculation of excitation energies in QM/QM or QM/polarizable-MM models was suggested. In the application to the binding pocket of different rhodopsins, polar.h reproduces the effect of polarization on the electrostatic potential and excitation energy, as compared to hybrid DFT calculations in a QM/QM/MM setup. Due to the strong electrostatic interaction between the chromophore and its host protein, the improved protein electrostatic model leads to significant corrections to the absorption maxima.

Dispersion and Charge Transfer

The inclusion of partial charge transfer (CT) and dispersive interactions between the chromophore and the protein environment is computationally involved. The CT can be included only by extending the region which is treated quantum mechanically. In fact, this work gives the first systematic analysis of inter-residual charge transfer across hydrogen-bonded networks. The major results are:

- The charge transfer is dominated by the delocalization of the excess charge of ionic groups, which is locally restricted. Therefore, the net charge on the chromophore converges quickly when the QM region is extended appropriately.
- The changes of the electrostatic potential due to further extensions of the QM region do not converge. Inclusion of ionic groups connected to the chromophore via more than 2–3 hydrogen bonds are futile and may even cause imbalances in the charge distribution that would be refined again in further extensions of the QM region.
- Hartree–Fock natural population analysis (NPA charges) represents an efficient and reliable tool to check the convergence of the chromophore net charge and define a suitable QM region that incorporates the major CT effects.

Dispersive interactions have been studied for the first time using extended MR-MP2 calculations. Their contribution to the excitation energy is significant only in cases where highly polarizable groups are in close steric contact with the chromophore, as in bR and psRII. This can be tested easily with empirical formulas for the dispersive redshift, when the distance parameter is evaluated properly, as suggested in this work.

Outlook

The achieved improved accuracy in the prediction of absorption maxima is decisive for the assessment of structural models by their optical properties. The methodological improvements are employed in ongoing studies on the protonation state of Glu181 in Rhodopsin (see section 6.4), the tuning mechanisms in the cone pigments, which are responsible for color vision, and the modeling of the late O state in the photocycle of bR.[321] Apart from excited-state calculations, also other kinds of theoretical spectroscopy, such as nuclear magnetic resonance (NMR) or resonance Raman (RR) may profit from the improved electrostatic representation of the protein environment. Further, in the field of bioenergetics, the calculation and decomposition of reaction barriers and enthalpies may be improved for reactions involving extended charge relocations.

Chapter 9

Appendix

9.1 Calibration of Thresholds within the SORCI Method

For all thresholds used within the SORCI method, appropriate values are determined in order to achieve a maximum of accuracy in the excitation energies of the lowest two valence states of the PSB of retinal and its model systems. The S_1 energy is requested to be converged within 0.1 eV of the method's limitation for a five-conjugated double bond model in vacuum, as well as in the polarizing field of a counter ion. For this benchmark, the structure published in Ref.[9] is used, including a PSB5 model of the Rh chromophore and point charges of the principal counter ion (see Figure 9.1). See section 3.3.4 for further information about the individual thresholds.

The range of active (unfrozen) orbitals that enter the CI calculation can be set via an energy criterion (E_{win}). For occupied orbitals a lower threshold of 3 hartree is chosen to establish the frozen-core approximation. An upper threshold limits the number of virtual orbitals. The latter is not computationally critical since the number of approximated natural orbitals that enter the final CI calculation is limited by the threshold T_{nat} (see below). However, in order to reduce the memory required for integral storage, a threshold of 3 hartree can be used without loss of accuracy in the case of PSB5 (see Table 9.2). This value can also be used safely for the complete chromophore, which has a lower ionization potential than the truncated models.

The reference space is constituted by all configurations from a RAS (6 electrons in 6 π orbitals with up to triple excitations) that contribute to any of the requested three

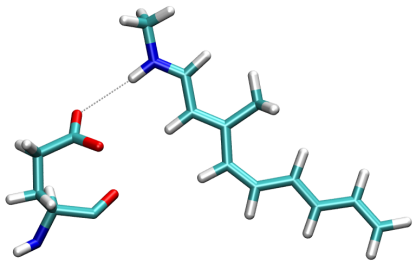

Figure 9.1: The setup of Ref.[9] used for calibration of SORCI thresholds; the Glu113 residue is represented by point charges.

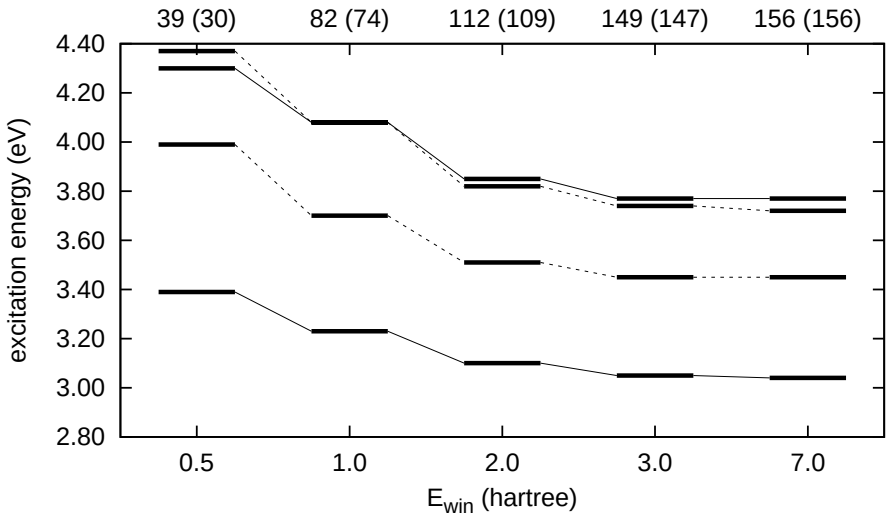

Figure 9.2: Dependence of vertical excitation energies (eV) on the range of non-frozen orbitals via energy threshold E_{win}. Upper line: number of non-frozen virtual orbitals for PSB5 and PSB5+Glu133 (in parentheses). Levels of the system PSB5+Glu133 are connected via dashed lines.

roots with a coefficient larger than T_{pre}. Figure 9.3 shows that the excitation energies for this system are not very sensitive to the size of the reference space. Surely, the accuracy could be improved by using huge reference spaces, but this is less efficient than to improve, e.g., T_{sel}. The strategy of SORCI is to use a small reference space and take care of strongly perturbing configurations in an additional variational step. Interestingly, the least CPU time was not obtained with the smallest number of configurations, but with $T_{\mathrm{pre}} = 10^{-3}$, which is the value employed in all calculations in this work.

Approximated natural orbitals (ANO) are kept frozen in the final calculation when their occupation numbers are below the threshold T_{nat}. As Figure 9.4 shows, convergency is achieved between values of 10^{-5} and 10^{-6}. The latter has been chosen for all calculations in this work.

The selection threshold T_{sel}, which divides the first-order interacting space into subspaces for the variational and second-order perturbation treatment is critically with respect to CPU time. As Figure 9.5 indicates, excitation energies are not entirely converged at $T_{\mathrm{sel}} = 10^{-6}$. Nonetheless, this value has been chosen as the default for two reasons: First, the increase of the S_1 excitation energy with tightening of the selection threshold (beyond 10^{-6}) might be systematic because of the overestimation of dynamic correlation in (MR-)MP2 compared to (MR-)CISD; on the other hand, the missing part of the dynamical correlation at the MR-CISD level (i.e., $T_{\mathrm{sel}} = 0$) would lower the excitation energy of the ionic S_1 state further. The latter applies also to the effect of completing the basis set. Thus, error cancelation can be expected. Second, the difference between the S_1 energies of the two test systems (i.e., the shift due to the counter ion) is already converged within 0.1 eV for $T_{\mathrm{sel}} = 10^{-5}$.

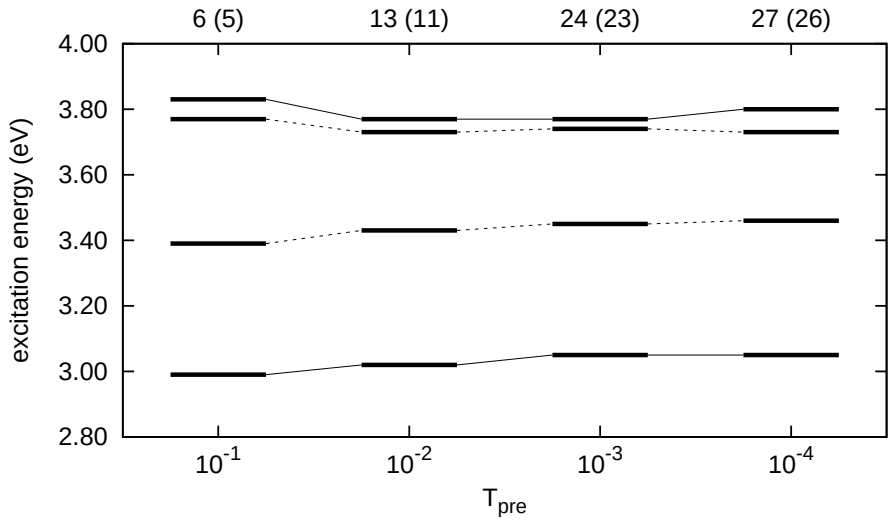

Figure 9.3: Dependence of vertical excitation energies (eV) on the reference space selection threshold T_{pre}. Upper line: number of configurations in the reference space (final MRD-DCI3 calculation), values for PSB5 and PSB5+Glu133 (in parentheses). Levels of the system PSB5+Glu133 are connected via dashed lines.

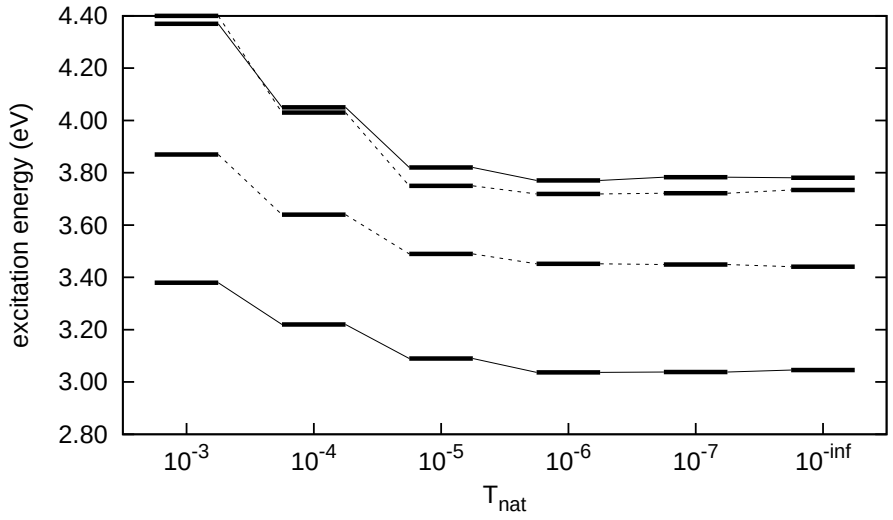

Figure 9.4: Dependence of vertical excitation energies (eV) on the natural orbital threshold T_{nat}. Levels of the system PSB5+Glu133 are connected via dashed lines.

9.2 Basis Set Convergency of SORCI Excitation Energies for PSB Systems

Finally, the basis set convergency of excitation energies shall be tested for several retinal models. For a minimal PSB3 model, fully converged values are not obtained within standard Pople basis sets. Diffuse augmentation functions and (at least) a triple zeta basis is required to achieve convergency within 0.1 eV. Surprisingly, the covalent S_2 state profits more from basis set extension than the ionic S_1 state. For the larger

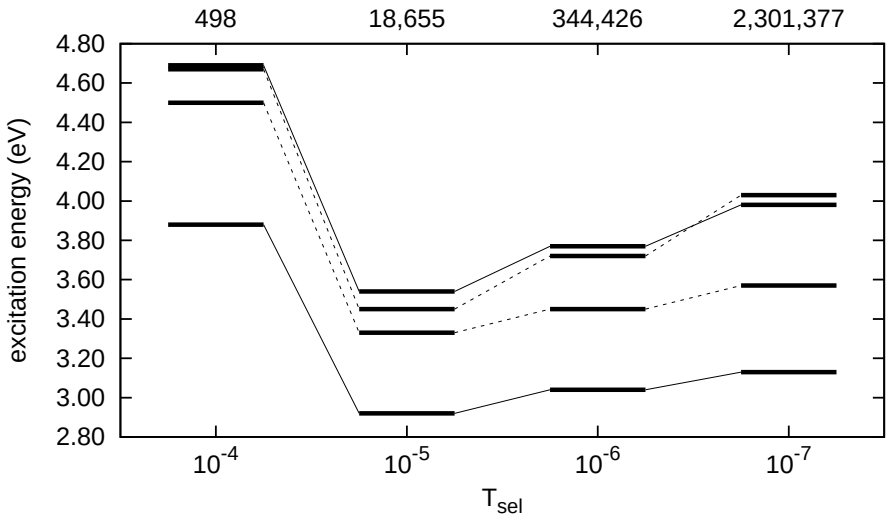

Figure 9.5: Dependence of vertical excitation energies (eV) on the selection threshold T_{sel}, which divides the first-order interacting space (FOIS). Top line: number of configuration state functions in the final variational step. Levels of the system PSB5+Glu133 are connected via dashed lines.

PSB5 model (4-*cis*-γ-methylnona-2,4,6,8-tetraeniminium cation), an augmented split-valence basis appears to be sufficient. For the full PSB chromophore, basis-set dependency is much less critically, since the density of the conjugated π-system is even more compact than for PSB5. Therefore, augmentation with diffuse functions is not necessary and the SV(P) set is used for the full chromophore throughout this work.

Table 9.1: Vertical excitation energies (eV) of PSB3 (*tZt*-penta-3,5-dieniminium cation, CASSCF geometry) for various basis sets. The dimension of the orbital space and auxiliary basis for the density fit (RI-approximation) are given.

Basis set	dim(MO)	dim(Aux)	S_1	S_2
SV(P)	100	432	4.38	5.64
aug-SV(P)	154	600	4.16	5.36
TZVP	162	432	4.21	5.43
aug-TZVP	248	600	4.07	5.23
aug-TZVPP	466	974	4.10	5.27
aug-cc-pVTZ	460	1004	4.06	5.24
6-31G*	100	454	4.37	5.63
6-311+G*	156	564	4.20	5.44
6-311++G**	188	636	4.18	5.41

Table 9.2: Vertical excitation energies (eV) of PSB5 (4-*cis*-γ-methylnona-2,4,6,8-tetraeniminium cation, CASSCF geometry) for various basis sets. The dimension of the orbital space and auxiliary basis for the density fit (RI-approximation) are given.

Basis set	dim(MO)	dim(Aux)	S_1	S_2
SV(P)	182	782	3.00	3.80
aug-SVP	379	1026	2.80	3.59
TZVP	293	782	2.84	3.56
aug-TZVP	448	1084	2.79	3.52

9.3 S_2 PES of PSB11 and Models, S_1/S_2 Single-Particle Properties

In PSB11 and the two model systems PSB3 and PSB5, TD-DFTB and TDDFT relaxation in the S_1 and S_2 states proceeds in opposite directions: in the latter, BLA decreases, the energy gap between S_1 and S_2 shrinks, and their oscillator strengths diverge (see Figure 9.6 and Table 9.3 for PSB5 results). The planar stationary point on the PSB5 S_2 PES (structure B in Figure5.7) agrees with the corresponding CASSCF geometry.

Since the wrong S_1 gradient observed at the FC point could be associated with a mixing or avoided crossing of S_1 and S_2, it is important to clarify if the two states do indeed exchange between structure A and C. In DFT, no many-electron wave function or diabatic states are available. Thus, the only evidence about the diabatic nature, or origin of the states, comes from the single-particle transition weights (i.e., the eigenvectors of the response matrix). The latter, are based on the KS orbitals. Thus, both orbitals and transition weights have to be compared in order to identify the states. Figure 9.6 (right) reveals that some orbitals of structure A and C differ significantly in their shape. Nonetheless, the corresponding orbitals can uniquely be assigned from the number of their nodal planes. Therefore, an exchange of orbitals can be ruled out. Table 9.3, finally, shows that the transition weights unambiguously characterize both states: at point A *and* C the S_1 state is clearly dominated by the HOMO $\rightarrow$ LUMO transition—these two orbitals do not qualitatively change between A and C. In contrast to S_1, this transition has only a minor contribution to the S_2 state (double-excitation are not represented in linear response theory). The conclusion that can be drawn from this information is that the wrong S_1 gradient cannot be ascribed to another (S_2) state (certainly, this does not rule out the existence of a crossing between the two states in a different region of the PES). Another clue for this point of view comes from the fact that structure B is in much better agreement with the S_2 stationary point of CASSCF than with the S_1 stationary point (see Figure 5.7).

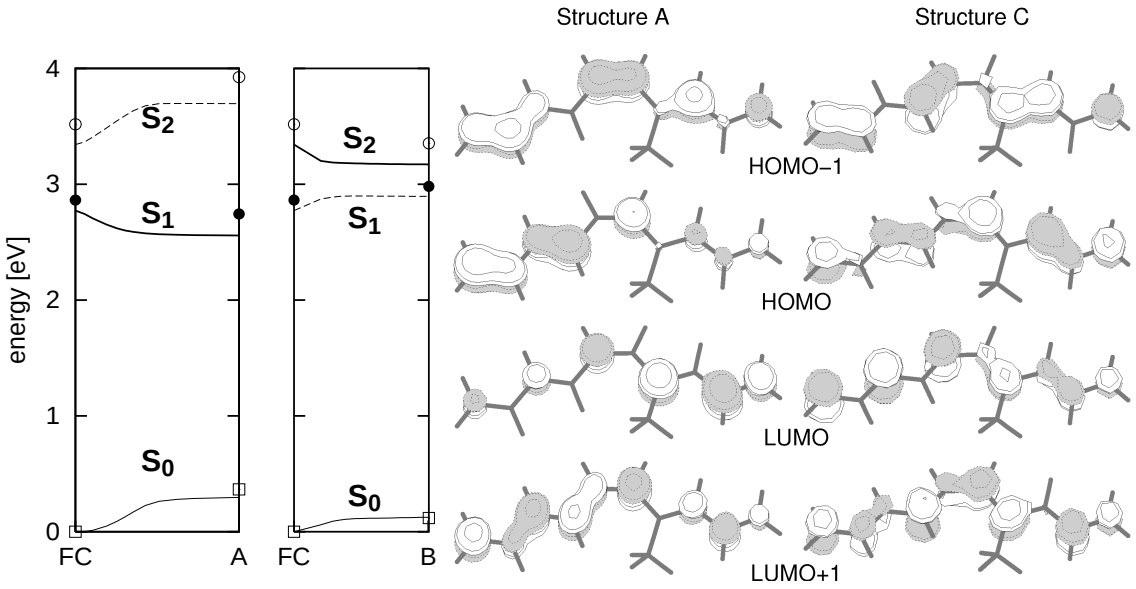

Figure 9.6: Left: PSB5 TD-DFTB energy profile along the S_1 (left) and S_2 (right) SD-paths starting from the FC point. TDDFT single point energies based on TD-DFTB geometries are represented by circles/squares. Right: KS orbitals of PSB5 in DFTB.

Table 9.3: Properties of S_1 and S_2 (in parentheses) in PSB5 (TD-DFTB values).

	A	FC	B	C	CI[a]
BLA (Å)	0.113	0.049	0.007	-0.032	-0.015
E (eV)	2.556 (3.697)	2.772 (3.342)	2.897 (3.171)	2.894 (3.381)	2.068 (3.860)
f	0.41 (0.46)	0.89 (0.39)	1.26 (0.02)	0.89 (0.31)	0.008 (0.050)
Transition weights:					
HOMO → LUMO	0.985 (0.066)	0.978 (0.116)	0.999 (0.008)	0.981 (0.081)	0.996 (0.000)
HOMO-1 → LUMO	0.153 (0.969)	0.179 (0.890)	0.009 (0.873)	0.174 (0.911)	0.071 (0.999)
HOMO → LUMO+1	0.081 (0.161)	0.104 (0.440)	0.014 (0.488)	0.085 (0.404)	0.002 (0.018)
Q(SB-side) (%)	59.9 (59.7)	61.7 (61.0)	61.4 (60.7)	54.7 (64.2)	40.4 (36.6)

E is the total energy relative to the *cis* S_0 minimum, f is the oscillator strength, and Q(SB-side) is the amount of positive charge located beyond the isomerizing bond on the nitrogen side determined from Mulliken atomic charges. [1]Last intermediate of the SD-path before SCF convergency is lost.

Bibliography

[1] Schreiber, M.; Buß, V. *Int. J. Quantum Chem.* **2003**, *95*, 882–889.

[2] Garavelli, M.; Celani, P.; Bernardi, F.; Robb, M. A.; Olivucci, M. *J. Am. Chem. Soc.* **1997**, *119*, 6891–6901.

[3] Garavelli, M.; Bernardi, F.; Robb, M.; Olivucci, M. *Int. J. of Photoenergy* **2002**, *4*, 57–68.

[4] González-Luque, R.; Garavelli, M.; Bernardi, F.; Merchán, M.; Robb, M. A.; Olivucci, M. *PNAS* **2000**, *97*(17), 9379–9384.

[5] Garavelli, M.; Cembran, A.; Bernardi, F.; Olivucci, M. draft, **2002**.

[6] Garavelli, M.; Vreven, T.; Celani, P.; Bernardi, F.; Robb, M.; Olivucci, M. *J. Am. Chem. Soc.* **1998**, *120*, 1285–1288.

[7] Page, C. S.; Olivucci, M. *J. Comput. Chem.* **2003**, *24*, 298–309.

[8] Garavelli, M.; Celani, P.; Yamamoto, N.; Bernardi, F.; Robb, M. A.; Olivucci, M. *J. Am. Chem. Soc.* **1996**, *118*, 11656–11657.

[9] Ferre, N.; Olivucci, M. *J. Am. Chem. Soc.* **2003**, *125*, 6868–6869.

[10] Schreiber, M.; Buß, V.; Sugihara, M. *J. Chem. Phys.* **2003**, *119*(23), 12045–12048.

[11] Birge, R. R.; Zhang, C. *J. Chem. Phys.* **1990**, *92*, 7178–7195.

[12] Berman, H.; Henrick, K.; Nakamura, H. *Nature Structural Biology* **2003**, *10*, 980.

[13] Berman, H.; Westbrook, J.; Feng, Z.; Gilliland, G.; Bhat, T.; Weissig, H.; Shindyalov, I.; Bourne, P. *Nucleic Acids Research* **2000**, *28*, 235–242.

[14] Zewail, A. In *Nobel Lecture, Chemistry*, 1999.

[15] Hylleraas, E. .; Undheim, B. *Z. Phys.* **1930**, *65*, 759–772.

[16] MacDonald, J. K. L. *Phys. Rev.* **1933**, *43*, 830–833.

[17] Veillard, A. In Diercksen, G. H. F., Sutcliffe, B. T., Veillard, A., Eds., *Computaional Techniques in Quantum Chemistry and Molecular Physics*, Vol. 15 of *NATO ASI Series C*, page 201. Reidel, Dodrecht, 1975.

[18] Roothaan, C. C. J. *Rev. Mod. Phys.* **1960**, *32*, 179.

[19] Knowles, P.; Schütz, M.; Werner, H.-J.; John von Neumann Institute for Computing, J. Grotendorst, 2000; Vol. 3 of *NIC Series;* pages 97–179; Modern methods and algorithms of quantum chemistry, proceedings, 2nd ed.

[20] Baerends, E. J.; Gritsenko, O. V. July **1997**, *101*(30), 5383–5403.

[21] Wang, J.; Jr, V. H. S. *Int. J. Quantum Chem.* **1995**, *56*(5), 509–519.

[22] Buijse, M. A.; Baerends, E. J. September **1990**, *93*(6), 4129–4141.

[23] Baerends, E. J. *Phys. Rev. Lett.* **2001**, *87*(13), 133004.

[24] Gritsenko, O. V.; Schipper, P. R. T.; Baerends, E. J. October **1997**, *107*(13), 5007–5015.

[25] Schipper, P. R. T.; Gritsenko, O. V.; Baerends, E. J. *Phys. Rev. A* **1998**, *57*, 1729–1742.

[26] Grüning, M.; Gritsenko, O. V.; Baerends, E. J. April **2003**, *118*(16), 7183–7192.

[27] Grüning, M.; Gritsenko, O. V.; van Gisbergen, S. J. A.; Baerends, E. J. October **2001**, *105*(40), 9211–9218.

[28] Cremer, D. *Mol. Phys.* **2001**, *99*(23), 1899–1940.

[29] Polo, V.; Kraka, E.; Cremer, D. *Mol. Phys.* **2002**, *100*(11), 1771–1790.

[30] Handy, N. C.; Cohen, A. J. March **2001**, *99*(5), 403–412.

[31] Møller, C.; Plesset, M. S. October **1934**, *46*(7), 0618–0622.

[32] Weigend, F.; Häser, M. October **1997**, *97*(1-4), 331–340.

[33] Werner, H.-J.; Manby, F. R.; Knowles, P. J. May **2003**, *118*(18), 8149–8160.

[34] Bartlett, R. J. *Annu. Rev. Phys. Chem.* **1981**, *32*, 359–401.

[35] Thomas, L. H. *Proc. Cambridge Philos. Soc.* **1927**, *23*, 542.

[36] Fermi, E. *Z. f. Physik* **1928**, *48*, 73.

[37] Slater, J. C. *Phys. Rev.* **1951**, *81*, 385.

[38] Hohenberg, P.; Kohn, W. *Phys. Rev.* **1964**, *136*, B864–B871.

[39] Levy, M. *Phys. Rev. A* **1982**, *26*, 1200.

[40] Gilbert, T. L. *Phys. Rev. B* **1975**, *12*, 2111–2120.

[41] Lieb, E. H. *Int. J. Quantum Chem.* **1983**, *24*, 243–277.

[42] Kohn, W.; Sham, L. J. *Phys. Rev.* **1965**, *140*, A1133–A1138.

[43] Parr, R.; Yang, W. *Density-Functional Theory of Atoms and Molecules*, Vol. 16 of *International Series of Monographs on Chemistry;* Oxford University Press, 1989.

[44] Ceperley, D. M.; Alder, B. J. *Phys. Rev. Lett.* **1980**, *45*, 566.

[45] Vosko, S. J.; Wilk, L.; Nusair, M. *Can. J. Phys.* **1980**, *58*, 1200–1211.

[46] Perdew, J. P.; Chevary, J. A.; Vosko, S. H.; Jackson, K. A.; Pederson, M. R.; Singh, D. J.; Fiolhais, C. *Phys. Rev. B* **1992**, *46*, 6671–6687.

[47] Perdew, J. P.; Burke, K.; Ernzerhof, M. October **1996**, *77*(18), 3865–3868.

[48] Becke, A. D. *J. Chem. Phys.* **1988**, *88*, 2547.

[49] Lee, C.; Yang, W.; Parr, R. *Phys. Rev. B* **1988**, *37*, 385.

[50] Colle, R.; Salvetti, O. *Theor. Chim. Acta* **1975**, *37*, 329.

[51] Cohen, A. J.; Handy, N. C. April **2001**, *99*(7), 607–615.

[52] Cremer, D.; Filatov, M.; Polo, V.; Kraka, E.; Shaik, S. *Int. J. Mol. Sci.* **2002**, *3*, 604–638.

[53] Gritsenko, O. V.; Baerends, E. J. *Theor. Chem. Acc.* **1997**, *96*, 44–50.

[54] Gritsenko, O. V.; van Gisbergen, S. J. A.; Görling, A.; Baerends, E. J. *J. Chem. Phys.* **2000**, *113*(19), 8478–8489.

[55] Zhao, Q.; Morrison, R. C.; Parr, R. G. *Phys. Rev. A* **1994**, *50*, 2138.

[56] Pople, J. A.; Segal, G. A. *J. Chem. Phys.* **1965**, *43*(10), S136–S151.

[57] Pople, J. A.; Beveridge, D. L.; Dobosh, P. A. *J. Chem. Phys.* **1967**, *47*(6), 2026–2033.

[58] Pople, J. A.; Santry, D. P.; Segal, G. A. *J. Chem. Phys.* **1965**, *43*(10), S129–S135.

[59] Oleari, L.; Sipio, L. D.; Michelis, G. D. *Mol. Phys.* **1966**, *10*(2), 97–109.

[60] Dewar, M. J. S.; Lo, D. H. *J. Am. Chem. Soc.* **1972**, *94*(15), 5296–5303.

[61] Dewar, M. J. S.; Thiel, W. *J. Am. Chem. Soc.* **1977**, *99*, 4899.

[62] Weber, W. *Ein neues semiempirisches NDDO-Verfahren mit Orthogonalisierungskorrekturen* PhD thesis, Universität Zürich, **1996**.

[63] Zerner, M. C.; Ridley, J. *Theor. Chim. Acta* **1973**, *32*, 111.

[64] Kolb, M. *Ein neues semiempirisches Verfahren auf Grundlage der NDDO Näherung* PhD thesis, Universität Wuppertal, **1991**.

[65] Kolb, M.; Thiel, W. *J. Comp. Chem.* **1993**, *14*(7), 775–789.

[66] Weber, W.; Thiel, W. *Theor. Chem. Acc.* **2000**, *103*, 495–506.

[67] Flicker, W. M.; Mosher, O. A.; Kuppermann, A. *Chem. Phys. Lett.* **1977**, *45*, 492.

[68] Kuppermann, A.; Flicker, W. M.; Mosher, O. A. *Chem. Rev.* **1979**, *79*, 77.

[69] Fujii, T.; Kamata, A.; Shimizu, M.; Adachi, Y.; Maeda, S. *Chem. Phys. Lett.* **1985**, *115*, 369.

[70] Leopold, D. G.; Pendley, R. D.; Roebber, J. L.; Hemley, J. R.; Vaida, J. V. *J. Chem. Phys.* **1984**, *81*, 4210.

[71] Heimbrook, L. A.; Kohler, B. E.; Levy, I. J. *J. Chem. Phys.* **1984**, *81*, 1592.

[72] Hudson, B. S.; Kohler, B. E.; Schulten, K. In Lim, E. C., Ed., *Excited States*, Vol. 6, pages 1–95. New York: Acad. Press, 1982.

[73] D´Amico, K. L.; Manos, C.; Christenson, R. L. *J. Am. Chem. Soc.* **1980**, *102*, 1777.

[74] Serrano-Andres, L.; Merchan, M.; Nebotgil, I.; Lindh, R.; Roos, B. O. *J. Chem. Phys.* **1993**, *98*, 3151.

[75] Serrano-Andres, L.; Merchan, M.; Lindh, R.; Roos, B. O. *J. Phys. Chem.* **1993**, *97*, 9360–9368.

[76] McDiarmid, R. *J. Chem. Phys.* **1976**, *64*, 514.

[77] McDiarmid, R. *Chem. Phys. Lett.* **1992**, *188*, 423.

[78] Packer, M. J.; Dalskov, E. K.; Enevoldsen, T.; Jensen, H. J. A.; Oddershede, J. *J. Chem. Phys.* **1996**, *105*, 5886.

[79] Dekkers, H. P. J. M.; Westra, S. W. T. *Mol. Phys.* **1975**, *30*(6), 1795–1811.

[80] Grimme, S.; Parac, M. *CHEMPHYSCHEM* **2003**, *4*(3), 292–295.

[81] Elstner, M.; Frauenheim, T.; Kaxiras, E.; Seifert, G.; Suhai, S. *phys. stat. sol.(b)* **2000**, *217/1*, 375.

[82] Elsner, M. *Surfaces and Extended Defects in Wurtzite GaN* Dissertation, Universität Paderborn, **1998**.

[83] Elstner, M. *Weiterentwicklung quantenchemischer Rechenverfahren für organische Moleküle und Polymere* Dissertation, Universität Paderborn, **1998**.

[84] Köhler, C. *Ber¨ucksichtigung von Spinpolarisationseffekten in einem dichtefunktionalbasierten Ansatz* Dissertation, Universität Paderborn, **2004**.

[85] Porezag, D. *Development of Ab-Initio and Approximate Density Functional Methods and their Application to Complex Fullerene Systems* Dissertation, Technische Universität Chemnitz-Zwickau, **1997**.

[86] Sternberg, M. *The Atomic Structure of Diamond Surfaces and Interfaces* Dissertation, Universität Paderborn, **2001**.

[87] Elstner, M. *Theor. Chem. Acc.* **2007**, *116*, 316–325.

[88] Elstner, M.; Porezag, D.; Jungnickel, G.; Elsner, J.; Haugk, M.; Frauenheim, T.; Suhai, S.; Seifert, G. *Phys. Rev. B* **1998**, *58*, 7260–7268.

[89] Otte, N.; Scholten, M.; Thiel, W. July **2007**, *111*(26), 5751–5755.

[90] Zhou, H.; Tajkhorshida, E.; Frauenheim, T.; Suhai, S.; Elstner, M. *Chem. Phys.* **2002**, *277*, 91–103.

[91] Harris, J. *Phys. Rev. B* **1985**, *31*, 1770.

[92] Foulkes, W. M.; Haydock, R. *Phys. Rev. B* **1989**, *39*, 12520–12536.

[93] Klopman, G. *J. Amer. Chem. Soc.* **1964**, *86*, 4550–4557.

[94] Ohno, K. *Theor. Chim. Acta* **1964**, *2*, 219.

[95] Elstner, M. July **2007**, *111*(26), 5614–5621.

[96] Casida, M. E. In Chong, D. P., Ed., *Recent Advances in Density Functional Methods, Part 1*, Vol. 1 of *Recent Advances in Computational Chemistry*. World Scientific, Singapore, 1995.

[97] Runge, E.; Gross, E. *Phys. Rev. Lett.* **1984**, *52*, 997.

[98] Yabana, K.; Bertsch, G. F. August **1996**, *54*(7), 4484–4487.

[99] Castro, A.; Appel, H.; Oliveira, M.; Rozzi, C.; Andrade, X.; Lorenzen, F.; Marques, M.; Gross, E.; Rubio, A. *Phys. Stat. Sol. B* **2006**, *243*, 2465–2488.

[100] Görling, A.; Heinze, H. H.; Ruzankin, S. P.; Staufer, M.; Rösch, N. *J. Chem. Phys.* **1999**, *110*, 2785.

[101] Furche, F. *J. Chem. Phys.* **2001**, *114*(14), 5982–5992.

[102] Furche, F.; Ahlrichs, R. *J. Chem. Phys.* **2002**, *117*(16), 7433–7447.

[103] Furche, F.; Ahlrichs, R.; Wachsmann, C.; Weber, E.; Sobanski, A.; Vögtle, F.; Grimme, S. *J. Am. Chem. Soc.* **2000**, *122*, 1717–1724.

[104] Niehaus, T. *Approximative Methoden in der zeitabhängigen Dichtefunktionaltheorie* Dissertation, Universität Paderborn, **2001**.

[105] Niehaus, T. A.; Suhai, S.; Della Sala, F.; Lugli, P.; Elstner, M.; Seifert, G.; Frauenheim, T. *Phys. Rev. B* **2001**, *63*, 085108.

[106] Niehaus, T.; Heringer, D.; Torralva, B.; Frauenheim, T. *Eur. Phys. J. D* **2005**, *35*, 467–477.

[107] Heringer, D.; Niehaus, T. A.; Wanko, M.; Frauenheim, T. *J. Comput. Chem.* **2007**, *28*, 2589 – 2601.

[108] Roos, B. O.; Taylor, P. R.; Siegbahn, P. E. M. *Chem. Phys.* **1980**, *48*, 157–173.

[109] Siegbahn, P. E. M.; Almlof, J.; Heiberg, A.; Roos, B. O. February **1981**, *74*(4), 2384–2396.

[110] Thorsteinsson, T.; Cooper, D. L.; Gerratt, J.; Karadakov, P. B.; Raimondi, M. June **1996**, *93*(6), 343–366.

[111] Malmquist, P. A.; Roos, B. O. *Chem. Phys. Lett.* **1989**, *155*(2), 189–194.

[112] Andersson, K.; Malmqvist, P. A.; Roos, B. O.; Sadlej, A. J.; Wolinski, K. July **1990**, *94*(14), 5483–5488.

[113] Andersson, K.; Malmqvist, P. A.; Roos, B. O. *J. Chem. Phys.* **1992**, *96*(2), 1218–1226.

[114] Andersson, K. April **1995**, *91*(1-2), 31–46.

[115] Neese, F. *J. Chem. Phys.* **2003**, *119*, 9428–9443.

[116] Neese, F.; Petrenko, T.; Ganyushin, D.; Olbrich, G. February **2007**, *251*(3-4), 288–327.

[117] Murphy, R. B.; Messmer, R. P. *Chem. Phys. Lett.* **1991**, *183*, 443–448.

[118] Grimme, S.; Waletzke, M. *Phys. Chem. Chem. Phys.* **2000**, *2*, 2075–2081.

[119] Strodel, P.; Tavan, P. September **2002**, *117*(10), 4667–4676.

[120] Strodel, P.; Tavan, P. *J. Chem. Phys.* **2002**, *117*(10), 4677.

[121] Koslowski, A.; Beck, M. E.; Thiel, W. *J. Comput. Chem.* **2003**, *24*, 714–726.

[122] Grimme, S.; Waletzke, M. *J. Chem. Phys.* **1999**, *111*, 5645.

[123] MacKerell, A. D.; Bashford, D.; Bellott, M.; Dunbrack, R. L.; Evanseck, J. D.; Field, M. J.; Fischer, S.; Gao, J.; Guo, H.; Ha, S.; Joseph-McCarthy, D.; Kuchnir, L.; Kuczera, K.; Lau, F. T. K.; Mattos, C.; Michnick, S.; Ngo, T.; Nguyen, D. T.; Prodhom, B.; Reiher III, W. E.; Roux, B.; Schlenkrich, M.; Smith, J. C.; Stote, R.;

Straub, J.; Watanabe, M.; Wiorkiewicz-Kuczera, J.; Yin, D.; Karplus, M. *J. Phys. Chem. B* **1998**, *102*, 3586–3616.

[124] Pettitt, B. M.; Karplus, M. *J. Am. Chem. Soc.* **1985**, *107*(5), 1166–1173.

[125] MacKerell, A. D. October **2004**, *25*(13), 1584–1604.

[126] Ponder, J. W.; Case, D. A. *Adv. Prot. Chem.* **2003**, *66*, 27–85.

[127] Wang, W.; Donini, O.; Reyes, C. M.; Kollman, P. A. *Annu. Rev. Biophys. Biomol. Struct.* **2001**, *30*, 211–243.

[128] Warshel, A.; Kato, M.; Pisliakov, A. V. November **2007**, *3*(6), 2034–2045.

[129] Cornell, W. D.; Cieplak, P.; Bayly, C. I.; Gould, I. R.; Merz, K. M.; Ferguson, D. M.; Spellmeyer, D. C.; Fox, T.; Caldwell, J. W.; Kollman, P. A. May **1995**, *117*(19), 5179–5197.

[130] Duan, Y.; Wu, C.; Chowdhury, S.; Lee, M.; Xiong, G.; Zhang, W.; Yang, R.; Cieplak, P.; Luo, R.; Lee., T. *J. Comput. Chem.* **2003**, *24*, 1999–2012.

[131] Brooks, B. R.; Bruccoleri, R. E.; Olafson, B. D.; States, D. J.; Swaminathan, S.; Karplus, M. *J. Comput. Chem.* **1983**, *4*(2), 187–217.

[132] Scott, W. R. P.; Hunenberger, P. H.; Tironi, I. G.; Mark, A. E.; Billeter, S. R.; Fennen, J.; Torda, A. E.; Huber, T.; Kruger, P.; van Gunsteren, W. F. May **1999**, *103*(19), 3596–3607.

[133] Oostenbrink, C.; Villa, A.; Mark, A. E.; Van Gunsteren, W. F. October **2004**, *25*(13), 1656–1676.

[134] Jorgensen, W. L.; Tiradorives, J. March **1988**, *110*(6), 1657–1666.

[135] Jorgensen, W. L.; Maxwell, D. S.; TiradoRives, J. November **1996**, *118*(45), 11225–11236.

[136] Warshel, A.; Levitt, M. *J. Mol. Biol.* **1976**, *103*(2), 227–249.

[137] Kato, M.; Warshel, A. June **2006**, *110*(23), 11566–11570.

[138] Muegge, I.; Qi, P. X.; Wand, A. J.; Chu, Z. T.; Warshel, A. January **1997**, *101*(5), 825–836.

[139] Piquemal, J. P.; Chelli, R.; Procacci, P.; Gresh, N. August **2007**, *111*(33), 8170–8176.

[140] Ren, P.; Ponder, J. W. *J. Phys. Chem. B* **2003**, *107*, 5933–5947.

[141] Lamoureux, G.; MacKerell, A. D.; Roux, B. September **2003**, *119*(10), 5185–5197.

[142] Cieplak, P.; Caldwell, J.; Kollman, P. July **2001**, *22*(10), 1048–1057.

[143] Stern, H. A.; Rittner, F.; Berne, B. J.; Friesner, R. A. August **2001**, *115*(5), 2237–2251.

[144] Lefohn, A. E.; Ovchinnikov, M.; Voth, G. A. July **2001**, *105*(28), 6628–6637.

[145] Guo, H.; Gresh, N.; Roques, B. P.; Salahub, D. R. October **2000**, *104*(41), 9746–9754.

[146] Burnham, C. J.; Li, J. C.; Xantheas, S. S.; Leslie, M. March **1999**, *110*(9), 4566–4581.

[147] Gao, J. *J. Comput. Chem.* **1997**, *18*, 1061–1071.

[148] Rick, S. W.; Stuart, S. J.; Berne, B. J. October **1994**, *101*(7), 6141–6156.

[149] Kaminsky, J.; Jensen, F. *J. Chem. Theory Comput.* **2007**, *3*, 1774 –1788.

[150] Chelli, R.; Procacci, P. November **2002**, *117*(20), 9175–9189.

[151] Gresh, N.; Kafafi, S. A.; Truchon, J. F.; Salahub, D. R. April **2004**, *25*(6), 823–834.

[152] Kaminski, G. A.; Stern, H. A.; Berne, B. J.; Friesner, R. A.; Cao, Y. X. X.; Murphy, R. B.; Zhou, R. H.; Halgren, T. A. December **2002**, *23*(16), 1515–1531.

[153] Rasmussen, T. D.; Ren, P. Y.; Ponder, J. W.; Jensen, F. May **2007**, *107*(6), 1390–1395.

[154] Gresh, N. *Curr. Pharm. Des.* **2006**, *12*(17), 2121–2158.

[155] Gresh, N.; Cisneros, G. A.; Darden, T. A.; Piquemal, J.-P. *J. Chem. Theory Comput.* **2007**, *3*, 1960 –1986.

[156] Maple, J. R.; Cao, Y. X.; Damm, W. G.; Halgren, T. A.; Kaminski, G. A.; Zhang, L. Y.; Friesner, R. A. *J. Chem. Theory Comput.* **2005**, *1*(4), 694–715.

[157] Chen, J. H.; Martinez, T. J. April **2007**, *438*(4-6), 315–320.

[158] Applequist, J.; Carl, J. R.; Fung, K.-K. *J. Am. Chem. Soc.* **1972**, *94*(9), 2952–2960.

[159] Thole, B. *Chem. Phys.* **1981**, *59*, 341–350.

[160] Russell, S. T.; Warshel, A. *J. Mol. Biol.* **1985**, *185*, 389–404.

[161] Miller, K. J. *J. Am. Chem. Soc.* **1990**, *112*, 8533–8542.

[162] Stout, J. M.; Dykstra, C. E. February **1998**, *102*(9), 1576–1582.

[163] Miller, K. J. November **1990**, *112*(23), 8543–8551.

[164] Palmo, K.; Krimm, S. September **2004**, *395*(1-3), 133–137.

[165] Drude, P. *The Theory of Optics;* Dover Publications: New York, 1959.

[166] Anisimov, V. M.; Lamoureux, G.; Vorobyov, I. V.; Huang, N.; Roux, B.; MacKerell, A. D. *J. Chem. Theory Comput.* **2005**, *1*(1), 153–168.

[167] Lamoureux, G.; Roux, B. August **2003**, *119*(6), 3025–3039.

[168] Ren, P. Y.; Ponder, J. W. December **2002**, *23*(16), 1497–1506.

[169] Swart, M.; van Duijnen, P. T. May **2006**, *32*(6), 471–484.

[170] Swart, M.; Van Duijnen, P. T.; Snijders, J. G. January **2001**, *22*(1), 79–88.

[171] Swart, M.; Snijders, J. G.; van Duinen, P. T. January **2004**, *4*(1-2), 419–425.

[172] Patel, S.; MacKerell, A. D.; Brooks, C. L. September **2004**, *25*(12), 1504–1514.

[173] Patel, S.; Brooks, C. L. January **2004**, *25*(1), 1–15.

[174] Kaminski, G. A.; Stern, H. A.; Berne, B. J.; Friesner, R. A. January **2004**, *108*(4), 621–627.

[175] Gresh, N.; Claverie, P.; Pullman, A. *Theor. Chim. Acta* **1984**, *66*(1), 1–20.

[176] Singh, U. C.; Kollman, P. A. December **1986**, *7*(6), 718–730.

[177] Thompson, M. A.; Schenter, G. K. *J. Phys. Chem.* **1995**, *99*, 6374–6386.

[178] Thompson, M. A. *J. Phys. Chem.* **1996**, *100*, 14492–14507.

[179] Sakurai, M.; Sakata, K.; Saito, S.; Nakajima, S.; Inoue, Y. *J. Am. Chem. Soc.* **2003**, *125*, 3108–3112.

[180] Illingworth, C. J. R.; Gooding, S. R.; Winn, P. J.; Jones, G. A.; Ferenczy, G. G.; Reynolds, C. A. *J. Phys. Chem. A* **2006**, *110*, 6487–6497.

[181] Warshel, A.; Sharma, P. K.; Kato, M.; Parson, W. W. November **2006**, *1764*(11), 1647–1676.

[182] Zhang, Y.; Lin, H.; Truhlar, D. G. *J. Chem. Theory Comput.* **2007**, *3*(4), 1378–1398.

[183] Luzhkov, V.; Warshel, A. *J. Am. Chem. Soc.* **1991**, *113*, 4491–4499.

[184] Warshel, A.; Chu, Z. T.; Hwang, J.-K. *Chem. Phys.* **1991**, *158*, 303–314.

[185] Field, M. J. *Mol. Phys.* **1997**, *91*, 835–845.

[186] Warshel, A.; Strajbl, M.; Villa, J.; Florian, J. *Biochemistry* **2000**, *39*(48), 14728–14738.

[187] Warshel, A.; Chu, Z. T. *J. Phys. Chem. B* **2001**, *105*, 9857–9871.

[188] Poulsen, T. D.; Kongsted, J.; Osted, A.; Ogilby, P. R.; Mikkelsena, K. V. *J. Chem. Phys.* **2001**, *115*, 2393–2400.

[189] Dupuis, M.; Aida, M.; Kawashima, Y.; Hirao, K. *J. Chem. Phys.* **2002**, *117*, 1256–1268.

[190] Strajbl, M.; Shurki, A.; Kato, M.; Warshel, A. *J. Am. Chem. Soc.* **2003**, *125*(34), 10228–10237.

[191] Dupuis, M.; Schenter, G.; Garrett, B.; Arcia, E. *J. Mol. Struct.* **2003**, *632*, 173–183.

[192] Kongsted, J.; Osted, A.; Mikkelsen, K. V.; Astrand, P.-O. *J. Chem. Phys.* **2004**, *121*, 8435–8445.

[193] Olsson, M.; Siegbahn, P.; Warshel, A. *J. Am. Chem. Soc.* **2004**, *126*(9), 2820–2828.

[194] Braun-Sand, S.; Strajbl, M.; Warshel, A. *Biophys. J.* **2004**, *87*(1), 2221–2239.

[195] Schutz, C. N.; Warshel, A. *Proteins: Struct., Funct., Bioinf.* **2004**, *55*, 711–723.

[196] Braun-Sand, S.; Burykin, A.; Chu, Z.; Warshel, A. *J. Phys. Chem. B* **2005**, *109*(1), 583–592.

[197] Klähn, M.; Braun-Sand, S.; Rosta, E.; Warshel, A. *J. Phys. Chem. B* **2005**, *109*(32), 15645–15650.

[198] Giese, T. J.; York, D. M. November **2007**, *127*(19), 194101.

[199] Senn, H. M.; Thiel, W. *Top. Curr. Chem.* **2007**, *268*, 173–290.

[200] Ferre, N.; Assfeld, X.; Rivail, J. L. April **2002**, *23*(6), 610–624.

[201] Thery, V.; Rinaldi, D.; Rivail, J. L.; Maigret, B.; Ferenczy, G. G. March **1994**, *15*(3), 269–282.

[202] Gao, J.; Amara, P.; Alhambra, C.; Field, M. J. *J. Phys. Chem. A* **1998**, *102*(24), 4714–4721.

[203] Rodriguez, A.; Oliva, C.; Gonzalez, M.; van der Kamp, M.; Mulholland, A. J. November **2007**, *111*(44), 12909–12915.

[204] Philipp, D. M.; Friesner, R. A. *J. Comput. Chem.* **1999**, *20*, 1468–1494.

[205] Fornili, A.; Loos, P. F.; Sironi, M.; Assfeld, X. August **2006**, *427*(1-3), 236–240.

[206] Zhang, Y. K.; Lee, T. S.; Yang, W. T. January **1999**, *110*(1), 46–54.

[207] Zhang, Y. K. August **2006**, *116*(1-3), 43–50.

[208] DiLabio, G. A.; Hurley, M. M.; Christiansen, P. A. *J. Chem. Phys.* **2002**, *116*, 9578–9584.

[209] Poteau, R.; Ortega, I.; Alary, F.; Solis, A. R.; Barthelat, J.-C.; Daudey, J.-P. *J. Phys. Chem. A* **2001**, *105*(1), 198–205.

[210] Bessac, F.; Alary, F.; Carissan, Y.; Heully, J. L.; Daudey, J. P.; Poteau, R. August **2003**, *632*, 43–59.

[211] Yasuda, K.; Yamaki, D. September **2004**, *121*(9), 3964–3972.

[212] Antes, I.; Thiel, W. *J. Phys. Chem. A* **1999**, *103*, 9290–9295.

[213] Ferre, N.; Olivucci, M. August **2003**, *632*, 71–82.

[214] Jung, G.; Werner, M.; Schneider, M. September **2008**, *9*(13), 1867–1874.

[215] Lin, H.; Truhlar, D. G. May **2005**, *109*(17), 3991–4004.

[216] Reuter, N.; Dejaegere, A.; Maigret, B.; Karplus, M. March **2000**, *104*(8), 1720–1735.

[217] Riccardi, D.; Schaefer, P.; Cui, Q. September **2005**, *109*(37), 17715–17733.

[218] König, P.; Hoffmann, M.; Frauenheim, T.; Cui, Q. *J. Phys. Chem. B* **2005**, *109*, 9082.

[219] Riccardi, D.; Li, G. H.; Cui, Q. May **2004**, *108*(20), 6467–6478.

[220] Vreven, T.; Morokuma, K. *J. Chem. Phys.* **2000**, *113*, 2969.

[221] Wesolowski, T. A.; Weber, J. January **1997**, *61*(2), 303–311.

[222] Wesolowski, T. A.; Weber, J. January **1996**, *248*(1-2), 71–76.

[223] Neutze, R.; Pebay-Peyroula, E.; Edmann, K.; Royant, A.; Navarro, J.; Landau, E. *Biochimica et Biophysica Acta - Biomembranes* **2002**, *1565*, 144–167.

[224] Stenkamp, R. E.; Filipek, S.; Driessen, C. A. G. G.; Teller, D. C.; Palczewski, K. *Biochimica et Biophysica Acta - Biomembranes* **2002**, *1565*, 168–182.

[225] Logunov, S. L.; Song, L.; El-Sayed, M. A. *J. Phys. Chem.* **1996**, *100*, 18586–18591.

[226] Kochendoerfer, G. G.; Lin, S. W.; Sakmar, T. P.; Mathies, R. A. *Trends Biochem. Sci.* **1999**, *24*, 300–305.

[227] Ren, L.; Martin, C. H.; Wise, K. J.; Gillespie, N. B.; Luecke, H.; Lanyi, J. K.; Spudich, J. L.; Birge, R. R. *Biochemistry* **2001**, *40*, 13906–13914.

[228] Houjou, H.; Koyama, K.; Wada, M.; Sameshima, K.; Inoue, Y.; Sakurai, M. *Chem. Phys. Lett.* **1998**, *294*, 162–166.

[229] Hayashi, S.; Ohmine, I. *J. Phys. Chem. B* **2000**, *104*, 10678–10691.

[230] Hayashi, S.; Tajkhorshid, E.; Pebay-Peyroula, E.; Royant, A.; Landau, E. M.; Navarro, J.; Schulten, K. *J. Phys. Chem. B* **2001**, *105*, 10124–10131.

[231] Hayashi, S.; Tajkhorshid, E.; Schulten, K. *Biophys. J.* **2002**, *83*, 1281–1297.

[232] Rajamani, R.; Gao, J. *J. Comp. Chem.* **2002**, *23*(1), 96–105.

[233] Vreven, T.; Morokuma, K. *Theor. Chem. Acc.* **2003**, *109*, 125–132.

[234] Mathies, R.; Stryer, L. *PNAS* **1976**, *73*(7), 2169–2173.

[235] Warshel, A. *J. Phys. Chem.* **1979**, *83*, 1640–1652.

[236] Houjou, H.; Inoue, Y.; Sakurai, M. *J. Phys. Chem. B* **2001**, *105*, 867–879.

[237] Houjou, H.; Inoue, Y.; Sakurai, M. *J. Am. Chem. Soc.* **1998**, *120*, 4459–4470.

[238] Kusnetzow, A.; Dukkipati, A.; Babu, K. R.; Singh, D.; Vought, B. W.; Knox, B. E.; Birge, R. R. *Biochemistry* **2001**, *40*, 7832–7844.

[239] T. H. Dunning, J. *J. Chem. Phys.* **1989**, *90*, 1007.

[240] Schäfer, A.; Horn, H.; Ahlrichs, R. *J. Chem. Phys.* **1992**, *97*, 2571–2577.

[241] Cembran, A.; Bernardi, F.; Olivucci, M.; Garavelli, M. *J. Am. Chem. Soc.* **2003**, *125*, 12509–12519.

[242] Nielsen, I. B.; Lammich, L.; Andersen, L. H. January **2006**, *96*(1), 018304.

[243] ORCA—An ab initio, density functional and semiempirical program package, Version 2.3 - Revision 09, February 2004, Max Planck Institut für Strahlenchemie, Mülheim. February **2004**.

[244] Grimme, S. *J. Comp. Chem.* **1994**, *15*, 424–432.

[245] TURBOMOLE V5-6, 10 Dec 2002, Copyright (C) 2002 University of Karlsruhe.

[246] Kendall, R. A.; Dunning, T. H.; Harrison, R. J. May **1992**, *96*(9), 6796–6806.

[247] Weigend, F.; Häser, M.; Patzelt, H.; Ahlrichs, R. September **1998**, *294*(1-3), 143–152.

[248] Elstner, M.; Frauenheim, T.; Suhai, S. *J. Mol. Struct. (Theochem)* **2003**, *632*, 29–41.

[249] Luecke, H.; Schobert, B.; Richter, H.; Cartailler, J.; Lanyi, J. *J. Mol. Biol.* **1999**, *291*, 899–911.

[250] Cui, Q.; Elstner, M.; Kaxiras, E.; Frauenheim, T.; Karplus, M. *J. Phys. Chem. B* **2001**, *105*, 569.

[251] Lee, H. M.; Kim, J.; Kim, C.-J.; Kim, K. S. *J. Chem. Phys.* **2002**, *116*, 6549–6559.

[252] Gaussian 98, Revision A.7, M. J. Frisch, G. W. Trucks, H. B. Schlegel, G. E. Scuseria, M. A. Robb, J. R. Cheeseman, V. G. Zakrzewski, J. A. Montgomery, Jr., R. E. Stratmann, J. C. Burant, S. Dapprich, J. M. Millam, A. D. Daniels, K. N. Kudin, M. C. Strain, O. Farkas, J. Tomasi, V. Barone, M. Cossi, R. Cammi, B. Mennucci, C. Pomelli, C. Adamo, S. Clifford, J. Ochterski, G. A. Petersson, P. Y. Ayala, Q. Cui, K. Morokuma, D. K. Malick, A. D. Rabuck, K. Raghavachari, J. B. Foresman, J. Cioslowski, J. V. Ortiz, A. G. Baboul, B. B. Stefanov, G. Liu, A. Liashenko, P. Piskorz, I. Komaromi, R. Gomperts, R. L. Martin, D. J. Fox, T. Keith, M. A. Al-Laham, C. Y. Peng, A. Nanayakkara, C. Gonzalez, M. Challacombe, P. M. W. Gill, B. Johnson, W. Chen, M. W. Wong, J. L. Andres, C. Gonzalez, M. Head-Gordon, E. S. Replogle and J. A. Pople, Gaussian, Inc., Pittsburgh PA, 1998.

[253] Garavelli, M.; Negri, F.; Olivucci, M. *J. Am. Chem. Soc.* **1999**, *121*, 1023–1029.

[254] Wanko, M.; Garavelli, M.; Bernardi, F.; Niehaus, T. A.; Frauenheim, T.; Elstner, M. *J. Chem. Phys.* **2004**, *120*, 1674–1692.

[255] Terstegen, F.; Buß, V. *J. Mol. Struct. (Theochem)* **1998**, *430*, 209–218.

[256] Bartl, F. J.; Fritze, O.; Ritter, E.; Herrmann, R.; Kuksa, V.; Palczewski, K.; Hofmann, K. P.; Ernst, O. P. October **2005**, *280*(40), 34259–34267.

[257] Casida, M. E.; Gutierrez, F.; Guan, J.; Gadea, F.-X.; Salahub, D.; Daudey, J.-P. *J. Chem. Phys.* **2000**, *113*(17), 7062.

[258] Tozer, D. J.; Amos, R. D.; Handy, N. C.; Roos, B. O.; Serrano-Andres, L. *Mol. Phys.* **1999**, *97*, 859–868.

[259] Dreuw, A.; Fleming, G. R.; Head-Gordon, M. *J. Phys. Chem. B* **2003**, *107*, 6500–6503.

[260] Dreuw, A.; Head-Gordon, M. *J. Am. Chem. Soc.* **2004**, *126*, 4007–4016.

[261] Dreuw, A.; Weisman, J. L.; Head-Gordon, M. *J. Chem. Phys.* **2003**, *119*(6), 2943–2946.

[262] Bifone, A.; de Groot, H. J. M.; Buda, F. *J. Phys. Chem. B* **1997**, *101*, 2954–2958.

[263] Ziegler, T.; Rauk, A.; Baerends, E. J. *Theor. Chim. Acta* **1977**, *43*, 261–271.

[264] Molteni, C.; Frank, I.; Parrinello, M. *J. Am. Chem. Soc.* **1999**, *121*, 12177–12183.

[265] Cembran, A.; Bernardi, F.; Olivucci, M.; Garavelli, M. *J. Am. Chem. Soc.* **2004**, *126*(49), 16018–16037.

[266] Garavelli, M.; Bernardi, F.; Robb, M. A.; Olivucci, M. *J. Mol. Struct. (Theochem)* **1999**, *463*, 59–64.

[267] Migani, A.; Robb, M. A.; Olivucci, M. *J. Am. Chem. Soc.* **2003**, *125*, 2804–2808.

[268] Hayashi, S.; Tajkhorshid, E.; Schulten, K. *Biophys. J.* **2003**, *85*, 1440.

[269] Vreven, T.; Bernardi, F.; Garavelli, M.; Olivucci, M.; Robb, M. A.; Schlegel, H. B. *J. Am. Chem. Soc.* **1997**, *119*, 12687–12688.

[270] Gao, J. *J. Am. Chem. Soc.* **1994**, *116*, 9324–9328.

[271] Luecke, H.; Richter, H. T.; Lanyi, J. K. *Science* **1998**, *280*, 1934.

[272] Buß, V.; Schreiber, M.; Fülscher, M. P. *Angew. Chem. Int. Ed.* **2001**, *40*, 3189–3190.

[273] Schreiber, M.; Buß, V.; Fülscher, M. P. *Phys. Chem. Chem. Phys.* **2001**, *3*, 3906–3912.

[274] Schreiber, M.; Buß, V. *Phys. Chem. Chem. Phys.* **2002**, *4*, 3305–3310.

[275] Fantacci, S.; Migani, A.; Olivucci, M. *J. Phys. Chem. A* **2004**, *108*, 1208–1213.

[276] Schwemer, J.; Langer, H. *Methods Enzymol.* **1982**, *81*, 182–190.

[277] Yokoyama, S. *Prog. Retinal Eye Res.* **2000**, *19*, 385–419.

[278] Andersen, L. H.; Nielsen, I. B.; Kristensen, M. B.; Ghazaly, M. O. A. E.; Haacke, S.; Nielsen, M. B.; Åxman Petersen, M. *J. Am. Chem. Soc.* **2005**, *127*, 12347–12350.

[279] Chizhov, I.; Schmies, G.; Seidel, R.; Sydor, J. R.; Lüttenberg, B.; Engelhard, M. *Biophys. J.* **1998**, *75*, 999–1009.

[280] Hoffmann, M.; Wanko, M.; Strodel, P.; König, P. H.; Frauenheim, T.; Schulten, K.; Thiel, W.; Tajkhorshid, E.; Elstner, M. *J. Am. Chem. Soc.* **2006**, *128*, 10808–10818.

[281] Wanko, M.; Hoffmann, M.; Strodel, P.; Koslowski, A.; Thiel, W.; Neese, F.; Frauenheim, T.; Elstner, M. *J. Phys. Chem. B* **2005**, *109*, 3606–3615.

[282] Hufen, J.; Sugihara, M.; Buss, V. *J. Phys. Chem.* **2004**, *108*, 20419–20426.

[283] Kusnetzow, A.; Singh, D. L.; Martin, C. H.; Barani, I. J.; Birge, R. R. *Biophys. J.* **1999**, *76*, 2370–2389.

[284] Fujimoto, K.; ya Hasegawa, J.; Hayashi, S.; Kato, S.; Nakatsuji, H. *Chem. Phys. Lett.* **2005**, *414*, 239–242.

[285] Matsuura, A.; Sato, H.; Houjou, H.; Saito, S.; Hayashi, T.; Sakurai, M. *J. Comput. Chem.* **2006**, *27*, 1623–1630.

[286] Gao, J.; Alhambra, C. *J. Am. Chem. Soc.* **1997**, *119*, 2962–2963.

[287] Bayly, C. I.; Cieplak, P.; Cornell, W. D.; Kollman, P. *J. Phys. Chem.* **1993**, *97*, 10269–10280.

[288] van Duijnen, P. T.; Swart, M. April **1998**, *102*(14), 2399–2407.

[289] Jensen, L.; van Duijnen, P. T.; Snijders, J. G. *J. Chem. Phys.* **2003**, *118*, 514–521.

[290] Champagne, B.; Perpète, E. A.; van Gisbergen, S. J. A.; Baerends, E.-J.; Snijders, J. G.; Soubra-Ghaoui, C.; Robins, K. A.; Kirtman, B. *J. Chem. Phys.* **1998**, *109*(23), 10489–10498.

[291] Champagne, B.; Perpète, E. A.; Jacquemin, D.; van Gisbergen, S. J. A.; Baerends, E.-J.; Soubra-Ghaoui, C.; Robins, K. A.; Kirtman, B. *J. Phys. Chem. A* **2000**, *104*(20), 4755–4763.

[292] van Gisbergen, S. J. A.; Schipper, P. R. T.; Gritsenko, O. V.; Baerends, E. J.; Snijders, J. G.; Champagne, B.; Kirtman, B. *Phys. Rev. Lett.* **1999**, *83*(4), 694–697.

[293] Gritsenko, O. V.; van Gisbergen, S. J. A.; Schipper, P. R. T.; Baerends, E. J. *Phys. Rev. A* **2000**, *62*, 012507.

[294] Giese, T. J.; York, D. M. June **2004**, *120*(21), 9903–9906.

[295] Giese, T. J.; York, D. M. October **2005**, *123*(16), 164108.

[296] Frähmcke, J.; Hoffmann, M.; Wanko, M.; Elstner, M. *J. Am. Chem. Soc.* **2008**.

[297] Neese, F. August , **2005**.

[298] Adamo, C.; Barone, V. December **1998**, *298*(1-3), 113–119.

[299] Okada, T.; Sugihara, M.; Bondar, A.; Elstner, M.; Entel, P.; Buss, V. *J. Mol. Biol.* **2004**, *342*, 571–583.

[300] Royant, A.; Nollert, P.; Edmann, K.; Neutze, R.; Landau, E. M.; Pebay-Peyroula, E.; Navarro, J. *PNAS* **2001**, *98*, 10131–10136.

[301] Dinner, A. R.; Lopez, X.; Karplus, M. *Theor. Chem. Acc.* **2003**, *109*, 118.

[302] Yang, Y.; Cui, Q. April **2007**, *111*(16), 3999–4002.

[303] Wanko, M.; Hoffmann, M.; Frauenheim, T.; Elstner, M. *J. Phys. Chem. B* **2008**, *112*, 11462–11467.

[304] Onsager, L. *J. Am. Chem. Soc.* **1936**, *58*, 1486–1493.

[305] Simonson, T.; Archontis, G.; Karplus, M. October **1997**, *101*(41), 8349–8362.

[306] Lee, F. S.; Chu, Z. T.; Warshel, A. *J. Comput. Chem.* **1993**, *14*, 161–185.

[307] Nathans, J. *Biochemistry* **1990**, *29*(41), 9746–9752.

[308] Reed, A. E.; Weinstock, R. B.; Weinhold, F. *J. Chem. Phys.* **1985**, *83*(2), 735–746.

[309] Gaussian 03, Revision B.04, M. J. Frisch, G. W. Trucks, H. B. Schlegel, G. E. Scuseria, M. A. Robb, J. R. Cheeseman, J. A. Montgomery, Jr., T. Vreven, K. N. Kudin, J. C. Burant, J. M. Millam, S. S. Iyengar, J. Tomasi, V. Barone, B. Mennucci, M. Cossi, G. Scalmani, N. Rega, G. A. Petersson, H. Nakatsuji, M. Hada, M. Ehara, K. Toyota, R. Fukuda, J. Hasegawa, M. Ishida, T. Nakajima, Y. Honda, O. Kitao, H. Nakai, M. Klene, X. Li, J. E. Knox, H. P. Hratchian, J. B. Cross, C. Adamo, J. Jaramillo, R. Gomperts, R. E. Stratmann, O. Yazyev, A. J. Austin, R. Cammi, C. Pomelli, J. W. Ochterski, P. Y. Ayala, K. Morokuma, G. A. Voth, P. Salvador, J. J. Dannenberg, V. G. Zakrzewski, S. Dapprich, A. D. Daniels, M. C. Strain, O. Farkas, D. K. Malick, A. D. Rabuck, K. Raghavachari, J. B. Foresman, J. V. Ortiz, Q. Cui, A. G. Baboul, S. Clifford, J. Cioslowski, B. B. Stefanov, G. Liu, A. Liashenko, P. Piskorz, I. Komaromi, R. L. Martin, D. J. Fox, T. Keith, M. A. Al-Laham, C. Y. Peng, A. Nanayakkara, M. Challacombe, P. M. W. Gill, B. Johnson, W. Chen, M. W. Wong, C. Gonzalez, and J. A. Pople, Gaussian, Inc., Pittsburgh PA, 2003.

[310] ORCA—An Ab Initio, DFT and Semiempirical electronic structure package, Version 2.6 - Revision 35, Universität Bonn. February **2008**.

[311] Clark, T.; Chandrasekhar, J.; Spitznagel, G. W.; Schleyer, P. V. *J. Comput. Chem.* **1983**, *4*(3), 294–301.

[312] Krishnan, R.; Binkley, J. S.; Seeger, R.; Pople, J. A. *J. Chem. Phys.* **1980**, *72*(1), 650–654.

[313] Longuet-Higgins, H. C.; Pople, J. A. *J. Chem. Phys.* **1957**, *27*, 192–194.

[314] Yan, E. C. Y.; Kazmi, M. A.; De, S.; Chang, B. S. W.; Seibert, C.; Marin, E. P.; Mathies, R. A.; Sakmar, T. P. *Biochemistry* **2002**, *41*(11), 3620–3627.

[315] Altun, A.; Yokoyama, S.; Morokuma, K. June **2008**, *112*(22), 6814–6827.

[316] Altun, A.; Yokoyama, S.; Morokuma, K. July **2008**, *84*(4), 845–854.

[317] Tachikawa, H.; Iyama. *J. Photoch. Photobio. B* **2004**, *76*, 55–60.

[318] Send, R.; Sundholm, D. September **2007**, *111*(36), 8766–8773.

[319] Altun, A.; Yokoyama, S.; Morokuma, K. *J. Phys. Chem. B* **2008**, *112*(51), 16883–16890.

[320] Altun, A.; Kumar, D.; Neese, F.; Thiel, W. December **2008**, *112*(50), 12904–12910.

[321] Phatak, P.; Frähmcke, J. S.; Wanko, M.; Hoffmann, M.; Strodel, P.; Smith, J.; Suhai, S.; Bondar, A.-N.; Elstner, M. *J. Am. Chem. Soc.* **2009**, *131*, 7064–7078.

Acknowledgements

First, I want to thank Prof. Thomas Frauenheim, who cordially adopted me in his group and arranged a smooth and continuous funding of my research at the Universities of Paderborn and Bremen, and Prof. Marcus Elstner, who invoked my interest in excited-state methodology and theoretical biophysics and supported me with advice and counsel through all the years.

The main financial support for this work was provided by the Deutsche Forschungsgemeinschaft in the framework of Forschergruppe 490 "Molecular Mechanism of Retinal Protein Action".

I am grateful to Prof. Walter Thiel for providing the OM2/GUGACI code, Prof. Paul Tavan for providing the individual-selection MRCI implementation, and Prof. Frank Neese for his great support with the SORCI code and his ORCA program suite.

I thank Thomas Niehaus for introducing me into TDDFT and Prof. Gotthard Seifert, Zoltán Hajnal, Uwe Gerstmann, Christof Koehler, and Paul Strodel for the many fruitful discussions during my struggle through problems of DFT, the DFTB method, and MRCI. Further, Marco Garavelli for hosting me in his Bologna group and explaining to me the view of the quantum chemist, Alessandro Cembran for his introduction to CASSCF, Prof. Markus Meuwly for a great time in Basel and discussions on proton transfer and Rydberg states.

I thank particularly my closest colleagues Dávid Heringer and Michael Hoffmann for the excellent and cheerful collaboration and Alessio Gagliardi for exciting discussion on general physics topics. Further Jan Frähmcke, who continued the molecular modeling work of Michael on bovine rhodopsins.

I thank our most committed secretaries Astrid Canisius, Simone Lange, Juliane Schoppe, Christine Frauenheim and the "voluntary" system administrators, who enabled me to work efficiently without caring about all the deeper technical issues, mostly, Michael Sternberg, Zoltán Hajnal, Christof Koehler, Peter König, Marc Amkreutz, and Jan Knaup.

I also thank all the people that contributed to the great atmosphere in and outside the group, joining me in cultural, social, and nerd activities ("…diese Tür?!"), badminton, sailing, hiking, gastronomic adventures, in particular, Dávid, Alessio, Enrica, Balint, Gabi, Betti, Pia, Boris, Michael, Jan, Marc, Christof, Peter, Prasad, Simone, Alessandro, Anna-Maria, Michele, Piero, Gemma, Adam, Ney, and Yong Wang.

Last but not least, I thank my grandfather, Franz Wanko, for giving me my first comprehensive definition of the notion *science*, my parents for all their love and support during my education, and my grandmother, Magdalene Harmsen-Wanko, for waiting so patiently for my degree.